

AD-A162 134

12

AD E 440 307

ARLCB-SP-85009

PROCEEDINGS OF THE
FOURTH U S ARMY SYMPOSIUM ON GUN DYNAMICS
VOLUME I OF II

HILTON INN OF THE PALM BEACHES
RIVIERA BEACH, FL

7-9 MAY 1985

DTIC
ELECTE
NOV 14 1985
S A

DTIC FILE COPY

SPONSORED BY

US ARMY ARMAMENT RESEARCH AND DEVELOPMENT CENTER
LARGE CALIBER WEAPON SYSTEMS LABORATORY
BENET WEAPONS LABORATORY
WATERVLIET, N. Y. 12189

APPROVED FOR PUBLIC RELEASE, DISTRIBUTION UNLIMITED

85 11 12 036

DISCLAIMER

The findings in this report are not to be construed as an official Department of the Army position unless so designated by other authorized documents.

The use of trade name(s) and/or manufacture(s) does not constitute an official indorsement or approval.

DISPOSITION

Destroy this report when it is no longer needed. Do not return it to the originator.

**PROCEEDINGS OF THE
FOURTH US ARMY SYMPOSIUM
ON GUN DYNAMICS**

**HILTON INN OF THE PALM BEACHES
RIVIERA BEACH, FL**

7-9 MAY 1985

EDITORS:

**DR. THOMAS E. SIMKINS,
BENET WEAPONS LABORATORY, LCWSL AMCCOM
DR. J. VASILAKIS,
BENET WEAPONS LABORATORY, LCWSL, AMCCOM**

SPONSORED BY

**US ARMY ARMAMENT RESEARCH AND DEVELOPMENT CENTER
LARGE CALIBER WEAPON SYSTEMS LABORATORY
BENET WEAPONS LABORATORY
WATERVLIET, N. Y. 12189**

| REPORT DOCUMENTATION PAGE | | READ INSTRUCTIONS BEFORE COMPLETING FORM |
|--|-------------------------------------|--|
| 1. REPO NUMBER ARLCB-SP-85009 | 2. GOVT ACCESSION NO. AD-A162134 | 3. RECIPIENT'S CATALOG NUMBER |
| 4. TITLE (and Subtitle) PROCEEDINGS, FOURTH U.S. ARMY SYMPOSIUM ON GUN DYNAMICS VOL.1 of II VOLS. | | 5. TYPE OF REPORT & PERIOD COVERED Final |
| | | 6. PERFORMING ORG. REPORT NUMBER |
| 7. AUTHOR(s) Editors: Dr. T. E. Simkins Dr. J. Vasilakis | | 8. CONTRACT OR GRANT NUMBER(s) |
| 9. PERFORMING ORGANIZATION NAME AND ADDRESS US Army Armament Research & Development Center Benet Weapons Laboratory, SMCAR-LCB-TL Watervliet, NY 12189-5000 | | 10. PROGRAM ELEMENT, PROJECT, TASK AREA & WORK UNIT NUMBERS N.A. |
| 11. CONTROLLING OFFICE NAME AND ADDRESS US Army Armament Research & Development Center Large Caliber Weapon Systems Laboratory Dover, NJ 07801-5001 | | 12. REPORT DATE May 1985 |
| | | 13. NUMBER OF PAGES 292 |
| 14. MONITORING AGENCY NAME & ADDRESS (if different from Controlling Office) | | 15. SECURITY CLASS. (of this report) Unclassified |
| | | 15a. DECLASSIFICATION/DOWNGRADING SCHEDULE |
| 16. DISTRIBUTION STATEMENT (of this Report) Approved for public release; Distribution unlimited | | |
| 17. DISTRIBUTION STATEMENT (of the abstract entered in Block 20, if different from Report) | | |
| 18. SUPPLEMENTARY NOTES Presented at the Fourth U.S. Army Symposium on Gun Dynamics, 7-9 May 1985, at the Hilton Inn of the Palm Beaches, Riviera Beach, Florida. | | |
| 19. KEY WORDS (Continue on reverse side if necessary and identify by block number) Acquisition Precision Ballistics Stabilization Barrel Vibration Target Acquisition Dynamics | | |
| 20. ABSTRACT (Continue on reverse side if necessary and identify by block number) This represents a compilation of thirty-four technical papers concerning analyses, design, measurement, and automation of gun dynamics. The authors represent a cross-section of the scientific and technical community, including universities, industrial, and Government research laboratories. | | |

TABLE OF CONTENTS

Page

VOLUME I

OPENING REMARKS:

Thomas E. Davidson, Armament Research and Development Center

GENERAL SESSION I.

CHAIRMAN:

Herbert E. Cohen, Army Materiel Systems Analysis Activity

1. A RE-EXAMINATION OF THE EQUATIONS OF MOTION OF A CURVED AND TWISTED GUN TUBE I-1

Herbert B. Kingsbury, University of Delaware and Ballistic Research Laboratory
2. NORMAL MODE ANALYSIS OF GUN TUBE DYNAMICS I-22

H. J. Sneek and R. Gast, Armament Research and Development Center
3. PROJECTILE FOUNDATION MOMENT GENERATION I-51

Edward M. Patton, Battelle, Pacific Northwest Laboratory
4. A NONLINEAR TRACKING FILTER I-68

Dominick Andrisani II, Purdue University; Frank Kuhl, Armament Research and Development Center; and Daniel Gleason, Wright-Patterson Air Force Base
5. STRUCTURED MANAGEMENT OF DATA ACQUISITION AND REDUCTION AT THE TEST SITE (SMARTS) I-86

Jeffrey M. Fornoff, Armament Research and Development Center
6. FINITE-ELEMENT ANALYSIS OF AN ANNULAR, REGENERATIVE PISTON . . . I-106

Cris Watson, Ballistic Research Laboratory



| | |
|--------------------|-------------------------------------|
| Accession For | |
| NTIS CRA&I | <input checked="" type="checkbox"/> |
| DTIC TAB | <input type="checkbox"/> |
| Unannounced | <input type="checkbox"/> |
| Justification | |
| By | |
| Distribution / | |
| Availability Codes | |
| Dist | Avail and/or Special |
| A-1 | |

GENERAL SESSION II.

CHAIRMAN:

Gary Anderson, Army Research Office

| | |
|---|-------|
| 1. PHOTOELASTICITY APPLIED TO GUN COMPONENTS | II-1 |
| Robert J. Radkiewicz and Robert A. Peterson, Armament Research and Development Center | |
| 2. IN-BORE PROJECTILE MOTION IN A 37-MM WEAPON SYSTEM | II-12 |
| Susan A. Coates and James N. Walbert, Ballistic Research Laboratory | |
| 3. THE RELATIONSHIP OF GUN DYNAMICS TO ACCURACY IN A 120-MM TANK GUN | II-33 |
| James N. Walbert, Ballistic Research Laboratory | |
| 4. A STUDY OF PROJECTILE ACCURACY | II-34 |
| Bailey T. Haug, Ballistic Research Laboratory | |
| 5. TORSIONAL IMPULSE STUDY FOR ARTILLERY FIRED 155 MM PROJECTILES | II-51 |
| Neil A. Lapetina, Sandia National Laboratories; John M. Miller, Harry Diamond Laboratories; and Kok Chung, Armament Research and Development Center | |
| 6. IN-BORE PROJECTILE MOTIONS | II-70 |
| Martin T. Soifer and Robert S. Becker, S&D Dynamics | |
| 7. AUTOMATED DYNAMIC ANALYSIS OF WEAPON SYSTEMS | II-89 |
| Philip Benzkofer, Armament Research and Development Center | |

GENERAL SESSION III.

Chairman:
Bruce P. Burns, Ballistic Research Laboratory

1. EFFECTS OF RECOILING MASS REDUCTION OF ACTIVE RECOIL CONTROL III-1

Philip E. Townsend, Armament Research and Development Center and Robert F. Gartner, Honeywell, Inc.
2. DYNAMIC MODELING OF THE ADVANCED GUN MOUNT FOR THE HOWITZER IMPROVEMENT PROGRAM III-12

William T. Zepp, Armament Research and Development Center
3. MEASUREMENTS OF MUZZLE BLAST SHAPING AND LOADING EXERTED UPON SURROUNDING STRUCTURES OF AIRCRAFT GUNS III-23

Gert Pauly, Erprobungsstelle der Bundeswehr
4. WEAPON RECOIL FORCES AND VEHICLE MOTIONS III-40

Martin D. Thomas, Royal Armament Research and Development Establishment

VOLUME II

- 5a. TECHNOLOGY REVIEW ON PROJECTILE GUN DISENGAGEMENT III-50

Rurik K. Loder, Ballistic Research Laboratory and Roger K. Fancett, Royal Armament Research and Development Establishment
- 5b. DESCRIPTION OF THE JOINT BRL-RARDE 40-MM FIRING EXPERIMENT TO DEFINE PROJECTILE LAUNCH III-51

Jimmy Q. Schmidt, Ballistic Research Laboratory and Thomas O. Andrews, Royal Armament Research and Development Establishment

| | <u>Page</u> |
|--|-------------|
| 5c. RESULTS OF THE BRL-RARDE 40 MM FIRING EXPERIMENT TO DEFINE PROJECTILE LAUNCH | III-76 |
| Rurik K. Loder and Emma M. Wineholt, Ballistic Research Laboratory and Roger K. Fancett, Royal Armament Research and Development Establishment | |
| 5d. DATA ANALYSIS PROCEDURE FOR THE SCHMIDT DISPLACEMENT TRANSDUCER TO EXTRACT PROJECTILE LAUNCH AND MUZZLE MOTION | III-77 |
| Rurik K. Loder and Emma M. Wineholt, Ballistic Research Laboratory | |
| 5e. ASSESSMENT OF THE SCHMIDT DISPLACEMENT TRANSDUCER AND A MEANS FOR THE DETERMINATION OF PROJECTILE LAUNCH AND MUZZLE MOTION | III-78 |
| Rurik K. Loder, Ballistic Research Laboratory and Roger K. Fancett, Royal Armament Research and Development Establishment | |

GENERAL SESSION IV.

Chairman:

Julian J. Wu, Research, Development & Standardization Group

| | |
|--|-------|
| 1. THE PREDICTED EFFECT IN GUN JUMP DUE TO CHANGES IN GUN CRADLE BEARINGS AND GUN BARREL STIFFNESS | V-92* |
| P. H. Penny, Royal Armament Research and Development Establishment and W. P. King, Royal Military College of Science | |
| 2. CORROBORATIVE MEASUREMENTS OF THE TRANSVERSE MOTION OF A GUN TUBE DURING FIRING | IV-1 |
| T. E. Simkins, G. A. Pflagl, and R. D. Scanlon, Armament Research and Development Center | |
| 3. THE DEVELOPMENT OF AN ALGORITHM FOR SHOT/BARREL INTERACTION CALCULATIONS | IV-17 |
| Peter G. Thomasson, Cranfield Institute of Technology | |

*This paper arrived too late to be included with the papers in this session.
It is the last paper in Volume II.

| | <u>Page</u> |
|--|-------------|
| 4. RECENT ADVANCES IN THE SHOCK-AID GUN MODELLING CAPABILITY . . . | IV-46 |
| K. Varce and M. Seymour, Hunting Engineering Limited | |
| 5. THE EFFECT OF BEARING CLEARANCE AND BARREL EXPANSION ON BARREL RESPONSE | IV-54 |
| David N. Bulman, Royal Military College of Science, | |
| 6. A SIMPLE THEORETICAL MODEL OF SHOT/BARREL INTERACTION WITHIN A SMOOTH BORE GUN | IV-77 |
| S. E. Powell, Royal Military College of Science | |
| 7. ANALYSIS OF SOURCES OF ERROR IN TANK GUN FIRING | IV-94 |
| Edward M. Schmidt and Joseph W. Kochenderfer, Ballistic Research Laboratory | |

GENERAL SESSION V.

Chairman:

Philip Benzkofer, Armament Research & Development Center

| | |
|--|------|
| 1. A THREE-DIMENSIONAL COLOR COMPUTER GRAPHICS PROGRAM FOR DISPLAY OF PROJECTILE GUN DYNAMICS | V-1 |
| Kathleen L. Zimmerman, Ballistic Research Laboratory | |
| 2. AN INSIGHT INTO GUN TUBE VIBRATIONS | V-12 |
| S. H. Chu, Armament Research and Development Center | |
| 3. LIGHT ARTILLERY RECOIL MECHANISMS | V-39 |
| Stephen G. Floroff and Norman T. Lionetti, Armament Research and Development Center | |
| 4. EFFECT OF THE FLICK RAMMING ENVIRONMENT ON SELECTED ARTILLERY FUZES | V-57 |
| Robert X. Brennan, Armament Research and Development Center | |

5. A SYSTEMS ANALYSIS OF LIQUID PROPELLANT IN A 155 MM SP
ARTILLERY SYSTEM V-79

Jack Brooks, Armament Research and Development
Center

6. AN INTEGRATED WEAPON ARMORED VEHICLE MODEL (IWAVM) AND
COMPUTER SIMULATION V-80

John Groff, Army Materiel Systems Analysis
Activity; James N. Walbert, Ballistics Research
Laboratory; and Thomas Dolce, Army Materiel Systems
Analysis Activity

FOREWORD

The precision of a gun system clearly involves the dynamics of the gun carrier, ground characteristics, and interior and exterior ballistics. It is a problem of enormous complexity and is often divided into different phases for investigative purposes. While the division of the task is convenient and often necessary, one should always keep in mind that the different phases interact and the dynamic forces are usually coupled. This fact necessitates an interactive process or, better yet, a complete system approach, if at all possible, to the precision problem.

During recent years, one has witnessed great strides in various branches of continuum mechanics, kinematic designs, and numerical and computer techniques for solving problems of great complexity as well as in the areas of experimental mechanics and instrumentation. It appears feasible now more than ever to gain understanding and to improve the design of gun systems for greater accuracy by exploiting the new technological advances. The present Symposium represents the continuing interest of the U.S. Army in this direction.

These proceedings contain nearly thirty-five papers presented at the Symposium held at the Hilton Inn of the Palm Beaches, Riviera Beach, FL, during 7-9 May 1985. The papers represent the current research efforts on gun dynamics and its effect on precision and design by industrial, university, and Department of Defense Laboratories in the United States and two allied nations - the United Kingdom and the Federal Republic of West Germany.

The editors gratefully acknowledge the work of Ellen Fogarty in preparing volumes I and II of Gun Dynamics, and her assistance in the collection of the papers and the required clearances.

LIST OF ATTENDEES

Gary L. Anderson
Army Research Office
P.O. Box 12211
Research Triangle Park, NC 27709-2211

Robert S. Becker
S&D Dynamics
755 New York Avenue
Huntington, NY 11743

Gerald A. Benedetti
Sandia National Laboratories
East Avenue
Livermore, CA 94550-0096

Willard R. Benson
Aerojet Ordnance Company
Rockaway Townsquare Office Park
33 Mt. Hope Avenue, Suite 103
Rockaway, NJ 07866

Philip Benzkofer
Armament Research & Development Center
SMCAR-SCA
Dover, NJ 07801-5001

John Bostonian III
Armament Research & Development Center
SMCAR-LCU-SI
Dover, NJ 07801-5001

Robert X. Brennan
Armament Research & Development Center
SMCAR-LCN
Dover, NJ 07801-5001

Jack Brooks
Armament Research & Development Center
SMCAR-LCS
Dover, NJ 07801-5001

David N. Bulman
Royal Military College of Science
Land Systems Group
Shrivenham
Swindon Wilts SN6 8LA England

Bruce P. Burns
Ballistic Research Laboratory
AMXBR-IBD
Aberdeen Proving Ground, MD 21005-5066

S. F. Chu
Armament Research & Development Center
SMCAR-LCA
Dover, NJ 07801-5001

Kok Chung
Armament Research & Development Center
SMCAR-LC
Dover, NJ 07801-5001

Susan A. Coates
Ballistic Research Laboratory
AMXBR-IBD
Aberdeen Proving Ground, MD 21005-5066

Herbert E. Cohen
Army Materiel Systems Analysis Activity
AMXSY-MP
Aberdeen Proving Ground, MD 21005-5071

P. A. Cox
Southwest Research Institute
6220 Culebra Road
P.O. Drawer 28510
San Antonio, TX 78284

Thomas E. Davidson
Armament Research & Development Center
SMCAR-LC
Dover, NJ 07801-5001

Thomas Dolce
Army Materiel Systems Analysis Activity
AMXSY-CB
Aberdeen Proving Ground, MD 21005-5071

Patricia M. Dutko
Armament Research & Development Center
SMCAR-LCA-G
Dover, NJ 07801-5001

Thomas F. Erline
Ballistic Research Laboratory
AMXBR-IBD
Aberdeen Proving Ground, MD 21005-5066

Roger K. Fancett
Royal Armament Research & Development
Establishment
Fort Halstead
Seven Oaks, Kent TN14 7BP
England

Stephen Floroff
Armament Research & Development Center
SMCAR-LCW-E
Dover, NJ 07801-5001

Jeffrey M. Fornoff
Armament Research & Development Center
SMCAR-TSB
Dover, NJ 07801-5001

Paul L. Fritch
Armament Research & Development Center
SMCAR-LC
Dover, NJ 07801-5001

Robert F. Gartner
Honeywell, Inc.
5901 South County Road 18
Edina, MN 55436-5000

Ronald Gast
Armament Research & Development Center
Benet Weapons Laboratory
Watervliet, NY 12189-5000

Daniel Gleason
Air Force Institute of Technology
Wright Patterson Air Force Base
Dayton, OH 45433

John Groff
Army Materiel Systems Analysis Activity
AMXSY-CB
Aberdeen Proving Ground, MD 21005-5071

Richard G. Hasenbein
Armament Research & Development Center
Benet Weapons Laboratory
Watervliet, NY 12189-5000

Bailey T. Haug
Ballistic Research Laboratory
AMXBR-IBD
Aberdeen Proving Ground, MD 21005-5066

David High
Hercules, Inc.
Allegany Ballistic Laboratory
P.O. Box 210
Cumberland, MD 21502

Tonney Hung
Armament Research & Development Center
SMCAR-SCS-E
Dover, NJ 07801-5001

Sidney S. Jacobson
Armament Research & Development Center
SMCAR-TDT
Dover, NJ 07801-5001

W. P. C. King
Royal Military College of Science
School of Mechanical Materials & Civil
Engineering
Shrivenham
Swindon Wilt: SN6 8LA England

Herbert B. Kingsbury
University of Delaware
Department of Mechanical & Aerospace
Engineering
Newark, DE 19711

Bruce Knutelsky
Armament Research & Development Center
SMCAR-LCA-M
Dover, NJ 07801-5001

George Kobori
FMC Corporation - Ordnance Division
1105 Coleman Avenue
Box 1201
San Jose, CA 95108

Frank Kuhl
Armament Research & Development Center
SMCAR-SCF-RE
Dover, NJ 07801-5001

Scott Langlie
FMC Corporation
Northern Ordnance Division
4800 E. River Road
Minneapolis, MN 55421

Neil A. Lapetina
Sandia National Laboratories
East Avenue
Livermore, CA 94550-0096

Norman T. Lionetti
Armament Research & Development Center
SMCAR-LCW-E
Dover, NJ 07801-5001

Rurik K. Loder
Ballistic Research Laboratory
AMXBR-IBD
Aberdeen Proving Ground, MD 21005-5066

John M. Miller
Harry Diamond Laboratories
DELHD-DE-FT
2800 Powder Mill Road
Adelphia, MD 20783-1197

Albert H. Mitchell
Armament Research & Development Center
SMCAR-SCA
Dover, NJ 07801-5001

Lionel Pasiuk
Naval Sea Systems Command
SEA-62R41
Washington, D.C. 20362-5101

Edward M. Patton
Battelle, Pacific Northwest Labs
Battelle Road
Richland, WA 99352

P. H. G. Penny
Royal Armament Research & Development
Establishment
Chobham Lane
Chertsey, Surrey KT16 OEE
England

Robert Peterson
Armament Research & Development Center
SMCAR-SCS-EW
Rock Island, IL 61299-7300

George Pflegl
Armament Research & Development Center
Benet Weapons Laboratory
Watervliet, NY 12189-5000

S. E. Powell
Royal Military College of Science
Land Systems Group
Shrivenham
Swindon Wilts SN6 8LA England

Robert J. Radkiewicz
Armament Research & Development Center
SMCAR-SCS-EW
Rock Island, IL 61299-7300

Frederick E. Saxe
Armament Research & Development Center
SMCAR-LCA-M
Dover, NJ 07801-5001

Edward M. Schmidt
Ballistic Research Laboratory
AMXBR-IBD
Aberdeen Proving Ground, MD 21005-5066

Jimmy Q. Schmidt
Ballistic Research Laboratory
AMXBR-IBD
Aberdeen Proving Ground, MD 21005-5066

Mark J. Seymour
Hunting Engineering Limited
Reddings Wood, Ampthill
Bedfordshire MK45 2HD England

Thomas E. Simkins
Armament Research & Development Center
Benet Weapons Laboratory
Watervliet, NY 12189-5000

Martin T. Soifer
S&D Dynamics
755 New York Avenue
Huntington, NY 11743

G. D. Stalley
Honeywell, Inc.
5901 S. County Road 18
Edina, MN 55436-5000

Martin Thomas
Royal Armament Research & Development
Establishment
Chobham Lane
Chertsey, Surrey KT16 0EE
England

Philip E. Townsend
Armament Research & Development Center
SMCAR-SCS
Dover, NJ 07801-5001

Tien-Yu Tsui
Army Materials & Mechanics Research
Center
Watertown, MA 02172

David G. Uhrig
Air Force Armament Laboratory
Guns and Projectiles Branch
AFALT/DLJG
Eglin Air Force Base, FL 32542

John D. Vasilakis
Armament Research & Development Center
Benet Weapons Laboratory
Watervliet, NY 12189-5000

Cris Watson
Ballistic Research Laboratory
AMXBR-IBD
Aberdeen Proving Ground, MD 21005-5066

Emma M. Wineholt
Ballistic Research Laboratory
AMXBR-IBD
Aberdeen Proving Ground, MD 21005-5066

Julian J. Wu
US Army Research, Development, &
Standardization Group (UK)
Box 65
FPO, NY 09510

Adam Zak
Aeronautical & Astronautical Engr Dept.
University of Illinois
104 S. Mathews Avenue
Urbana, IL 61801-2997

William T. Zepp
Armament Research & Development Center
SMCAR-LCW-S
Dover, NJ 07801-5001

John R. Zimmerman
Armament Research & Development Center
SMCAR TSE-L
Dover, NJ 07801-5001

Kathleen L. Zimmerman
Ballistic Research Laboratory
AMXBR-IBD
Aberdeen Proving Ground, MD 21005-5066

TITLE: A Re-examination of the Equations of Motion of a Curved
and Twisted Gun Tube
Herbert B. Kingsbury
Department of Mechanical and Aerospace Engineering
University of Delaware, Newark DE 19711 and
Visiting Research Consultant
Interior Ballistics Division
Ballistic Research Laboratory
Aberdeen Proving Ground, MD 21005-5006

ABSTRACT:

The work described in this paper was motivated by a requirement for a general analytical model of a gun tube to be used to study dynamic effects and interactions caused by such phenomena as large displacements and rotations, initial space curvature of the gun tube axis, variable cross section shape and area, initial twist of cross section principal axes, and transverse shear deformation and rotating inertia.

In this paper a derivation of the equilibrium equations for a rod with general space curvature is first presented. This derivation is similar to that presented by A.E.H. Love, although more rigorous in its examination of the relative importance of higher order terms in Taylor's series expansions.

A completely general set of small strain but large displacement and rotation strain-displacement equations is then formulated for a curved and twisted rod. In these equations the displacement components are referred to the local tangent, principal normal and bi-normal space coordinates rather than to fixed global coordinates. No assumptions regarding the structural action or mode of deformation of the rod are made so that the functional form of the the displacement components is left unspecified.

Next, a technical theory of rods with space curvature is developed based on the assumptions that cross sections remain plane and undeformed. The displacements are expressed as appropriate linear combinations of three central curve displacement components and three rotation components. The equations are then further simplified by elimination of transverse shear and rotatory inertia effects. When these equations are combined the equilibrium equations, a system of four coupled equilibrium equations in the four displacement and rotation variables result.

BIOGRAPHY:

PRESENT ASSIGNMENT: Professor, Department of Mechanical and Aerospace Engineering, University of Delaware, Newark, DE.

PAST EXPERIENCE: Assistant Professor, Pennsylvania State University, State College, PA (1966-1968), Engineer with General Electric Company, Missile and Space Division, Philadelphia, PA (1964-1966), Scientist with Dyna-Structures Inc., Springfield, PA (1961-1964).

DEGREES HELD: B.S.M.E., University of Connecticut (1958). M.S.M.E., University of Pennsylvania (1960), Ph.D. E.M., University of Pennsylvania (1964).

A RE-EXAMINATION OF THE EQUATIONS OF MOTION OF A CURVED AND TWISTED GUN TUBE

HERBERT B. KINGSBURY
U.S. ARMY BALLISTIC RESEARCH LABORATORY
ABERDEEN PROVING GROUND, MD 21005-5006

1. Introduction

The work described in this report was motivated by the need to explain observed inconsistencies between measured dynamic response data and response predictions of various analytical and finite element models of gun tubes.

Although the study of vibrations of rods and bars is one of the most ancient in structural mechanics, a completely general formulation of the problem is difficult to find in the literature.

One of the seminal treatments of the derivation of equations of motion of rods with initial curvature appears in the text on Elasticity by A.E.H. Love [1]. Although restrictive forms of Love's equations are used directly, or are re-derived, by subsequent investigators of small amplitude vibrations of curved rods, there are deficiencies in Love's work which render his strain-displacement equations unsuitable as the starting point for a general examination of the motion of rods with space curvature. In Love's work, the final state of deformation is assumed to be such that cross sections remain plane and normal to the centerline of the deformed rod. By these assumptions not only is transverse shear deformation excluded but, as will be shown, kinematical inconsistencies are introduced.

Equations governing both static and dynamic deformation of curved rods are employed in such areas of structural mechanics as vibrations of curved beams, large deflection and stability analysis of beams and columns and non-linear dynamics, including stability of oscillations of beams and strings.

In spite of the large number of papers dealing with these subjects, there does not appear to have been a re-examination of Love's strain-displacement equations or a more general independent derivation. The equations of motion employed by the various investigators are either those presented by Love or are derived for each particular application on an "ad-hoc" basis.

In this paper a derivation of the equilibrium equations for a rod with general space curvature is presented in Section II. This derivation is similar to that presented by Love, although it is somewhat more rigorous in its examination of the relative importance of higher order terms in Taylor's

kingsbury

series expansions.

A completely general set of small strain but large displacement and rotation strain-displacement equations is then formulated in Section III for a rod with initial twist and arbitrary space curvature. In these equations the displacement components are referred to the local tangent, principal normal and bi-normal space curve coordinates rather than to fixed global coordinates. No assumptions regarding the structural action or mode of deformation of the rod are made so that the functional form of the displacement components is left unspecified.

In Section IV a linearized form of the general strain-displacement equations is first presented. A technical theory of rods with space curvature is then developed based in the usual beam theory assumptions that cross sections remain plane and undeformed. The displacements are then expressed as appropriate linear combinations of three central curve displacement components and three rotation components. The linearized strain displacement equations phrased in terms of the central curve displacements and cross section rotations are then used to derive force-moment-strain-curvature equations for a linear elastic rod. The equations are then further simplified by elimination of transverse shear and rotatory inertia effects. When these equations are combined the equilibrium equations, a system of four coupled equilibrium equations in the four displacement and rotation variables results.

2. Equilibrium Equations For A Rod Element

A. Force and Moment Equilibrium

A typical element of a rod with space curvature is shown in Figure 1.

The line joining centroids of cross sections is a space curve whose radius (ρ), or curvature $\kappa=1/\rho$, and torsion (λ) are arbitrary functions of arc length (s). The shape of the cross sections is arbitrary but assumed to be a continuous function of s . At the centroid of any cross section an orthogonal coordinate system (x,y,z) is constructed with corresponding unit vectors i, j, k , such that k is the unit tangent vector to the space curve determined by the line of centroids while i and j are the principal normal and bi-normal vectors respectively so that $j \times k = i$.

The principal directions of the cross section area of the rod with respect to the centroid are, in general, inclined with respect to the x, y coordinates. The angle between these two sets of coordinate axes may vary continuously with s for the case of a pre-twisted rod.

Figure 2 shows a section of curved rod of incremental length δs lying between points O and O' of the space curve of centroids. By the usual definition, the face at O is a negative face since its outward normal points in the direction opposite to the local tangent vector while the face at O' is a positive face. The usual sign convention for stress components in positive and negative faces will be employed and the force and moment resultants of the stress components ($\sigma_{xz}, \sigma_{yz}, \sigma_{zz}$) acting on a cross section of area A are

kingsbury

defined as

$$V_i = \int_A \sigma_{iz} dA, \quad i = x, y, z \quad (1a)$$

$$M_x = \int_A y \sigma_{zz} dA, \quad (2a)$$

$$M_y = - \int_A x \sigma_{zz} dA, \quad \text{and} \quad (2b)$$

$$M_z = \int (x \sigma_{yz} - y \sigma_{xz}) dA. \quad (2c)$$

The force and moment resultants acting at cross sections at points "s" and $s + \delta s$ are shown in Figure 3.

The force and moment resultants per unit length of centroidal curve of the tractions acting on the lateral surface and of the body forces acting in the interior of the element are represented by:

$$\mathbf{T} = T_x \mathbf{i} + T_y \mathbf{j} + T_z \mathbf{k} \quad (3a)$$

$$\mathbf{m} = m_x \mathbf{i} + m_y \mathbf{j} + m_z \mathbf{k}. \quad (3b)$$

For problems involving motion of the rod element, the force \mathbf{T} will contain terms involving inertia forces while the moment \mathbf{m} may contain moments of inertia forces about the three axes.

A free-body diagram of a rod element is shown in Figure 4 when points O and O' are again points in the curve of centroids at positions "s" and "s + δs " respectively. The force and moment resultants acting on the rod cross sections of these positions are indicated as well as the surface traction vector and surface traction moment resultant at a typical point $s + \zeta$ where $s < s + \zeta < s + \delta s$.

$\bar{\mathbf{R}}$ is the position vector of the point $x + \zeta$ relative to O while \mathbf{R}' is the position vector of O' relative to O .

The condition of force equilibrium applied to the rod element yields the following equation

$$\mathbf{V}(s) + \mathbf{V}(s + \delta s) + \int_s^{s+\delta s} \mathbf{T} ds = 0. \quad (4)$$

Upon expressing $\mathbf{T}(s + \zeta)$ in terms of $\mathbf{T}(s)$ and its derivatives at $\zeta=0$ using Taylor's series,

$$\int_s^{s+\delta s} \mathbf{T} ds = \mathbf{T}(s) \delta s + \left. \frac{\partial \mathbf{T}}{\partial s} \right|_s (\delta s)^2 / 2 + \dots \quad (5)$$

kingsbury

Returning to Eq. (4), we next express $V(s + \delta s)$ in terms of its value and those of its derivatives at $\delta s = 0$ using vector Taylor's series.

$$V(s + \delta s) = V(s^+) + \left. \frac{\partial V}{\partial s} \right|_s \delta s + \dots \quad (6)$$

The symbol " s^+ " is used in Eq. (6) as a reminder that this force acts on a positive face of the element.

The rate of change of the unit tangent, principal normal and binormal vectors with respect to arc length are given by the Serret - Frenet formulae as

$$dk/ds = 1/\rho \lambda \equiv \kappa i, \quad (7a)$$

$$\frac{dj}{ds} = -\lambda i, \text{ and} \quad (7b)$$

$$di/ds = \lambda j - \kappa k \quad (7c)$$

where $\kappa (= 1/\rho)$ is the local curvature of the line of centroids.

Combining Eqs. (7) and (6) and substituting this result and Eq. (5) into Eq. (4) yields three scalar equations which express the condition of force equilibrium for a rod element

$$\partial V_x / \partial s - \lambda V_y + \kappa V_z + T_x = 0, \quad (8a)$$

$$\partial V_y / \partial s + \lambda V_x + T_y = 0, \text{ and} \quad (8b)$$

$$\partial V_z / \partial s - \kappa V_x + T_z = 0. \quad (8c)$$

Next, the conditions for moment equilibrium are formulated from consideration of the free-body diagram of Figure 4. Summing moments about point 0 yields

$$\begin{aligned} M(s) + M(s + \delta s) + R' \times V(s + \delta s) \\ + \int_s^{s+\delta s} \bar{R} \times T(s) ds + \int_s^{s+\delta s} m ds = 0 \end{aligned} \quad (9)$$

Again the terms appearing in Eq. (9) must be expressed in terms of their values and those of their derivatives at " s ".

In Figure 4, R_0 , R'_0 and P are position vectors of points, at positions

kingsbury

"s", "s + δs" and "s + ζ" relative to a fixed point Q. If $\mathbf{R}'(s)$ is the position vector of any point in the space curve relative to O we may write

$$\begin{aligned} \mathbf{R}' &= \mathbf{R}'_0 - \mathbf{R}_0 \\ &= \left. \frac{d\mathbf{R}}{ds} \right|_s \delta s + \frac{1}{2} \left. \frac{d^2\mathbf{R}}{ds^2} \right|_s (\delta s)^2 + \dots \\ &= \mathbf{k} \delta s + \kappa/2 \mathbf{i} (\delta s)^2, \end{aligned} \quad (10a)$$

since by definition $\mathbf{k} = d\mathbf{R}/ds$ and by Eq. (7a) $d\mathbf{k}/ds = \kappa \mathbf{i}$.

In a similar way it is found that

$$\bar{\mathbf{R}} = \mathbf{P} - \mathbf{R}_0 = \mathbf{k}\zeta + \kappa/2 \mathbf{i} \zeta^2 \quad (10b)$$

Consequently,

$$\int_s^{s+\delta s} \bar{\mathbf{R}} \times \mathbf{T} ds = \mathbf{k}(s) \times \mathbf{T} \frac{1}{2} (\delta s)^2 \quad (11)$$

and

$$\mathbf{R}' \times \mathbf{V}(s + \delta s) = \mathbf{k} \times \mathbf{V}(s^+) \delta s + \left[\frac{1}{2} \kappa \mathbf{i} \times \mathbf{V}(s^+) + \mathbf{k} \times \left. \frac{\partial \mathbf{V}}{\partial s} \right|_{s^+} \right] (\delta s)^2 \quad (12)$$

Finally, substitution of the result given by Eqs. (11) and (12) into Eq. (9) and division by δs yields the following vector moment equilibrium equations in the limit as $\delta s \rightarrow 0$.

$$\left. \frac{\partial \mathbf{M}}{\partial s} \right|_{s^+} + \mathbf{k} \times \mathbf{V}(s^+) + \mathbf{m}(s) = 0 \quad (13)$$

To obtain the scalar equations represented by Eq. (13), $\mathbf{M}(s^+)$ is expressed in terms of its vector components and the Serret-Frenet formulae are used to transform the derivatives of the unit vectors.

The three scalar equations representing the conditions of moment equilibrium for the rod element become

$$\frac{\partial M_x}{\partial s} - \lambda M_y + \kappa M_z - V_y + m_x = 0, \quad (14a)$$

$$\frac{\partial M_y}{\partial s} + \lambda M_x + V_x + m_y = 0, \text{ and} \quad (14b)$$

kingsbury

$$\frac{\partial M_z}{\partial s} - \kappa M_x + m_z = 0 . \quad (14c)$$

Although the manner of derivation of the equations of force and moment equilibrium for a curved rod used above is different from that presented by Love [1] the resulting equations are essentially identical. Differences in form result from differences in force and moment sign conventions and because Love employs local coordinate axes which are the principal directions of the area of the local cross section of the rod rather than the natural space curve coordinates.

In general, the local x, y, z , coordinates are the deformed coordinates of the centroidal curve of the rod. The torsion and curvature terms appearing in Eqs. (12) and (21) are the total values of these quantities consisting of the sums of their initial values and their respective changes due to deformation of the centroidal curve. For small deformation analysis the initial coordinates and initial values of λ and κ are employed.

The reader is referred to a paper by E. Reissner [2] for corresponding large displacement curved beam equilibrium equations in which the force and moment components are referred to the undeformed coordinates.

B. Inertia Forces and Couples

The inertia body force, F_I , acting at any point, Q , in a cross section is defined by

$$F_I = - \gamma \ddot{u}_Q \quad (15)$$

where γ is the mass density of the material of that point, u_Q is the displacement vector associated with that point and superscript "dot" indicates differentiation with respect to time.

The displacement vector u_Q is expressed in terms of the local space curve coordinates as

$$u_Q = u i + v j + w k$$

where u, v , and w are the scalar displacement components in the x, y and z directions respectively.

Since the local coordinate system is moving in the fixed (inertial) reference frame, the acceleration vector may be expressed in the form:

$$\ddot{u}_Q = a_Q + \alpha \times u_Q + \omega \times (\omega \times u_Q) + 2 \omega \times \dot{v}_Q \quad (16)$$

where

$$\dot{v}_Q = \dot{u} i + \dot{v} j + \dot{w} k ,$$

$$a_Q = \ddot{u} i + \ddot{v} j + \ddot{w} k ,$$

kingsbury

and ω and α are the angular velocity and angular acceleration vectors respectively of the local coordinates in the fixed reference frame. For problems involving small rotations and/or small displacements of the rod cross the non-linear terms in Eq. (23) may often be neglected in comparison with a_Q .

The inertia forces and couples per unit length of rod arising from the three body force components for small motions are given by:

$$T_{Ij} = \int_A \alpha \ddot{u}_j dA \quad j = x, y, z \quad (17)$$

$$m_{Ix} = - \int_A \gamma y \ddot{w} dA, \quad (18a)$$

$$m_{Iy} = \int_A \gamma x \ddot{w} dA \quad (18b)$$

$$m_{Iz} = \int_A \gamma y \ddot{u} dA - \int_A \gamma x \ddot{v} dA. \quad (18c)$$

3. Strain-Displacement Equations

Equations relating the components of strain at a point in the rod to the displacement field are derived by considering the change in length of a line segment connecting to arbitrarily close points of the rod as the rod is deformed.

Figure 5 shows two adjacent cross-sections of the rod before deformation. The centroidal curve has initial curvature κ_0 and torsion λ_0 .

The centroid of one cross-section is point O and the other, at a small distance δs along the curve, is O'. The vector principal normal, binormal and tangent at O are \underline{i} , \underline{j} and \underline{k} respectively while the corresponding vectors at O' are denoted by \underline{i}' , \underline{j}' and \underline{k}' . Coordinates x, y, z directed along \underline{i} , \underline{j} and \underline{k} respectively comprise a local coordinate system with origin at O. Corresponding coordinates at O' are \bar{x} , \bar{y} and \bar{z} .

Point Q lies in the cross-section at O while Q' lies in that at O'. It is assumed that Q and Q' are initially arbitrarily close so that the position vector of Q', \underline{r} can be expressed as

$$\begin{aligned} \underline{r} &= \delta x \underline{i} + \delta y \underline{j} + \delta z \underline{k} \\ \underline{r} &= r \underline{n} = r \ell \underline{i} + r m \underline{j} + r n \underline{k} \end{aligned} \quad (1)$$

where δx , δy , and δz are arbitrarily small distances, r is the magnitude of \underline{r} and ℓ , m, n are the direction cosines of \underline{r} .

Figure 6 illustrates the initial and final positions of these material points as Q and Q' undergo displacements \underline{u}_Q and $\underline{u}_{Q'}$. The magnitude of the position vector of Q' with respect to Q, \underline{r}' is found by use of the following

kingsbury

vector equation relating the initial and final relative position vectors of these points to their respective displacement vectors.

$$\bar{\mathbf{r}} = \mathbf{r} + \mathbf{u}_{Q'} - \mathbf{u}_Q . \quad (4)$$

The displacement vector at point Q', adjacent to point Q, can then be expressed as

$$\mathbf{u}_{Q'} = \mathbf{u}_Q + \frac{\partial \mathbf{u}_Q}{\partial x} \delta x + \frac{\partial \mathbf{u}_Q}{\partial y} \delta y + \frac{\partial \mathbf{u}_Q}{\partial z} \delta z \quad (5)$$

where higher order terms in this Taylor's series expansion of the displacement vector about point Q have been dropped. The vector derivatives appearing in Eq. (6) are next presented in terms of their vector components,

$$\frac{\partial \mathbf{u}_Q}{\partial x} = \frac{\partial u}{\partial x} \mathbf{i} + \frac{\partial v}{\partial x} \mathbf{j} + \frac{\partial w}{\partial x} \mathbf{k} , \quad (6a)$$

$$\frac{\partial \mathbf{u}_Q}{\partial y} = \frac{\partial u}{\partial y} \mathbf{i} + \frac{\partial v}{\partial y} \mathbf{j} + \frac{\partial w}{\partial y} \mathbf{k} , \quad (6b)$$

$$\frac{\partial \mathbf{u}_Q}{\partial z} = \left(\frac{\partial u}{\partial z} - \lambda_0 v + \kappa_0 w \right) \mathbf{i} + \left(\frac{\partial v}{\partial z} + \lambda_0 u \right) \mathbf{j} + \left(\frac{\partial w}{\partial z} - u \kappa_0 \right) \mathbf{k} \quad (6c)$$

where the Serret-Frenet formulae have been used to express the rate of change of the local coordinate unit vectors along the curve in terms of the local curvature and torsion.

Substitution of Eqs. (5) and (6) into (4) and using Eq. (1) yields the following result for the position vector of Q' relative to Q:

$$\begin{aligned} \bar{\mathbf{r}} = & \mathbf{r} \left[\ell \left(1 + \frac{\partial u}{\partial x} \right) + m \frac{\partial u}{\partial y} + n \left(\frac{\partial u}{\partial z} - \lambda_0 v + \kappa_0 w \right) \right] \mathbf{i} \\ & + \mathbf{r} \left[\ell \frac{\partial v}{\partial x} + m \left(1 + \frac{\partial v}{\partial y} \right) + n \left(\lambda_0 u + \frac{\partial v}{\partial z} \right) \right] \mathbf{j} \\ & + \mathbf{r} \left[\ell \frac{\partial w}{\partial x} + m \frac{\partial w}{\partial y} + n \left(1 - \kappa_0 u + \frac{\partial w}{\partial z} \right) \right] \mathbf{k} . \end{aligned} \quad (7)$$

If the magnitudes of \mathbf{r} and $\bar{\mathbf{r}}$ are denoted by r and \bar{r} respectively, then the unit elongation, e , of the original line segment is given by ($e \ll 1$) or

$$e = \frac{1}{2} \left(\frac{\bar{r}^2}{r^2} - 1 \right) . \quad (8)$$

Upon squaring the magnitudes of the vector $\bar{\mathbf{r}}$ given by Eq. (7), substituting the result into Eq. (8), and grouping the resulting terms as coefficients of the products of the direction cosines ℓ , m and n , the elongation, e , may be expressed in the following form,

$$e = \epsilon_{xx} \ell^2 + \epsilon_{yy} m^2 + \epsilon_{zz} n^2 + 2\epsilon_{xy} \ell m + 2\epsilon_{xz} \ell n + 2\epsilon_{yz} mn \quad (9)$$

kingsbury

where

$$\epsilon_{xx} = \frac{\partial u}{\partial x} + 1/2 \left[\left(\frac{\partial u}{\partial x} \right)^2 + \left(\frac{\partial v}{\partial x} \right)^2 + \left(\frac{\partial w}{\partial x} \right)^2 \right], \quad (10a)$$

$$\epsilon_{yy} = \frac{\partial v}{\partial y} + 1/2 \left[\left(\frac{\partial u}{\partial y} \right)^2 + \left(\frac{\partial v}{\partial y} \right)^2 + \left(\frac{\partial w}{\partial y} \right)^2 \right], \quad (10b)$$

$$\begin{aligned} \epsilon_{zz} = & \frac{\partial w}{\partial z} - \kappa_0 u + 1/2 \left[\left(\frac{\partial u}{\partial z} \right)^2 + \left(\frac{\partial v}{\partial z} \right)^2 + \left(\frac{\partial w}{\partial z} \right)^2 \right] \\ & + 1/2 \left[(\kappa_0^2 + \lambda_0^2) u^2 + \lambda_0^2 v^2 + \kappa_0^2 w^2 - 2 \lambda_0 \kappa_0 v w \right. \\ & \left. - 2 \lambda_0 v \frac{\partial u}{\partial z} + 2 \lambda_0 u \frac{\partial v}{\partial z} - 2 \kappa_0 u \frac{\partial w}{\partial z} + 2 \kappa_0 w \frac{\partial u}{\partial z} \right], \quad (10c) \end{aligned}$$

$$2 \epsilon_{xy} = \frac{\partial u}{\partial y} + \frac{\partial v}{\partial x} + \frac{\partial u}{\partial x} \frac{\partial u}{\partial y} + \frac{\partial v}{\partial x} \frac{\partial v}{\partial y} + \frac{\partial w}{\partial x} \frac{\partial w}{\partial y}, \quad (10d)$$

$$\begin{aligned} 2 \epsilon_{xz} = & \frac{\partial u}{\partial z} + \frac{\partial w}{\partial x} - \lambda_0 v + \kappa_0 w + \frac{\partial u}{\partial x} \frac{\partial u}{\partial z} + \frac{\partial v}{\partial x} \frac{\partial v}{\partial z} \\ & + \frac{\partial w}{\partial x} \frac{\partial w}{\partial z} - \lambda_0 v \frac{\partial u}{\partial x} + \kappa_0 w \frac{\partial u}{\partial x} + u \frac{\partial v}{\partial x} - \kappa_0 u \frac{\partial w}{\partial x}, \quad (10e) \end{aligned}$$

$$\begin{aligned} 2 \epsilon_{yz} = & \frac{\partial v}{\partial z} + \frac{\partial w}{\partial y} + \lambda_0 u + \frac{\partial u}{\partial y} \frac{\partial u}{\partial z} + \frac{\partial v}{\partial y} \frac{\partial v}{\partial z} + \frac{\partial w}{\partial y} \frac{\partial w}{\partial z} \\ & + \lambda_0 u \frac{\partial v}{\partial y} - \kappa_0 u \frac{\partial w}{\partial y} - \lambda_0 v \frac{\partial u}{\partial y} + \kappa_0 w \frac{\partial u}{\partial y}. \quad (10f) \end{aligned}$$

By definition, the quantities ϵ_{xx} , ϵ_{yy} , ϵ_{zz} , ϵ_{xy} , ϵ_{xz} , and ϵ_{yz} are the normal and shear strains at Q referred to the local coordinates at P. Eqs. (10) therefore constitute the required strain-displacement equations.

Clearly, various approximate forms of Eq. (10) may be formulated depending upon the simplifying assumptions appropriate for a given problem. These formulations may postulate small deformations with large displacements; small deformation with small displacements but large curvatures and/or torsions; small curvatures and torsions; or various other combinations of simplifying assumptions. It is also noted that consideration of buckling or of stretch-stiffening effects requires retention of non-linear terms in Eq. (10).

4. A Technical Theory Of Rods With Initial Curvature And Torsion

A. Displacement Functions

A linearized "engineering" theory of curved rods is next developed on the

kingsbury

basis of assumptions employed in the strength of materials formulations for the bending and torsion of prismatic bars.

The fundamental assumption of both technical beam theory and that of torsion of straight rods is cross sections unchanged in size and shape after the structure is bent or twisted. It is not necessary to initially postulate that cross sections remain normal to the bent centerline.

A typical cross section is therefore assumed to undergo a small rotation about each of the three coordinate axes while its centroid is displaced along each of these axes. These assumptions imply the following form for the displacement functions,

$$w(x,y,z) = w_0(z) - x \alpha_y(z) + y \alpha_x(z) , \quad (1a)$$

$$v(x,y,z) = v_0(z) + x \phi(z) , \text{ and} \quad (1b)$$

$$u(x,y,z) = u_0(z) - y \phi(z) . \quad (1c)$$

In Eq. (1), u_0 , v_0 and w_0 are the displacement components at a point on the centroidal curve (the origin of the local x,y coordinates) while

α_x , α_y and ϕ are small angles of rotation about the x , y and z axes in that order, as shown in Figure 7.

It is noted that theory of torsion of bars with non-circular cross sections requires the addition to Eq. (1) of a term representing warping of the cross section. Introduction of such a term would greatly complicate the ensuing development with very little effect on the state of stress other than near a fixed boundary. For this reason, the displacement functions of Eq. (1) will be employed irrespective of the shape of the cross section of the bar.

B. Strain-Displacement Equations

Substitution of Eq. (1) into the linearized form of Eqs. (10) yields the following expressions for the components of strain,

$$\epsilon_{xx} = \epsilon_{yy} = \epsilon_{xy} = 0 , \quad (2a)$$

$$\epsilon_{zz} = \frac{\partial w_0}{\partial z} - x \frac{\partial \alpha_y}{\partial z} + y \frac{\partial \alpha_x}{\partial z} - \kappa_0 (u_0 - y\phi) , \quad (2b)$$

$$2 \epsilon_{xz} = \frac{\partial u_0}{\partial z} - \alpha_y - \lambda_0 v_0 + \kappa_0 w_0 + y \left(\kappa_0 \alpha_x - \frac{\partial \phi}{\partial z} \right) - x (\lambda_0 \phi + \kappa_0 \alpha_y) , \quad (2c)$$

$$2 \epsilon_{yz} = \frac{\partial v_0}{\partial z} + \lambda_0 u_0 + \alpha_x + x \frac{\partial \phi}{\partial z} - y \lambda_0 \phi . \quad (2d)$$

The condition that cross sections remain normal to the centroidal curve can be invoked locally at $x=0$, $y=0$ or, alternatively, in an average sense by integrating Eqs. (2c) and (2d) over the cross section. In either case, the following equations expressing the vanishing of transverse shear deformation

kingsbury

(in the above meaning) result:

$$\alpha_y = \frac{\partial u_0}{\partial z} - \lambda_0 v_0 + \kappa_0 w_0 \quad (3a)$$

$$\alpha_x = -\frac{\partial v_0}{\partial z} - \lambda_0 u_0 \quad (3b)$$

C. Inertia Forces and Moments

The inertia force resultants and couples per unit length are obtained by introducing the assumed displacement functions into Eqs. (II-17) and (II-18) and carrying out the indicated integrations.

The resulting expressions, assuming no variation of mass density within a cross section, are presented below.

$$T_{Ij} = -\gamma \ddot{u}_j A \quad (u_j = u, v, w) \quad (4)$$

$$m_{Ix} = -\gamma I_{xx} \ddot{\alpha}_x + \gamma I_{xy} \ddot{\alpha}_y, \quad (5a)$$

$$m_{Iy} = \gamma I_{xy} \ddot{\alpha}_x - \gamma I_{yy} \ddot{\alpha}_y, \text{ and} \quad (5b)$$

$$m_{Iz} = -\gamma J_p \ddot{\phi}, \quad (5c)$$

where the moments and products of inertia appearing in Eqs. (5) may be functions of the z coordinate for rods with initial twist.

D. Moment-Curvature and Force-Displacement Equations

The stress-strain relations are predicated on the assumptions that the rod is constructed from a isotropic linear material which is elastically homogeneous in each cross section and that the normal stress components in the directions transverse to the centroidal curve are small in comparison with the normal stress component σ_{zz} .

The applicable stress-strain equations then become

$$\sigma_{zz} = E \epsilon_{zz}, \quad \sigma_{xz} = 2G \epsilon_{xz}, \quad \sigma_{yz} = 2G \epsilon_{yz} \quad (7)$$

The required equations are next obtained by combining Eqs. (2) and (3) with the definitions of the various force and moment resultants given by Eq. (II-1). This yields

$$M_x = -E I_{xy} \frac{\partial \alpha_y}{\partial z} + E I_{xx} \left(\frac{\partial \alpha_x}{\partial z} + \kappa_0 \phi \right), \quad (8a)$$

$$M_y = -E I_{yy} \frac{\partial \alpha_y}{\partial z} - E I_{xy} \left(\frac{\partial \alpha_x}{\partial z} + \kappa_0 \phi \right) \quad (8b)$$

kingsbury

$$M_z = G J_p \frac{\partial \phi}{\partial z} - G I_{xx} \kappa_o \alpha_x + G I_{xy} \kappa_o \alpha_y, \quad (8c)$$

$$V_x = k_x AG \left(\frac{\partial u_o}{\partial z} - \alpha_y - \lambda_o v_o + \kappa_o w_o \right), \quad (8d)$$

$$V_y = k_y AG \left(\frac{\partial v_o}{\partial z} + \lambda_o u_o + \alpha_x \right), \quad (8e)$$

$$V_z = E A \left(\frac{\partial w_o}{\partial z} - \kappa_o u_o \right). \quad (8f)$$

The coefficients k_x and k_y appearing in Eqs. (8d) and (8e) are Timoshenko shear coefficients [3]

The complete system of equations constituting the linear, technical, theory of rods with space curvature is comprised by Eqs. (II-8) and II-14 along with Eqs. (4), (5) and (8) of this section.

E. Displacement Equations Of Equilibrium Neglecting Transverse Shear Deformation And Rotatory Inertia

In this formulation transverse shear strains are neglected in the sense defined by Eq. (3). Since rotatory inertia generally has less effect upon predictions of frequency and motion than has transverse shear deformation, it is consistent to set terms involving α_x and α_y equal to zero although rotational inertia effects about the z^x axis are retained. Equations (8d) and (8c) for V_x and V_y respectively become inconsistent because, although ϵ_x^z and ϵ_y^z are set equal to zero on the average, equilibrium considerations require non-zero transverse shear forces. These forces are eliminated from the equilibrium equations by solving for V_y and V_x and substituting these results into the remaining four equations.

The functions α_x and α_y are eliminated from Eq. (8) by use of Eq. (3). The resulting expressions for the moments and V_z in terms of the four displacement and rotation functions are then substituted into the equilibrium equations. The resulting equations can be presented in the following form:

$$\sum_{j=0}^u A_{ij} u_{o,j} + \sum_{j=0}^u B_{ij} v_{o,j} + \sum_{j=1}^3 C_{ij} w_{o,j} + \sum_{j=0}^2 D_{ij} \phi_{o,j} = F_i \quad z = 1,2,3,4 \quad (9)$$

where

$$u_{o,j} = d^j u_o / dx^j \text{ etc/}$$

The fifty-eight coefficients non-zero appearing in Eq. (9) are presented in Appendix A. There it is seen that these coefficients depend upon the

kingsbury

geometric properties of the space curve described by the centroids of the cross sections, the geometry of the cross section and its relationship to the local vector principal normal and binormal, the elastic moduli of the material, and the variations of these quantities along the rod.

It is noted that in the general case described by Eq. (9), all motions are fully coupled since all variables appear in each equation. This means, for instance, that any exciting force will cause motion involving all four displacement and rotation variables. Also, solution of the free vibration problem will yield mode shapes which will each have four corresponding natural frequencies.

REFERENCES

1. A.E.H. Love, A Treatise On The Mathematical Theory of Elasticity, 4th Ed., Dover Publications, New York, 1927.
2. E. Reissner, "On One-Dimensional Large-Displacement Finite-Strain Beam Theory," Studies In Applied Math Vol. 52, pp 87-95, 1973.
3. G.R. Cowper, "The Shear Coefficients in Timoshenko Beam Theory," ASME J. Applied Mechanics, Vol. 33, No. 2 pp 335-340, 1966.

APPENDIX A

COEFFICIENTS APPEARING IN EQUATIONS (IV-9)

$$\begin{aligned}
A_{12} &= \kappa_o (G+E) I_{xy} \\
A_{11} &= \lambda_o \kappa_o (G+E) I_{xx} + (\kappa_o G I_{xy})' \\
A_{10} &= \kappa_o \lambda_o (G I_{xx})' + (\kappa_o' \lambda_o + \kappa_o \lambda_o') G I_{xx} + \kappa_o \lambda_o' E I_{xy} \\
B_{12} &= \kappa_o (G+E) I_{xx} \\
B_{11} &= (\kappa_o G I_{xx})' - \kappa_o \lambda_o (G+E) I_{xy} \\
B_{10} &= -\kappa_o \lambda_o (G I_{xy})' - \kappa_o' \lambda_o G I_{xy} - \kappa_o \lambda_o' (G+E) I_{xy} \\
C_{11} &= \kappa_o^2 (G+E) I_{xy} \\
C_{10} &= \kappa_o^2 (G I_{xy})' + \kappa_o \kappa_o' (2G+E) I_{xy} \\
D_{12} &= G I_P \\
D_{11} &= (G J_P)' \\
D_{10} &= -\kappa_o^2 E I_{xx} \\
A_{24} &= E I_{yy} \\
A_{23} &= 2(E I_{yy})' - \lambda_o E I_{xy} \\
A_{22} &= (E I_{yy})'' + 2\lambda_o' E I_{xy} - \lambda_o^2 E (2I_{xx} + I_{yy}) \\
A_{21} &= \lambda_o (E I_{xy})'' + 4\lambda_o' (E I_{xy})' + (3\lambda_o'' - \lambda_o^3) E I_{xy} \\
&\quad + \kappa_o^2 \lambda_o G I_{xy} - 2\lambda_o^2 (E I_{xx})' - 5\lambda_o \lambda_o' E I_{xx} \\
A_{20} &= \kappa_o^2 E A - 2\lambda_o \lambda_o' (E I_{xx})' - (2\lambda_o \lambda_o'' + \lambda_o'^2) E I_{xx} \\
&\quad + \kappa_o^2 \lambda_o^2 G I_{xx} + \lambda_o' (E I_{xy})'' + 2\lambda_o'' (E I_{xy})' \\
&\quad + (\lambda_o''' - \lambda_o' \lambda_o^2) E I_{xy} \\
B_{24} &= E I_{xy} \\
B_{23} &= 2(E I_{xy})' - 2\lambda_o E I_{xx} - \lambda_o E I_{yy} \\
B_{22} &= -2\lambda_o (E I_{yy})' - 3\lambda_o' E I_{yy} - 2\lambda_o (E I_{xx})' \\
&\quad - \lambda_o' E I_{xx} + (E I_{xy})'' + \lambda_o^2 E I_{xy} \\
B_{21} &= -\lambda_o (E I_{yy})'' - 4\lambda_o' (E I_{yy})' + (\lambda_o^3 - 3\lambda_o'') E I_{yy}
\end{aligned}$$

kingsbury

$$\begin{aligned}
 & + \kappa_o^2 \lambda_o GI_{xx} + 2\lambda_o^2 (EI_{xy})' - 5 \lambda_o \lambda_o' EI_{xy} \\
 B_{20} = & - \lambda_o' (EI_{yy})'' - 2\lambda_o'' (EI_{yy})' + (\lambda_o^2 \lambda_o' - \lambda_o''') EI_{yy} \\
 & + 2\lambda_o \lambda_o' (EI_{xy})' + (2\lambda_o \lambda_o'' + \lambda_o'^2) EI_{xy} - \kappa_o^2 \lambda_o^2 GI_{xy} \\
 C_{23} = & \kappa_o EI_{yy} \\
 C_{22} = & 2\kappa_o (EI_{yy})' + 3\kappa_o' EI_{yy} - 2\lambda_o \kappa_o EI_{xy} \\
 C_{21} = & \kappa_o (EI_{yy})'' + 4\kappa_o' (EI_{yy})' + (3\kappa_o'' - \lambda_o^2 \kappa_o) EI_{yy} \\
 & - 2\kappa_o \lambda_o (EI_{xy})' - (4\lambda_o \kappa_o' + \lambda_o' \kappa_o) EI_{xy} - \kappa_o EA \\
 C_{20} = & \kappa_o' (EI_{yy})'' + 2\kappa_o'' (EI_{yy})' + (\kappa_o''' - \kappa_o' \lambda_o^2) EI_{yy} \\
 & - 2\lambda_o \kappa_o' (EI_{xy})' - (2\lambda_o \kappa_o'' + \lambda_o' \kappa_o') EI_{xy} \\
 & + \kappa_o^3 \lambda_o GI_{xy} \\
 D_{22} = & - \kappa_o EI_{xy} \\
 D_{21} = & 2\lambda_o \kappa_o EI_{xx} + \kappa_o \lambda_o GJ_P - 2\kappa_o (EI_{xy})' \\
 & - 2\kappa_o' EI_{xy} \\
 D_{20} = & 2\kappa_o \lambda_o (EI_{xx})' + (\lambda_o' \kappa_o + 2\lambda_o \kappa_o') EI_{xx} \\
 & - \kappa_o (EI_{xy})'' - 2\kappa_o' (EI_{xy})' + (\lambda_o^2 \kappa_o - \kappa_o''') EI_{xy} \\
 A_{34} = & - EI_{xy} \\
 A_{33} = & - \lambda_o EI_{xx} - 2\lambda_o EI_{yy} - 2(EI_{xy})' \\
 A_{32} = & - 2\lambda_o (EI_{xx})' - 3\lambda_o' EI_{xx} - 2\lambda_o (EI_{yy})' - \lambda_o' EI_{yy} \\
 & - (EI_{xy})'' - \lambda_o^2 EI_{xy} + \kappa_o^2 GI_{xy} \\
 A_{31} = & - \lambda_o (EI_{xx})'' - 4\lambda_o' (EI_{xx})' + (\lambda_o^3 - 3\lambda_o''') EI_{xx} \\
 & + \kappa_o^2 \lambda_o GI_{xx} - 2\lambda_o^2 (EI_{xy})' - 5\lambda_o \lambda_o' EI_{xy} \\
 & + \kappa_o^2 (GI_{xy})' + 2\kappa_o \kappa_o' GI_{xy} \\
 A_{30} = & - \lambda_o' (EI_{xx})'' - 2\lambda_o'' (EI_{xx})' + (\lambda_o' \lambda_o^2 - \lambda_o''') EI_{xx} \\
 & + \kappa_o^2 \lambda_o (GI_{xx})' + \kappa_o (2\kappa_o' \lambda_o + \kappa_o \lambda_o') GI_{xx} \\
 & - 2\lambda_o \lambda_o' (EI_{xy})' - (2\lambda_o \lambda_o'' + \lambda_o'^2) EI_{xy} \\
 B_{34} = & - EI_{xx}
 \end{aligned}$$

$$\begin{aligned}
 B_{33} &= -2(EI_{xx})' - \lambda_o EI_{xy} \\
 B_{32} &= -(EI_{xx})'' + \lambda_o^2 EI_{xx} + \kappa_o^2 GI_{xx} + 2\lambda_o^2 EI_{yy} \\
 &\quad + 2\lambda_o' (EI_{xy}) \\
 B_{31} &= 2\kappa_o \kappa_o' GI_{xx} + \kappa_o^2 (GI_{xx})' + 5\lambda_o \lambda_o' EI_{yy} \\
 &\quad + (3\lambda_o'' - \lambda_o^3) EI_{xy} + \kappa_o^2 \lambda_o GI_{xy} \\
 &\quad + 4\lambda_o' (EI_{xy})' + \lambda_o (EI_{xy})'' \\
 B_{30} &= (2\lambda_o'^2 + 2\lambda_o \lambda_o'') EI_{yy} + 2\lambda_o^2 (EI_{yy})' \\
 &= (\lambda_o''' - \lambda_o^2 \lambda_o') EI_{xy} - (2\kappa_o \kappa_o' \lambda_o + \kappa_o^2 \lambda_o'') GI_{xy} \\
 &\quad + 2\lambda_o'' (EI_{xy})' - \lambda_o \kappa_o^2 (GI_{xy})' + \lambda_o' (EI_{xy})'' \\
 C_{33} &= -\kappa_o EI_{xy} \\
 C_{32} &= -2\lambda_o \kappa_o EI_{yy} - \kappa_o' EI_{xy} - 2\kappa_o (EI_{xy})' \\
 C_{31} &= -(2\lambda_o \kappa_o' + \kappa_o \lambda_o'') EI_{yy} - 2\lambda_o \kappa_o (EI_{yy})' \\
 &\quad + (\lambda_o^2 \kappa_o - 3\kappa_o''') EI_{xy} + \kappa_o^3 GI_{xy} - 4\kappa_o' (EI_{xy})' \\
 &\quad - \kappa_o (EI_{xy})'' \\
 C_{30} &= -(2\lambda_o \kappa_o'' + \lambda_o' \kappa_o') EI_{yy} - 2\lambda_o \kappa_o' (EI_{yy})' \\
 &\quad + (\lambda_o^2 \kappa_o' - \kappa_o''') EI_{xy} + 4\kappa_o^2 \kappa_o' GI_{xy} \\
 &\quad - 2\kappa_o'' (EI_{xy})' + \kappa_o^3 (GI_{xy})' - \kappa_o' (EI_{xy})'' \\
 D_{32} &= \kappa_o (EI_{xx} + GJ_p) \\
 D_{31} &= \kappa_o' (2EI_{xx} + GJ_p) + 2\kappa_o \lambda_o EI_{xy} \\
 &\quad + 2\kappa_o (EI_{xx})' + \kappa_o (GJ_p)' \\
 D_{30} &= (\kappa_o'' - \lambda_o^2 \kappa_o) EI_{xx} + (2\lambda_o \kappa_o' + \kappa_o \lambda_o'') EI_{xy} \\
 &\quad + 2\kappa_o' (EI_{xx})' + \kappa_o (EI_{xx})'' + 2\kappa_o \lambda_o (EI_{xy})' \\
 A_{43} &= \kappa_o EI_{yy} \\
 A_{42} &= \kappa_o (EI_{yy})' \\
 A_{41} &= -\kappa_o \lambda_o^2 EI_{xx} - \kappa_o EA + 2\lambda_o' \kappa_o EI_{xy} + \lambda_o \kappa_o (EI_{xy})' \\
 A_{40} &= -\kappa_o \lambda_o \lambda_o' EI_{xx} - \kappa_o' EA + \kappa_o \lambda_o'' EI_{xy}
 \end{aligned}$$

kingsbury

$$\begin{aligned}
 & -\kappa_o (EA)' + \kappa_o \lambda_o' (EI_{xy})' \\
 B_{43} &= \kappa_o EI_{xy} \\
 B_{42} &= -\lambda_o \kappa_o EJ_P + \kappa_o (EI_{xy})' \\
 B_{41} &= -2\kappa_o \lambda_o' EI_{yy} - \lambda_o \kappa_o (EI_{yy})' + \kappa_o \lambda_o^2 EI_{xy} \\
 B_{40} &= -\lambda_o'' \kappa_o EI_{yy} - \lambda_o' \kappa_o (EI_{yy})' + \kappa_o \lambda_o \lambda_o' EI_{xy} \\
 C_{42} &= EA + \kappa_o^2 EI_{yy} \\
 C_{41} &= 2\kappa_o \kappa_o' EI_{yy} + \kappa_o^2 (EI_{yy})' + (EA)' \\
 & \quad - \kappa_o^2 \lambda_o EI_{xy} \\
 C_{40} &= \kappa_o \kappa_o'' EI_{yy} + \kappa_o \kappa_o' (EI_{yy})' - \kappa_o \kappa_o' \lambda_o EI_{xy} \\
 D_{41} &= -\kappa_o^2 EI_{xy} \\
 D_{40} &= \kappa_o^2 \lambda_o EI_{xx} - \kappa_o \kappa_o' EI_{xy} - \kappa_o^2 (EI_{xy})'
 \end{aligned}$$

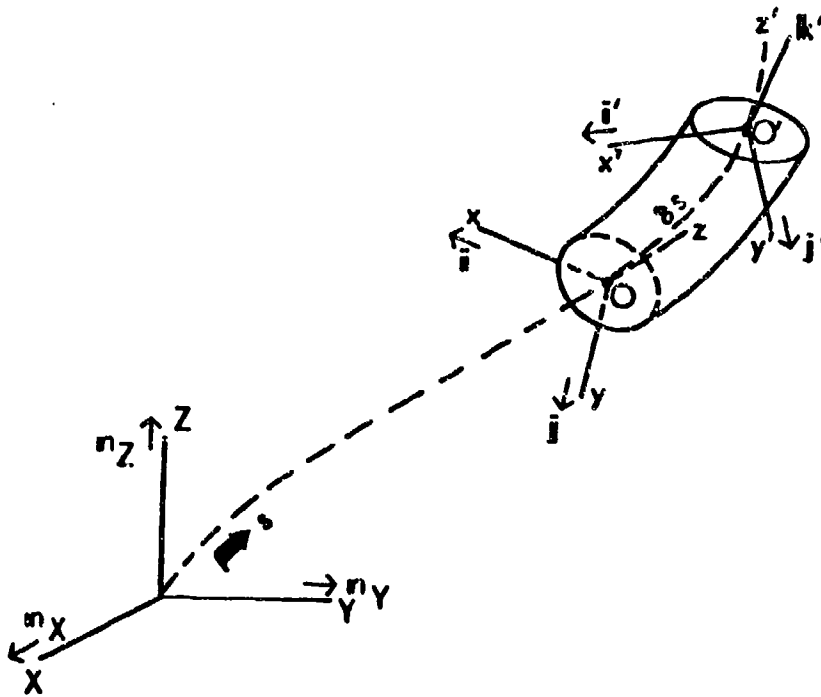


Figure 1. Space Curve Coordinates

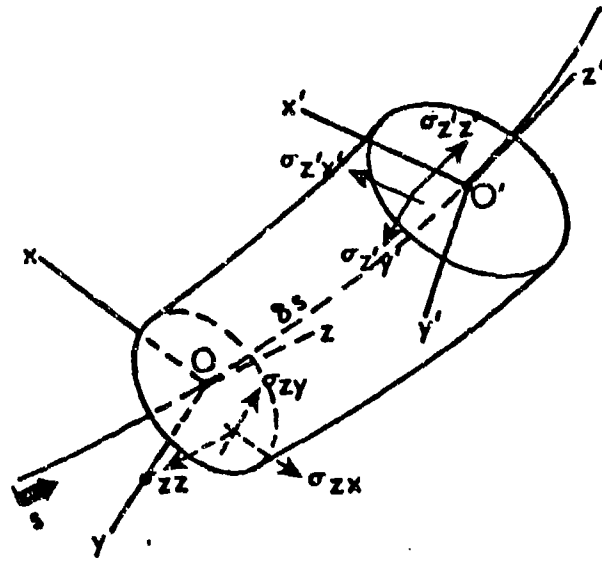


Figure 2. Stress Sign Convention

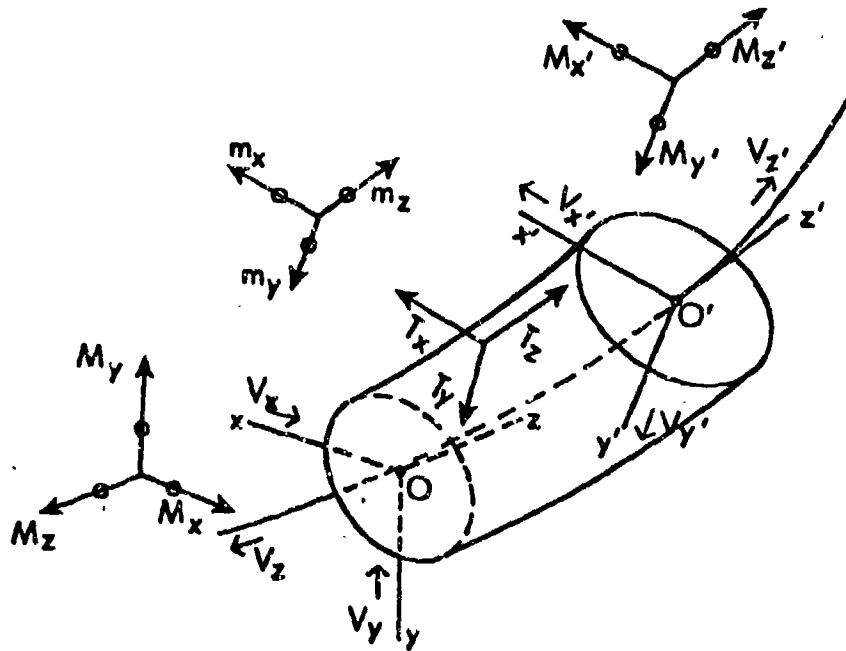


Figure 3. Force and Moment Resultants on Rod Element

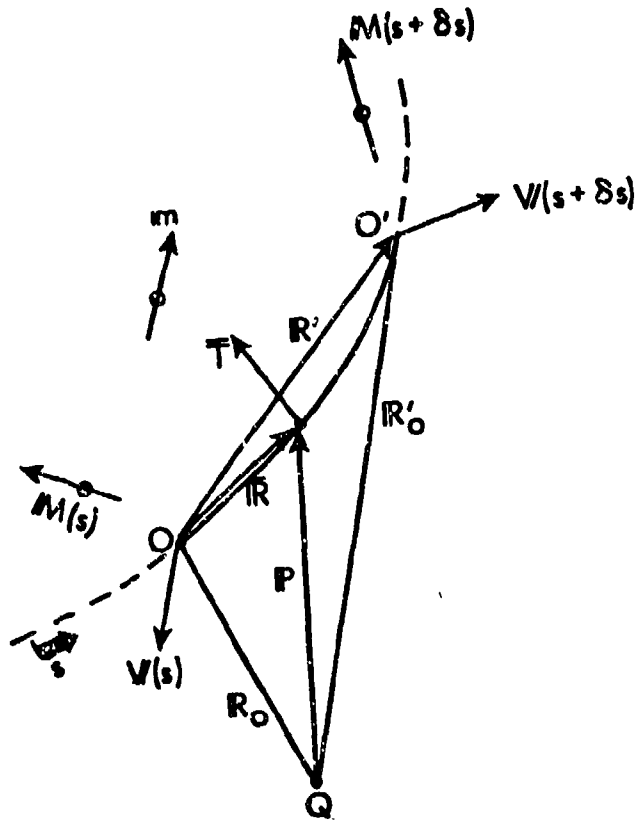


Figure 4. Free Body Diagram of Rod Element

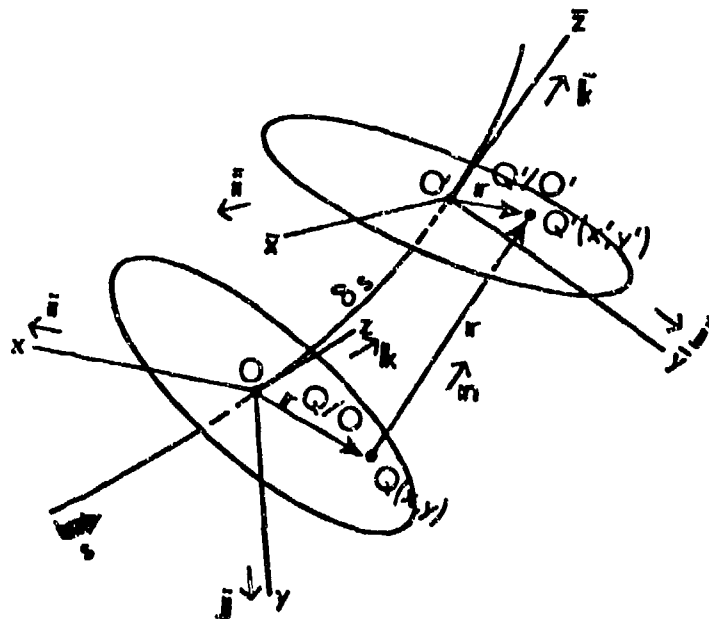


Figure 5. Adjacent Cross Section Before Deformation

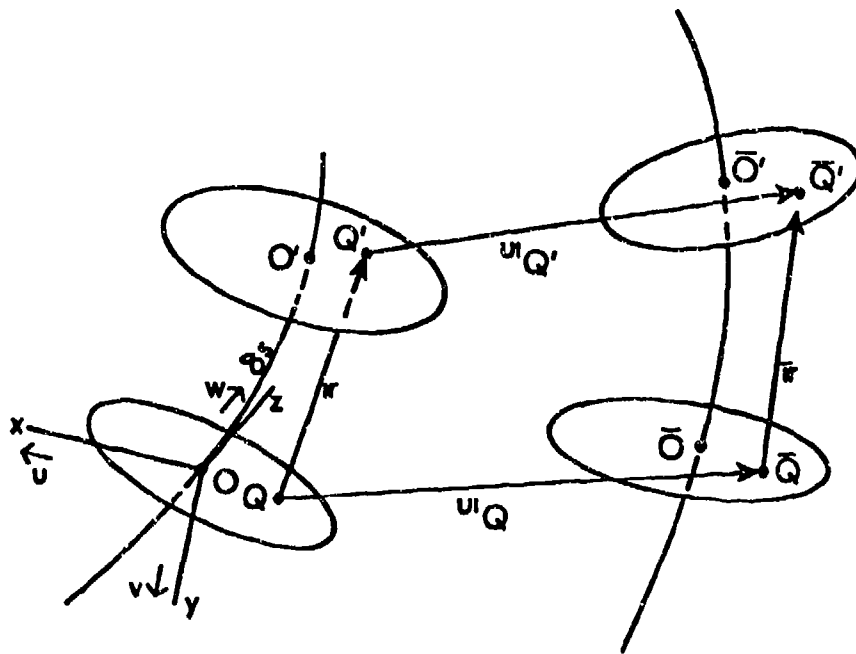


Figure 6. Displacements of Points of Adjacent Cross Section

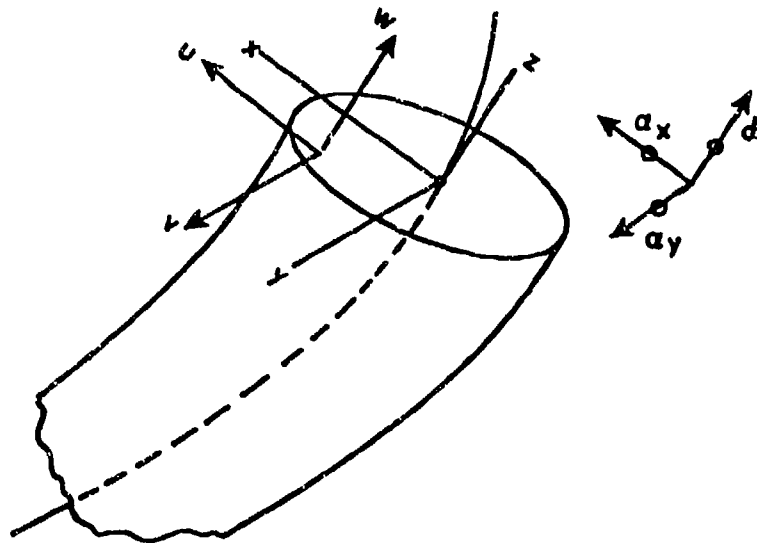


Figure 7. Displacement and Rotation Components

SNECK and GAST*

TITLE: Normal Mode Analysis of Gun Tube Dynamics
H. J. SNECK and R. GAST*
U. S. Army Armament, Munitions, and Chemical Command
Armament Research and Development Center
Large Caliber Weapon Systems Laboratory
Benet Weapons Laboratory
Watervliet, NY 12189-5000

ABSTRACT:

The Euler beam equation model of a uniform gun tube is solved with elastic supports which simulated the tube mount. Transverse and rotational displacements of the supports are permitted. The beam loadings account for the recoil inertia of the tube, pressure-curvature effects, projectile trajectory inertia within the tube, projectile rotational inertia, projectile eccentricity, gravity droop, initial bend, and mount friction during recoil. Mode shapes and transverse tube displacements are calculated for a range of firing conditions. A computer program expedites the calculation of the tube response at various stages of the projectile transit through the tube. The effect of the various loadings is assessed.

BIOGRAPHY: SNECK

PRESENT ASSIGNMENT: WAE with Benet Weapons Laboratory and Professor of Mechanical Engineering at Rensselaer Polytechnic Institute, Troy, NY.

PAST EXPERIENCE: Teacher and Researcher in the areas of fluid mechanics, heat transfer, vibrations, and machine dynamics. Consultant to industry in the above areas.

DEGREES HELD: BME, Rensselaer Polytechnic Institute (1951)
M. Eng., Yale University (1952)
Ph.D, Rensselaer Polytechnic Institute (1962)

NORMAL MODE ANALYSIS OF GUN TUBE DYNAMICS

H. J. SNECK AND R. GAST*
 U.S. ARMY ARMAMENT, MUNITIONS, AND CHEMICAL COMMAND
 ARMAMENT RESEARCH AND DEVELOPMENT CENTER
 LARGE CALIBER WEAPON SYSTEMS LABORATORY
 BENET WEAPONS LABORATORY
 WATERVLIET, NY 12189-5000

1. NOMENCLATURE

| | | |
|----------------------|---|---|
| A_1, B_1, C_1, D_1 | = | mode shape coefficients |
| A | = | cross-section area of tube |
| $a_x(t)$ | = | axial acceleration of tube |
| e | = | projectile eccentricity |
| E | = | Young's modulus |
| g | = | gravitation acceleration |
| G | = | shear modulus |
| H | = | step function |
| I | = | second moment of the beam cross-section area |
| $I_1(t)$ | = | $\int_0^l P(x,t) \phi_1(x) dx$ |
| J | = | polar moment of inertia |
| k | = | support ring stiffness; shear factor $\pi^2/12$ |
| K_y | = | equivalent support lateral stiffness |
| K_θ | = | equivalent support torsional stiffness |
| l | = | tube length |
| l_p | = | projectile length |
| M | = | moment |
| M_i | = | $\int_0^l \frac{w}{g} \phi_1^2 dx$ |
| P, P(t) | = | ballistic pressure |
| P(x,t) | = | excitation loads |
| q_i | = | time depend portion of displacement |
| R_i | = | inside tube radius |
| R_o | = | outside tube radius |
| S | = | support-ring span |
| t | = | time |
| V | = | shear force |

| | | |
|-----------------|---|--|
| W | = | weight of tube |
| w | = | W/l = weight of tube per unit length |
| W_p | = | projectile weight |
| $w_p = W_p/l_p$ | = | projectile weight per unit length |
| x | = | axial coordinate |
| x_p | = | projectile coordinate, axial |
| x_p | = | projectile velocity |
| y | = | lateral coordinate, tube displacement |
| $y_d(x,t)$ | = | dynamic tube displacement |
| $Y(x)$ | = | static tube displacement |
| μ | = | coefficient of friction |
| δ | = | Dirac delta function |
| θ_0 | = | phase angle |
| τ | = | rifling twist |
| ϕ_i | = | mode shapes |
| ω_i | = | natural frequencies |
| \cdot | = | time differentiation |
| $'$ | = | spatial differentiation |

2. INTRODUCTION

The analysis of gun tube dynamics is usually approached via one of two broad avenues. One approach relies on the initial discretization of the system into lumped elements followed by the direct solution of the resulting algebraic equations through computer codes. The finite-element method is typical of these techniques. The other approach utilizes the classical mode-shape formulation which yields a system of ordinary, coupled, differential equations for the time-dependent response. These equations, which have time dependent coefficients and forcing functions, are then integrated using standard numerical integration techniques and a computer.

The second avenue is followed in this paper. There are several reasons for this choice. First, the method is straightforward requiring few modeling or computational approximations. The ordinary differential equations (ODE's) which result occur at the end of the analysis so that they faithfully portray the physical model to that point. The only approximations made to obtain the solutions for the transverse displacements result from the methods used to integrate these ODE's. Since highly refined integration techniques are available, accurate solutions of these equations can be obtained.

The second reason for choosing the classical approach is its accessibility. Each component of the solution can be directly related to the mechanics of the system, and therefore has a physical interpretation. This feature is particularly important in parametric studies which seek to determine causality and sensitivity.

Third, the analytical method has already been used with good success to analyze the dynamic response of small caliber weapons [1]. The results obtained were compared with carefully controlled laboratory experiments and shown to be superior to the finite element method predictions.

Finally, and probably most important, time-displacement tube loadings are not easily incorporated into the finite models. They enter into the ODE coefficients and forcing functions in a precise and straightforward way. The ODE coefficients indicate the degree of static and dynamic coupling present at any instant. Coupling of the ODE's plays an important role in the determination of the "apparent frequency" spectrum and tube response.

3. BEAM EQUATION

The equation which describes the transverse motion of a vibrating beam is:

$$(EIy'')'' + \frac{w}{g} \ddot{y} - (J + \frac{EIw}{gkAG})y'' + (\frac{Jw}{gkAG})\dot{y} = P(x,t) - w \quad (1)$$

This equation expresses a balance between the beam stiffness (including shear effects), translational and rotatory inertia, and the applied forces, all on a per unit length basis.

An order-of-magnitude analysis for an M58-105 mm tube shows that the terms which account for shear and rotatory inertia contribute little to the equation when the model frequencies are less than 10^4 Hz. Since the highest frequencies anticipated are of the order of 10^3 Hz, the simpler Euler formulation was used, i.e.,

$$(EIy'')'' + \frac{w}{g} \ddot{y} = P(x,t) - w \quad (2)$$

where $(\prime) \equiv \partial/\partial y$ and $(\dot{}) \equiv \partial/\partial t$. Warlen [1] found that the Euler equation accurately predicted the response of 7.62 mm test gun tube.

In most beam problems, excitation is provided by the term $P(x,t)$ which is usually prescribed. It will be shown that the excitation of a gun tube cannot be expressed as $P(x,t)$, but is given instead by a time-displacement function of the form $f(x,t,y',y'',y',y)$.

4. METHOD OF SOLUTION FOR A UNIFORM TUBE

When the beam cross-section is uniform, the solution of the homogeneous Euler equation is obtained by assuming that

$$y_c = \sum_{i=1}^N \phi_i(x)T_i(t) \quad (3)$$

Separation of the equation yields ODE's for the mode shapes which are

$$\phi_i^{IV} - n_i^4 \phi_i = 0 \quad (4)$$

where

$$n_i^4 = \frac{w}{gEI} \omega_i^2 \quad (5)$$

The mode shape functions which satisfy these ODE's are

$$\begin{aligned} \phi_i = & A_i \cosh(n_i l)(x/l) + B_i \sinh(n_i l)(x/l) \\ & + C_i \cos(n_i l)(x/l) + D_i \sin(n_i l)(x/l) \end{aligned} \quad (6)$$

The coefficients A_i may be set equal to unity. The values of $n_i l$, B_i , C_i , and D_i are determined by the boundary conditions at the tube support and at the muzzle. The natural frequencies of the tube are then given by

$$\omega_i = (n_i l)^2 \left(\frac{gEI}{w l^4} \right)^{1/2} \quad (7)$$

The solution for $T_i(t)$ is

$$T_i = E_i \cos \omega_i t + F_i \sin \omega_i t \quad (8)$$

where the constants E_i and F_i depend on the initial conditions.

For non-dissipative boundary conditions, the mode shapes are orthogonal to each other with respect to the weighing function w/g so that

$$\int_0^l \frac{w}{g} \phi_i \phi_j dx = \begin{cases} 0 & \text{when } i \neq j \\ M_i & \text{when } i = j \end{cases} \quad (9)$$

If it is also assumed that the solution of the non-homogeneous Euler beam partial differential equation (PDE) takes the form

$$y_p = \sum_{i=1}^N \phi_i(x) q_i(t) \quad (10)$$

then the orthogonality of the mode shapes yield ODE's for $q_i(t)$ which are

$$\ddot{q}_i + \omega_i^2 q_i = \frac{1}{M_i} \int_0^l P(x,t) \phi_i(x) dx \quad (11)$$

Because the gun-tube forcing function is of the form $F(x,t,y',y'',\dot{y}',\ddot{y})$ instead of $P(x,t)$, the assumed solutions must also be inserted into the right-hand side integral. This results in additional q_i , \dot{q}_i , and \ddot{q}_i terms on the left-hand side of the ODE's above. The integrals which remain on the right-hand side have integrands of the classical form $P(x,t)\phi_i(x)$ which depend on the initial tube displacements. When integrated over the tube length, the right-hand sides become time-dependent driving functions for the coupled ODE's. The numerical solution of these ODE's for $q_i(t)$ completes the analysis.

5. EXCITATION FORCES

Five sources of excitation have been identified by various investigators. Their formulations will be presented below.

5.1 Recoil Inertia Load

This load is caused by the deflection of the tube from the recoil axis. The resulting axial inertial force tends to straighten the tube, returning it to concentricity with this axis. Its contribution to the excitation is given by [2]:

$$\frac{w}{g} a_x(t) [(l-x)y']' \quad (12)$$

5.2 Pressure-Curvature Load

This load results from the difference in the transverse projected area of the tube caused by bending. Its contribution is given by [2]:

$$-\pi R_1^2 P(t) y'' H(x_p - x) \quad (13)$$

where the Heaviside step function is defined as

$$H = 1 \quad \text{when} \quad 0 \leq x \leq x_p \quad (14)$$

$$H = 0 \quad \text{when} \quad x > x_p \quad (15)$$

5.3 Projectile Trajectory Loading

The projectile, although of considerably less mass than the tube, can exert a significant transverse force on the tube when it accelerates along a curved path. The per unit length force exerted by its motion is given by [2]:

$$-\frac{w_p}{g} [y + 2x_p \dot{y}' + x_p^2 y''] \delta(x_p - x) \quad (16)$$

where $\delta(x_p - x)$ is the Dirac delta function.

5.4 Projectile Eccentricity Load

Wu [3] has postulated the existence of a couple exerted on the tube when the projectile propelling force does not pass through the projectile's mass center. The transverse unit loading is formulated with the aid of the derivative of the Dirac function as

$$\left(\frac{P(t) \pi R_1^2 e}{l_p} \right) \delta'(x_p - x) \sin(\theta_0 + 2\pi x_p) \quad (17)$$

The term $2\pi x_p$ accounts for the projectile revolution in a rifled tube.

5.5 Projectile Rotational Load

As the projectile moves down a rifled tube, its mass center rotates causing a centrifugal load on the bore. The transverse vertical component of this force is given by

$$\frac{w_p}{g} [(2\pi\dot{x}_p)^2 e \sin(\theta_0 + 2\pi\tau x_p) - (2\pi\tau x_p e \cos(\theta_0 + 2\pi\tau x_p))] \delta(x_p - x) \quad (18)$$

6. BEAM FORMULATION FOR GUN TUBE

When the excitation terms are introduced into the Euler beam formulation, the total displacement is described by

$$\begin{aligned} EIy^{IV} + \frac{w}{g} \ddot{y} &= \frac{w}{g} a_x(t) [(l-x)y']' - \pi R_1^2 p y'' H(x_p - x) \\ - \frac{w_p}{g} [y + 2\dot{x}_p \dot{y}' + \dot{x}_p^2 y'' + g] \delta(x_p - x) &+ \left(\frac{P\pi R_1^2 e}{l_p^2} \right) \delta'(x_p - x) \sin(\theta_0 + 2\pi\tau x_p) - w \\ &+ \frac{w_p e}{g} [(2\pi\dot{x}_p)^2 \sin(\theta_0 + 2\pi\tau x_p)] \delta(x_p - x) \end{aligned} \quad (19)$$

The dead weight of the projectile is introduced by the addition of g to the projectile acceleration.

It is convenient to express the total displacement as the sum of dynamic and static contributions, i.e.,

$$y(x, t) = y_d(x, t) + Y(x) \quad (20)$$

The static displacement satisfies the equation

$$EIY^{IV} = -w \quad (21)$$

while the dynamic displacement satisfies the equation

$$\begin{aligned} EIy_d^{IV} + \frac{w}{g} \ddot{y}_d &= \frac{w}{g} a_x(t) [(l-x)y_d']' - \pi R_1^2 p y_d'' H(x_p - x) \\ - \frac{w_p}{g} [y_d + 2\dot{x}_p \dot{y}_d' + \dot{x}_p^2 y_d'' + g] \delta(x_p - x) &+ \left(\frac{P\pi R_1^2 e}{l_p^2} \right) \delta'(x_p - x) \sin(\theta_0 + 2\pi\tau x_p) \\ + \frac{w_p e}{g} [(2\pi\dot{x}_p)^2 \sin(\theta_0 + 2\pi\tau x_p)] \delta(x_p - x) &- \frac{w}{g} a_x(t) [(l-x)Y']' - \pi R_1^2 p Y'' H(x_p - x) \\ - \frac{w_p}{g} [\dot{x}_p^2 Y'' + \ddot{x}_p Y' + g] \delta(x_p - x) & \end{aligned} \quad (22)$$

Deviations of the tube from straightness due to manufacturing tolerances or thermal distortion can also be incorporated into the static displacement term.

7. BOUNDARY CONDITIONS WITHOUT SUPPORT FRICTION

Because the recoil displacement is very small during the period of shot ejection, the tube supports are modeled by springs attached to the tube as illustrated in Figure 1. The torsional and translational springs shown are not independent. Their interdependence will be developed in a later section devoted to modeling the support stiffness.

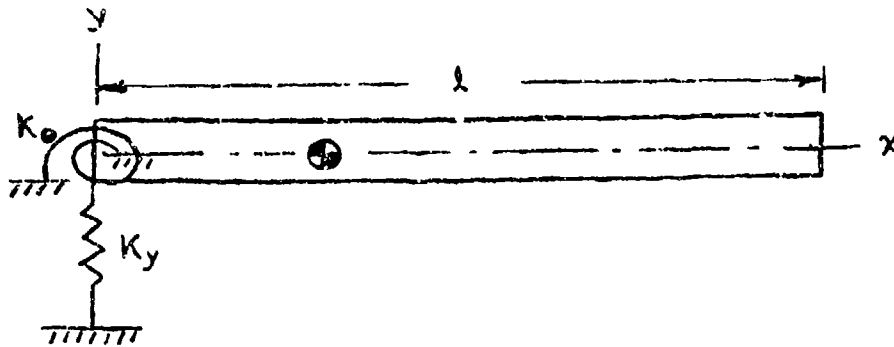


Figure 1. Tube with Supports.

The model boundary conditions for the total displacements at the free end are

$$M(l,t) = 0 = \frac{\partial^2 y}{\partial x^2}(l,t) \quad (23)$$

$$V(l,t) = 0 = \frac{\partial^3 y}{\partial x^3}(l,t) \quad (24)$$

and at the support end

$$M(0,t) = EI \frac{\partial^2 y}{\partial x^2}(0,t) = K_\theta \frac{\partial y}{\partial x}(0,t) \quad (25)$$

$$V(0,t) = EI \frac{\partial^3 y}{\partial x^3}(0,t) = -K_y y(0,t) \quad (26)$$

8. STATIC DISPLACEMENTS

The support springs must oppose the preload couple M_0 caused by the muzzle-heavy tube. For convenience, it is assumed that the springs are adjusted so that the tube slope is zero at the breech end, $x = 0$. When the boundary conditions and this restriction are applied to the solution of the

static deflection ODE, the equation for the gravity droop of the tube is found to be

$$EI[Y(x) - Y(0)] = -\left(\frac{w}{24}\right)x^4 + \left(\frac{w\ell}{6}\right)x^3 - \left(\frac{w\ell^2}{4}\right)x^2 \quad (27)$$

where $Y(0) = -\frac{w\ell}{K_y}$, $M_0 = \frac{w\ell^2}{2}$, and $Y'(0) = 0$.

9. NATURAL FREQUENCIES AND MODE SHAPES

The boundary conditions are satisfied by the mode shape functions when

$$\cosh n_1 \ell + B_1 \sinh n_1 \ell - C_1 \cos n_1 \ell - D_1 \sin n_1 \ell = 0 \quad (28)$$

$$\sinh n_1 \ell + B_1 \cosh n_1 \ell + C_1 \sin n_1 \ell - D_1 \cos n_1 \ell = 0 \quad (29)$$

$$EI n_1 (A_1 - C_1) = K_\theta (B_1 + D_1) \quad (30)$$

$$EI n_1^3 (B_1 - D_1) = -K_y (A_1 + C_1) \quad (31)$$

The quantity $n_1 \ell$ is obtained from the determinant of the matrix of the coefficients of B_1 , C_1 , and D_1 which yields the transcendental characteristic equation

$$\begin{aligned} [1 - \cos n_1 \ell \cosh n_1 \ell] + \frac{K_y \ell^3}{EI} \left[\frac{\cos n_1 \ell \sinh n_1 \ell - \sin n_1 \ell \cosh n_1 \ell}{(n_1 \ell)^3} \right] \\ - \frac{k_\theta \ell}{EI} \left[\frac{\cos n_1 \ell \sinh n_1 \ell + \sin n_1 \ell \cosh n_1 \ell}{n_1 \ell} \right] \\ + \frac{K_y \ell^3}{EI} \frac{k_\theta \ell}{EI} \left[\frac{1 + \cos n_1 \ell \cosh n_1 \ell}{(n_1 \ell)^4} \right] = 0 \end{aligned} \quad (32)$$

The coefficient $K_y \ell^3 / EI$ is a measure of the transverse stiffness of the support relative to the tube stiffness, and $K_\theta \ell / EI$ is a measure of the support torsional stiffness relative to the tube stiffness.

Once the values of $n_1 \ell$ are determined from the characteristic equation, the coefficients in the mode shape functions are given by:

$$A_1 = 1 \quad (33)$$

$$\begin{aligned} B_1 = \frac{1}{\Delta} \{ [1 + \sinh n_1 \ell \sin n_1 \ell - \cosh n_1 \ell \cos n_1 \ell] \\ - \frac{K_\theta \ell}{EI} \left[\frac{\sinh n_1 \ell \cos n_1 \ell + \cosh n_1 \ell \sin n_1 \ell}{n_1 \ell} \right] \} \end{aligned} \quad (34)$$

$$C_1 = \frac{1}{\Delta} \left\{ [\sinh n_1 \ell \cos n_1 \ell - \cosh n_1 \ell \sin n_1 \ell] + \frac{K_\theta \ell}{EI} \left[\frac{1 + \cosh n_1 \ell \cos n_1 \ell - \sinh n_1 \ell \sin n_1 \ell}{n_1 \ell} \right] \right\} \quad (35)$$

$$D_1 = \frac{1}{\Delta} \left\{ [\sinh n_1 \ell \sin n_1 \ell + \cosh n_1 \ell \cos n_1 \ell - 1] + \frac{K_\theta \ell}{EI} \left[\frac{\sinh n_1 \ell \cos n_1 \ell + \cosh n_1 \ell \sin n_1 \ell}{n_1 \ell} \right] \right\} \quad (36)$$

where

$$\Delta = [\sinh n_1 \ell \cos n_1 \ell - \cosh n_1 \ell \sin n_1 \ell] + \frac{K_\theta \ell}{EI} \left[\frac{1 + \sinh n_1 \ell \sin n_1 \ell + \cosh n_1 \ell \cos n_1 \ell}{n_1 \ell} \right] \quad (37)$$

The "orthogonality integral" can be expressed in terms of these coefficients and the relative stiffness. When normalized to the tube length, it is given by the formula

$$\int_0^1 \phi_1^2 d\left(\frac{x}{\ell}\right) = \frac{1}{4} \left\{ [\cosh n_1 \ell + B_1 \sinh n_1 \ell + C_1 \cos n_1 \ell + D_1 \sin n_1 \ell]^2 + 3 \frac{K_y \ell^3}{EI} \left[\frac{(1+C_1)^2}{(n_1 \ell)^4} \right] + \frac{K_\theta \ell}{EI} \left[\frac{(B_1+D_1)^2}{(n_1 \ell)^2} \right] \right\} \quad (38)$$

10. SUPPORT STIFFNESS

Figure 2 is a schematic of the tube support system. Linear springs simulate the support rings used in U.S. tank concentric mounts.

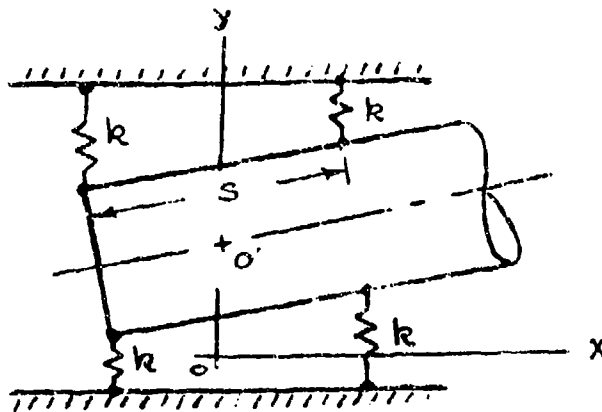


Figure 2. Frictionless Support Model.

The springs in this particular system can be related to the generalized stiffnesses K_y and K_θ by equating the sums of their forces and moments. The result is

$$K_y = 2k \quad (39)$$

$$K_\theta = \left(\frac{s}{2}\right)^2 K_y \quad (40)$$

The interdependence of K_y and K_θ is also established by these relations.

11. ORDINARY DIFFERENTIAL EQUATIONS FOR $q_1(\tau)$

When the assumed solution is substituted into the nonhomogeneous Euler beam equation, the following set of ODE's are generated

$$\begin{aligned} & \ddot{q}_1 + \frac{W_p}{W} \left[\frac{\phi_1(x_p)}{\int_0^1 \phi_1^2 d(\frac{x}{l})} \right] \left\{ \sum_{j=1}^N \phi_j(x_p) q_j \right\} \\ & + \frac{W_p}{W} \left[\frac{2(\frac{x_p}{l}) \phi_1(x_p)}{\int_0^1 \phi_1^2 d(\frac{x}{l})} \right] \left\{ \sum_{j=1}^N [l \phi_j'(x_p) \dot{q}_j] \right\} + \omega_1^2 q_1 \\ & + \frac{W_p}{W} \left[\frac{\phi_1(x_p)}{\int_0^1 \phi_1^2 d(\frac{x}{l})} \right] \left\{ \left(\frac{x_p}{l}\right)^2 \sum_{j=1}^N [l^2 \phi_j''(x_p) q_j] \right\} \\ & + \frac{\pi R_1^2 p(t)}{W l \int_0^1 \phi_1^2(x) d(\frac{x}{l})} \left\{ \phi_1(x_p) \sum_{j=1}^N [l \phi_j'(x_p) q_j] \right\} \\ & + \int_{x_p/l}^1 l \phi_1'(x) \sum_{j=1}^N [l \phi_j(x) q_j] d(\frac{x}{l}) \\ & - \int_0^1 \left(\frac{x}{l}\right) l \phi_1'(x) \sum_{j=1}^N [l \phi_j(x) q_j] d(\frac{x}{l}) \right\} = I_1(t) \quad (41) \end{aligned}$$

The second term on the left-hand side of this equation contains the mass coupling terms between the projectile and the tube. The third term is a pseudo-damping term which results from the Coriolis acceleration of the projectile. In the classical beam problem, the fourth term, $\omega_1^2 q_1$, would determine the frequency of response $q_1(t)$. In this problem, the remaining four static coupling terms influence the "apparent" natural frequencies of the system at each stage of the shot ejection.

The forcing function for each equation depends on the five applied loads summed according to the notation

$$I_1(t) = \sum_{N=1}^{N=5} I_1^{(N)}(t) \quad (42)$$

The individual contributions to this sum are:

11.1 Recoil Inertia

$$I_1^{(1)}(t) = \left[\frac{W a_x(t)}{\int_0^1 \phi_1^2 d\left(\frac{x}{\ell}\right)} \right] (n_1 \ell) \left(\frac{\ell^2}{2EI} \right) \left\{ \int_0^1 \left(\frac{x}{\ell} \right) \left(1 - \frac{x}{\ell} \right) \left[(1+a_2) - (1+a_3) \left(\frac{x}{\ell} \right) + \frac{1}{3} (1+a_4) \left(\frac{x}{\ell} \right)^2 \right] \left[\sinh n_1 \ell \left(\frac{x}{\ell} \right) + B_1 \cosh n_1 \ell \left(\frac{x}{\ell} \right) - C_1 \sin n_1 \ell \left(\frac{x}{\ell} \right) + D_1 \cos n_1 \ell \left(\frac{x}{\ell} \right) \right] d\left(\frac{x}{\ell} \right) \right\} \quad (43)$$

where a_2 , a_3 , and a_4 can be chosen to simulate a bent tube and are all zero if the tube is perfectly straight.

11.2 Pressure Curvature

$$I_1^{(2)}(t) = \frac{\pi R_1^2 P(t) g}{\int_0^{x_p/\ell} \phi_1^2 d\left(\frac{x}{\ell}\right)} \left[\frac{\ell^2}{2EI} \right] \left\{ \int_0^{x_p/\ell} \left[\left(1 - \frac{x}{\ell} \right)^2 + a_2 - 2a_3 \left(\frac{x}{\ell} \right) + a_4 \left(\frac{x}{\ell} \right)^2 \right] \left[\cosh n_1 \ell \left(\frac{x}{\ell} \right) + B_1 \sinh n_1 \ell \left(\frac{x}{\ell} \right) + C_1 \cos n_1 \ell \left(\frac{x}{\ell} \right) + D_1 \sin n_1 \ell \left(\frac{x}{\ell} \right) \right] d\left(\frac{x}{\ell} \right) \right\} \quad (44)$$

11.3 Projectile Trajectory

$$I_1(3) = \frac{W_p}{1} \frac{\ell^3}{3EI} \left(\frac{x_p}{\ell} \right)^2$$

$$\left\{ \left(\frac{x_p}{\ell} \right)^2 \left[\left(1 - \frac{x_p}{\ell} \right)^2 + a_2 - 2a_3 \left(\frac{x_p}{\ell} \right) + a_4 \left(\frac{x_p}{\ell} \right)^2 \right] - g \left(\frac{2EI}{W\ell^3} \right) \right\}$$

$$\left\{ \cosh n_1 \ell \left(\frac{x_p}{\ell} \right) + B_1 \sinh n_1 \ell \left(\frac{x_p}{\ell} \right) + C_1 \cos n_1 \ell \left(\frac{x_p}{\ell} \right) + D_1 \sin n_1 \ell \left(\frac{x_p}{\ell} \right) \right\} \quad (45)$$

11.4 Projectile Rotation

$$I_1(4)(t) = \frac{W_p e}{W \int_0^1 \phi_1^2 d\left(\frac{x}{\ell}\right)} \left\{ (2\pi x_p)^2 \sin(\theta_0 + 2\pi x_p) \right\}$$

$$- (2\pi x_p) \cos(\theta_0 + 2\pi x_p) \left\{ \cosh n_1 \ell \left(\frac{x_p}{\ell} \right) + B_1 \sinh n_1 \ell \left(\frac{x_p}{\ell} \right) \right.$$

$$\left. + C_1 \cos n_1 \ell \left(\frac{x_p}{\ell} \right) + D_1 \sin n_1 \ell \left(\frac{x_p}{\ell} \right) \right\} \quad (46)$$

11.5 Projectile Eccentricity

$$I_1(5)(t) = \left[\frac{\pi R_1^2 P(t) g}{W \int_0^1 \phi_1^2 d\left(\frac{x}{\ell}\right)} \right] (n_1 \ell) \left(\frac{x_p}{\ell} \right)$$

$$\left\{ \left[\sinh n_1 \ell \left(\frac{x_p}{\ell} \right) + B_1 \cosh n_1 \ell \left(\frac{x_p}{\ell} \right) \right. \right.$$

$$\left. \left. - C_1 \sin n_1 \ell \left(\frac{x_p}{\ell} \right) + D_1 \cos n_1 \ell \left(\frac{x_p}{\ell} \right) \right] \right\}$$

$$\left[\sin(\theta_0 + 2\pi x_p) \right] \quad (47)$$

The complete solution of the PDE is

$$y = \sum_{i=1}^N \phi_i(T_1 + q_1) \tag{48}$$

Since the initial conditions for the dynamic displacement are $y(x,0) = \dot{y}(x,0) = 0$, then $q_1(0) + T_1(0) = \dot{q}_1(0) + \dot{T}_1(0) = 0$. Letting $E_1 = F_1 = 0$ in Eq. (8) yields the initial conditions $q_1(0) = \dot{q}_1(0) = 0$.

12. EFFECT OF SUPPORT FRICTION

Figure 3 models the supports when the tube is allowed to slide within the supports as it recoils rearward. If there is no clearance between the tube and the mount the moment generated by the friction is

$$M_f = \mu y(0,t) K_y R_0 \tag{49}$$

In terms of the dynamic deflection this moment is given by

$$M_f = \mu K_y R_0 y_d(0,t) - \mu w l R_0 \tag{50}$$

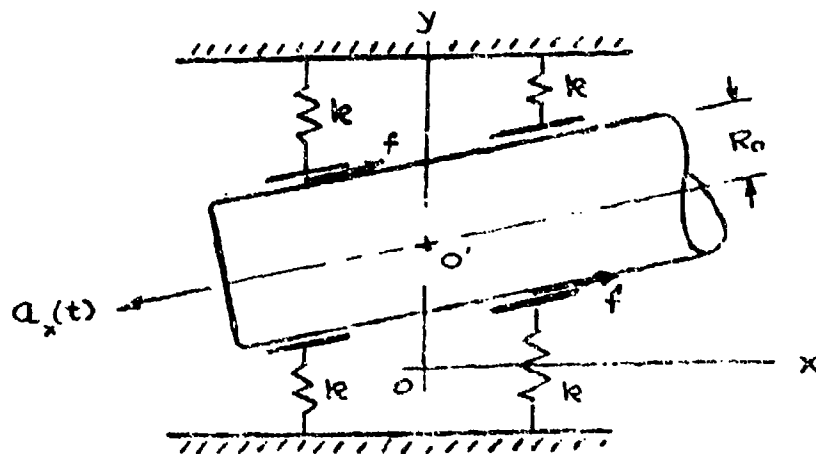


Figure 3. Tube Support with Friction.

The quantity $\mu w l R_0$ is an externally applied couple due to the static load which augments the $I_1(t)$ terms. Its contribution is

$$I_1^{(6)}(t) = - \left[\frac{\mu g}{\int_0^1 \phi_i^2 d(\frac{x}{l})} \right] \left(\frac{R_0}{l} \right) (n_1 l) (B_1 + D_1) \tag{51}$$

The modified mount-end moment boundary condition is

$$EI n_1^2(A_1 - C_1) = K_0 n_1(B_1 + D_1) + \mu K_y R_0(A_1 + C_1) \quad (52)$$

The mount-end shear boundary condition is

$$EI \frac{\partial^3 y}{\partial x^3}(0, t) = -K_y y(0, t) + \mu K_y |y(0, t)| y'(0, t) \quad (53)$$

Since $\mu y'(0, t) \ll 1$, the contribution of friction to this boundary condition can be neglected.

The determination of the natural frequencies and mode shapes is a straightforward computation. Unfortunately, the mode shapes are not orthogonal since it can be shown that

$$\int_0^1 \phi_1 \phi_1 d\left(\frac{x}{\ell}\right) = \frac{\mu R_0 K_y \ell^2}{EI} \left[\frac{(n_j \ell)(B_j + D_j)(1 + C_1) - (n_1 \ell)(B_1 + D_j)(1 + C_j)}{(n_j \ell)^4 - (n_1 \ell)^4} \right] \quad (54)$$

Non-orthogonality also leads to further modification of the forcing functions.

Calculations with $\mu \leq 1.25$ and support stiffness of $50(10^3)$ to $250(10^3)$ lb/in. show infinitesimal (third place) variations in the eigenvalues when compared to the frictionless values. Since the mode shapes with friction depend on the eigenvalues, they will also be insignificantly influenced by friction. Thus it appears that the effects of friction can be determined quite accurately using the frictionless eigenvalues and mode shapes in conjunction with the forcing term $I_1^{(6)}(t)$. The computed results reported in the following sections were obtained this way.

13. INTRODUCTION TO DYNAMIC ANALYSIS CODE: 'DYNAM'

In keeping with the ideas set forth at the outset, the writing of a computer code entitled 'DYNAM' was initiated. The goal of this exercise was to provide a quick vibrations analysis used for keeping a watchful eye upon tube dynamics during the critical shot ejection period. This is considered useful for comparing the responses of current or proposed systems against accuracy and was accomplished by incorporating the theoretical analysis into an efficient computer code to be used as an engineering tool within the cannon and mount design loop. A usable release of 'DYNAM' was made available four months after its inception and is continually being updated whenever new driving influences or more efficient numerical techniques become applicable.

The theoretical model coded in 'DYNAM' like others manages some things well, others not so well, and the rest not at all. For mode shape determination, the tube and mount are connected as shown in Figure 2. By itself the tube is treated as a finite length beam of constant cross-section

restrained through an axial and torsional linear spring mounted at the breech end. The modelling weakness existing here is that most gun tubes do not have constant cross-sections along their full length and the interaction between the gun and mount may be much more complicated. The saving grace for the former condition is that L/D ratios for gun tubes are very large, thus minimizing these inherent shortcomings. For the latter condition a stronger justification is needed. The interaction between a gun and mount is known to be a very complicated process possibly indicating a type of non-linear reaction. The coded model views support connections as linear springs rigidly attached to both gun and mount. There is no allowance for clearance or non-linearities. This could pose a serious limitation should actual reactions differ greatly from those modelled. In any event the analyst has the option of setting a spring rate as well as a wheelbase anywhere between zero and infinity thus allowing the support connection to be free, fixed, simple, or anywhere in between.

The complexity of the system PDE was greatly reduced by neglecting the rotatory and shear effects. A cursory order of magnitude study conducted on the resulting Euler beam formulation indicates that the effect of employing the simpler model would be of little concern for modal frequencies less than 10,000 Hertz. This may, however, limit the total number of natural frequencies that may be considered for a particular application. Neglecting these effects may cause convergence difficulties as solutions employing higher order roots are attempted. In addition, the numerical integration scheme has an impact upon convergence. A multi-step non-correcting method is employed as the ODE solver which may require the use of fine time increments to insure solution convergence. The penalty here is the cost of using an extensive amount of computer time as the need for a greater number of integration time steps increases.

The internal workings of 'DYNAM' is very detailed, therefore, an extensive trip through the code is outside the scope of this work. What will be presented instead is a cursory look at the general program flow, the inputs it needs, and the resulting output.

'DYNAM' accepts as input fifty-six single value variables as well as a table of transients related to ballistics and recoil forces. The entries and tables can be broadly segmented into five groups, the first of which concerns tube definition. Cylinder geometry, initial shape, density, and the material's modulus of elasticity are part of this group. The next group concerns projectile characteristics. Weight, eccentricity and shot spin comprise all of this group's data. The third group contains the variables defining the tube's interaction with the mount. Contained here is information regarding support stiffness and wheelbase, coefficient of friction, and radial location between sliding components. Filling the next group are all the transient tables mentioned above. The last set contains the program control data including various switches controlling output design, excitation forces to be considered, type of solution to be run, the number and accuracy of the natural frequencies, as well as the integration and output time steps.

Output can generally be divided into two broadly based groups: (1) results of normal modes analysis, and (2) complete dynamic history of gun tube flexure. The first set of outputs may be calculated independently of the second, but not vice versa. Dynamic portion needs the results of the normal modes section to establish the terms of the system's differential equation of motion. In regard to normal modes, 'DYNAM' calculates the roots, natural frequencies, and coefficients of the mode shape functions and files the results for independent graphing. The number of roots to be considered is requested of the analyst and is limited to twenty. Output generated as a result of the dynamic analysis includes transverse displacement, velocity, and slope of the breech, muzzle, and three equally-spaced locations in between. These calculations are reported as functions of time. At four equally-spaced time intervals, a file containing tube shape is generated as well.

The internal workings of 'DYNAM' can, in general, be divided into three segments. During the initial segment, mode shape analysis for the tube and mount is performed in the absence of any transient driving forces which in essence determines the free vibration modes of the system. By invoking the Method of False Position [4], the characteristic equation is solved yielding the natural vibration frequencies of the model. Straightforward calculations for determining the coefficients of the mode shape equations and files containing numeric data pertaining to the natural frequencies and mode shapes are then generated.

The analysis can be terminated here allowing a review of the calculations or may continue into the last two sections. In general, the second portion of code generates solutions to the second order differential equation relating the mode shapes, driving forces, and time dependent functions. The ordinary differential equations describing the time dependency contains terms of the function Q and its first two derivatives (all are $N \times 1$ vectors). The coefficient matrices are $N \times N$ in size where N is the number of natural frequencies considered. The rightside driving forces are lumped into an $N \times 1$ vector. All this information is passed on to the solving routine which initially determines the vector equation for the second derivative of the Q function. N ordinary uncoupled differential equations in time will be generated, the solution of which can be handled by well-established numerical procedures.

Integrations in time are performed by an Adams-Bashfort Backward Difference Scheme [5]. It is a multi-step method requiring derivative evaluations at four preceding time steps for each integration performed. This method was chosen because it is a straightforward, easily coded procedure not requiring continual time interval updates, backstepping, etc., used by self-correcting methods. Unfortunately, convergence criterion cannot be set a priori and very fine time increments may be needed for solutions to settle down. Self-correcting procedures may assure convergence, but would require a much more complicated code and probably would not execute a converged solution with a much greater real time saving. Better integration procedures are continually being evaluated for use in later editions of this code. Transient analysis continues until the dynamic input tables are exhausted at which point the third and final portion of the code assumes control.

In this final portion, the results of the previous two sections are combined yielding solutions to the Euler beam equation. The mode shape equations are transposed into a $1 \times N$ matrix and multiplied into the Q-vectors resulting in a dimensionalized transient vibration picture of the tube. Currently, this output is internally controlled yielding tube shapes at four equally-spaced time intervals and complete transient dynamics at five equally-spaced points on the tube. Output of this type will provide the analyst with both a "snapshot" of the tube at various times in the cycle, as well as a graphic representation of vibration buildup as the shot approaches and passes a point on the tube. In addition, dynamic animation can be achieved by the use of graphic routines which access numeric files generated by 'DYNAM'.

14. CONVERGENCE STUDY OF DYNAMIC ANALYSIS CODE: 'DYNAM'

Any mathematical model which allegedly mimics a physical system has certain limitations, a list of which has previously been presented for the model described herein. Any dynamic model requiring numerical integrating techniques should, as a bare minimum, establish convergence standards early on in its development cycle. In dynamic modelling requiring approximate integrating schemes, convergence is established when system responses approach a limit as the number of integration time steps increases. The limit for cases such as these could be a single value or a complete transient response over the total cycle. In addition, if a convergent limit can be confirmed by experimental methods, the model can then be utilized to accurately predict system responses due to a variety of parameter changes. This will circumvent the need for extensive testing. Many times, however, this link between the theoretical and real is weak. A model's convergence can still be established independently by repeating the analysis using a greater number of integration time steps rendering better accuracy for each solution. Convergence is reached when the results of subsequent calculations become indistinguishable from each other. The validity of these calculations may be suspect without the proper corroborating evidence, however, much can still be learned about the system's relative behavior by comparing various responses as the model's parametric muscles are exercised.

For the case presented here, convergence is a two-faceted item in that both time and space dimensions must be considered in its establishment. Since all continuous systems possess an infinite number of natural vibration frequencies, the model should approach reality as both the number of natural frequencies considered and the number of integration time steps approach infinity independently. Due to finiteness of computer resources and time, the most accurate solution cannot be tested. Instead, a reasonable tradeoff must be determined. Additionally, the link to reality cannot be made at this time due to the lack of a database containing the type of measurements needed for comparison.

The numerical scheme used for integrations in time has a derived equation for error estimates which is proportional to the fifth power of the step size and the fourth derivative of the function being integrated. Since we are not dealing with closed form functional relationships, estimating error limits prior to model execution is difficult if not impossible. Given all

this tenuous water in which we are treading, a heuristic approach will be used for determining the conditions of convergence. A number of independent runs of a given system will be made and a comparison between various output relationships will be used to determine when repeatability is achieved. The only parameters varied between each run will be the number of roots and the integration time step.

Before beginning this study, a few words about the type of results that will be used to assure solution convergence should be made. The underlying reason for conducting analysis of this type is to predict shot accuracy at the target so that in designing a gun system this parameter can be monitored and possibly optimized. The most critical point during a projectile's travel towards a target occurs at the instant of shot ejection. During this time the gases and projectile cause the gun to react violently. If a reasonable convergence criterion can be established at this point, convergence throughout the remainder of the cycle would be assured. There are three plots which most effectively portray a projectile's initial entrance into free flight. They are:

1. tube profile at projectile exit
2. transverse deflection of muzzle versus time
3. transverse velocity of muzzle versus time.

The graphs generated will be studied as both integration time steps and the number of modes considered are varied for a given weapons system.

The gun system to be used in the study is the M68 gun mounted in the M60 tank. The M392E3 trainer round, which has a muzzle velocity of 4900 ft/sec and develops 60,000 psi chamber pressure during its six millisecond excursion along the tube's bore, will generate the ballistic driving forces. The stiffness between the gun and mount will be set at 100,000 lb/in. and the wheelbase will be 22 inches. The tube itself is modelled as a cylindrical beam 7.23 in. O.D. by 4.13 in. I.D. by 210 in. long. Additionally, a .010-inch eccentricity will be set into the projectile in order to drive the two eccentric dependent excitation forces.

A preliminary calculation indicated that for the above conditions the tenth mode of vibration occurs at a frequency of 1100 Hertz, while the twentieth mode occurs at 5150 Hertz. Since an earlier order-of-magnitude study indicated that shear effects which have been neglected will become a factor at about 10,000 Hertz, it appears that using twenty modes will keep the model well within the framework of the analysis. Due to the extensive computation time needed to run a twenty-modes solution, it was decided to set twelve mode shapes as the upper limit in order to achieve tolerable execution times. The range of values for the independent variables used in the convergence study will be:

number of modes: 6, 8, 10, 12
integration time step: 20, 10, 5, 2.5 microseconds

The results of the convergence study are contained in Figures 4, 5, and 6. On each of the figures four graphs are shown, each one containing four plots. These four plots indicate system responses for the four time steps chosen within the given number of mode shapes. The four graphs per figure show the response for the various modes considered. In Figure 4 the tube profile at projectile exit is indicated for the various integration time steps and mode shapes. Within each mode shape, the four tube dynamic profiles appear to be superimposed upon each other. This condition definitely indicates solution convergence within each mode. This characteristic is present on the remaining figures of muzzle displacement and transverse velocity as well. The actual shapes are somewhat different as more modes are used in analysis. Use of six mode shapes yields a rather flat profile, whereas when eight, ten, or twelve modes are used, a well-defined non-linear shape results. The difference in profile between ten and twelve modes is very slight indicating that total convergence is being approached at these levels. The overall maximum deflection varies from -0.012 to -0.020 inches at 40 to 60 inches from the breech end. At the muzzle end the results are more uniform. Tip deflections run about 0.007 inches for all cases considered.

On the two figures which follow, transient responses of the muzzle end are shown. The transient range runs from the initiation of ballistic pressure up to projectile exit (about 6 m-s). Results indicate that the muzzle displacements predicted by all 16 cases are similar and approach convergence at ten mode shapes. The muzzle raises somewhat steadily as the shot progresses down the bore. The maximum deflections achieved are between 0.007 and 0.009 inches. The transient response of the muzzle's transverse speed indicates the greatest deviations between modes. A cyclic pattern just before projectile exit becomes more pronounced as more modes are considered, however, the difference between response at projectile exit is negligible for ten or twelve modes. In all there is a swing of about 4 in./sec of the muzzle at exit considering all 16 cases.

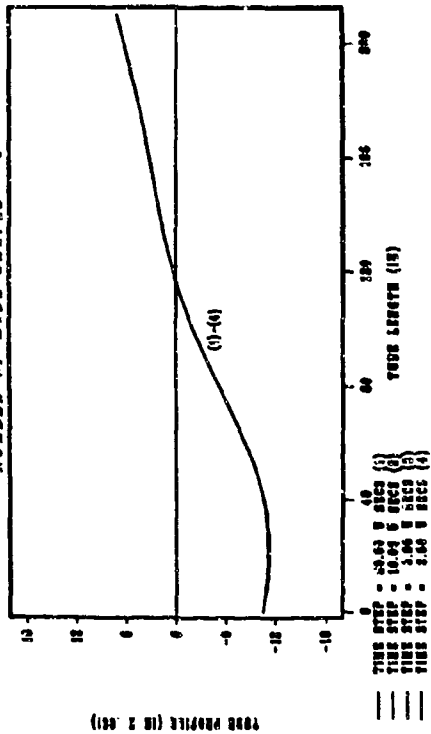
In light of these calculations, it appears that both within mode as well as overall, solution convergence can be claimed. This assures us that the model can be used with confidence to compare the change of response induced by the change of an individual parameter (i.e., sensitivity study). This will be the tone of the concluding portion of this paper. The ten mode shapes model with a ten microsecond integration time step will be used during this study due to the convergence level it established.

15. SENSITIVITY STUDY OF GUN ACCURACY AND VIBRATION

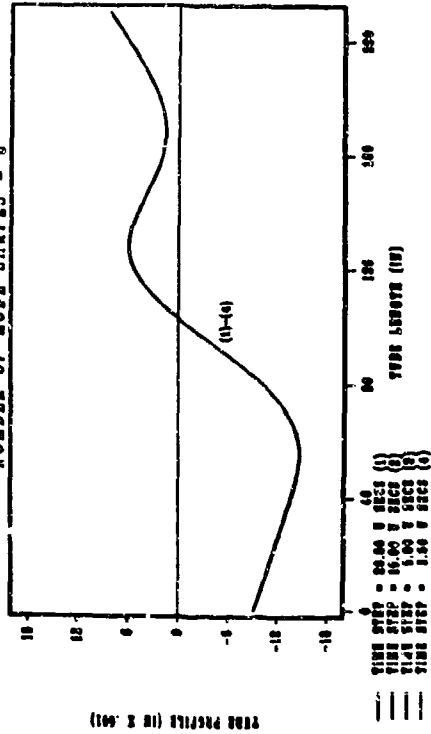
Pure dynamic analysis of gun vibrations is of little value without using the calculated information to predict the projectile's impact point at the target. In the concluding portion of this paper a shot impact model will be proposed and its sensitivity to a number of weapons system parameters will be tested to establish potential dispersion patterns. In addition, tube vibrations will be studied in pseudo-animation to gain insight into relative motion during and after projectile's in-bore presence.

The initial conditions of a projectile's exterior flight toward a

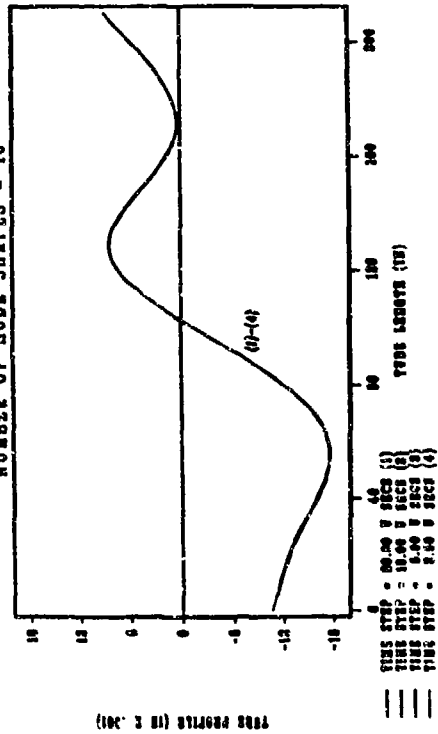
CONVERGENCE STUDY: TUBE SHAPE AT PROJECTILE EXIT
NUMBER OF MODE SHAPES = 6



CONVERGENCE STUDY: TUBE SHAPE AT PROJECTILE EXIT
NUMBER OF MODE SHAPES = 6



CONVERGENCE STUDY: TUBE SHAPE AT PROJECTILE EXIT
NUMBER OF MODE SHAPES = 10



CONVERGENCE STUDY: TUBE SHAPE AT PROJECTILE EXIT
NUMBER OF MODE SHAPES = 12

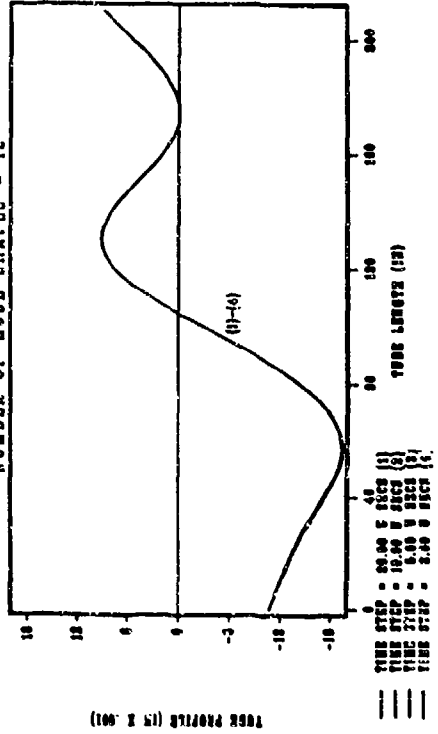
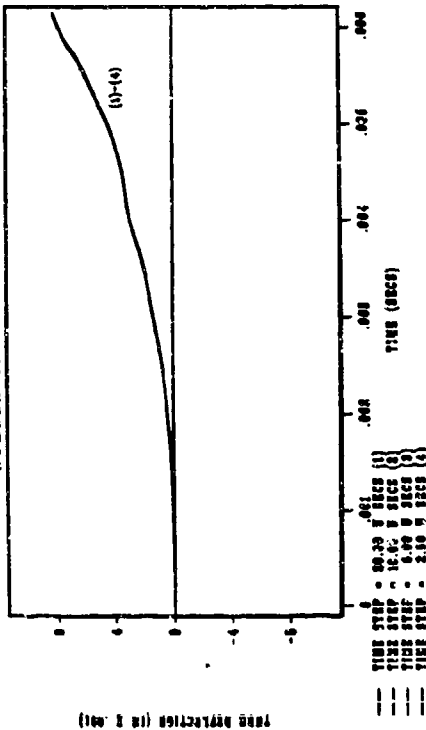
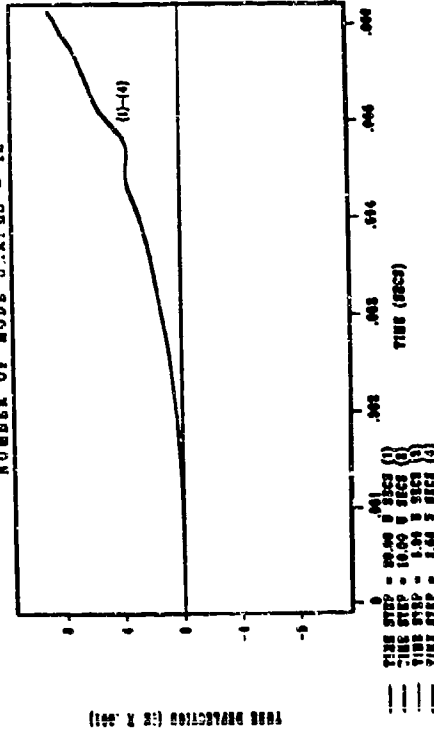


Figure 4. Convergence Study: Tube Shape.

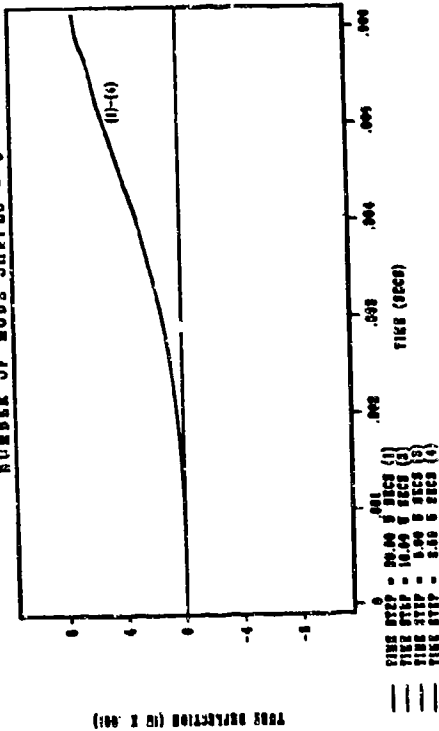
CONVERGENCE STUDY: MUZZLE DEFLECTION VS TIME
NUMBER OF MODE SHAPES = 8



CONVERGENCE STUDY: MUZZLE DEFLECTION VS TIME
NUMBER OF MODE SHAPES = 12



CONVERGENCE STUDY: MUZZLE DEFLECTION VS TIME
NUMBER OF MODE SHAPES = 6



CONVERGENCE STUDY: MUZZLE DEFLECTION VS TIME
NUMBER OF MODE SHAPES = 10

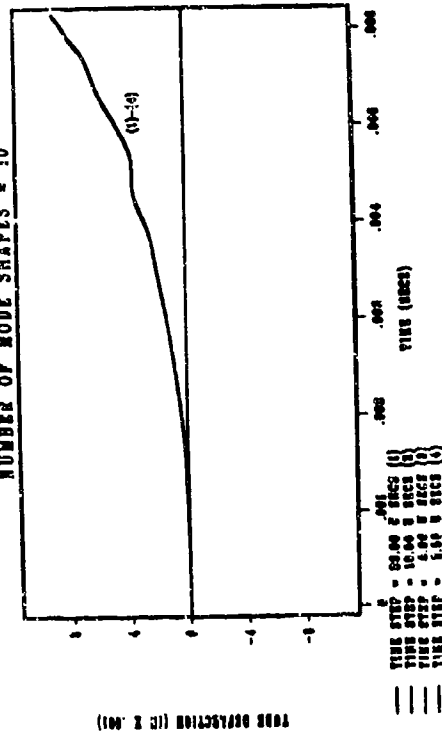
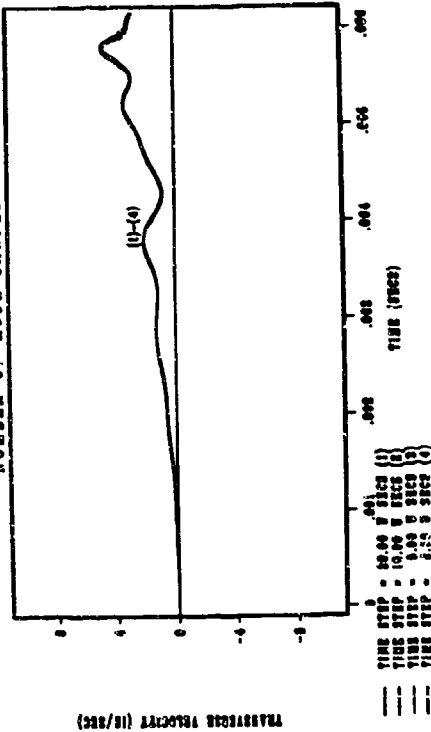
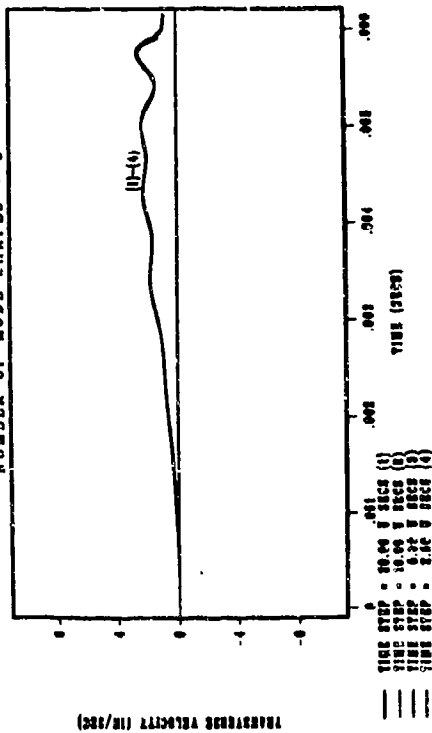


Figure 5. Convergence Study: Muzzle Deflection.

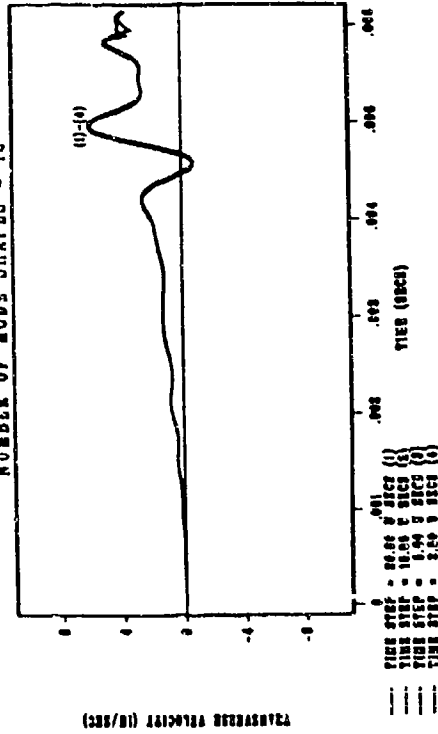
CONVERGENCE STUDY: TRANSVERSE MUZZLE SPEED VS TIME
NUMBER OF MODE SHAPES = 8



CONVERGENCE STUDY: TRANSVERSE MUZZLE SPEED VS TIME
NUMBER OF MODE SHAPES = 6



CONVERGENCE STUDY: TRANSVERSE MUZZLE SPEED VS TIME
NUMBER OF MODE SHAPES = 12



CONVERGENCE STUDY: TRANSVERSE MUZZLE SPEED VS TIME
NUMBER OF MODE SHAPES = 10

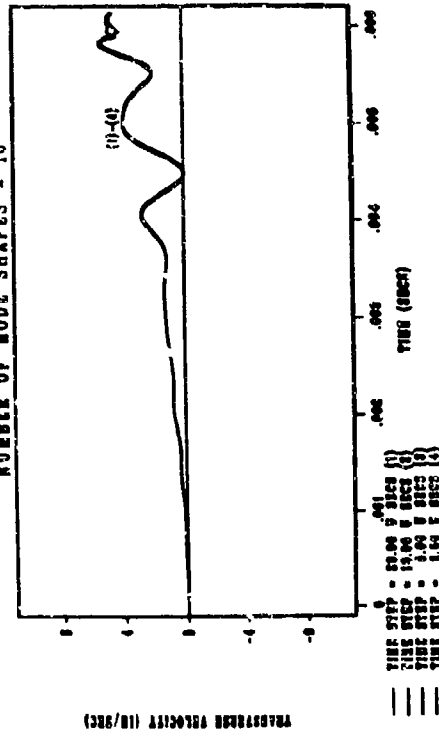


Figure 6. Convergence Study: Muzzle Velocity.

target are directly related to the kinematics of its in-bore travel. The projectile is generally confined to an in-bore path created by the vibrating tube. At exit, the kinematic conditions of the path may cause deviations in the projectile's flight toward the target. A geometric representation of this proposed impact can be found in Figure 7. Its contributing components include the displacement, slope, and transverse velocity of the tube's muzzle at projectile exit. These three conditions have been applied to the projectile's initial entry into free flight and have been projected to the target according to the equations shown on the figure. The model is idealized in that all contributions are given full rating values when in fact some (e.g., transverse velocity) may be attenuated due to ambient flight conditions. The model, however, will be used to calculate a single value dispersion factor for a particular combination of weapon system parameters.

To conduct the study systematically, a set of baseline system parameters will be chosen. Some of these will be labeled test parameters and will be allowed to vary in a prescribed manner throughout subsequent dynamic modelling executions, while the rest will remain at baseline values. Dispersion patterns will be calculated using the geometry previously described and the results will be graphically presented for all combinations and variations considered. Conclusions will be drawn from a study of this data. The weapon system to be used will be much the same as the one used in the convergence study. As previously mentioned, ten mode shapes will be sufficient to accurately portray the physical system and ten microsecond integration time steps will be used in the transient analysis. The same ballistics will be used, however, an additional four milliseconds will be added in order to study the effects of post ejection vibrations. This will be done to gain insight into relative motions between both phases in the ballistic cycle.

The sensitivity study will include four system parameters. The first is the tube support condition provided by the mount. The physics of tube support is a very obscure area, but is considered by experts to be a major contribution to tube motion. For this reason, all support conditions will be tested against the remaining independent parameters to gain insight into its interactive effect on gun motion. Five types of support conditions from free to fixed will be tested (see Table 1). The second test parameter will be the tube's bending resistance which is proportional to the outer diameter of the cylindrical beam used as the gun model. The tube becomes less flexible as this dimension increases. The state of projectile imbalance will be the third parameter tested. Imbalance contributes to two of the external driving loads discussed earlier. The first is the projectile's rotational load, while the second is the reacting load needed to preserve the projectile's in-bore path. This load is directly proportional to the projectile's wheelbase and the ballistic driving force behind it. The round being used in the study rotates with the rifling, therefore, imbalance will drive both of these forces. Due to the presence of both loads, two independent parameters within the imbalance envelope will be considered: the magnitude and location of the imbalance at projectile exit. Both of these will be varied independently including a wide range of possibilities. The last parameter concerns the tube's static deformation. When a mounted tube is

MODEL OF SHOT DISPERSION

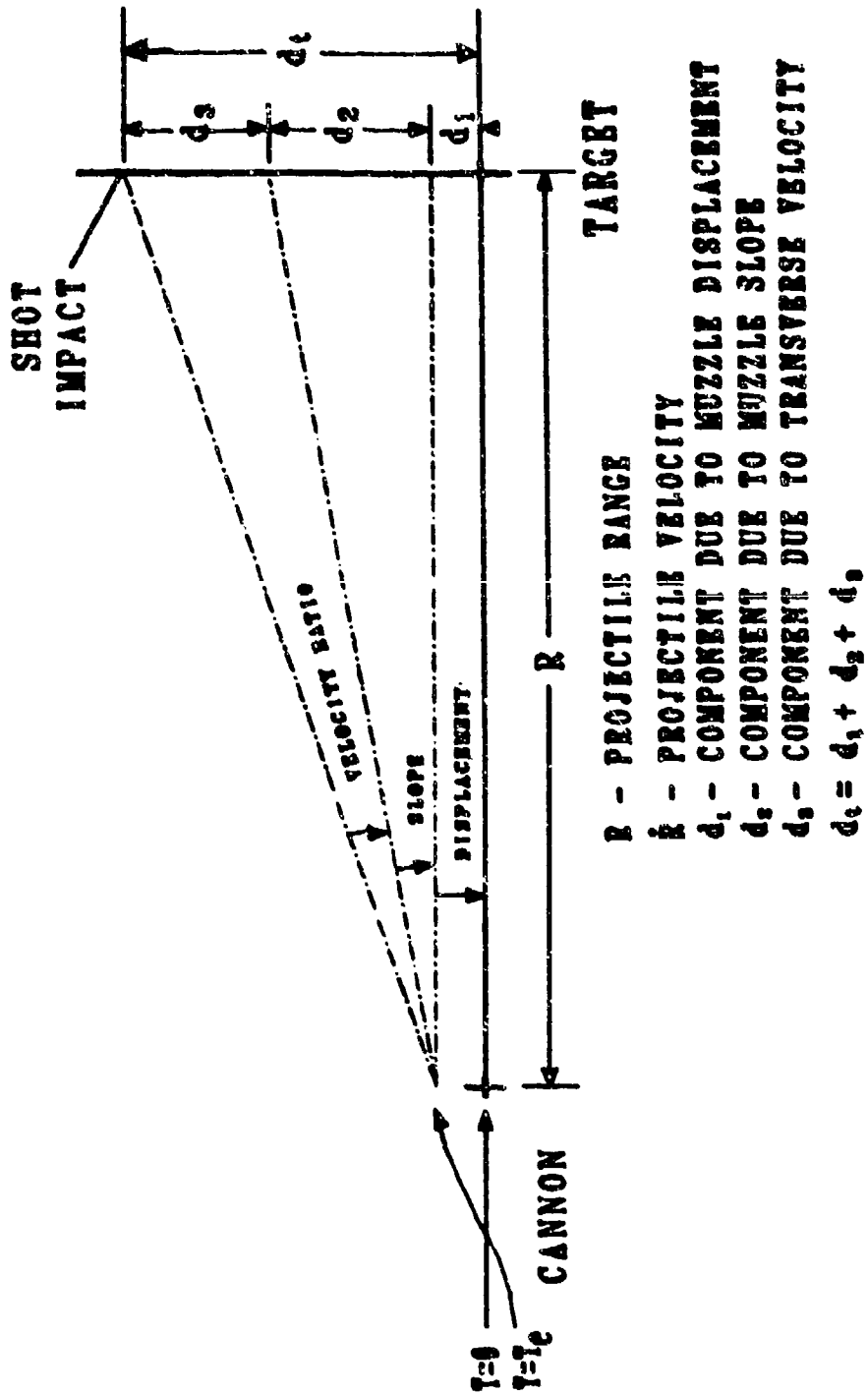


Figure 7. Shot Impact Geometry.

SNECK and GAST*

at rest, it assumes a curved shape due to its own weight. Superimposed upon this could be additional curvature due to manufacturing tolerances and/or thermal distortion due to environmental and operational heat loads. There are three input coefficients which may be used to augment or negate the natural droop of the tube. This option will be exercised for a variety of static shapes. The values for the various test parameters are shown in Table 1 with baseline levels appropriately indicated. A total of 85 runs have been made, the results of which will be reported in the following manner.

TABLE 1. SENSITIVITY STUDY TEST PARAMETERS VALUES

| Value I.D. Number | | 1 | 3 | 5 | 7 | 9 |
|--|-------------------------------------|---------------|----------------|------------------------|----------------|-----------------|
| Physical Parameter | | | | | | |
| M O U N T | Displacement Stiffness → | Free 10**0 | Light 10**3 | Medium 10**5 (B) | Heavy 10**7 | Fixed 10**10 |
| | Rotational Stiffness → | 10**0 | 10**5 | 10**7 (B) | 10**9 | 10**11 |
| | KR(lb/in./rad) | | | (B) | | |
| T U B E | Bending Resistance → | 5.00 | 6.00 | 6.50 (B) | 7.00 | 8.00 |
| | Beam O.D. (in.) | | | (B) | | |
| | Initial Curvature → | 0 | 50 | 100 (B) | 150 | 200 |
| | % Static Droop | | | (B) | | |
| P R O J E C T I L E | Imbalance Magnitude → | .0000 | .0033 | .0050 (B) | .0067 | .0100 |
| | Eccentricity (in.) | | | (B) | | |
| | Imbalance Location → | 90 | 180 | 225 (B) | 270 | 360 |
| | Projectile Exit (Deg) 90 ==> Top | | | (B) | | |

(B) ==> Baseline value

The first is in regard to impact dispersion for the range of values within a particular tube or projectile test parameter for all mount stiffnesses. Impact locations will be plotted against support conditions. For a given test parameter a pair of symbols at each stiffness will indicate the potential impact dispersion for the full range of test parameter values.

The second form of data reporting is in regard to tube shape during various portions of the ballistic cycle. To enhance analysis of this type, a Fortran written animation routine employing Tektronix hardware and software was written. Basically, the routine receives tube shape calculations from 'DYNAM' and draws the shape and projectile location on the graphic display tube at user specified time intervals of the ballistic cycle. Each deformed shape comprises one frame in the animation. When the visibilities of all dynamic frames are sequentially switched from on to off and vice versa with appropriate delays between operations, the illusion of vibratory motion prevails. Playback speeds can be controlled by the user and range from a single frame to about 100 frames per second. In the animation, the tube is represented by its centerline. The animation can be recorded on a video tape recorder for transmission to areas remote to the graphic display unit. A selected number of animations will be presented at this Symposium.

16. RESULTS AND CONCLUSIONS

Graphical results of the dispersion calculations for all runs can be found in Figure 10. The vertically placed symbols placed at each stiffness label indicate the maximum and minimum impact response for the test parameter considered. The continuous line connects the baseline responses and is the same on all graphs. With the exception of the tubes bending resistance, all of the parameters were tested at their full range of values. When the tube's O.D. was tested at five inches, excessive vibrations and dispersion resulted; thus this point was eliminated from the study. A number of observations can be made in regard to the information contained on these charts.

In regard to baseline values of all test parameters:

1. Dispersion responses best for a free support condition.
2. A degradation in dispersion response is evident as support stiffness increases.
3. For the fixed support condition dispersion response is slightly worse than for the free end case.

In regard to a tube's bending resistance and initial curvature:

1. Tubes offering greater bending resistance and less initial curvature showed better accuracy.
2. The greatest variation in impact response occurs in the mid-range values of support stiffness.

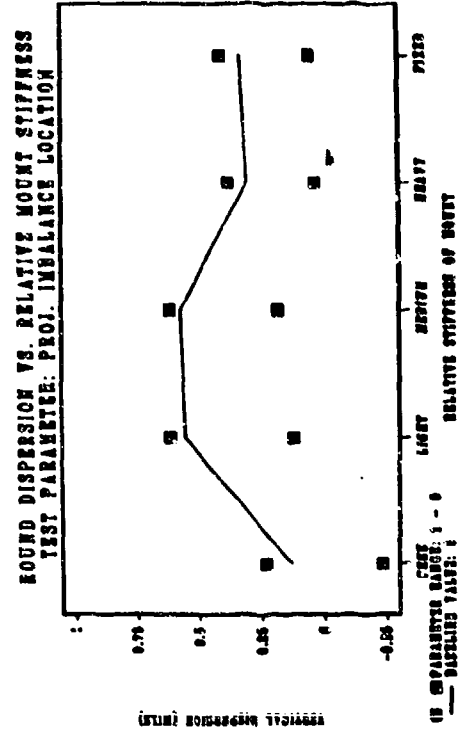
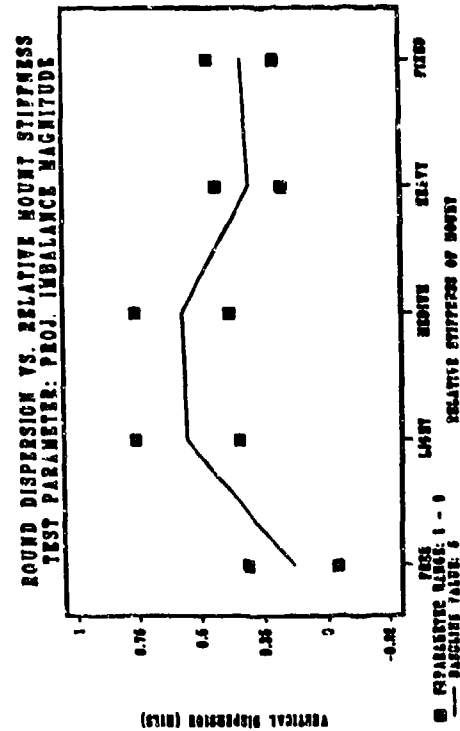
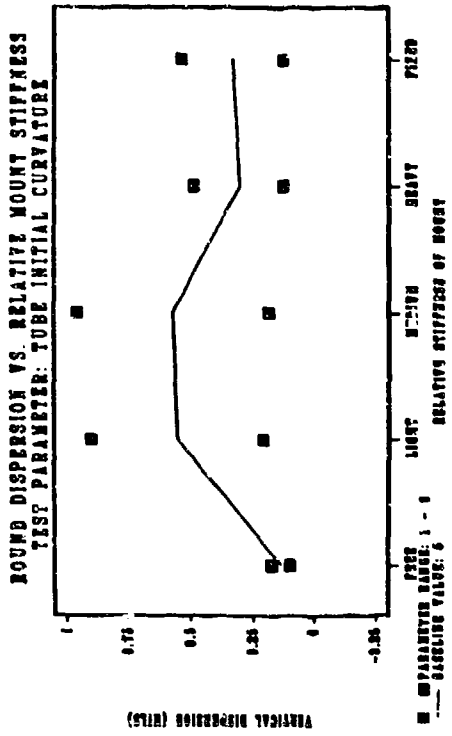
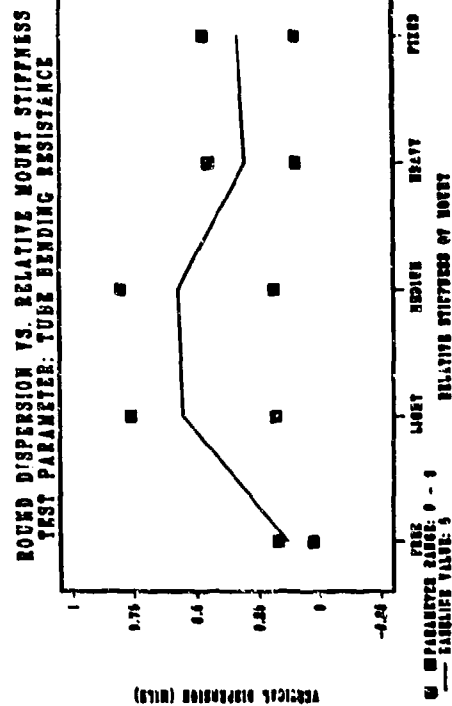


Figure 8. Dispersion Calculations.

In regard to a projectile's condition of balance:

1. Perfectly balanced projectiles impact closer to the aim point than others.
2. The impact point of a round is directly proportional to the magnitude of its imbalance.
3. The location of its imbalance at projectile exit affects its impact point.

From the results of the above study, it appears that tube motion and accuracy can be affected significantly by many of the physical features inherent in the weapon system. The few which have been analyzed attest to this. We would recommend that this model be pursued in greater depth, incorporating other system characteristics as well as conducting laboratory-controlled firing tests to verify the analytical results.

REFERENCES

1. D. Warken, K. Wolf, R. Heiser, and J. Ballman, "The Effect of Barrel Curvature and Projectile Unbalance on Excitation of Gun Vibrations," Proceedings Third U.S. Army Symposium on Gun Dynamics, Vol. II, 1982, p. III-43.
2. T. E. Simkins, "Transverse Response of Gun Tubes to Curvature-Induced Load Functions," Proceedings Second U.S. Army Symposium on Gun Dynamics, 1978, p. I-67.
3. J. J. Wu, "On the Dynamic Forces in Gun Tube Motions Analysis," Proceedings Third U.S. Army Symposium on Gun Dynamics, Vol. II, 1982, p. III-86.
4. S. D. Conte, Elementary Numerical Analysis, McGraw-Hill, NY, 1965, pp. 40-41.
5. S. D. Conte, Elementary Numerical Analysis, McGraw-Hill, NY, 1965, pp. 226-228.

TITLE: Projectile Foundation Moment Generation
EDWARD M. PATTON
Battelle, Pacific Northwest Laboratory
Richland, Washington 99352

ABSTRACT:

A three year project was initiated at Battelle, Pacific Northwest Laboratory under the sponsorship of the US Army Ballistic Research Laboratory to assess the moment created by the cocking or balloting motion of an obturated projectile in the bore of a large caliber gun. The study focused on the ability of the nylon obturator band to generate this moment in a single bore contact projectile, and the magnitude of the moment that is produced for a given transverse angular disturbance of the projectile.

The results of the overall study showed that the nylon obturators do impart a significant moment to the gun barrel when the projectile cocks in bore. The magnitude of this moment at a given angular disturbance can be compared to the moment that is induced when the center of gravity of the projectile is roughly two thirds of a caliber behind the center of rotation of the projectile at the time of maximum acceleration of the projectile in bore. This is not a second order effect, and in fact could dominate other disturbance forces at other locations or times during travel down the gun barrel. This is particularly true early in the ballistic cycle as the obturator is being extruded through the forcing cone at the end of the chamber. It will in fact have a large effect on the ability of the projectile designer to produce effective minimum weight projectile designs.

BIOGRAPHY:

PRESENT ASSIGNMENT: Technical Leader, Computer Aided Engineering, Battelle, Pacific Northwest Laboratory, Richland, WA.

PAST EXPERIENCE: Research Engineer and Senior Research Engineer at Battelle (1980-present).

DEGREES HELD: BS Biology, University of Oregon, BSME and MSME, Oregon State University.

PROJECTILE FOUNDATION MOMENT GENERATION

EDWARD M. PATTON
BATTELLE, PACIFIC NORTHWEST LABORATORY
RICHLAND, WASHINGTON 99352

1. INTRODUCTION

This paper represents the presentation of three years of effort conducted at Pacific Northwest Laboratory under funding and direction of the US Army Ballistic Research Laboratory. The thrust of the effort has been to investigate the interaction between typical nylon obturators of APFSDS projectiles and the gun tube, when a projectile experiences balloting (wobbling) motion. It had been thought in the past that the moment imparted to the projectile which is reacted by the gun barrel when the projectile cocks in-bore was an insignificant quantity. The results of this study show that, in fact this moment is probably the dominant force on the projectile early in the ballistic cycle [1,2].

The project was a combination of an analytical and experimental study to determine the magnitude of the foundation moment, and the influence that design of the obturator has on the magnitude of the moment. The experimental work was initially done with a static test fixture which simulated the gun bore, the interference between projectile and gun bore, and a simulated obturated projectile. This fixture is shown schematically in Figure 1. Initial results showed that the moment inducing bar was much too flexible, and a much stiffened fixture was constructed for the remainder of the first year of testing. That fixture is shown in Figure 2. At the end of the first year of testing and analysis, it became evident that sliding contact between the projectile and gun bore was very important. Section 2 describes in detail the testing for the first year, and Section 3 the analysis of that testing. A suitable projectile launching device, shown in Figure 3, was constructed during the second year of the project, and data were taken for a sliding projectile which was caused to have a prescribed angular disturbance. Sections 4 and 5 describe the testing and analysis respectively for the second year. The experimental tasks for the third year were intended to extend the band geometry from the simple flat band used for the first two years of testing to a geometry more characteristic of the obturator bands used on common APFSDS projectiles. A schematic of the four band geometries, and the projectile used in the third year of testing are shown in Figure 4. Section 6 describes the results of the third year of test and analysis.

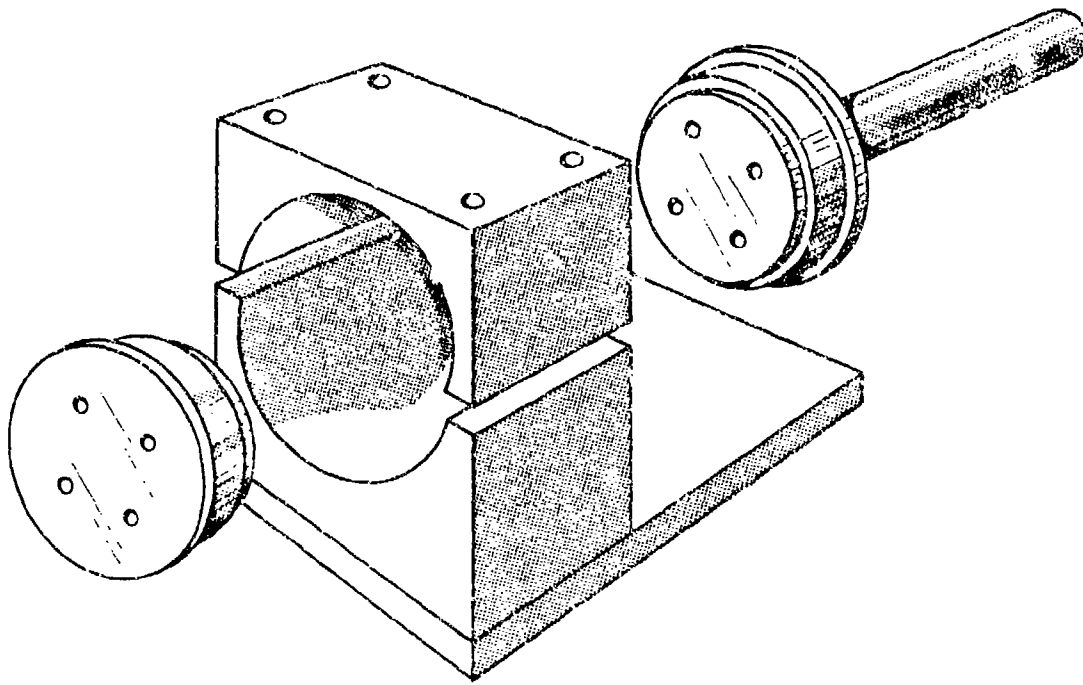


Figure 1. First Test Fixture

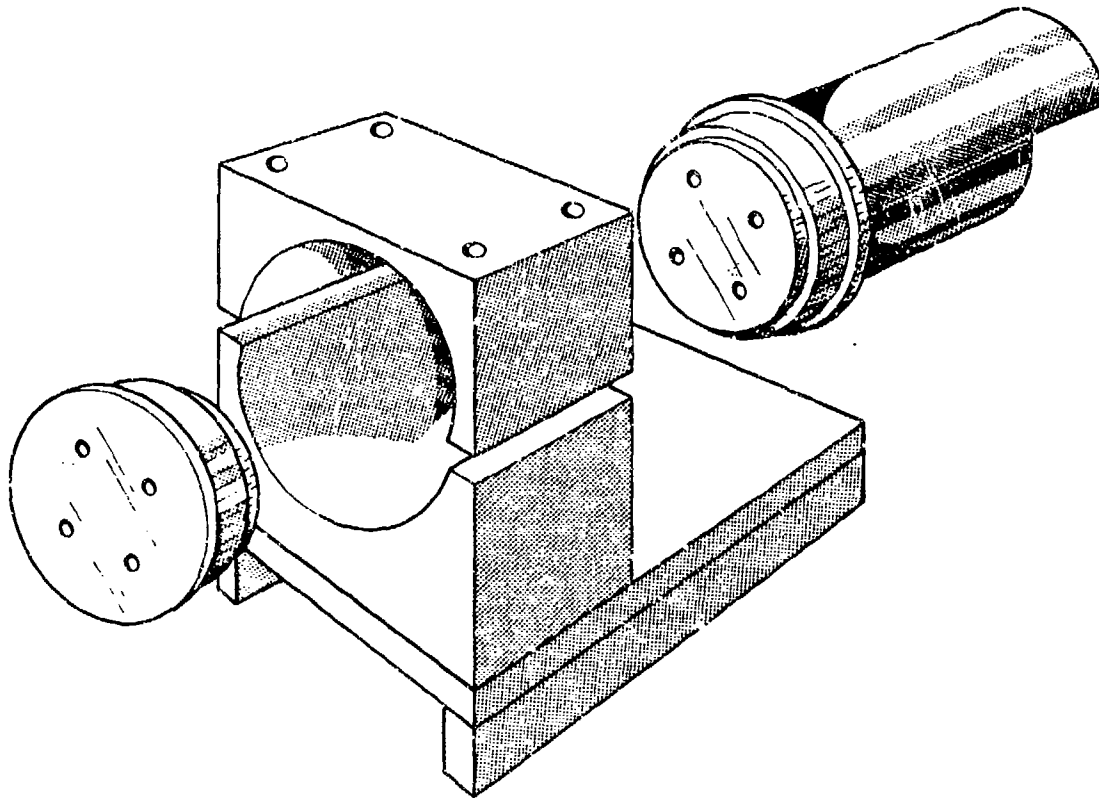


Figure 2. Stiffened Test Fixture

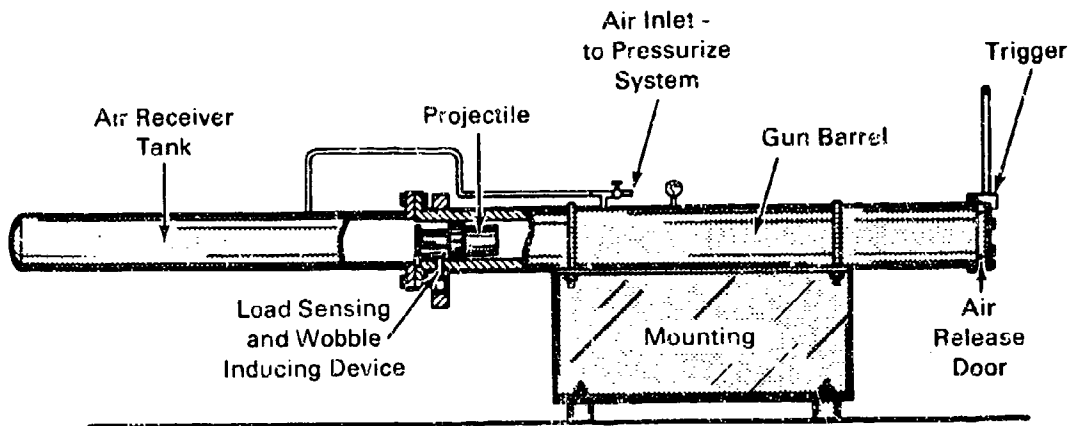
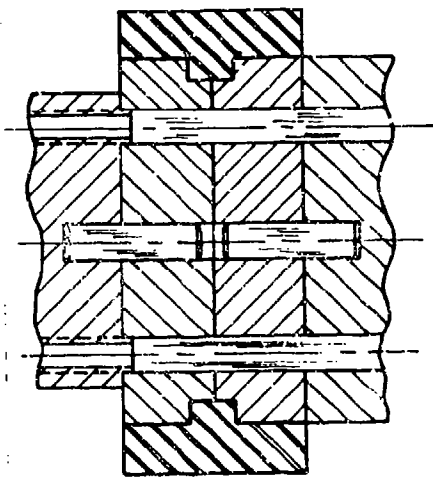
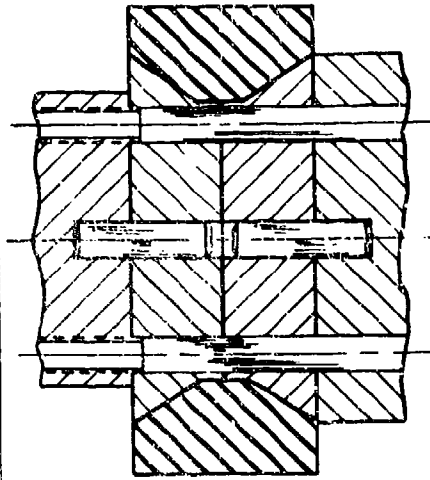


Figure 3. Projectile Launching Device

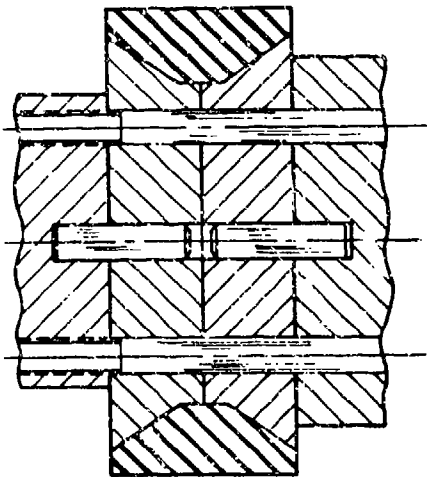
The analytical work for this project consisted of using the finite element method to model the projectile and its angular disturbance. Initially, fully elastic material properties were used for the nylon obturator materials, and two dimensional calculations were attempted. Three dimensional analyses were then conducted, along with material characterization tests for the nylon material used in the simulated obturator. An initial scoping study was performed to determine the mesh refinement necessary to give accurate results in the calculations. Initially a 15 degree circumferential element size was deemed adequate for the linear analysis, but the non-linear analysis required a somewhat more refined mesh (10 degree circumferential element size). In fact, it is still one of the overriding concerns of this author whether or not the finite element method will prove to be the correct tool to model this phenomenon. More about these concerns and some conclusions about the foundation moment and this project are included as Section 7 of this paper.



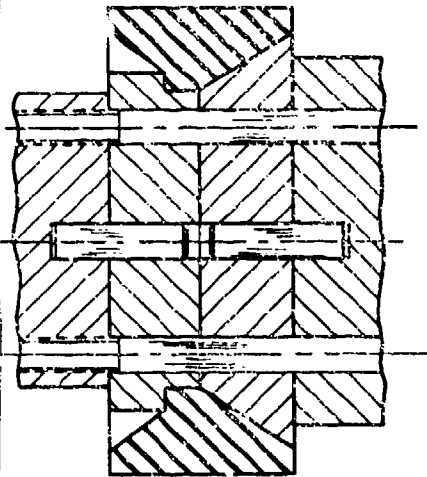
Band A



Band B



Band C



Band D

Figure 4. Schematics of Bands for Third Year

2. STATIC TEST APPATARUS AND PROCEDURES

The schematic of Figure 1 shows a fairly thin moment inducing bar. Originally, this was made of aluminum, and was fairly flexible. At the outset of the project, it was not expected that the foundation moment would be of very large magnitude. Instead, it has been traditionally thought that the nylon obturator band did not provide any resistance to transverse rotation of the projectile. The initial test results with the fixture in Figure 1 proved that the nylon indeed provided a large resistance to rotation. A much stiffened static test fixture was constructed, and results were generated using that fixture. The final configuration of that fixture is shown in Figure 2 as described above. The central portion of the fixture is made of steel, and is considerably more stiff than the original. The base of the fixture also had to be stiffened, resulting in the two welded stiffeners shown in the figure.

To take the data, the fixture was mounted flat on a rigid surface, and a clip gage was mounted underneath the end of the moment inducing bar. A load of known magnitude was applied to the top of the bar, and deflections of the end of the bar were measured with the clip gage. Characteristic output from that testing is shown in Figure 5. This data was taken with the final configuration of the static test fixture, with the stiffened central core and fixture base.

3. ANALYSIS OF STATIC FIXTURE - FIXED VERSUS SLIDING

Several finite element analyses were performed initially as scoping calculations, and to determine if the finite element method would adequately model the foundation moment. All finite element analyses for the three years of this project were performed using the finite element code ANSYS [3]. ANSYS has a large library of elements, and a large suite of capabilities both linear and non-linear, and both two and three dimensional. This allowed the author to use one single code for all of the analyses performed. The code was also available at low cost on an in-house computer.

All of the two dimensional analyses were performed with the same basic element, a two dimensional isoparametric quadrilateral element with several options. One of the options exercised was that of modelling a disc with a nylon outer band constrained at its edge, and displaced in the center. The plane strain option available with that element was exercised in this analysis, which was performed in an attempt to determine the circumferential mesh refinement necessary to adequately model the static test fixture, and ultimately the foundation moment for a typical projectile. Figure 6 shows the mesh used to perform the plane strain calculations. Another option of the element is an axisymmetric solid with non-axisymmetric (harmonic) loading (this is actually a separate element type in ANSYS, but the element defaults to the same as the main axisymmetric element if no harmonic loading is present). Figure 7 shows the mesh used for this calculation. This particular option on the isoparametric element does not allow material non-linearities. Preliminary calculations showed that the nylon band would probably be under sufficient

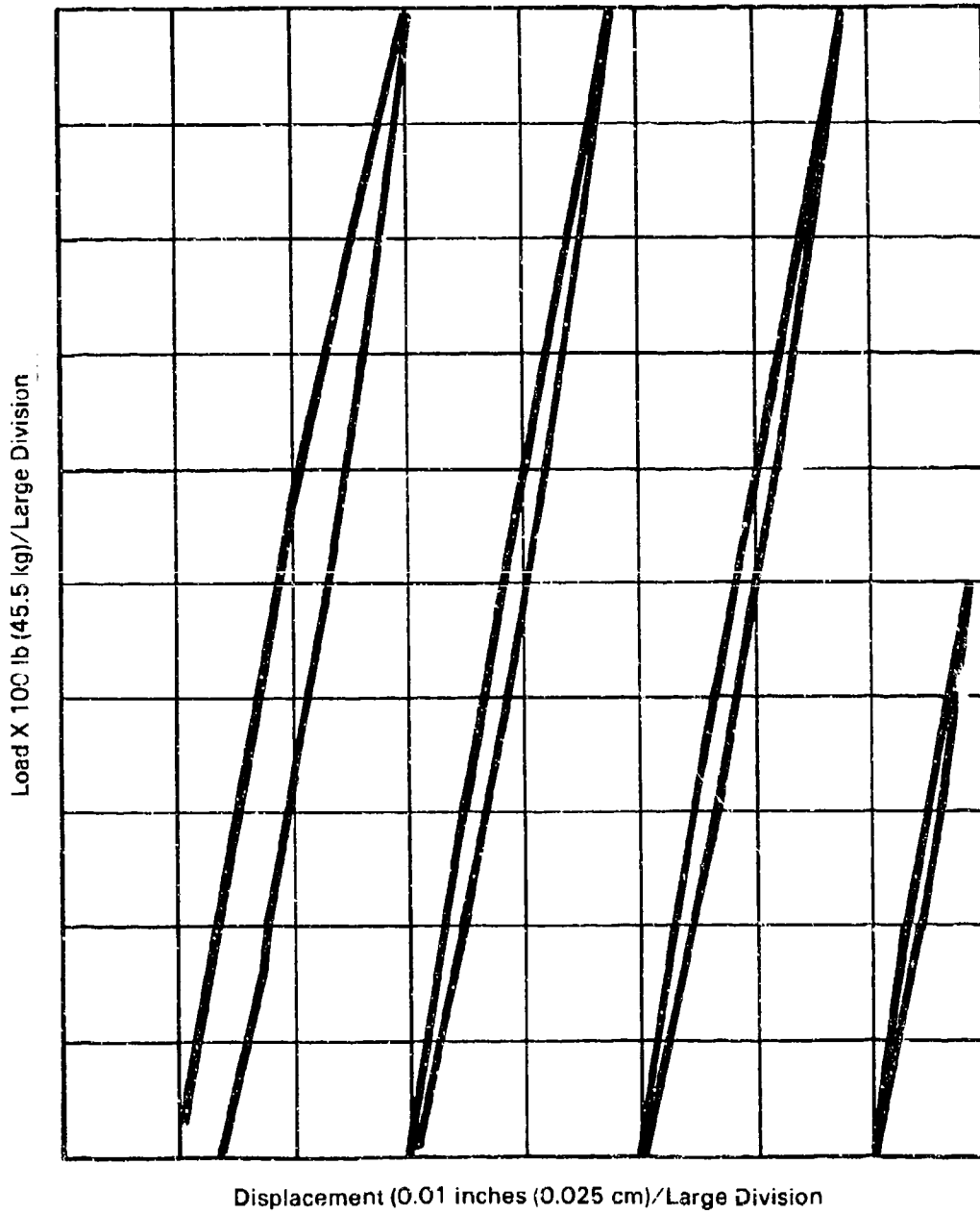


Figure 5. Characteristic Test Output

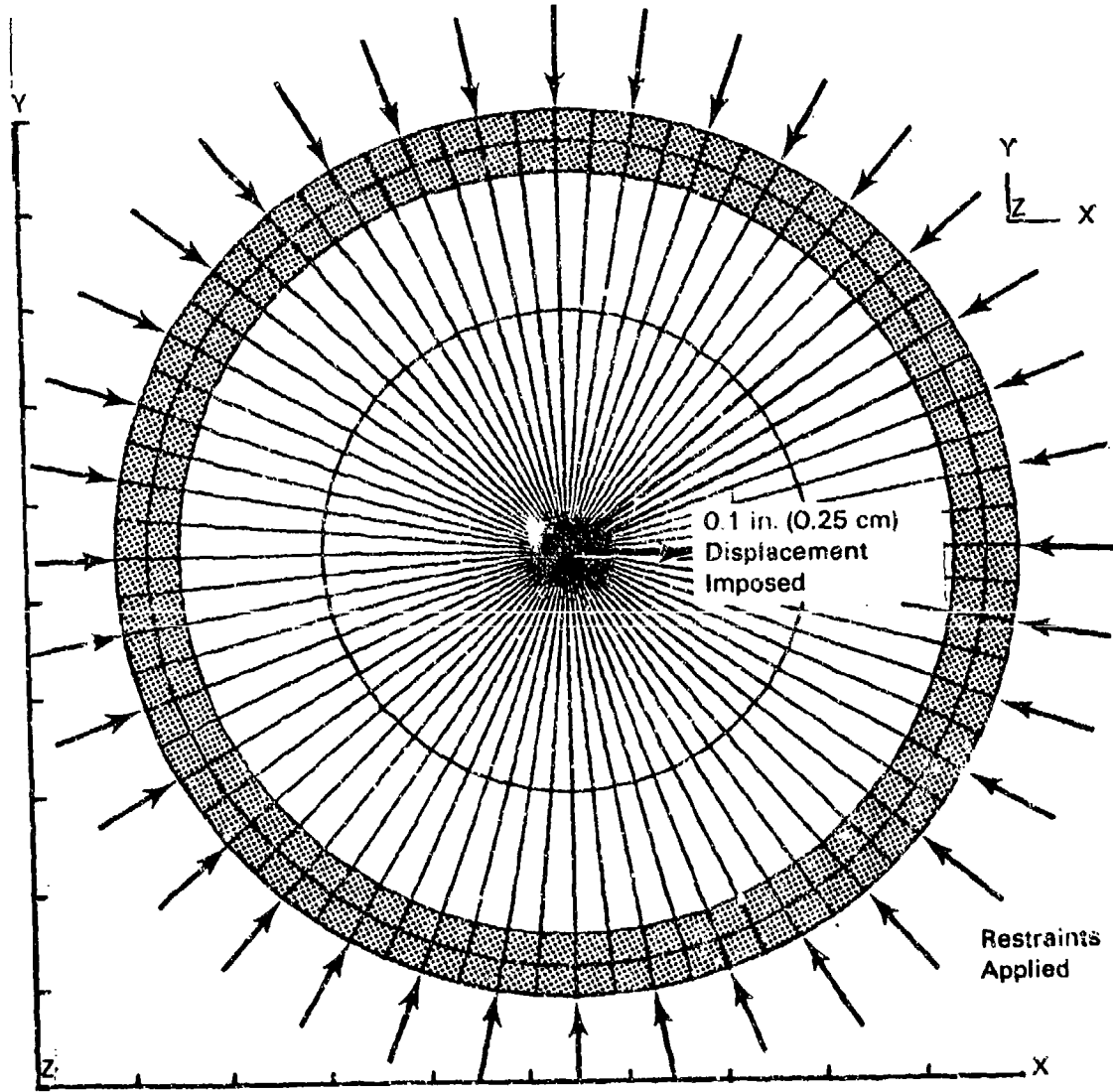


Figure 6. Two Dimensional Plane Strain Mesh

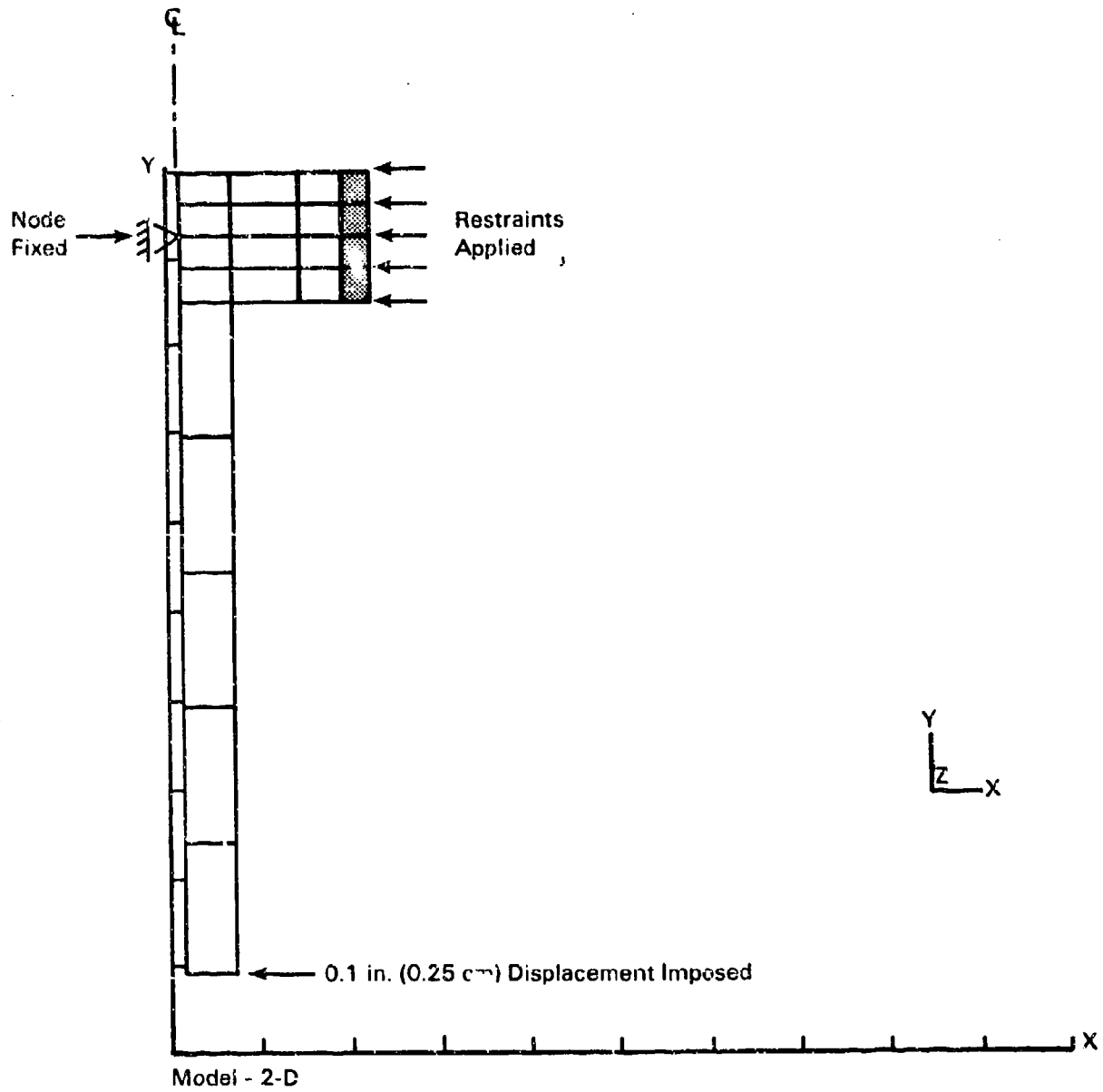


Figure 7. Two Dimensional Axisymmetric Mesh

stress that it would behave in a non-linear fashion, and as such it was deemed important to perform three dimensional calculations with a representative material curve. The two dimensional calculations were thus used to determine the circumferential mesh refinement required for the three dimensional calculations. Figure 8 is the result of a sensitivity study performed to determine the required circumferential element size for the three dimensional calculations. A circumferential size of 15 degrees was selected for the three dimensional calculations from this sensitivity study. Figure 9 shows the final three dimensional mesh used to perform the calculations modeling the stiffened static test fixture.

The calculations were initially performed with the outside of the nylon completely fixed in the axial and radial directions. Those results proved to overestimate the foundation moment significantly. Another analysis was run relaxing the axial boundary condition, with some surprising results. The predicted foundation moment with only radial fixity was one fifth of the predicted foundation moment with both radial and axial fixity. An analytical estimate of the difference between these two boundary conditions substantiated this result [?]. It became apparent that measurement of the foundation moment in a fixture which did not allow the nylon band to slide in relation to the simulated gun barrel would not be representative of an actual gun firing an actual projectile. The second year of testing therefore concentrated on constructing a suitable projectile launching device with which a prescribed angular deflection could be input, and the force required to produce that angular deflection could be measured.

4. PROJECTILE LAUNCHING DEVICE

The device constructed to launch the model projectile is shown in Figure 3 as described in Section 1. The rear of this device is a section of six inch schedule 40 steel pipe with a pressure cap welded on one end, and a pressure flange welded on the other end. This flange is mated with a flange welded on the end of a length of actual gun barrel approximately six feet in length, provided by BRL. At the flange (breech) end of the gun barrel is a ramp-like device for inducing an angular deflection into the projectile, and measuring the force required to produce that deflection. The projectile is made of aluminum, with a faceted steel rear end plate. This plate is precision machined and measured such any one of several known angular deflections can be induced. Each of the flats of the faceted plate produces a different angular deflection when that flat is caused to ride up and over the ramp-like deflection inducing, force measurement device. Under the tall end of the ramp (muzzle end) is a rod which actuates a piezoelectric force transducer. The output from the force transducer is captured on a digital oscilloscope, and recorded. Several projectiles have been successfully launched using this device, and at several different angular deflections. Initially, there was also a trap door device at the muzzle end which was used to trigger the system. The entire system was pressurized (both receiver tank and gun barrel) to the maximum available building air pressure (about 125 psi). The triggered trap door mechanism was then released, releasing air pressure in front of the projectile, causing the projectile to accelerate down the gun barrel.

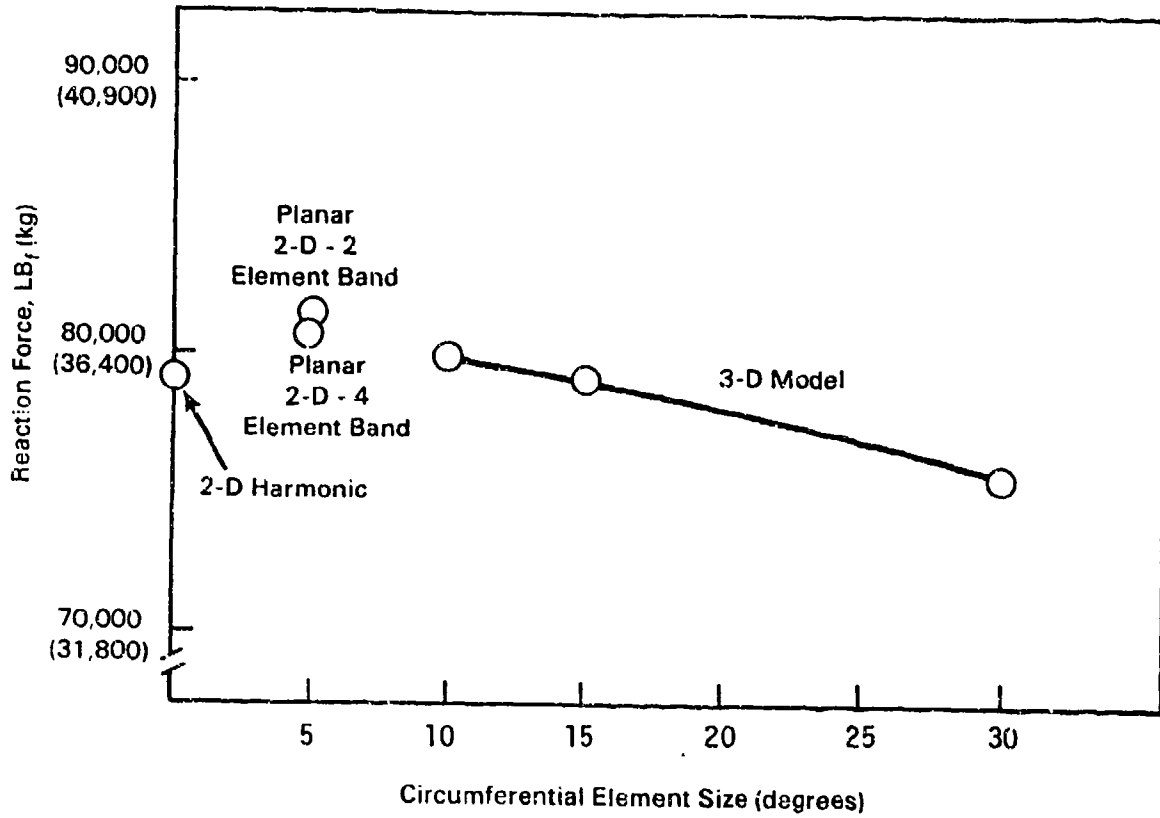


Figure 8. Mesh Size Sensitivity Study

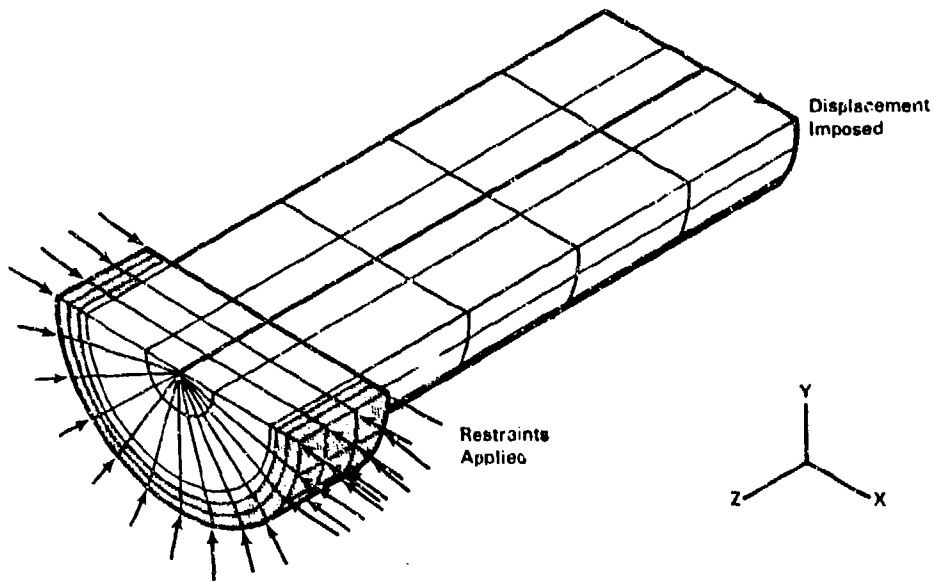


Figure 9. First Year Three Dimensional Mesh

The bands used for the initial testing were machined to have a minimum of interference between the gun barrel and the band (i.e. a tight slip fit). The foundation moment measured, however, was much less than that calculated in the analysis portion of the work. It was obvious that a good deal of interference between the projectile and the gun barrel was required so that no part of the nylon band would lose contact with the gun barrel when the projectile was cocked in bore. Therefore, more bands were made with an interference of approximately 10 mils. The projectiles with these bands required a considerable force to load into the gun barrel, as the nylon had to be compressed radially by 10 mils. They also required significantly more than the building air pressure to launch. At this point, the triggered trap door mechanism was abandoned, the projectiles were seated with a hydraulic ram, and a nitrogen bottle was used to provide the necessary pressure in the receiver tank. The pressure was raised behind the projectile until static friction was overcome (approximately 600 psⁱ), and the projectile accelerated over the ramp and down the gun barrel.

5. ANALYSIS OF SLIDING PROJECTILES

The three dimensional finite element mesh used to perform the calculations for the second year's work is shown in Figure 10. The darkened area around the center is the modelled nylon band. Note from the figure that the analysis was performed with the band fixed radially all of the way around the projectile. This more closely models the condition when there is an interference between the nylon band and the gun barrel. The predicted foundation moment using this set of boundary conditions was considerably higher than what was measured in the first tests. The tests were then conducted with the nylon band interference, and the band in compression at the outset of the test. These test results provided a significantly higher force output, but were still much lower than the finite element predictions. Several approaches were taken to determine the nature of this discrepancy, as shown in Figure 11. The stiffness of the nylon was changed, as well as the number of radial constraints. The "fixed" in the figure represents a radial constraint imposed on the entire outer surface of the nylon band. The "released" refers to a selected number of those restraints being released in order to model the projectile without any radial interference. Clearly, the actual case is somewhere between the "released" boundary conditions with a softer nylon (elastic modulus of 200,000 psi), and the "fixed" boundary with the stiffer nylon properties (elastic modulus 520,000 psi). The testing and analysis of the third year was intended to determine both what the actual foundation moment would be, and to extend the results to band geometries characteristic of typical APFSDS projectiles.

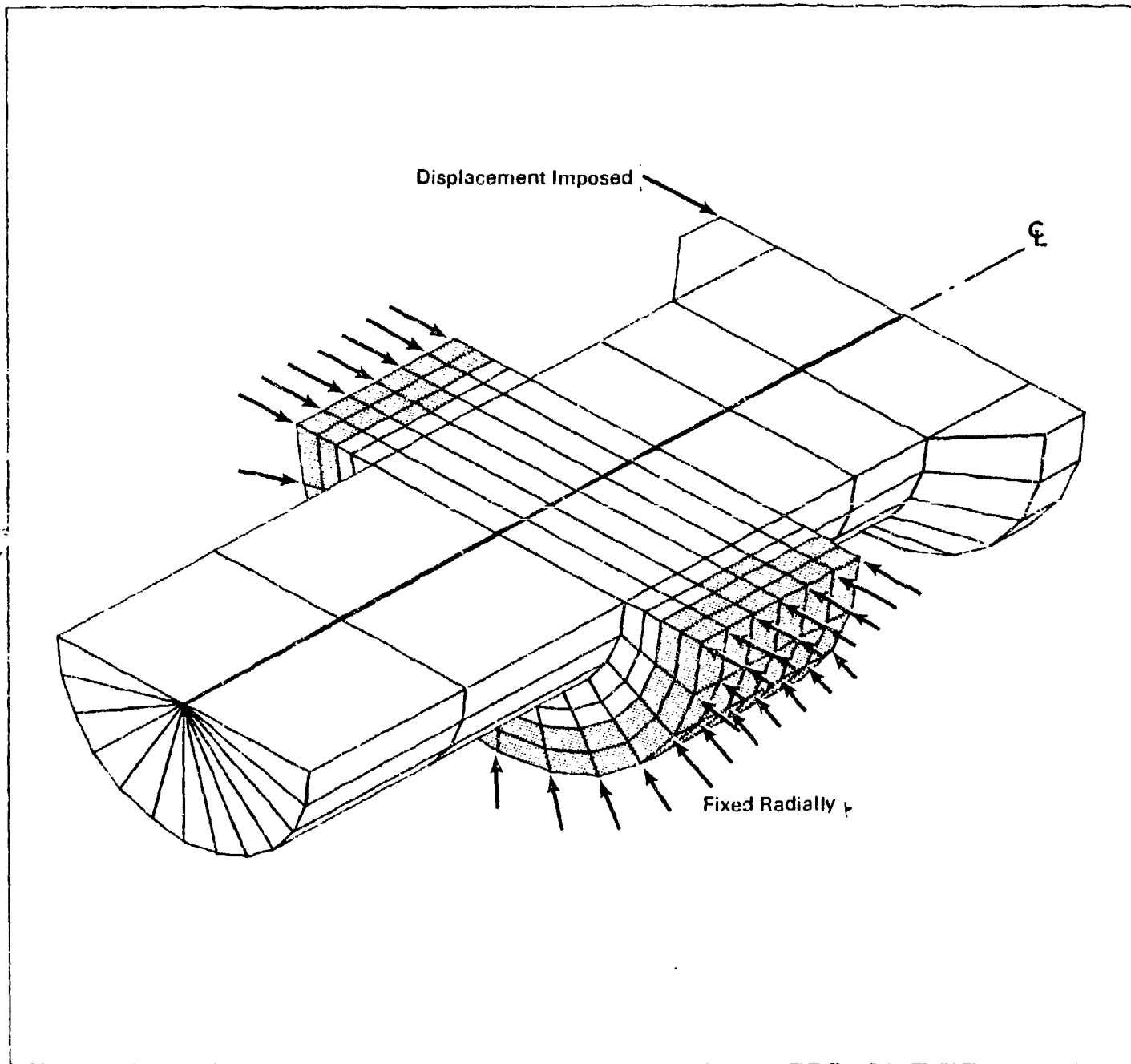


Figure 10. Second Year Three Dimensional Mesh

6. THIRD YEAR - TEST AND ANALYSIS

The third year of testing and analysis, as stated above, was intended to iron out the discrepancies between test and analysis, and to model and test band geometries more characteristic of the typical APFSDS obturator. Figure 4, as stated in Section 1, is a schematic of the band designs tested during that year's work. Also, as part of that project, a complete material characterization study was performed to determine both static and dynamic material curves for the nylon material used in the tests. Also included in that material characterization work was the testing of the nylon material in hydrostatic compression. The tests run for this project do not subject the nylon to a high state of hydrostatic compression, but an actual gun firing situation does. The nylon obturator is subjected to a hydrostatic loading of approximately 50,000 psi, upon which is superimposed the loading of projectile balloting. The material property characterization work will be reported in a separate document from the report of the third year of the foundation moment study.

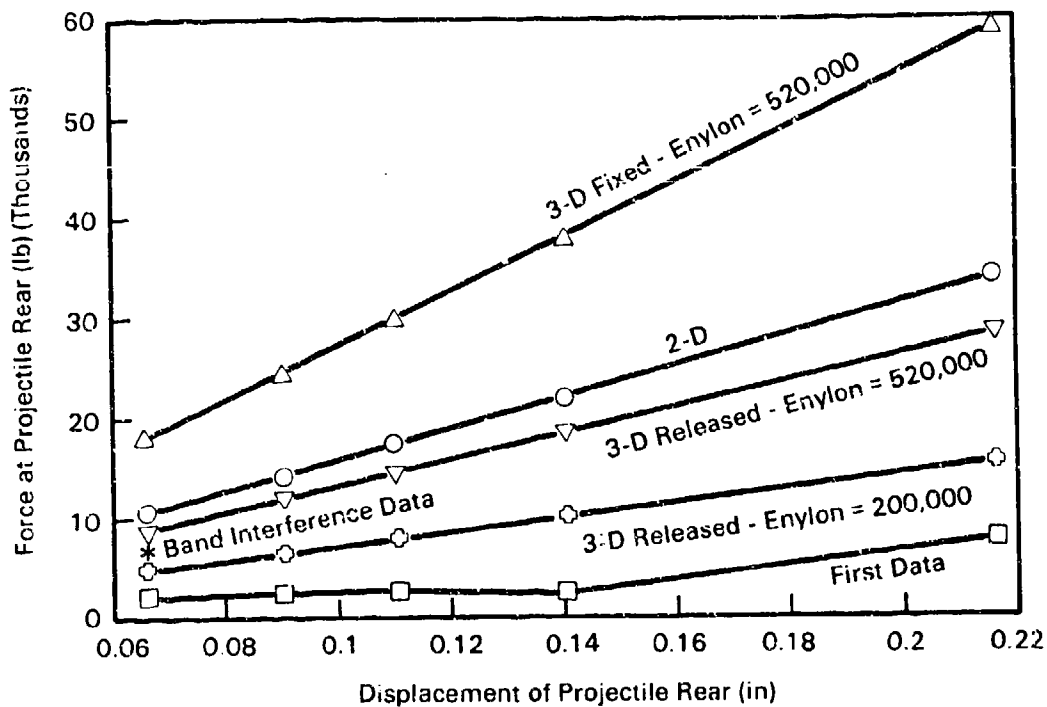


Figure 11. Finite Element and Test Results for Second Year

The results of the finite element analysis for the third year are reported below in Table 1. Note that the results are still much higher than what was measured experimentally. Obviously, the boundary restraints are not modelled accurately. It is questionable, however, whether an obturator in an actual gun firing condition can have anything but complete radial restraint. As stated before, the obturator is in a state of very high hydrostatic loading, mostly because of the propellant gasses, and the restraints of the projectile and gun bore. No part of that obturator will lose contact with the gun barrel under actual firing conditions. To that extent, our experiment cannot accurately model the response of an obturator to such conditions. Some knowledge about those conditions, and the conditions of our test, however, allow us to make qualitative statements about the foundation moment, and the interior ballistic response of the obturator. One would expect that the foundation moment would be higher for an obturator undergoing large hydrostatic compression than for the bands used in our tests. Our tests then, if anything, will under-predict the foundation moment.

TABLE 1. THIRD YEAR FINITE ELEMENT RESULTS

| <u>Band Geometry</u> | <u>Force for .1 inch deflection</u> | <u>.3 inch deflection</u> |
|----------------------|-------------------------------------|---------------------------|
| Straight (band A) | 13,000 pounds | 27,540 pounds |
| V-band (band C) | 11,400 pounds | 22,800 pounds |
| V-notch (band D) | 6,340 pounds | 15,300 pounds |

All of the projectile testing for the third year was done at the same imposed displacement, 0.09 inches. Table 2 summarizes the measurements taken for the twenty bands tested, as averages for each band design. The band designs are those shown schematically in Figure 4, and identified as bands A, B, C, and D. The test results are fairly consistent, and closely match the results of the second year's tests. This is a good result, and shows us that the foundation moment that we are measuring is in fact correct for the boundary conditions imposed. The test results are, as stated above, and as they were in the second year of testing, considerably lower than the finite element predictions. Again, the boundary conditions for those predictions are as yet poorly understood, as evidenced by the differences between measured and calculated results.

TABLE 2. TEST RESULTS FOR THIRD YEAR

| <u>Band</u> | <u>Measured Force</u> |
|-------------|-----------------------|
| A | 4430 pounds |
| B | 4970 pounds |
| C | 5160 pounds |
| D | 2410 pounds |

7. CONCLUSIONS

The major conclusion that can be reached from the three years of the foundation moment project is that the foundation moment is large. It in fact is most probably the dominant force on a projectile early in the ballistic cycle. The magnitude of the foundation moment is on the order of the magnitude of the overturning moment induced by having the center of gravity approximately one half to two thirds of a caliber behind the center of transverse rotation at the projectile's maximum acceleration. The magnitude of the foundation moment does not change with acceleration, and therefore is considerably larger in relation to the position of the center of gravity of the projectile at anything other than maximum acceleration. This result is contrary to current thought about the foundation moment. Current interior ballistic models that include the projectile and its interaction with the gun barrel during firing do not take this capacity of the obturator band to induce a moment into consideration. Certainly the foundation moment must be taken into consideration in any future work or extensions to current models if the interior ballistic predictions are to be correct.

A second conclusion can be drawn from the finite element analysis that has been performed within the scope of this project. That is that the use of the finite element method for prediction of structural response in interior ballistics is a difficult task, and fraught with severe limitations at present. The expense and man-power effort required to run a complete three dimensional non-linear analysis of a projectile with complicated geometry may be prohibitive. It may well be that approximate methods linked with a good experimental data base may prove to be the preferred method to deal with this problem in the projectile design environment. The three dimensional analyses performed for this project used the geometry of the test projectiles, which is considerably simpler than that of a characteristic APFSDS projectile. Those analyses required approximate 160 megabytes of disc storage space per analysis, and ran for two and one half days on an APOLLO DN420 computer. This is a significant investment in computer resource, for a simple geometry. A typical APFSDS projectile would require significantly more resource. The limitations of available computer resources, and researchers knowledgeable both in the field of interior ballistics and the finite element method are formidable. A complete interior ballistic simulation using this method for a single projectile does not seem at this time to be practical. Further research into analytical techniques for interior ballistic simulation are required, and should be pursued.

REFERENCES

1. Patton, E. M., Simonen, F. A., and Strobe, L. A., PROJECTILE FOUNDATION MOMENT GENERATION, ARBRL-CR-00514, June, 1983.
2. Patton, E. M., Shotwell, L. R., Strobe, L. A., and Ellis, D. R., PROJECTILE FOUNDATION MOMENT GENERATION - PHASE II, ARBRL-CR-00530, August, 1984.
3. ANSYS User Manual, Swanson Analysis Systems, Inc. ANSYS is a proprietary engineering analysis computer program owned, marketed, and supported by Swanson Analysis Systems, Inc., Houston, PA.

TITLE: A Nonlinear Tracking Filter

DR. DOMINICK ANDRISANI II
Assistant Professor
School of Aeronautics and Astronautics
Purdue University, West Lafayette, Indiana 47907

DR. FRANK P. KUHL
U.S. Army Armament Research and Development Center
Dover, N.J. 07801-5001

CAPT. DANIEL GLEASON, USAF
Air Force Institute of Technology
Wright Patterson Air Force Base, Dayton, Ohio

ABSTRACT:

The subject of this paper is tracking the present position of an aircraft and predicting its future position. A tracking filter is developed that uses aircraft attitude angles (yaw, pitch, roll) in addition to the usual radar measurements. Computer simulation of tracker performance when tracking violently maneuvering aircraft indicates a dramatic improvement is obtained by using attitude information.

The approach taken is to develop a twelve state extended Kalman filter that models both translational and rotational degrees of freedom. By measuring and estimating attitude it is possible to approximately determine the magnitude and direction of the force system acting on the vehicle and therefore determine vehicle linear acceleration. Knowledge of acceleration is then used to improve the estimate of present and future position of the vehicle being tracked. Simulation of a T-38 aircraft performing a 5g turn indicates that a six-to-one improvement in tracking accuracy is possible using this method compared to conventional trackers.

BIOGRAPHY: DR. Dominick Andrisani II

PAST EXPERIENCE: Senior Engineer, Calspan Corporation, Buffalo, N.Y., (1972-1980); Aerospace Technologist, NASA Langley Research Center, Hampton, Va., (1970-1972).

DEGREES HELD: B.S.A.E. Rensselaer Polytechnic Institute (1970), Troy, N.Y.; M.S.E.E. and Ph.D. E.E. from the State University of N.Y. at Buffalo (1975,1979).

ANDRISANI, KUHL, GLEASON

A NONLINEAR TRACKING FILTER

DR. DOMINICK ANDRISANI II
ASSISTANT PROFESSOR
SCHOOL OF AERONAUTICS AND ASTRONAUTICS
PURDUE UNIVERSITY
WEST LAFAYETTE, INDIANA 47907

and

DR. FRANK P. KUHL
U.S. ARMY ARMAMENT RESEARCH AND DEVELOPMENT CENTER
DOVER, N.J. 07801-5001

and

CAPT. DANIEL GLEASON, USAF
AIR FORCE INSTITUTE OF TECHNOLOGY
WRIGHT PATTERSON AIR FORCE BASE
DAYTON, OHIO

1. INTRODUCTION

The subject of this paper is tracking the present position of an aircraft and predicting the future position of that aircraft. Many tracking systems in commercial and military use today use only range, elevation angle, and azimuth angle measurements from a radar system. In this paper aircraft attitude angles (yaw, pitch, roll) are also provided to the tracker. An experimental comparison, contained herein, of tracker performance when tracking violently maneuvering aircraft indicates a dramatic improvement is obtained by using attitude information.

Radar measurements have proven to provide satisfactory accuracy when tracking vehicles in unaccelerated flight. However, when a vehicle is quickly maneuvering, past and present position are not a sufficient basis for accurate prediction of future vehicle position. One of the most powerful means available to a pilot for accelerating his vehicle involves changing the magnitude and direction of his aerodynamic lift vector. To do this the pilot changes the aircraft attitude with

respect to the inertial frame and changes his orientation with respect to the wind. These attitude changes are strongly correlated with vehicle acceleration, as will be shown in this paper, and can be used to substantially improve the accuracy of acceleration estimates. With improved acceleration estimates, the accuracy of trajectory prediction is improved.

Typically modern tracking filters employ three identical uncoupled estimators for the three translational degrees of freedom. Each estimator may be of one of the following types[1].

$$\begin{aligned} \alpha \text{ Filter: } \dot{x}(t) &= w(t) \\ \alpha\text{-}\beta \text{ Filter: } \ddot{x}(t) &= w(t) \\ \alpha\text{-}\beta\text{-}\gamma \text{ Filter: } \dddot{x}(t) &= w(t) \end{aligned}$$

The symbol $x(t)$ denotes position in either north, east, or vertical directions while $w(t)$ denotes white noise. Based on these dynamical models, state estimators are constructed that attempt to reconcile the behavior of the mathematical model with the measurement of position.

Prediction from time t to time $t+T$ is accomplished with the following simple formulas.

$$\begin{aligned} \alpha \text{ Predictor: } \hat{x}(t+T) &= \hat{x}(t) \\ \alpha\text{-}\beta \text{ Predictor: } \hat{x}(t+T) &= \hat{x}(t) + T\dot{\hat{x}}(t) \\ \alpha\text{-}\beta\text{-}\gamma \text{ Predictor: } \hat{x}(t+T) &= \hat{x}(t) + T\dot{\hat{x}}(t) + \frac{1}{2}T^2\ddot{\hat{x}}(t) \end{aligned}$$

The symbol $\hat{}$ is used to denote an estimate of position, velocity or acceleration. State vectors for these models are of order one, two, and three respectively. Note that the α Predictor states that the future position is the same as the present position. The $\alpha\text{-}\beta$ Predictor is based on a nonzero but constant vehicle velocity. The $\alpha\text{-}\beta\text{-}\gamma$ Predictor is based on a nonzero but constant acceleration. Thus only the last predictor can handle a curved trajectory.

Each of these filters does a poor job of modeling vehicle acceleration. In fact, only the $\alpha\text{-}\beta\text{-}\gamma$ Filter estimates an acceleration state. In this case the model specifies that the rate of change of acceleration is white noise. Thus the model provides very little meaningful information regarding

acceleration, i.e. the acceleration model is purely stochastic. Furthermore, the estimator will attempt to estimate acceleration (the second derivative of position) using only position measurements. This process is frequently unsatisfactory because differentiation of one waveform, even approximately, to obtain another amplifies noise.

Alternate models for acceleration have also been proposed. Singer[2] and others discuss exponentially correlated acceleration of the form

$$\ddot{x} = -1/\tau \ddot{x} + w.$$

In a recent paper Berg[3] proposes a more complex acceleration model given by

$$\ddot{x} = -1/\tau \ddot{x} - 1/\gamma w + c$$

where c is computed as a function of the most recent estimates of vehicle velocity and acceleration. The function c represents an adaptive estimate of the mean vehicle jerk based upon the assumption that the vehicle is in a coordinated turn. As with most other previous approaches, the two methods mentioned above are limited by the problems of trying to determine acceleration from only position measurements.

In this paper an improved tracker is developed in which the mathematical model of vehicle acceleration is substantially improved. This is done by the incorporation of vehicle attitude measurements into the tracker. The relationship between attitude and vehicle acceleration is then used to generate an improved estimate of both the magnitude and direction of vehicle acceleration that in turn can be used to generate an improved prediction of future position. Using attitude measurements to estimate the direction of vehicle acceleration in the tracking scenario was first suggested by Kendrick et.al.[4]. In this paper attitude is also used to estimate the magnitude of vehicle acceleration. In reference[5], Lefas uses aircraft roll angle measurements to improve acceleration estimates. The roll angle measurement is obtained by the tracker using a telemetry-like link between the aircraft and the tracker. Improved trackers of the type developed in this paper have important application to the tracking of commercial aircraft for air traffic control and collision avoidance.

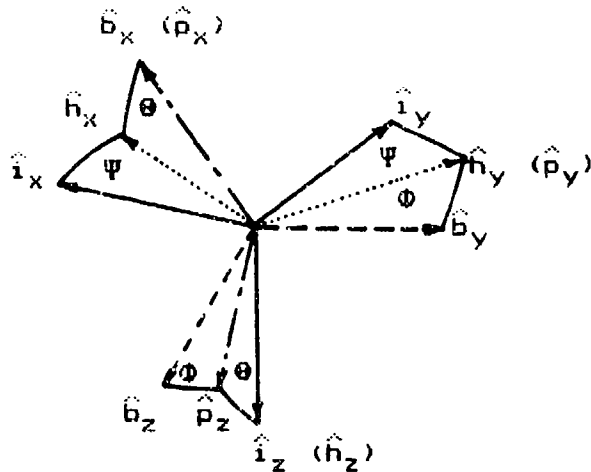
2. REPRESENTATION OF VEHICLE ORIENTATION

This section presents a way of mathematically representing the attitude of a vehicle in three dimensional space. While many methods are possible, the approach taken here involves using Euler angles[6]. Three Euler angles are required, heading angle Ψ , pitch angle θ , and roll angle ϕ .

Two frames of reference are pertinent to this study. The first is the inertial frame with orthogonal unit vectors \hat{i}_x , \hat{i}_y , and \hat{i}_z . The origin of this frame is the tracker, which is assumed to be fixed in the inertial frame. Unit vector \hat{i}_x points north, \hat{i}_y points east, and \hat{i}_z points down. The second is called the vehicle body frame and is denoted by orthogonal unit vectors \hat{b}_x , \hat{b}_y , \hat{b}_z . The origin of this frame is the vehicle center of mass. Unit vector \hat{b}_x points out the vehicle nose, \hat{b}_y points out the right wing, and \hat{b}_z is perpendicular to \hat{b}_x and \hat{b}_y going out the bottom of the vehicle.

Assume that the vehicle body frame is translated so that its origin coincides with the origin of the inertial frame. The arbitrary orientation of the vehicle body frame with respect to the inertial frame can be specified by a series of three consecutive rotations as shown in Figure 1. The first rotation is about unit vector \hat{i}_z by an amount Ψ , the heading angle. The new orientation is specified by the heading frame unit vectors \hat{h}_x , \hat{h}_y , and \hat{h}_z . Note $\hat{h}_z = \hat{i}_z$. The second rotation is about unit vector \hat{h}_y by an amount θ , the pitch angle. The new orientation is specified by unit vectors \hat{p}_x , \hat{p}_y , and \hat{p}_z . Note that $\hat{p}_y = \hat{h}_y$. The third rotation is about unit vector \hat{p}_x by an amount ϕ , the roll angle. This final orientation is now aligned with the vehicle body unit vectors \hat{b}_x , \hat{b}_y , and \hat{b}_z . Note that $\hat{b}_x = \hat{p}_x$. Thus the ordered sequence of Euler angle rotations Ψ , θ , ϕ , about the unit vectors indicated in Figure 1 provides the means of representing the orientation of the vehicle body with respect to the inertial frame.

The significance of this sequence of rotations is that if any vector is given in terms of one set of unit vectors, it can be transformed into any other set of unit vectors using a transformation that involves the sine and cosine of the Euler angles. Appendix 1 describes the transformations in detail.



Start with $\hat{i}_x, \hat{i}_y, \hat{i}_z$
 Rotation 1 of angle Ψ about \hat{i}_z giving $\hat{h}_x, \hat{h}_y, \hat{h}_z = \hat{i}_z$
 Rotation 2 of angle Θ about \hat{h}_y giving $\hat{p}_x, \hat{p}_y = \hat{h}_y, \hat{p}_z$
 Rotation 3 of angle Φ about \hat{p}_x giving $\hat{b}_x = \hat{p}_x, \hat{b}_y, \hat{b}_z$
 End with $\hat{b}_x, \hat{b}_y, \hat{b}_z$

Figure 1 Three Consecutive Euler Angle Rotations: Ψ, Θ, Φ .

3. MODELING OF THE TRANSLATIONAL DEGREES OF FREEDOM

A powerful new approach for modeling the translational degrees of freedom is described in this section. Specifically, the approach involves solving for the magnitude and direction of the force system acting on the vehicle using attitude information. In this way an explicit expression for acceleration is obtained in terms of attitude and velocity. This substantially improves the accuracy of acceleration estimates.

Determination of the complete force system on a flying vehicle is a difficult task even with a cooperative vehicle. Practical considerations in the tracking scenario suggest that

considerable simplifications in force system modeling may be required. It will be shown by simulation that the simplifications suggested in this paper aid in tracking accuracy yet do not require excessive amounts of data about the aircraft being tracked.

The following simplifying assumptions will be made in the representation of the force system acting on the flight vehicle.

1. Thrust generated by the vehicle powerplant exactly cancels aerodynamic drag. Therefore neither thrust or drag are modeled.
2. The pilot of the vehicle performs only coordinated turns. Commercial airline pilots fly this way all the time because turn coordination means coffee in a cup does not spill. Military pilots tend to fly this way to minimize the fatigue of their bodies being thrown from side to side. The mathematical result of turn coordination is that the resultant of aerodynamic and thrust forces lies in the $\hat{b}_x-\hat{b}_z$ plane.
3. The atmosphere is stationary with respect to the inertial frame. This means that the air flow over the aircraft is due entirely to the inertial velocity of the vehicle and that the angle of attack (defined in Appendix 2) can be determined from the Euler angles and the components of inertial velocity (see Appendix 2). Furthermore, since the aerodynamic lift vector is perpendicular to the wind and lies in the $\hat{b}_x-\hat{b}_z$ plane, the direction of the lift vector can be found in terms of the Euler angles and the components of inertial velocity (see Appendix 2).
4. The magnitude of the aerodynamic lift can be expressed with the following formula:

$$L = \frac{1}{2} \rho V^2 S C_{L\alpha} \alpha$$

where ρ is the atmospheric density, V is vehicle airspeed, S is wing area, $C_{L\alpha}$ is the vehicle lift curve slope, and α is the angle of attack (defined in Appendix 2).

5. The force of gravity (weight) on the vehicle is given by $M g \hat{i}_z$ where M is vehicle mass and g is the

ANDRISANI, KUHL, GLEASON

acceleration of gravity (32.2 ft/sec²). This is the flat earth assumption.

With these assumptions it is possible to compute the total force vector acting on the vehicle as:

$$F = \hat{i}_x [\cos\psi \sin\alpha \cos\theta - \cos\psi \cos\alpha \cos\theta \sin\theta - \sin\psi \cos\alpha \sin\theta]L \\ + \hat{i}_y [\sin\psi \sin\alpha \cos\theta - \sin\psi \cos\alpha \cos\theta \sin\theta + \cos\psi \cos\alpha \sin\theta]L \\ + \hat{i}_z [-\sin\alpha \sin\theta - \cos\alpha \cos\theta \cos\theta]L + Mg$$

Equations of motion for the three degrees of freedom in translation can be derived directly from Newton's Second Law of Motion and are presented in Table 1.

Definitions:

Vehicle Inertial Velocity:

$$\vec{v} = \dot{x} \hat{i}_x + \dot{y} \hat{i}_y + \dot{z} \hat{i}_z$$

Vehicle Position:

$$\vec{p} = x \hat{i}_x + y \hat{i}_y + z \hat{i}_z$$

Angle of attack:

$$\cos\alpha = A/v_p$$

$$\sin\alpha = C/v_p$$

$$v_p = \sqrt{A^2 + C^2}$$

$$A = \cos\theta \cos\psi \dot{x} + \cos\theta \sin\psi \dot{y} - \sin\theta \dot{z}$$

$$C = (\cos\theta \sin\theta \cos\psi + \sin\theta \sin\psi) \dot{x} \\ + (\cos\theta \sin\theta \sin\psi - \sin\theta \cos\psi) \dot{y} + \cos\theta \cos\theta \dot{z}$$

Lift:

$$L = \frac{1}{2} \rho (\dot{x}^2 + \dot{y}^2 + \dot{z}^2) S C_{L\alpha} \alpha$$

State Vector:

$$\vec{x} = [\dot{x} \dot{y} \dot{z} x y z]^T$$

Equations of Motion:

$$\ddot{x} = [\cos\psi \sin\alpha \cos\theta - \cos\psi \cos\alpha \cos\theta \sin\theta - \sin\psi \cos\alpha \sin\theta]L/M$$

$$\ddot{y} = [\sin\psi \sin\alpha \cos\theta - \sin\psi \cos\alpha \cos\theta \sin\theta + \cos\psi \cos\alpha \sin\theta]L/M$$

$$\ddot{z} = [-\sin\alpha \sin\theta - \cos\alpha \cos\theta \cos\theta]L/M + g$$

Table 1 Translational Equations of Motion

4. MODELING OF THE ROTATIONAL DEGREES OF FREEDOM

This section presents a mathematical approach to modeling the rotational degrees of freedom. As with translation, modeling the three rotational degrees of freedom requires six differential equations.

Several definitions are required. Angular velocity of the vehicle body frame with respect to the inertial frame is defined as

$$\bar{\omega}^{bi} = p \hat{b}_x + q \hat{b}_y + r \hat{b}_z.$$

The external moment resultant acting about the vehicle center of mass is given by

$$\bar{M} = l \hat{b}_x + m \hat{b}_y + n \hat{b}_z$$

where l is the rolling moment, m is the pitching moment, and n is the yawing moment.

The relationship between the angular velocity components p , q , and r and the time derivative of the Euler angles are given in [6] as

$$\begin{aligned}\dot{\Phi} &= p + q \sin\Phi \tan\theta + r \cos\Phi \tan\theta \\ \dot{\Theta} &= q \cos\Phi - r \sin\Phi \\ \dot{\Psi} &= (q \sin\Phi + r \cos\Phi) / \cos\theta.\end{aligned}$$

If we assume that \hat{b}_x , \hat{b}_y , and \hat{b}_z correspond to principal directions of the vehicle so that products of inertia are zero, then Euler's equations of motion [6] for rotation are given by

$$\begin{aligned}I_{xx} \dot{p} + (I_{zz} - I_{yy}) qr &= l \\ I_{yy} \dot{q} + (I_{xx} - I_{zz}) pr &= m \\ I_{zz} \dot{r} + (I_{yy} - I_{xx}) pq &= n.\end{aligned}$$

Define the sideslip angle β (see Appendix 2) as the angle that the wind makes with the \hat{b}_x - \hat{b}_z plane. The external moment vector, as described in [6] can be written as

$$\begin{aligned}l &= k_1 \beta + k_2 p + k_3 r + k_4 \delta_a + k_5 \delta_r \\ m &= k_6 V_x + k_7 \alpha + k_8 q + k_9 \delta_e + k_{10} \\ n &= k_{11} \beta + k_{12} p + k_{13} r + k_{14} \delta_a + k_{15} \delta_r\end{aligned}$$

where V_x is the component of inertial velocity in the \hat{b}_x direction and δ_a , δ_r , and δ_e are the aileron, rudder and, elevator surface deflections. Constants $k_1 - k_{15}$ are generally

ANDRISANI, KUHL, GLEASON

known for a specific vehicle or can be computed using methods outlined in [6] for fixed wing aircraft and [7] for rotary wing aircraft.

On first thought it may seem imperative that all the constants $k_1 - k_{15}$ be accurately known. However, the tracker has no knowledge of the control surface deflections, so k_4 , k_5 , k_9 , k_{14} , and k_{15} are useless. Furthermore, in the case where the vehicle is violently maneuvering the moments caused by the control surface motion are large compared to the other moments. Thus for the highly maneuvering situation, it may be appropriate to set all the constants to zero and compensate for this gross but warranted approximation in another way (e.g. by adding process noise to the state estimator). A further benefit of setting the constants to zero is that the rotational equations of motion become uncoupled from the translational equations of motion. This fact makes it possible (although not necessarily desirable) to estimate vehicle attitude independently of vehicle translation.

5. SIMULTANEOUS ESTIMATION OF ORIENTATION AND TRANSLATION

The cornerstone of this paper involves the simultaneous estimation of attitude and translation of the vehicle being tracked. In this way the estimate of attitude can be used to estimate vehicle acceleration and to improve trajectory prediction accuracy. Specifically, the method exploits the strong correlation between attitude and acceleration. This correlation is obvious when one recalls that an aircraft intending to turn will bank its wings. Banking has the effect of changing the direction of the lift vector and creating an acceleration to the side that curves the trajectory. Furthermore, an aircraft that wants to climb will lift up its nose to increase the angle of attack. This increases the magnitude of the lift vector and the vehicle climbs. It is important to note that the change in attitude occurs before any significant curving of the trajectory occurs. Thus using attitude measurements provides information about future trajectory curvature before radar measurements observe that curvature.

It has been suggested in the previous section that the estimation of vehicle attitude might be performed independently of the estimation of vehicle translation. While this approach has some benefits, it suffers from one important drawback. To a first approximation the vehicle will point in the direction of its velocity vector. Thus the velocity vector can be used to derive an approximation to the heading and pitch angles, which might be useful in eliminating ambiguities that might be inherent in other types of measurements.

A single glance at the translational equations of motion in Table 1 clearly shows how important the vehicle orientation is in modeling translation. This resulted because orientation information was used to determine both the magnitude and direction of the lift vector. To determine lift magnitude the vehicle specific constant $C = \frac{1}{2} \rho V^2 S C_{L\alpha} / M$ is required. The need to obtain this information may be problematic in some tracking scenarios. However, it is believed that even an approximation to its value will greatly improve the estimation of acceleration.

In summary, all twelve equations of motion in inertial frame components are presented in Table 2. Note that process noise terms $w_1 - w_6$ have been added to six of the state equations. The process noise terms are assumed to be gaussian, white, and statistically independent from each other, from the measurement noise, and from the state initial condition. More sophisticated process noise models are possible such as colored process noise but these require additional state variables.

The estimator for the state model of Table 2 requires measurements of aircraft attitude (three Euler angles) and vehicle position (assumed to be in the form of range R , elevation angle δ , and azimuth angle η). Optional measurements might include range rate \dot{R} , elevation rate $\dot{\delta}$, and azimuth rate $\dot{\eta}$. All of these measurements are described in Table 3. Note that each measurement has a measurement noise term $v_1 - v_9$ added to account for measurement uncertainty. The measurement noise terms are assumed to be gaussian, white, and statistically independent from each other, from the process noise, and from the state initial condition.

$$\begin{aligned}\dot{p} &= [-(I_{zz} - I_{yy}) qr + k_1 \theta + k_2 p + k_3 r + k_4 w_1] / I_{xx} \\ \dot{q} &= [-(I_{xx} - I_{zz}) pr + k_7 \alpha + k_8 q + k_9 w_2] / I_{yy} \\ \dot{r} &= [-(I_{yy} - I_{xx}) pq + k_{11} \theta + k_{12} p + k_{13} r + k_{15} w_3] / I_{zz} \\ \dot{\phi} &= p + q \sin\theta \tan\theta + r \cos\theta \tan\theta\end{aligned}$$

$$\dot{\theta} = q \cos\theta - r \sin\theta$$

$$\dot{\psi} = (q \sin\theta + r \cos\theta) / \cos\theta$$

$$\ddot{x} = [\cos\psi \sin\alpha \cos\theta - \cos\psi \cos\alpha \cos\theta \sin\theta - \sin\psi \cos\alpha \sin\theta] L/M + w_4$$

$$\ddot{y} = [\sin\psi \sin\alpha \cos\theta - \sin\psi \cos\alpha \cos\theta \sin\theta + \cos\psi \cos\alpha \sin\theta] L/M + w_5$$

$$\ddot{z} = [-\sin\alpha \sin\theta - \cos\alpha \cos\theta \cos\theta] L/M + g + w_6$$

$$\dot{x} = \dot{\bar{x}}$$

$$\dot{y} = \dot{\bar{y}}$$

$$\dot{z} = \dot{\bar{z}}$$

$$\text{State Vector: } \bar{x} = [p \ q \ r \ \theta \ \psi \ \dot{x} \ \dot{y} \ \dot{z} \ x \ y \ z]$$

Angle of attack:

$$\cos\alpha = A/v_p$$

$$\sin\alpha = C/v_p$$

$$v_p = \sqrt{A^2 + C^2}$$

$$A = \cos\theta \cos\psi \dot{x} + \cos\theta \sin\psi \dot{y} - \sin\theta \dot{z}$$

$$C = (\cos\theta \sin\theta \cos\psi + \sin\theta \sin\psi) \dot{x}$$

$$+ (\cos\theta \sin\theta \sin\psi - \sin\theta \cos\psi) \dot{y} + \cos\theta \cos\theta \dot{z}$$

Lift:

$$L = \frac{1}{2} \rho (\dot{x}^2 + \dot{y}^2 + \dot{z}^2) S C_{L\alpha} \alpha$$

Table 2 Equations of Motion

$$\Phi_m = \Phi + v_1$$

$$\Theta_m = \Theta + v_2$$

$$\Psi_m = \Psi + v_3$$

$$R = [x^2 + y^2 + z^2]^{1/2} + v_4$$

$$\eta = \tan^{-1}(y/x) + v_5$$

$$\xi = \tan^{-1}[-z/(x^2 + y^2)] + v_6$$

$$\dot{R} = [x\dot{x} + y\dot{y} + z\dot{z}]/[x^2 + y^2 + z^2]^{1/2} + v_7$$

$$\dot{\eta} = (x\dot{y} - y\dot{x})/(x^2 + y^2) + v_8$$

$$\dot{\xi} = [z(x\dot{x} + y\dot{y}) - \dot{z}(x^2 + y^2)]/[x^2 + y^2 + z^2)(x^2 + y^2)^{1/2}] + v_9$$

Table 3 Measurement Equations

Tables 2 and 3 contain a set of highly nonlinear state equations and highly nonlinear measurements. The state equations are continuous differential equations while the measurements are assumed to be available only at discrete equally spaced time points. To construct a state estimator for this problem, the Continuous-Discrete Extended Kalman Filter described in [8] is used. This suboptimal approach to nonlinear estimation has been shown to give satisfactory results in many applications (e.g. [9]).

6. AN EXAMPLE

This section provides a brief example that illustrates the superior performance of the tracker described in this paper. A six-to-one improvement in tracking accuracy is shown compared to a conventional tracker.

In order to test the hypothesis that modeling and estimating the attitude degrees of freedom improves tracking accuracy, a simulation of a T-38 aircraft performing a 5g turn to the right was conducted. The maneuver is shown in Figure 2 where the position of the aircraft is indicated with the aircraft symbol.

ANDRISANI, KUHL, GLEASON

The outline of the aircraft symbol also gives an indication of aircraft roll angle in this top view. Data is presented in Figure 2 at one second intervals although the tracking filters were using data at 1/30 second intervals. Aircraft velocity was 440 feet/second (260 knots) in an easterly direction at the start of the maneuver. Halfway between the second and third aircraft symbol in Figure 2 the pilot initiates his banking turn to the right. A maximum roll angle of 78 degrees is obtained between the seventh and eighth symbols in the figure.

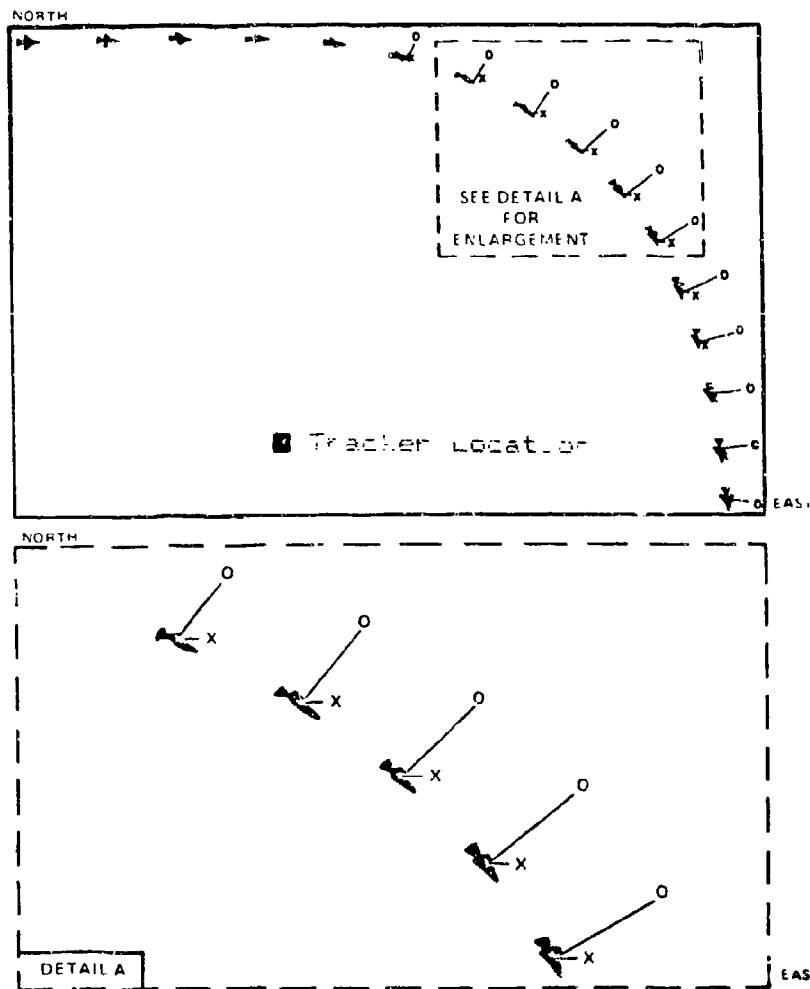


Figure 2 Comparison of a Translation Tracker ("o") Versus an Attitude-Translation Tracker ("x") for a T-38 Performing a 5g Turn.

Based upon this simulated maneuver the nine measurements shown in Table 3 were computed. Using realistic noise variances each of the measurements was corrupted with gaussian white statistically independent noise.

Two trackers are compared in Figure 2. The first, called the Translation Tracker was based upon an extended Kalman filter that used only the last six of the equations of motion in Table 2 with $L=g=0$. This tracker also used only the fourth through ninth measurements of Table 3. The second tracker, called the Attitude-Translation Tracker[10], used all equations of Table 2 and all measurements of Table 3. This tracker also assumed

$$k_1 = k_3 = k_6 = k_8 = k_{10} = k_{11} = k_{12} = k_{13} = 0$$

with all other constants known exactly. Both trackers were asked to predict the aircraft position one second into the future based upon the estimate of the current vehicle motion. The one second predictions are shown next to the actual aircraft positions.

Figure 2 shows a very important trend. The Attitude-Translation Tracker ("x") with its improved ability to determine acceleration is considerably more accurate in predicting vehicle position than the Translation Tracker ("o"). The maximum predicted position error is 42 feet for the Attitude-Translation Tracker versus 250 feet for the Translation Tracker. It is clear that the Attitude-Translation Tracker provides a six-to-one improvement.

7. CONCLUSIONS

This paper develops a nonlinear tracking filter that models both the rotational and translational degrees of freedom. This is accomplished by means of a twelve state extended Kalman filter that uses not only radar data but also measurements of the attitude of the aircraft being tracked. By measuring and estimating attitude it is possible to approximately determine the magnitude and direction of the force system acting on the vehicle and therefore determine vehicle linear acceleration. Knowledge of acceleration is then used to improve the estimate of present and future position of the vehicle being tracked. Simulation of a T-38 aircraft performing a 5g turn indicates that a dramatic improvement in tracking accuracy is possible using this method compared to conventional trackers.

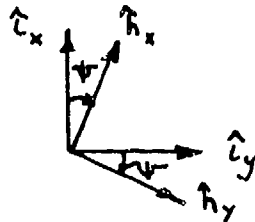
8. REFERENCES

1. R. J. Fitzgerald, "Simple Tracking Filters: Closed Form Solutions," IEEE Transactions on Aerospace and Electronic Systems, Vol. AES-17, No.6, November 1981.
2. R. A. Singer, "Estimating Optimal Tracking Filter Performance for Maneuvering Targets," IEEE Transactions on Aerospace and Electronic Systems, Vol. AES-6, No. 4, July 1970, pp. 473-483.
3. R. F. Berg, "Estimation and Prediction for Maneuvering Targets," IEEE Transactions on Automatic Control, Vol. AC-28, No.3, March 1983.
4. J. D. Kendrick, F. S. Maybeck, and J. G. Reid, "Estimation of Aircraft Target Motion Using Orientation Measurements," IEEE Transactions on Aerospace and Electronic Systems, Vol. AES-17, No. 2, March 1981.
5. C. C. Lefas, "Using Roll-Angle Measurements to Track Aircraft Maneuvers," IEEE Transactions on Aerospace and Electronic Systems, Vol. AES-20, No. 6, November 1984, pp. 672-681.
6. J. Roskam, Airplane Flight Dynamics and Automatic Control, Part 1. Roskam Aviation and Engineering Corporation, 1979.
7. E. Seckel, Stability and Control of Airplanes and Helicopters, Academic Press, 1964.
8. A. Gelb, ed., Applied Optimal Estimation, The M.I.T. Press, 1974.
9. R. F. Wisner, J. A. Tabaczynski, and M. Athans, "A Comparison of Three Nonlinear Filters," Automatica, Vol. 5, 1969, pp.487-496.
10. D. Andrisani II, R. D. Mitchell, and F. P. Kuhl, "Trajectory Prediction for Maneuvering Aircraft," presented at the Sixth Meeting of the Coordinating Group on Modern Control Theory, October 24-25, 1984, Fort Eustis, Va.

9. APPENDIX 1: AXES SYSTEMS

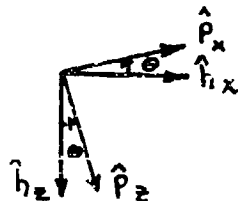
This appendix describes the relationships between the various reference frames and unit vectors used in this paper. Assume that \hat{i}_x , \hat{i}_y , \hat{i}_z are inertially fixed unit vectors with \hat{i}_x

pointing north, \hat{i}_y pointing east and \hat{i}_z pointing down. The orthogonal heading frame unit vectors, \hat{h}_x , \hat{h}_y , \hat{h}_z , differ from \hat{i}_x , \hat{i}_y , \hat{i}_z by the heading angle Ψ as shown below. Angle Ψ is a rotation about $\hat{i}_z = \hat{h}_z$.



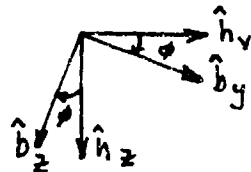
$$\begin{aligned}\hat{h}_x &= \hat{i}_x \cos\Psi + \hat{i}_y \sin\Psi \\ \hat{h}_y &= -\hat{i}_x \sin\Psi + \hat{i}_y \cos\Psi \\ \hat{h}_z &= \hat{i}_z\end{aligned}$$

A third set of orthogonal unit vectors \hat{p}_x , \hat{p}_y , \hat{p}_z differ from \hat{h}_x , \hat{h}_y , \hat{h}_z by the pitch angle θ as shown below. Angle θ is a rotation about $\hat{h}_y = \hat{p}_y$.



$$\begin{aligned}\hat{p}_x &= \hat{h}_x \cos\theta - \hat{h}_z \sin\theta \\ \hat{p}_y &= \hat{h}_y \\ \hat{p}_z &= \hat{h}_x \sin\theta + \hat{h}_z \cos\theta\end{aligned}$$

Finally, the fourth set of orthogonal unit vectors called the body frame unit vectors \hat{b}_x , \hat{b}_y , \hat{b}_z differ from \hat{p}_x , \hat{p}_y , \hat{p}_z by the roll angle Φ as shown below. Roll angle Φ is a rotation about $\hat{p}_x = \hat{b}_x$.



$$\begin{aligned}\hat{b}_x &= \hat{p}_x \\ \hat{b}_y &= \hat{p}_y \cos\Phi + \hat{p}_z \sin\Phi \\ \hat{b}_z &= -\hat{p}_y \sin\Phi + \hat{p}_z \cos\Phi\end{aligned}$$

Using the three groups of equations given above, a vector expressed in any set of unit vectors can be expressed in any other set of unit vectors.

10. APPENDIX 2: LIFT, ANGLE OF ATTACK, AND ANGLE OF SIDESLIP

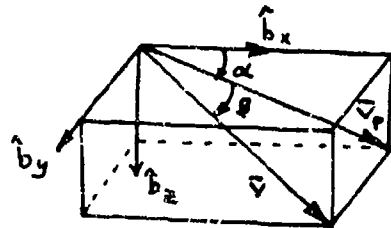
The angles of attack and sideslip serve to orient the wind incident on the aircraft with the body frame unit vectors. In this paper it has been assumed that the air mass is still, therefore the wind is opposite to the inertial velocity. If

$$\vec{v} = U \hat{h}_x + V \hat{h}_y + W \hat{h}_z$$

then in terms of body frame unit vectors

$$\begin{aligned} \vec{v} &= [U \cos\theta - W \sin\theta] \hat{b}_x \\ &\quad + [V \cos\theta + (U \sin\theta + W \cos\theta) \sin\theta] \hat{b}_y \\ &\quad + [-V \sin\theta + (U \sin\theta + W \cos\theta) \cos\theta] \hat{b}_z \\ &= V_x \hat{b}_x + V_y \hat{b}_y + V_z \hat{b}_z. \end{aligned}$$

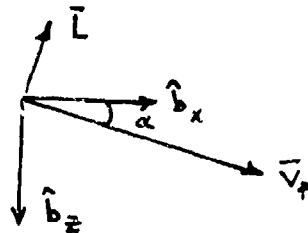
The angle of attack α and angle of sideslip θ are shown below.



From the above sketch the following relationships can be derived.

$$\sin\theta = \frac{V_y}{\sqrt{V_x^2 + V_y^2 + V_z^2}} \qquad \sin\alpha = \frac{V_z}{\sqrt{V_x^2 + V_z^2}}$$

By definition the lift vector lies in the \hat{b}_x - \hat{b}_z plane and is perpendicular to the wind vector. The situation is shown below.



Note that \vec{v}_p is the projection of \vec{v} on the \hat{b}_x - \hat{b}_z plane. Thus

$$\vec{L} = L [\sin\alpha \hat{b}_x - \cos\alpha \hat{b}_z]$$

where L is the magnitude of the lift vector defined in Section 3.

Structured Management of Data Acquisition
and Reduction at the Test Site
(SMARTS)

written by

Mr. Jeffrey M. Fornoff
25-JUL-1984

U.S. Army Armament, Munitions and Chemical Command (AMCCOM)
Armament Research and Development Center (ARDC)
Technical Services Directorate (TSD)
Battlefield and Automation Support Division (BASD)
Techniques and Applications
Dover, New Jersey 07801

ABSTRACT

This paper describes the development and use of the SMARTS system (Structured Management of Data Acquired and Reduced at the Test Site) implemented at ARDC Dover, NJ. SMARTS is a computer-based system designed to meet the vast data reduction and archiving requirements of various large caliber weapons testing. The system allows the test engineer to tailor data acquisition and processing to the particular needs of the weapons test. Once a particular test environment has been defined with the system, the test engineer may rapidly acquire test data, reduce (process) it, and display the data in graphical form at the test site. The SMARTS system can support and operate any number of test site locations simultaneously. All data which is collected from the various test sites is automatically archived at a central point and can later be recalled for review or undergo further processing at any time.

The SMARTS system operates with the cooperation of two computers and a microprocessor which communicate with each other. The two computers used are a PDP 11/34 and a VAX 11/780 which communicate using DECnet communications software [1]. The PDP 11/34 also uses a IEEE-488 General Purpose Interface Bus (GPIB) to communicate with an Intel 8086 microprocessor both of which are located at the test site. The VAX, located at a remote computing center, serves the 11/34 as an auxiliary processor and data repository. The test engineer controls the system using the PDP 11/34 mini-computer whose function is to control all data flow between the computers and microprocessor. The microprocessor controls a specialized set of programmable high-speed analog to digital converters, each of which contains up to 64K bytes of memory. Test data acquired by the A/Ds is first stored in A/D memory. The 11/34 transfers the raw data from the A/Ds to the VAX where it is stored on mass-storage devices. The VAX processes the raw data and transmits graphical and tabular data back to the 11/34 where it is output to the engineer for evaluation. This immediate feedback mechanism allows the engineer to make judgments about the experiment on a test-by-test basis, allowing him to make possible modifications or avoid hazardous conditions concerning the test. This immediate feedback method is also cost saving in that the engineer can stop testing as soon as sought-after results are found rather than requiring a large amount of samples be tested in hopes of later finding the phenomenon.

The SMARTS system solves many of the problems encountered in the past when reducing test data. Previous methods have used analog recorders to capture signals where the tapes would then be digitized (at a later date) and processed. This meant the test engineer was not afforded the ability to view any processed data while the test was being done. The use of the SMARTS system allows the engineer to bypass the use of analog tape (and degradation of signals) entirely and provides him with immediate valuable results of the test.

PRESENT ASSIGNMENT: Electronics Engineer, U.S. Army Armament, Munitions and Chemical Command, ARDC, Dover, NJ.

DEGREES HELD: B.S.E.E. Virginia Polytechnic Institute and State University (1981).

[1] PDP-11, VAX and DECnet are trademarks of Digital Equipment Corporation.

PREFACE

The design and operation of the SMARTS (Structured Management of Data Acquisition and Reduction at the Test Site) System implemented at the Armament Research and Development Center (ARDC) in Dover, NJ, is to acquire and reduce test data in a near real-time environment and to display processed data at the test site. The SMARTS system is designed to allow test engineers to receive immediate feedback of test results while the tests are being performed.

The advantage to the SMARTS system is that the test engineer may obtain reduced test data within seconds after test data has been acquired. Previous methods of data reduction included recording test signals onto analog magnetic tape which would later be digitized. The digital data would then be reduced using software on a digital computer. This method of data reduction is needlessly time-consuming and does not allow the test engineer to view the reduced test data until well after the test has been completed.

The SMARTS system has been structured to allow any type of data reduction to be performed on test data via user specific data reduction programs. The type of data reduction to be performed is selected by the test engineer at the time of the test along with all the test signals that are to be acquired. Test data is captured with a set of high-speed programmable analog-to-digital (A/D) converters with up to 64K byte memories each. All data that SMARTS acquires is stored on disk files at a central computing center where they are archived for future use.

The design and operation of the SMARTS system at ARDC, Dover, NJ, has been designed to handle any type of data acquisition requirements in any type of laboratory or test environment.

CHAPTER 1

SYSTEM DESIGN AND IMPLEMENTATION

SMARTS (Structured Management of Data Acquired and Reduced at the Test Site) is a general purpose data acquisition and processing system designed to acquire vast amounts of multi-channel data, process it, and display graphical and tabular data at the test site. The system supports any number of test sites, each of which can acquire and process data independently. Each test site utilizes the processing power of a remote computing center which houses all site specific software used to process test data. The operation of the SMARTS system at ARDC, Dover, NJ, has been designed to handle any type of data acquisition requirements in any type of laboratory or test environment.

Data is acquired with a specially designed chassis which contains a set of high-speed programmable analog-to-digital (A/D) converters controlled by a microprocessor. Data acquired from the A/Ds is transmitted by a laboratory computer to a central processing site where data from all test sites is archived. A larger computer, located at the central processing site, is responsible for processing and analyzing all test data which is transmitted to it from the various test sites. User and test site specific software that analyzes each particular set of test data is implemented at the central processing site, conserving and utilizing computing resources more efficiently. Test results are transmitted back to the various test sites within seconds where test engineers may review processed test data as it is being acquired.

SMARTS system hardware and software components will be described and relationships between components will be discussed. Further chapters describe operation of the SMARTS system at both the test site and at the central processing facility.

SYSTEM DESIGN AND IMPLEMENTATION

1.1 PROCESSING REQUIREMENTS

Current data acquisition requirements at ARDC, Dover, involve acquiring and processing Pressure vs. Time data of various large caliber weapons. Tests involve measuring pressure differentials inside gun tubes as they are fired using various types of charges. This type of data is very transient in nature and can be difficult to capture using conventional analog-to-digital converters. Test signals are often poor and the test data often contains noise spikes and line noise due to testing conditions. In addition, the actual data in question may only last a few milliseconds. In order to provide sufficient resolution for this type of transient analysis, sampling rates must be high in order to capture sought-after phenomena.

Conventional methods of capturing such test data involves recording the test signals on an analog tape recorder. Once all test data has been recorded on analog tape, the tape is then digitized (usually at a computer facility) and processed into graphical and tabular form. This procedure is very time consuming and does not afford the engineer any kind of test results as he is performing the test. Moreover, test signals are subject to the shortcomings of analog tape (i.e. phase shifting, distortion, drop-out, etc.) which compound problems of error analysis. The SMARTS system bypasses the use of the analog tape recorder and digitizes all test signals directly. Since the system is also computer controlled, the test engineer may obtain processed test results at the test site while the tests are being performed.

To meet the need for versatile data acquisition, a special high-speed programmable A/D converter was developed at ARDC, Dover. This special A/D can capture transient data using sampling rates up to 500 kHz yielding a resolution of two microseconds per sample. Data collected by each A/D is saved in a local memory which can hold up to 65,536 data samples. This allows test engineers to acquire high-resolution data for over 130 mS at the 500 kHz sampling rate. The A/Ds can be programmed to acquire data at different clock rates and trigger independently or together on a wide variety of signal conditions including time-zero (T0), threshold voltage, and external clocking.

SYSTEM DESIGN AND IMPLEMENTATION

1.2 GENERAL SYSTEM DESIGN

The SMARTS system consists of three main processing components which cooperate with each other in performing the tasks of data acquisition, data processing, and data storage (see figure 1-1). The three main components are a DEC VAX 11/780 computer, a DEC PDP 11/34 computer, and an Intel 8080 microprocessor controlled A/D chassis. The test engineer interfaces with the PDP 11/34 which controls all aspects of SMARTS system operation. The PDP 11/34 communicates with the A/D chassis via an IEEE-488 communications interface (GPIB) and communicates with the VAX 11/780 using a DECnet communications interface and software. The PDP 11/34 and A/D chassis are located at the test site where the analog data is to be acquired. Here the PDP 11/34 controls data acquisition via the A/D chassis and controls the data transfers to and from the VAX. The VAX is responsible for processing the huge amounts of data which are acquired and sending back graphical and tabular data to the PDP 11/34 where it can be displayed to the test engineer. The VAX is also responsible for archiving all data which is acquired by all test sites on the SMARTS system.

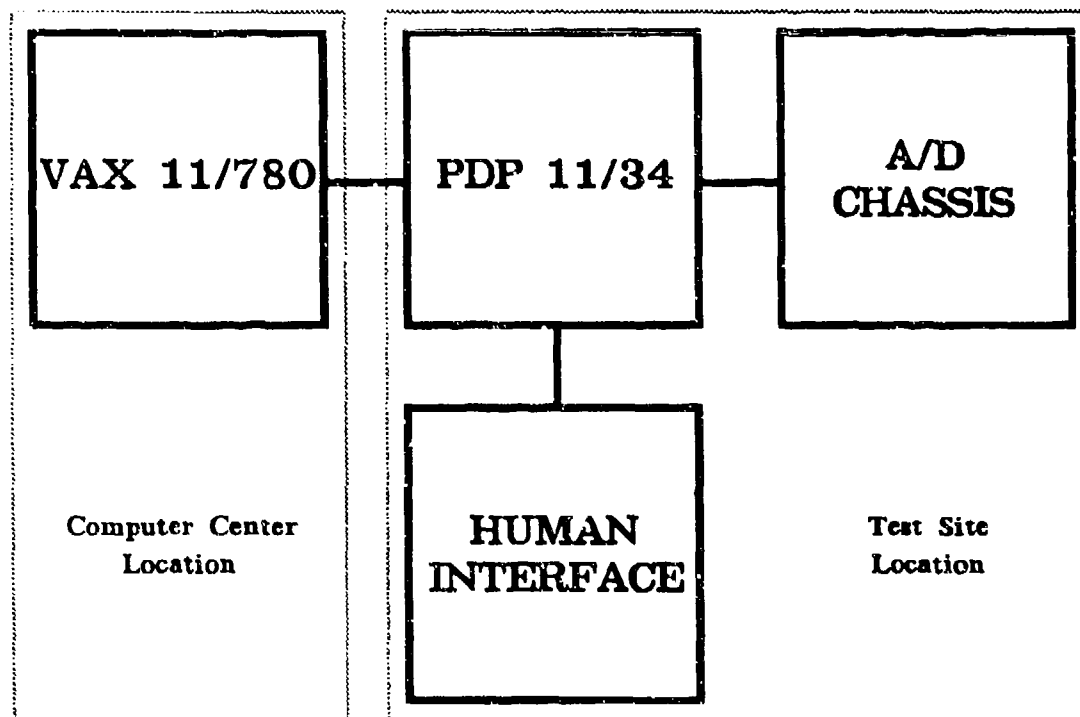


Figure 1-1
SMARTS System Functional Components.

SYSTEM DESIGN AND IMPLEMENTATION

1.3 DATA ACQUISITION SUBSYSTEM

The data acquisition subsystem consists of a set of programmable high-speed A/Ds, an Intel 8080 microprocessor and an IEEE-488 GPIB interface in a specially built self-contained chassis. The chassis holds up to 12 A/Ds along with the 8080 processor board, the GPIB interface board and power supply. An additional four A/D boards may be addressed by the SMARTS system to allow up to 16 channels of data to be acquired.

1.3.1 Programmable A/D Design

Special high-speed programmable A/D boards designed at ARDC, Dover, were developed for use in the SMARTS system. Each A/D may be programmed to acquire data on a wide variety of signal conditions. Test signals may vary +/-5 volts peak-to-peak at 0 volts DC offset. Signals outside this voltage range will be clipped at either +5 volts or -5 volts.

Each A/D can be programmed to acquire data independently or dependently based on acquisition criteria determined by the test engineer. Features for which each A/D can be programmed include the following:

- Digitization resolution may be set acquire 8- to 12-bit data.
- Sampling rates can be set as high as 750 kHz.
- An A/D may trigger on a T0 pulse in a normal mode or trigger on a T0 pulse as a master or slave.
- An A/D may trigger on a threshold voltage (high or low) and may also trigger this condition as a master or slave.
- Up to 65,536 samples of pretrigger data may be saved.
- Clocking of data into A/D memory may be delayed for any period of time once all triggering conditions have been met.

The test engineer has complete control over each A/D in how each is to be programmed. These features allow great flexibility for a wide variety of data acquisition applications. The following sections describe the above programmed features of the A/Ds in more detail.

SYSTEM DESIGN AND IMPLEMENTATION

1.3.1.1 Sampling Resolution

Each A/D can be programmed to digitize data using 8-12 bits of resolution. If less than 12 bits are used for digitization the A/D is said to be in the short cycling mode. The short cycling mode of the A/D affects the maximum sampling rate and the accuracy at which a signal can be digitized (see table 1-1). In short cycling modes, the A/D can sample a signal much faster, yielding a higher time resolution but sacrificing the accuracy of the digitized value. At 12-bit resolution test signals can be measured to within an accuracy of ± 1.22 mV, and at 8-bit resolution the accuracy is ± 19.53 mV.

1.3.1.2 Sampling Rates

Each A/D can be programmed to digitize data using an internal or external clock. Internal clock rates are determined by dividing down a 2 MHz master clock located on each board. Using the internal clock, a maximum sampling rate of 500 kHz is possible at 12-bit resolution and a maximum sampling rate of 666 kHz is possible at 8-bit resolution. If an external clock is supplied, a maximum sampling rate of 750 kHz is possible at 8-bit resolution.

Sampling of data values may also be done on an event basis using the external clock input of each A/D. This feature allows the A/D to sample and record a process in which events occur infrequently or on an irregular basis.

| Bits Resolution | Maximum Sampling Rates | | Digitizing Accuracy (+/-) |
|--------------------|------------------------|----------------|------------------------------|
| | Internal Clock | External Clock | |
| 12 | 500 kHz | 500 kHz | 1.22 mV |
| 11 | 500 kHz | 541 kHz | 2.44 mV |
| 10 | 500 kHz | 595 kHz | 4.88 mV |
| 9 | 500 kHz | 656 kHz | 9.77 mV |
| 8 | 666 kHz | 750 kHz | 19.53 mV |

Table 1-1
A/D Sampling Specifications

SYSTEM DESIGN AND IMPLEMENTATION

1.3.1.3 T0 Triggering

Each A/D may be programmed to trigger on a T0 pulse which is provided to the A/D chassis. Three modes of T0 triggering may be selected: Master, Slave, Normal. In the normal T0 triggering mode an A/D board will wait for a T0 pulse as part of its data acquisition criteria. If the A/D has been set up as a master T0, it will trigger any and all slave T0 boards which are in the A/D chassis when the master board triggers on T0. Any number of A/D boards may be set up in the normal or slave T0 triggering mode, but only one board may be set up as a T0 master.

1.3.1.4 Threshold Triggering

Each A/D may be programmed to trigger on data signal values greater or less than a given threshold voltage. Three modes of threshold triggering may be selected: Master, Slave, Normal. In the normal threshold triggering mode an A/D board will wait for its data signal to reach its threshold value as part of its data acquisition criteria. If the A/D has been set up as a master threshold trigger, it will trigger any and all slave threshold triggering A/D boards when it is triggered on its own threshold value. Any number of A/D boards may be set up in the normal threshold triggering mode, but only one board may be set up as a threshold master.

1.3.1.5 Pretriggered Data

Each A/D may be programmed to save any amount of pretriggered data up to the amount samples allowed to be stored in A/D memory (either 16K or 64K). Pretriggered data consists of the data immediately prior to the last triggering condition set up for that A/D board. This mode is often useful when phenomenon prior to a known event needs to be studied.

1.3.1.6 Clock Delay

Each A/D may be programmed to delay acquiring data for any length of time after all triggering conditions have been met. This feature allows signals to be acquired at a period of time when an event is suspected to occur.

SYSTEM DESIGN AND IMPLEMENTATION

1.3.2 A/D Controller Design

The A/D controller consists of an Intel 8080 microprocessor which has been programmed to control all aspects of each A/D within the chassis. The 8080 handles operation requests from the host computer (PDP 11/34) via an IEEE-488 General Purpose Interface Buss (GPIB). Control commands which can be sent to the A/D controller are:

- Master clear all A/D boards. This resets all boards to a known quiescent state.
- Read the status of a particular board. Status bits which can be decoded are: board present, memory size (16K or 64K), memory full and pretrigger count error.
- Setup acquisition parameters for a board. These include any of the features for which an A/D board can be programmed (see section 1.3.1).
- Start acquisition. This instructs all boards to acquire data according to their last acquisition parameters.
- Read data of a particular board. Any part of the A/D memory may be transferred to the host computer.
- Reset a particular board to the setup state. This resets a board to the conditions specified in their last setup acquisition parameters command.
- Swap mode command for data transfers may be specified. This causes each byte of every data word to be reversed in order of data transmission. This controller command can be a convenience for the host computer which receives the data.

The SMARTS system uses direct memory access (DMA) for all its data transfers over the GPIB. This greatly improves the speed of data transmission between A/D memory and the PDP 11/34.

1.4 DATA MANAGEMENT SUBSYSTEM

The data management subsystem consists of a PDP 11/34 computer with an IEEE-488 GPIB interface to the A/D chassis and a DECnet communication interface to a remote VAX 11/780 computer. It is the job of the 11/34 to coordinate all types of data transfers which take place in the SMARTS

SYSTEM DESIGN AND IMPLEMENTATION

system. It is also the computer to which the test engineer controls all aspects of data acquisition and processing. Terminals for system operation and graphics output are connected to the 11/34 along with disk devices for temporary data storage.

The SMARTS system may operate in one of two modes depending whether a network link is present to the auxiliary processor, the VAX 11/780. If a network connection exists between the PDP 11/34 and the VAX 11/780, all data which is acquired is transferred to the VAX where it is processed and stored. If a network connection does not exist or has failed for some reason the acquired data is stored on disk locally on the 11/34. This operation assures the engineer that acquired data will not be lost due to network link errors. This also allows the engineer to acquire data even when the VAX 11/780 is not available for processing.

1.4.1 Operator Controls

The test engineer or operator of the SMARTS system controls all aspects of system operation from a terminal through a series of menus. On-line help is provided for each option of every menu as an aid for easy operation. Through the use of menus the test engineer may specify what kind of testing is to be done and how each A/D is to be configured for data acquisition. The engineer may also specify what kind of data processing is to be performed when test data is sent to the VAX 11/780. All data processing is performed on the VAX 11/780 rather than the PDP 11/34 due to the processing limitations of the 11/34 and the vast amounts of data which must be handled. This design also frees any user dependency on the PDP 11/34 since no user specific software is present on the computer. Only SMARTS system software is present on the 11/34 which allows all test sites which utilize the SMARTS system to be identical in operation.

1.4.2 A/D Communications

The SMARTS system transmits and receives information and data to the A/D chassis through the use of A/D controller commands (discussed in section 1.3.2). The test engineer controls the setup parameters of each A/D and acquisition of data through the use of high-level operations under menu control. The SMARTS system automatically translates these high-level operations into one or more controller commands which are sent to the A/D chassis.

SYSTEM DESIGN AND IMPLEMENTATION

1.4.3 Auxiliary Processor Communications

The PDP 11/34 controls an auxiliary processor, the VAX 11/780, through a DECnet communications link. Through instructions by the engineer, the 11/34 directs the VAX in what kind of processing is to take place with data which is transmitted to it. The 11/34 also directs the VAX to send back processed graphical and tabular data to the test site where it can be studied by the engineer.

Because of the distance a test site may be from the central computing center, DECnet communications take place over a closed circuit cable transmission system (CCCTS) via the use of high-speed modems. Any number of test sites may communicate with the VAX using the cable system and DECnet network communications links.

1.5 DATA PROCESSING SUBSYSTEM

The data processing subsystem consists of a VAX 11/780 with a DECnet communications interface and link to the SMARTS system on the PDP 11/34. It is the responsibility of the VAX to handle all data processing of each test site and to archive the data for future reference. The VAX used at ARDC, Dover, also has the capability to provide high resolution graphics suitable for report quality work. The SMARTS system uses the VAX in two different operating modes:

- as a slave processing operation over a network link to the PDP 11/34 and
- as a post processing batch operation utilized by SMARTS software engineers.

The slave processing operation mode is utilized by the SMARTS system with control governed by the test engineer. The post processing batch operation mode is utilized by SMARTS software engineers at the computer center.

1.5.1 Network Data Processing

The network data processing mode of the SMARTS system is a slave process to the PDP 11/34 at the test site. The test engineer selects the type of data processing to be performed based on the type of test data which is to be acquired. The PDP 11/34 then instructs the VAX to perform the specific data processing and optionally to return processed information to the test site in the form of plots and

SYSTEM DESIGN AND IMPLEMENTATION

tabular data. The VAX also performs the data archiving function of the SMARTS system. All data which is acquired is stored on-line for future reference. When on-line storage becomes full, the oldest data is removed to digital tape where it can be stored indefinitely. All data which is archived is identified by date and the test site which it came from and also by the type of test which produced the data.

1.5.2 Batch Data Processing

The batch data processing mode of the SMARTS system can be utilized at any time by software engineers at the central computing center. Here, all raw data may be reprocessed at any time to produce high-resolution graphical output or other information. This operational mode of the SMARTS system is designed to allow engineers to re-create and/or review test data as it was acquired during the actual test. It can also serve to allow engineers to re-process data using additional software at a later date to examine unexpected phenomenon in the test data.

CHAPTER 2

SYSTEM OPERATIONS

This chapter describes the operational aspects of the SMARTS system and how test engineers interface to the system to perform necessary data acquisition functions. The operation of the SMARTS system has been made as friendly to the test engineer as is possible with the use of an A/D setup catalog and project configuration files. The use of these high-level components make it very easy for the test engineer to quickly acquire data with a minimum of data entry from the terminal keyboard.

2.1 PDP 11/34 OPERATION

SMARTS system operation is initiated by the test engineer at a remote test site by starting up the SMARTS system software package on the PDP 11/34. The system software immediately ascertains the status of the SMARTS system hardware and displays this information to the test engineer. All functional A/D boards which are present in the A/D chassis are listed along with the amounts of A/D memory contained on each. SMARTS system software creates a network link to the VAX 11/780 and receives the current time and date from the VAX. Once the status of the system has been displayed, the SMARTS system becomes operational to the test engineer. Through the use of menus, the engineer performs operations to acquire and process test data.

The environment which is provided by the SMARTS system to allow the test engineer to acquire and process test data is aided by the use of an A/D setup catalog and project configuration files. These constructs are provided by the SMARTS system to allow the test engineer to establish a test project within the system and to automatically configure each A/D in the A/D chassis with the proper acquisition parameters for the test. An operational block diagram of the SMARTS system environment is illustrated in figure 2-1.

SYSTEM OPERATIONS

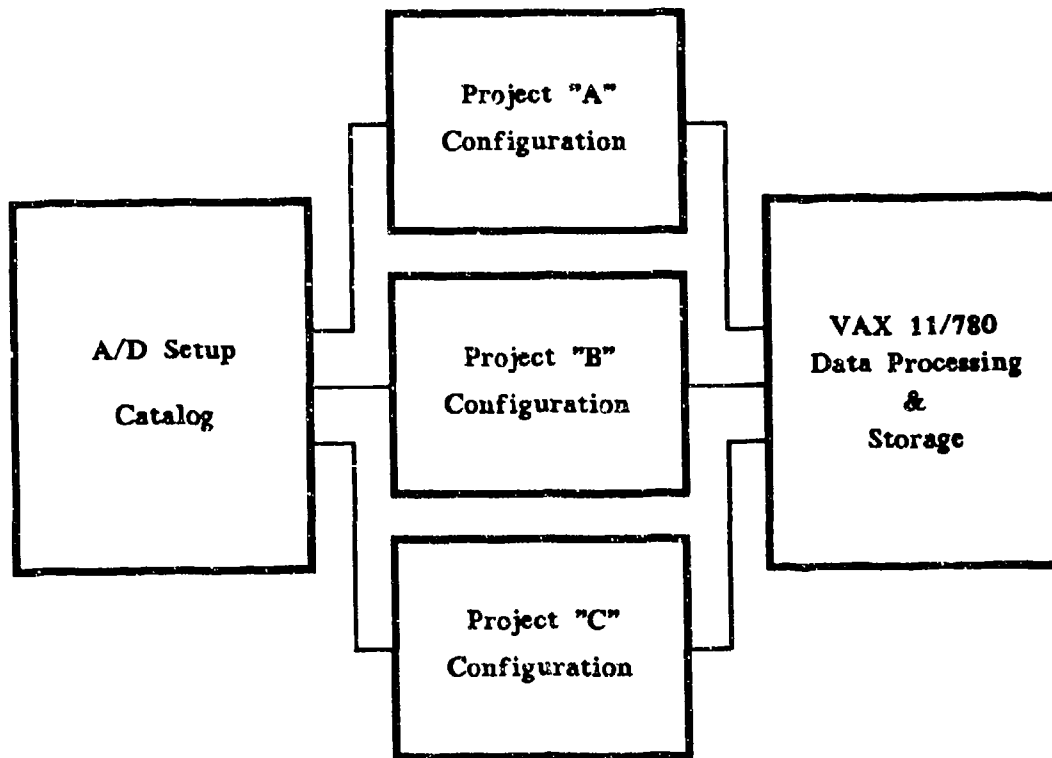


Figure 2-1
SMARTS Project Configuration Environment

2.1.1 A/D Setup Catalog

The SMARTS system maintains a catalog of A/D setup parameter files which describe a particular state to which an A/D board may be set or programmed (see section 1.3.1). The test engineer can create these setup files and store them into the A/D setup catalog by means of menu selection. The SMARTS system allows the engineer to:

- Create and add an A/D setup file to the catalog
- Delete an A/D setup file from the catalog
- List the names of all A/D setup files in the catalog
- Display the contents of a particular A/D setup file

Each A/D setup file which is created is assigned a name by the test engineer and is the mechanism by which the SMARTS system identifies a particular set of A/D setup parameters.

SYSTEM OPERATIONS

2.1.2 Project Configuration

The SMARTS system maintains a list of projects under which tests are performed. Each project is given a name assigned by the test engineer to represent a particular test environment for data acquisition. In this environment the test engineer determines how many channels of data are to be acquired, how each A/D should be set to acquire the data and how the data should be processed by the VAX. This information is maintained by the SMARTS system as a set of project configuration files. The SMARTS system allows the test engineer to:

- Create a new project and define the test environment. This includes assigning a name to the project.
- List the names of all projects.
- Enter a project environment to acquire data.
- Modify a project environment and optionally save this new environment in the project configuration files.

When the test engineer enters a project to acquire data, the project configuration files are read and the test environment is automatically configured for him. Information which is maintained in project configuration files includes the following:

- The test engineer's name
- Test specific data such as tube, charge and projectile parameters
- A/D channel assignments for test signals and the associated A/D setup parameter file(s)
- Functional assignments of the test signals. This may include the type of test data being acquired such as breech pressure or forward pressure, etc.
- Processing instructions for data from each A/D channel including plotting instructions, if any

Associated with each project in the SMARTS system is a unique processing program which is used to process the test data. These project-specific processing programs are initiated on the VAX 11/780 by the PDP 11/34 via the DECnet network link established by the 11/34.

SYSTEM OPERATIONS

2.1.3 Stand-alone Mode

All test data which is acquired under a specific project is transmitted to the VAX which processes the data using project-specific processing programs. If, for some reason, the network link is unavailable, the 11/34 stores the data on local disk storage. When this event occurs, the SMARTS system is said to be in the stand-alone mode. Data may still be acquired in the stand-alone mode, but immediate processing of the data will not be performed. The SMARTS system will still generate graphics information for the test engineer to review; however, the data which is displayed will be the raw A/D data instead of the processed data which is returned by the VAX. The SMARTS system can operate in the stand-alone mode as long as local disk storage is available to store the test data. The standard SMARTS hardware configuration allows up to 10 Mbytes of storage to be used for data storage in the stand-alone mode.

Once the network link is reestablished to the VAX the test data which has been stored locally on the PDP 11/34 is transferred to the VAX. The project-specific processing programs can then be used in the batch data processing mode (see section 1.5.2) to produce the final processed test data which can be given to the test engineer.

2.2 VAX 11/780 OPERATION

When SMARTS system operation is started at a remote test site, a DECnet network link is established between the test site (PDP 11/34) and the VAX 11/780. When this link is established the VAX verifies that the 11/34 is a valid SMARTS system test site and allows it access to the VAX SMARTS system software. This software allows the SMARTS system to create new test site project accounts and process project-specific data. Any number of test site accounts may be created and supported at any time. Each test site may acquire data and process it simultaneously without the knowledge of other test site operations.

2.2.1 Test Site Accounts

The SMARTS system maintains any number of active test site accounts on the VAX and provides separate facilities for data processing and storage for each account. Each test site account may have any number of active projects stored on-line for immediate access. Older project accounts are backed up to digital tape with permission of the test

SYSTEM OPERATIONS

engineer involved with the project. Anytime a project is activated at a SMARTS test site, a redundant log file is created on both the 11/34 and the VAX. This log file contains a record of all data transactions which occur in regards to data acquisition and processing. The SMARTS system uses these files to keep track of acquired data and data processing instructions for use by other post processing programs.

2.2.2 Project Specific Analysis

Each project account under each test site account on the VAX contains the project-specific data processing software which is used in association with the test data. This software contains the data processing-specific algorithms used to process test data. The SMARTS system uses the output of these programs to provide the test engineer with immediate feedback of processed results in the form of graphics and tabular data.

Additional processing may also be performed on the VAX to provide high-resolution graphics output and high-volume tabular data using the resources on the VAX. Current resources include a high resolution electrostatic plotter, a high-resolution laser plotter, and a medium-speed line printer for tabular data.

CHAPTER 3

CONCLUSIONS

The SMARTS system has been designed to provide the test engineer with processed results as quickly as possible. Data communication speed has been maximized due to the vast amounts of raw data that is transferred. High-speed DMA GPIB data transfers are utilized when transferring data from A/D memory to the PDP 11/34 and high-speed DECnet network transfers are made to transfer data from the 11/34 to the VAX. Double buffering techniques are used and asynchronous I/O transfers are utilized whenever possible.

3.1 SYSTEM PERFORMANCE

In a typical test, it takes approximately 5 to 10 seconds to transfer one full channel of A/D data (16K), process it and produce a graphics plot for the test engineer at the test site. This process takes slightly longer when the SMARTS system is utilized in the stand-alone mode.

Post processing which is performed by the VAX to provide high-resolution graphics is postponed until all test data from a project has been acquired to allow optimal response time for the test site. Once a project has been exited for the day, all post processing is accomplished in a (network) batch mode. In most cases, the test engineer may receive final report quality output by the end of the day. This turn-around time is greatly improved over other methods of data acquisition and data processing which could take up to a week or more.

CONCLUSIONS

3.2 EXPANSION CAPABILITIES

The SMARTS system has been designed with expansion capabilities built into the system. The system can be easily expanded to:

- Allow test engineers to review old data from a specific project
- Allow one SMARTS test site account access data from other test site accounts
- Allow test engineers to call for additional data processing directly at a later date

Many other capabilities are possible with the use of the VAX, SMARTS system software, and a little imagination.

ACKNOWLEDGMENTS

The author would like to thank the following people for their contributions and help in preparing this paper: Leonard Goldsmith for the initial idea of a SMARTS-like system and the design of the A/D boards, Helen Swanson for her valuable assistance in editing the paper and Donald Gulliksen for giving the author incentive to write the paper in the first place. Special thanks to Diane Swanson, whose help and moral support in this endeavor was especially appreciated.

REFERENCES

1. Fornoff, J. M., Microprocessor Controlled A/D GPIB Communication, 23-MAR-82.

"Finite-Element Analysis of an Annular, Regenerative Piston"

Cris A. Watson *

U.S. Army Ballistic Research Laboratory,
Aberdeen Proving Ground, MD
21005

ABSTRACT

The U.S. Army is currently investigating regenerative injection concepts in its liquid propellant gun technology program. In this concept, a differential area, regenerative piston is used to pump a liquid propellant into the combustion chamber. The present design utilizes an annular regenerative piston. The piston, which is the subject of this finite-element analysis, presents complex design challenges. The piston must withstand the large pressures encountered in the combustion chamber and the high accelerations due to these pressures. Since seals act along the piston's surfaces, any deformation may result in a loss of pressure or failure. The piston resembles a thin shell that is bounded by a grease column and the supporting chamber wall on the outside, and liquid pressure on the inside. The piston accelerates rearward as a result of the unbalanced force due to the differential area of the piston. It is slowed down by a damping taper on the center rod which gradually reduces the injection area available for propellant flow. The rear of the piston is exposed to atmospheric pressure.

This analysis employs the SAAS-II Finite Element Computer Program. The program features automatic mesh generation, multiple material selection, and a bilinear, elastic-plastic, stress-strain curve approximation. Gun pressures and piston acceleration were determined directly from pressure-time records obtained during test firings and from initial ballistic simulations. The objective of this analysis is to determine if the present annular piston is suitable for high performance firings where the chamber pressure may be as high as 700 MPA. Brief explanations of the operation of the regenerative gun, methods used in the finite element analysis, and the results are provided.

BIOGRAPHY:

PRESENT ASSIGNMENT: Mechanical engineer, Advanced Ballistic Concept Branch, Interior Ballistic Division, Ballistic Research Laboratory, Aberdeen Proving Ground, Maryland.

DEGREES HELD: B.S.M.E. Georgia Institute of Technology (1983)

"Finite -Element Analysis of an Annular,
Regenerative Piston"

Cris A. Watson
U.S. Army Ballistic Research Laboratory,
Aberdeen Proving Ground, MD 21005-5066

INTRODUCTION

General Electric Ordnance Systems Division (GEOSD) at Pittsfield, MA, under contract to the BRL, has designed and fabricated a 30-mm regenerative liquid propellant gun (RLPG) system. The fixture was installed at BRL in July of 1984. The fixture is now being used to evaluate liquid monopropellants and study various features of the RLPG cycle.

To obtain a set of structural and performance limits for the 30-mm RLPG, a finite element analysis was undertaken on the most highly stressed component of the fixture, the annular piston. The piston is a thin-walled, annular cylinder. Initial and boundary conditions for the finite-element analysis were obtained from both pressure and piston travel records taken during actual firings and interior ballistic simulations.

The information obtained from the analysis will be used to determine if this 30-mm RLPG can be used in high pressure liquid propellant gun firings. Chamber pressures may be as high as 700 MPa which, because of the differential area piston, may produce up to 1000 MPa in the liquid reservoir.

REGENERATIVE GUN PROPULSION

Most studies of liquid gun propulsion technology have been directed toward the bulk-loaded approach. While the bulk-loaded approach is simpler mechanically, the regenerative technique offers greater control over the ballistic cycle.

The regenerative cycle utilizes a differential area piston to pump propellants into a combustion chamber. Figure 1 illustrates a simple regenerative piston that was extensively studied at GEOSD. The propellant burns in the combustion chamber, sustaining the pressure which drives the piston. While the simple system shown in Figure 1 is adequate for performing various parametric tests, it is not acceptable for practical systems.

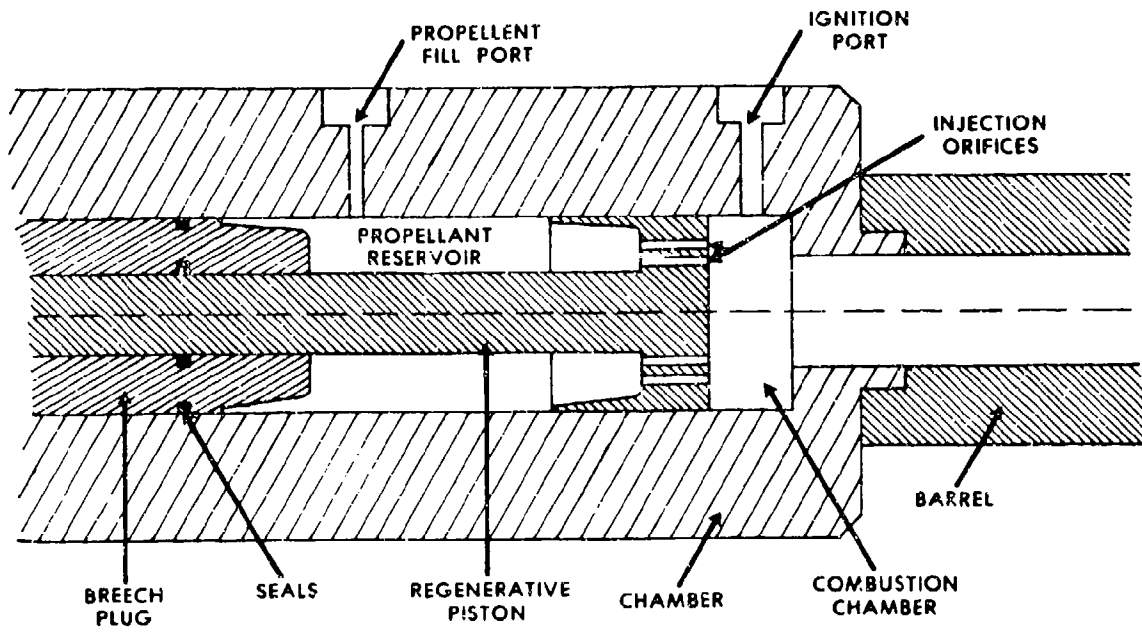


FIGURE 1. Basic Regenerative Liquid Propellant Gun (RLPG)

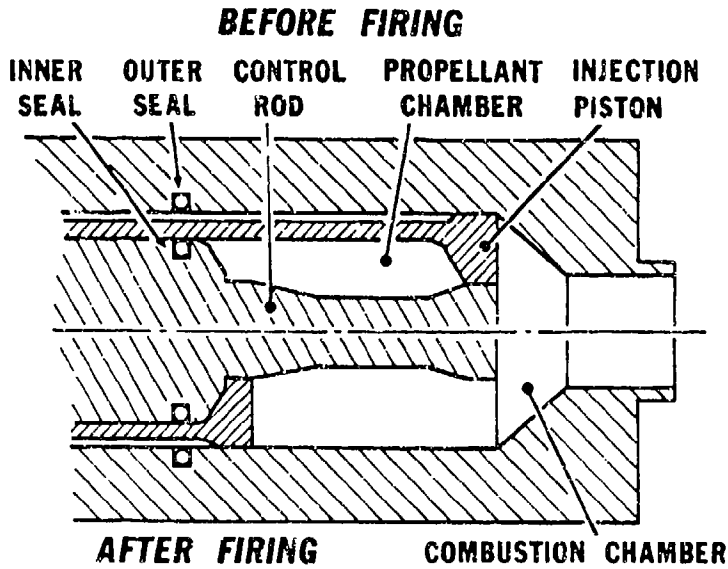


FIGURE 2. Annular Piston RLPG

For practical systems, methods must be provided for rapid projectile, propellant, and igniter loading; confinement of the liquid propellant to the reservoir prior to ignition; possibly prepressurization of the liquid propellant to reduce the risk of ignition from adiabatic compression of bubbles in the liquid propellant; and a capability for variable charge loading in the case of artillery applications. One approach for satisfying these requirements is a configuration which uses an annular piston similar to that shown in Figure 2.

The 30-mm RLPG at the BRL test facility uses an annular piston to inject a monopropellant into the chamber. The propellant enters the combustion chamber as an annular sheet, where it breaks up into droplets and burns. The injection is controlled by tapers on the central rod. The constant diameter portion of the rod controls the maximum pressure. The charge length may be varied by changing the length of the constant diameter section.

The RLPG cycle starts with the transducer block forward, resting against the rear of the piston. The piston is supported by a spacer in the forward part of the combustion chamber. As the fill cycle begins, propellant is forced through a check valve in the rod and enters the liquid propellant reservoir. Ullage is removed through a port in the transducer block. Pressure in the reservoir forces the transducer block back until it encounters a stopping cone on the rod. The system is prepressurized to 7 MPa to reduce the chance of ignition due to adiabatic compression of residual ullage. The fixture is then ready to fire. A solid propellant igniter is used to initiate the cycle. As pressure in the combustion chamber increases due to the igniter, the piston moves back, generating a gap between the piston and the rod. Propellant enters the combustion chamber through this gap, where it breaks up and begins to burn. The forward taper of the rod controls the start-up of the cycle. The system approaches a steady state condition as the pressure generated by the burning propellant forces the piston rearward through the constant diameter section of the rod. As the piston encounters the rear taper, the injection area decreases causing the liquid pressure to increase, which in turn decelerates the piston. The piston stops when it contacts the face of the transducer block, ending the RLPG cycle.

STRESS ANALYSIS PROCEDURE

Stress data was generated using the SAAS II finite element computer code¹. Input parameters were generated by scaling firing data taken from the 30-mm RLPG, see Table 1.

1. S.G. Sawyer, "BRLESC Finite Element Program for Axisymmetric Plane Strain, and Plane Stress, Orthotropic Solids with Temperature-Dependent Material Properties", BRL Report #1539, Ballistic Research Laboratory, Aberdeen Proving Ground, MD March 1971 (AD 727702)

The scaled firing data represents pressures which would be encountered in higher pressure operating regimes. A quasi-static, steady-state linear analysis was adequate for this problem because the fundamental frequency of mechanical vibration of the piston is an order of magnitude higher than the pressure pulse. Figure 3 shows the static load placement and boundary conditions.

The piston was manufactured using 13-8 precipitation-hardened stainless steel hardened to a Rockwell C-scale of 38-42. A summary of the properties of the 13-8 stainless steel used for the 30-mm annular piston are given in Table 2.

Table 1. Loads Used in the Stress Analysis Calculations

| Stress Analysis # | Combustion Chamber Pressure (MPa) | Liquid Reservoir Pressure (MPa) | Grease Pressure (MPa) |
|-------------------|-----------------------------------|---------------------------------|-----------------------|
| 1 | 413 | 578 | 462 |
| 2 | 482 | 675 | 539 |
| 3 | 551 | 771 | 617 |
| 4 | 620 | 868 | 694 |
| 5 | 689 | 964 | 771 |
| 6 | 558 | 781 | 624 |

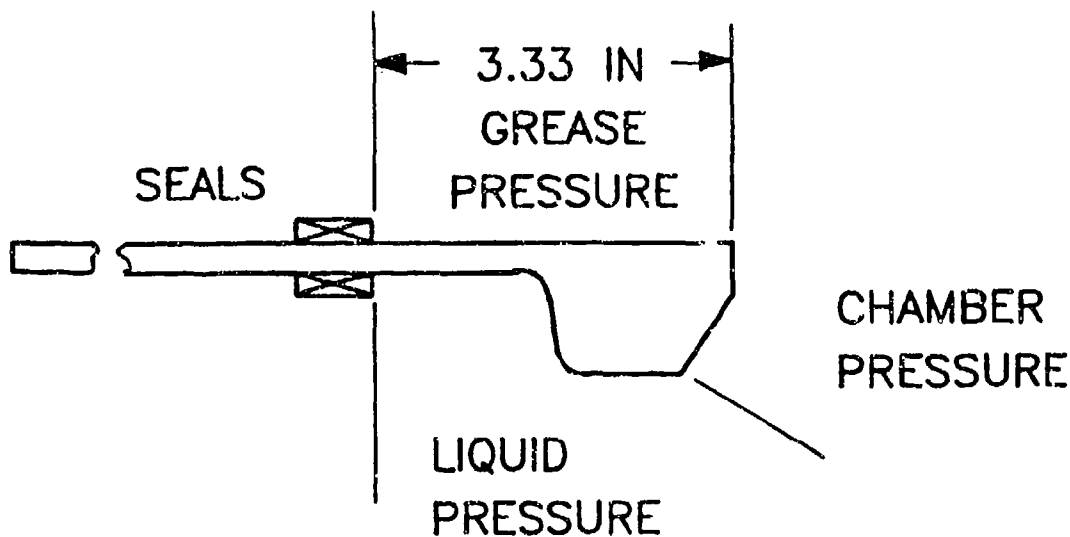


FIGURE 3. Static Pressure Loads and Boundary Conditions

Table 2. Material Properties of the Annular Piston
13-8 PH Stainless Steel 2

| | | |
|-----------------------|-------------|---------------------------|
| Modulus of Elasticity | = 205.8 GPa | (2.94×10^7 psi) |
| Poisson's Ratio | = .28 | |
| Shear Modulus | = 79.9 GPa | (1.16×10^7 psi) |
| Yield Stress | = 1240 MPa | (1.80×10^5 psi) |

RESULTS

The maximum effective stresses (von Mises criterion) in the piston are plotted in Figure 4. This plot represents the computed maximum effective stresses for six analyses using the scaled pressure data from Table 1. Figure 4 shows that the maximum effective stress exceeds the yield stress, 1240 MPa, when the chamber pressure exceeds 558 MPa .

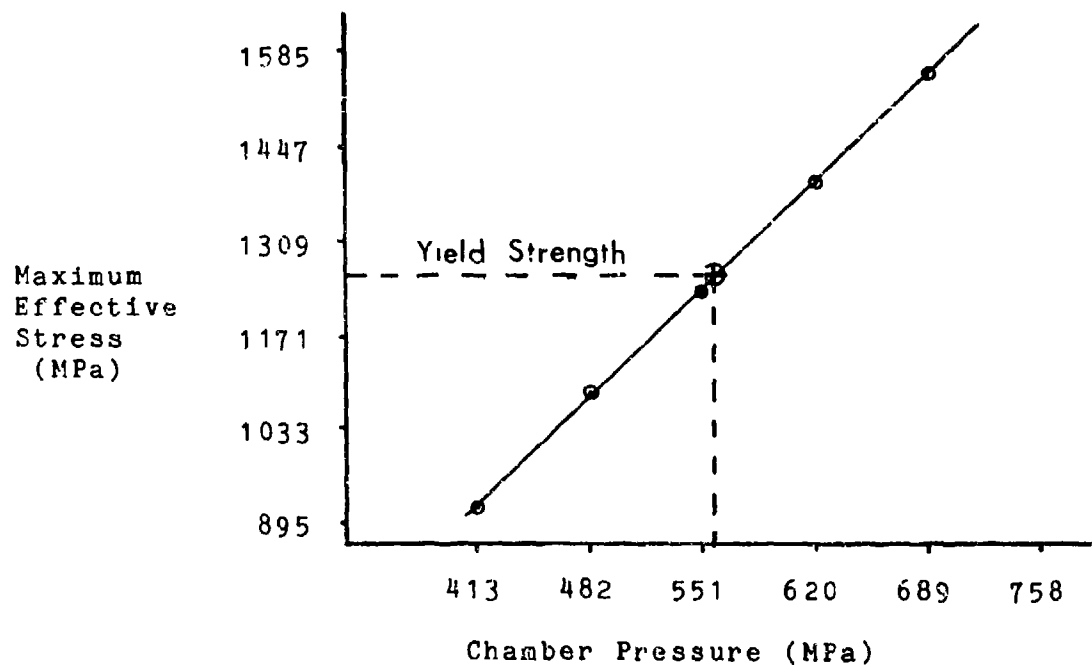


Figure 4. Maximum Effective Stress vs Chamber Pressure

2. Republic Steel Corp., "Precipitation Hardenable Stainless Steels, PH 13-8 Mo, 15-5 PH, PH 15-7 Mo, 17-4 PH, 17-7 PH", 1975.

Figures 5-11 shows effective, radial, axial, and hoop stress contours plotted graphically along the length of the piston. Figures 12 and 13 shows the undeformed and the deformed grid under 558 MPa chamber pressure, 781 MPa liquid reservoir pressure, and 624 MPa grease pressure. The piston fails at the thin walled section between the piston head and the seal location. Failure in this location results in increased clearance between seal and piston and promotes leakage.

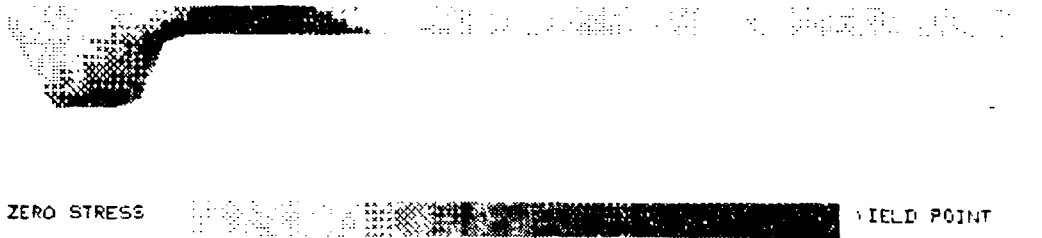


Figure 5. Effective Stress Contours at 558 MPa Chamber Pressure

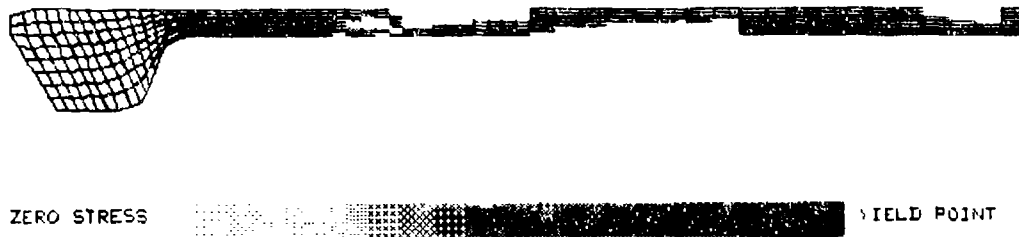


Figure 6. Radial Tension Stress Contours at 558 MPa Chamber Pressure

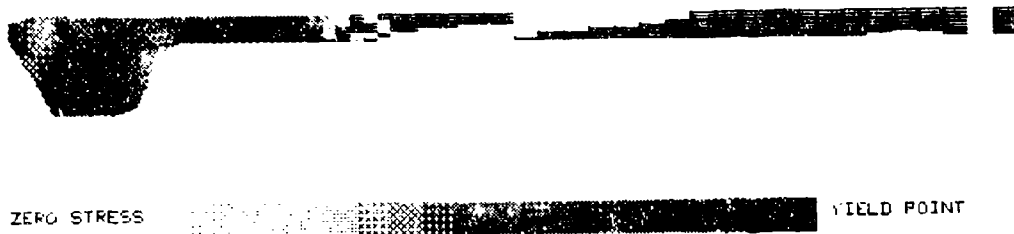


Figure 7. Radial Compression Stress Contours at 558 MPa Chamber Pressure

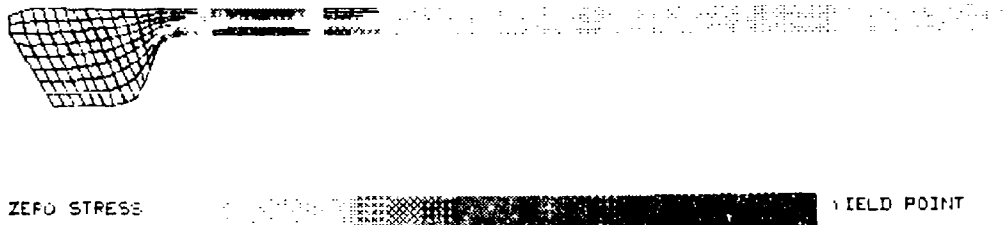


Figure 8. Axial Tension Stress Contours at 558 MPa Chamber Pressure

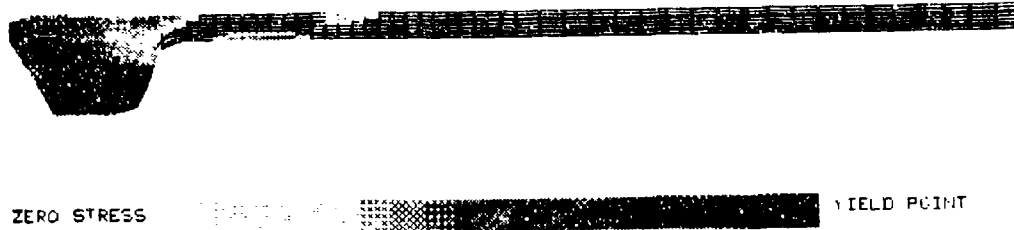


Figure 9. Axial Compression Stress Contours at 558 MPa Chamber Pressure



Figure 10. Hoop Tension Stress Contours at 558 MPa Chamber Pressure

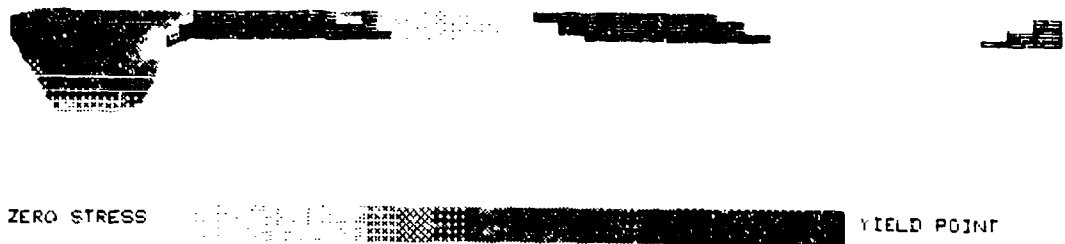


Figure 11. Hoop Compression Stress Contours at 558 MPa Chamber Pressure



Figure 12. Undeformed Grid

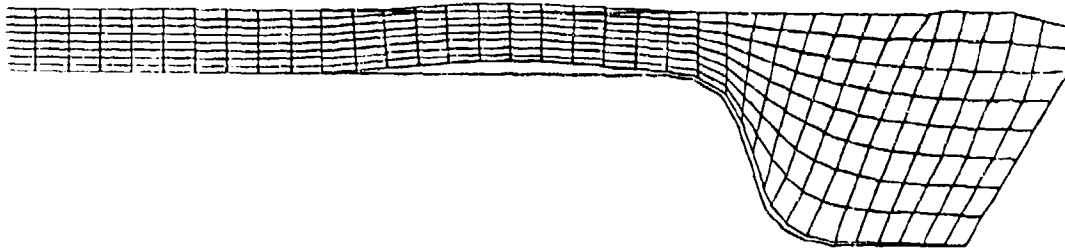


Figure 13. Deformed Grid (Enlarged)

CONCLUSION

Results from the stress analyses show that the thin-walled section of the piston will undergo permanent deformation when the chamber pressure exceeds 558 MPa. This is due to the grease pressure being lower than the liquid pressure. The present piston, which was designed for lower operating pressures (350 MPa), is not suitable for a gun system where the chamber pressure will exceed 558 MPa, and where unbalanced pressures exist across the thin-walled section. The piston must be strengthened to withstand the higher effective stress levels at higher operating pressures, and should also be re-designed to reduce unbalanced pressures across the thin-walled section.

REFERENCES

1. S.G. Sawyer, "BRLESC Finite Element Program for Axisymmetric Plane Strain, and Plane Stress, Orthotropic Solids with Temperature-Dependent Material Properties", BRL Report #1539, Ballistic Research Laboratory, Aberdeen Proving Ground, MD March 1971 (AD # 727702)
2. Republic Steel Corp., "Precipitation Hardenable Stainless Steels, PH 13-8 Mo, 15-5 PH, PH 15-7 Mo, 17-4 PH, 17-7 PH", 1975.

RADKIEWICZ and PETERSON

TITLE: Photoelasticity Applied to Gun Components
ROBERT J. RADKIEWICZ and ROBERT A. PETERSON
US Army Armament Research and Development Center
Rock Island, IL 61299

ABSTRACT:

New Army requirements for lighter, more powerful guns for next generation lightweight helicopters and air defense systems will force gun designers to apply more sophisticated theoretical and experimental methods to developmental guns. This paper will describe an experimental technique, photoelasticity, to measure full field strain patterns that can assist in designing lighter guns. The gun strain patterns can be measured during individual component static loading or, by using high-speed photography, during gun firing.

A brief introduction into photoelasticity is provided in this paper, describing the theoretical basis for the technique, the instrument used to measure strain patterns, and recent advances in photoelastic coatings that have made their application to guns more realistic.

An initial study of gun components to determine principle strain directions is described. Results of statically loading the gun components is discussed and an example of the strain pattern obtained statically is shown.

Finally, results of full field strain measurements during firing of the XM230, 30mm gun are reported. The photoelastic coating of the XM230 that was used during these tests is described. Findings on photographic frame rates, coating thickness and other pertinent parameters required for strain measurement during gun firing is reported.

BIOGRAPHY:

PRESENT ASSIGNMENT: Chief, Ware Simulatin Group, US Army Armament Research and Development Command, 1977 to present.

PAST EXPERIENCE: Electronics Engineer, GEN T. J. Rodman Laboratory, Rock Island, IL, 1970 to 1977.

DEGREES HELD: Bachelor of Science (EE), University of Toledo, Toledo, OH, 1964; Master of Science (EE), University of Notre Dame, Notre Dame, IN, 1966.

PHOTOELASTICITY APPLIED TO GUN COMPONENTS

ROBERT J. RADKIEWICZ
*ROBERT A. PETERSON
US ARMY ARMAMENT RESEARCH AND DEVELOPMENT CENTER
FIRE CONTROL AND SMALL CALIBER WEAPON SYSTEMS LABORATORY
ROCK ISLAND, IL 61299

1. INTRODUCTION

Recent results obtained from applying photoelasticity to the measurement of strains in the XM230, 30mm chain gun[®] are reported in this paper. Photoelasticity is a technique for measuring full field plane strain patterns of a material and provides significant advantages over classical strain measurements using strain gages.

Typical uses for photoelasticity include: (a) identification of high stress areas or no stress areas in components; (b) design of new system components; (c) reduction of weight of designed systems; (d) confirmation of math model results.

This paper provides a brief overview of the photoelastic technique, an explanation of the gun selected for this study, the total program plan for this study, and finally, the results achieved to date.

2. THEORETICAL BACKGROUND

The physical phenomena behind photoelasticity is the change in the refractive index of a transparent material when subjected to stress. With no stress applied, the material is homogeneous. However, when a stress is applied, the optical properties of the material change, causing the index of refraction to vary along the lines of principal stress. This property is taken advantage of by shining polarized light through the stressed translucent material and viewing the light through another polarizer (typically called the analyzer). This configuration is called a plane polariscope. A circular polariscope is shown in figure 1. This is easily converted to the plane polariscope by removal of two quarterwave filters shown in the light transmission path.

[®] Trade Mark, Hughes Helicopter, Inc.

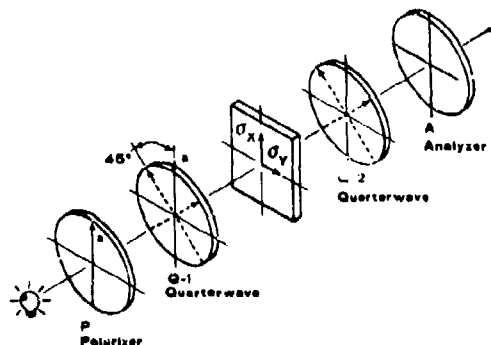
CIRCULAR POLARISCOPE

FIGURE 1

With no stress applied to the photoelastic material and the analyzer axis aligned at 90° to the polarizer, no light is transmitted through the analyzer. As stress is applied interference fringes, called isoclinic lines which are parallel with the direction of the analyzer, can be seen on the material through the analyzer. By rotating the analyzer axes, a map of isoclinic lines for the material can be generated. The direction of principal strain may be plotted from the isoclinics by drawing lines through the isoclinics at the same angle as the isoclinic occurred on the analyzer and connecting these lines from isoclinic to isoclinic.

The magnitude of the principal strains can be measured by inserting quarterwave plates in the light path of the plane polariscope, producing circularly polarized light. The principal of this circular polariscope, shown in figure 1, is the change in transmission velocity of the components of white light through the stressed photoelastic material. Looking through the analyzer, colored interference fringes are seen on the material and vary proportionally to the stress applied to the material. The equations describing this phenomena are straight forward and are covered in detail in reference 1. By applying a known stress and strain to a simply shaped section of photoelastic material, calibration of the colored fringes in terms of plane strain can easily be made.

What has been described above is a transmission polariscope, and is used for proposed designs of components. These components are made from the photoelastic material and the plane strains are measured.

3. APPLICATION ON THE XM230 GUN

For systems already built, such as the gun used in this experiment, a reflection polariscope is used. The photoelastic material is applied to the gun components with a reflective glue. The polarized light, either planar

or circular, is then reflected from the surface of the component being measured and through the analyzer which is located next to the polarizer.

Photoelastic material must be applied to components being measured so that strains are exactly transmitted from the component under stress to the photoelastic material. Commercially available kits have been successfully used to apply both the coating and reflective glue. The material is initially mixed in a liquid state and poured in a leveled form to a uniform thickness. When the material solidifies to a pliable state, it is fitted exactly to the components to be measured and allowed to harden on the components. The photoelastic material is then trimmed and glued to the components.

The commercial coatings available today provide significant improvements over previous material. It is not as susceptible to aging and humidity, allowing coating to remain on components for months without degradation, and tests can be repeated or modified since this coating is not destroyed during testing as many other types of coatings are.

The techniques of photoelasticity are being applied to gun components because they offer a method of refining gun design methods and reducing gun component weights. The XM230, 30mm gun, presently used on the Apache helicopter, was chosen for this program since it is a candidate weapon for the LHX helicopter; the next generation of Army lightweight helicopters. This gun, in its present configuration, weighs 121 lbs (figure 2). Firing rate of the gun is 625 spm, and it is required to be able to fire a maximum 900 round burst. This latter requirement led to the design of the barrel primarily using heat sink considerations rather than stiffness considerations.

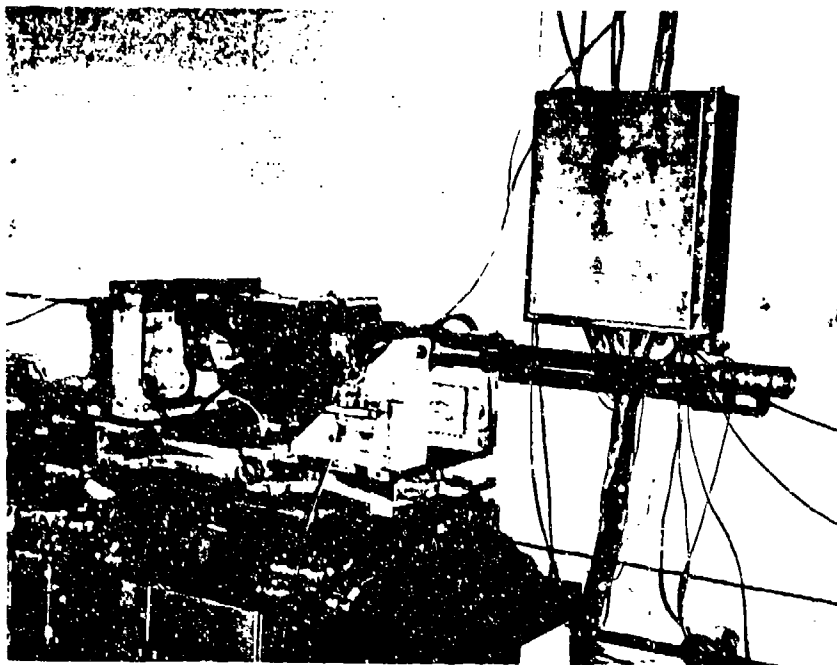


FIGURE 2: XM230, 30MM GUN ON HARD MOUNT

Since the LHX will be approximately half the gross weight of the Apache, the number of rounds it can carry will be limited to significantly less than the Apache, and burst length requirements will be nearly an order of magnitude less than for the Apache. Conventional design of a new barrel, based primarily on stiffness, will produce considerable weight savings for a new lightweight XM230. This program, therefore, concentrated its study on the remainder of the XM230 gun.

The procedure for this program was to examine the XM230 gun mechanism for candidates for weight reduction. Photoelastic coating was then applied to these components to determine areas of low stress. These areas are now being analyzed in further detail and, where easily possible, parts will be redesigned or material will be removed. After weight reduction of components, photoelastic coating will again be applied to the gun and measurements will be repeated to assure that unexpected high stress areas are not generated in any of the modified gun components.

As mentioned above, the XM230 was analyzed without the barrel. Weight of the XM230 receiver and feeder used in this program is 85.75 lbs. Initial analysis of the gun indicates a possible weight reduction of 11 lbs or 13%. Based on this analysis, photoelastic coating was applied to four gun components. Two external components and two internal components were chosen because they would be most significant in total weight reduction. The table below lists the parts coated:

TABLE 1

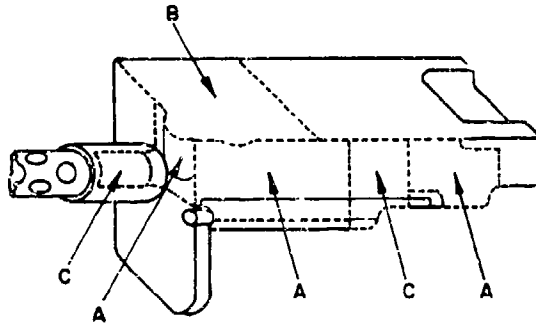
Gun Parts Coated with Photoelastic Coating

| | |
|---------------------|----------|
| 1. Receiver | External |
| 2. Feeder Housing | External |
| 3. Feeder Sprocket | Internal |
| 4. Rear Round Guide | Internal |

The gun receiver, of course, was the largest component analyzed. Three separate mixes of photoelastic material were used to cover the areas of interest. A map of these three coatings on the receiver of the XM230 is shown in figure 3. A calibration strip was included in the pouring for each individual section to insure uniformity of the coating, and this was confirmed. Calibration constants for the three separate coatings varied by less than 4 percent. The actual photoelastic coating on the receiver of the XM230 gun is shown in figure 4. (Figs. 3 & 4 on following pg.)

The thickness of the coating used on the gun parts was from 0.080 inches to 0.100 inches. This thickness is necessary because of the low strain levels typical in gun components due to design safety considerations. The sensitivity of the coating is proportional to its thickness and for this program provided a sensitivity of 1500 $\mu\epsilon$ to 1150 $\mu\epsilon$ per fringe. To accurately measure strain magnitudes by matching dominate isochromatic fringe colors for analysis of photographs or film, a minimum of 0.6 fringes

PHOTOELASTIC COATING
APPLICATION MAP



XM230 RECEIVER

FIGURE 3: COATING MAP FOR XM230 GUN

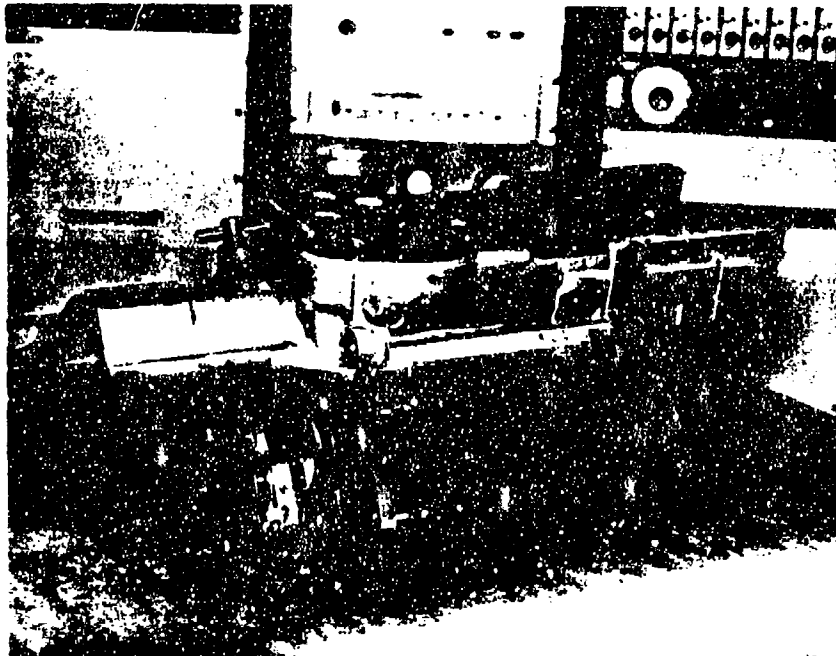


FIGURE 4: COATING APPLIED TO THE XM230 GUN

must be seen through the analyzer. This indicated a minimum of $700 \mu\epsilon$ had to be present in the components measured. The strain directions could be measured for much lower levels of excitation, since the isoclinic lines were visible at lower strain excitations.

The thickness of the photoelastic coating, however, does provide a trade-off in frequency response of the material. Wave propagation across the coating is directly proportional to the coating thickness. Therefore, the frequency response of the coating is inversely proportional to twice the thickness when using a reflective polariscope. With a coating thickness of 0.1 inch, frequency response is on the order of 40 KHz. This was considered adequate since the maximum peak pressure of a round of ammunition was achieved over 1 msec. Therefore, it is expected this coating would accurately transmit all peak strains during gun firing.

4. STATIC TESTING

Testing of gun components was performed both statically and dynamically. The internal gun components could, of course, only be tested statically since they could not be viewed during gun operation by the polariscope. Also, strains in the external components, the receiver and the feeder housing, were viewed with static loading of the gun at the approximate stall torque of the gun drive motor.

A vertical shaft that connected to the drive strain of the gun was loaded with a torque wrench to 88.8 in-lbs. At the same time, the feeder sprocket was restrained from moving, simulating a feed system jam. The polariscope was then used to view the strain patterns in the receiver and feeder housing. The set-up of the polariscope viewing the feeder housing is shown in figure 5.



FIGURE 5: POLARISCOPE VIEWING XM230 FEEDER HOUSING

No significant strain levels were recorded during this testing, indicating system design was either primarily based on gun firing loads, or was very conservative.

The two gun internal components examined were removed from the gun for testing and fixtures were designed to apply static loads to these components. Only testing of the feeder sprocket will be described here. The feeder sprocket is used in the XM230 gun to accept rounds from a feeder transfer housing and hand them off to an indexing sprocket for the bolt carrier. Only one round at a time is handled by the feeder sprocket and it is constant rotation during operation of the gun motor. Figure 6 shows one set of the fingers of the feeder sprocket used for handling the rounds. Photoelastic coating can be seen on one of the fingers of the sprocket.

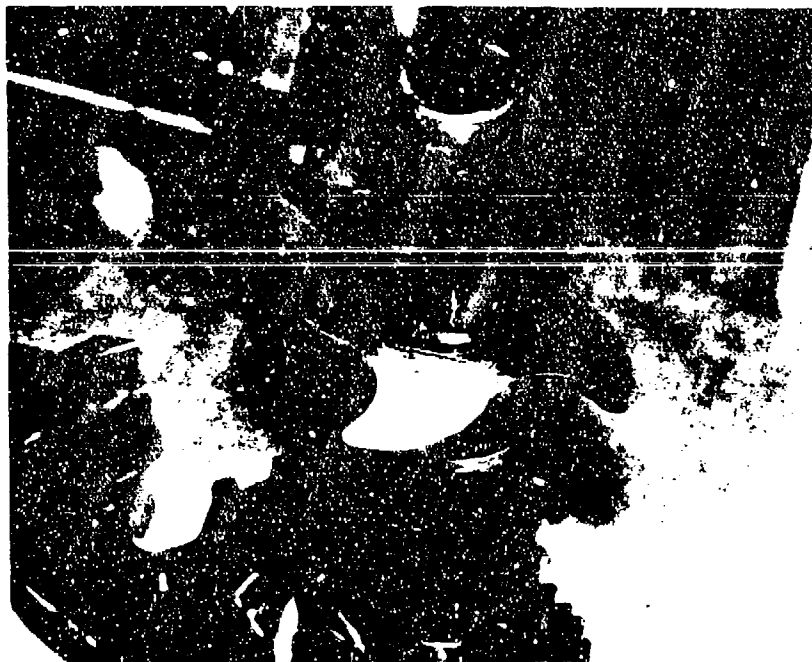


FIGURE 6: FEEDER SPROCKET COATING

A fixture was designed to apply the equivalent of 457 in-lbs of torque to a simulated round sitting in the feeder sprocket finger. Isoclinic lines with this load applied were plotted. The isostatic strain lines for compression and tension were then plotted and are shown in figures 7 and 8 on the following page.

**FEEDER SPROCKET ISOSTATIC LINES
(COMPRESSION)**

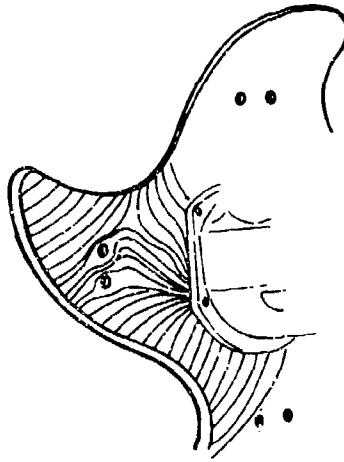


FIGURE 7: PRINCIPAL STRAIN IN COMPRESSION

**FEEDER SPROCKET ISOSTATIC LINES
(TENSION)**

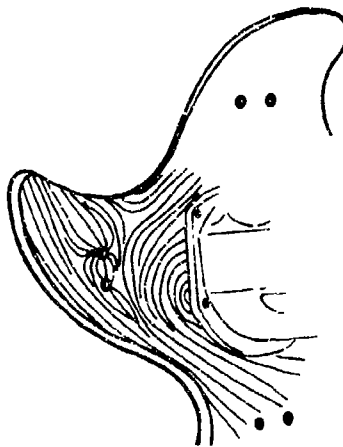


FIGURE 8: PRINCIPAL STRAIN IN TENSION

The point of load application can be seen in figure 7 as slightly to the right of the safety wire holes in the feeder sprocket finger and in the curved section where the round fits in the finger. The maximum strain occurred at the sprocket shaft almost directly to the right of the lower safety wire hole where the compression lines in figure 7 concentrate. The maximum strain measured at that point was 1080 $\mu\epsilon$.

Data obtained during this testing will now be compared to a finite element analysis of gun components. The math model will provide both magnitude and direction of component principal strains. Measurements taken to date are being used to emphasize areas of modeling concentration and to define grid size areas. Results of this effort are not yet available.

From the initial static results, however, areas of weight saving are being identified. For instance, the feeder sprocket fingers have no appreciable strain levels in their central region and it is reasonable to remove material from this area with one or more holes. The size and shape of the weight reduction holes will be determined upon completion of the math model. These holes will then be inserted in the feeder sprocket and strain measurements will be repeated to insure no unexpected stress concentrations arise.

5. DYNAMIC TESTING

Dynamic testing of the XM230 gun is being performed by taking high speed photographs of the photoelastic coating during gun firing. A test set-up with a high speed camera viewing the top of the receiver through the analyzer of the polariscope is shown in figure 9 on the following page.

This set-up only allowed camera speeds of 500 frames/sec due to the limited light level provided by the polariscope. With a modified light fixture, rates have been increased to 1000 frames/sec. A totally new light fixture is being designed that will allow rates of 2000 frames/sec to be shot in the near future.

At most, three round bursts have been used during photography to insure that heating of the gun does not affect the measurements. During firing a maximum of 3 to 4 pictures of measurable strain are seen in the receiver during the round pressure pulse. A maximum strain level of 1060 $\mu\epsilon$ was measured along the left hand side of the receiver and transmission of the load along the receiver can be seen. Results, however, are not consistent from round to round since camera speed has not been high enough. It is expected this problem will be resolved as camera speed is increased to 2000 frames/sec.

The initial high speed photographs, however, have confirmed expected loading paths for the receiver and identified the areas of highest and lowest strain. Measurements at higher camera speeds will be taken before any weight reduction is started on the receiver.



FIGURE 9: HIGH SPEED CAMERA WITH POLARISCOPE

6. SUMMARY

The program to date has shown that photoelasticity is a viable tool for measuring strains in gun components, both statically and dynamically. A chief advantage of this technique is that it provides the full field strain pattern so that actual loading paths and stress concentrations can be quickly and easily identified. Used in conjunction with a finite element model of components, it can quickly verify the model and lead to suggested areas of weight savings. It is expected that weight savings suggested by the measurements on the XM230 will be implemented on selected gun components and confirmatory measurements on the modified components will be completed by the end of 1985.

7. REFERENCE:

1. Zandman, F.; Redner, S; and Dolly, J. W.; "PHOTOELASTIC COATINGS," Iowa State University Press, Ames, IA, 1977

TITLE: In-Bore Projectile Motion in a 37-mm Weapon System
SUSAN A. COATES
JAMES N. WALBERT, Ph.D.
U.S. Army Ballistic Research Laboratory
Aberdeen Proving Ground, Maryland 21005-5066

ABSTRACT:

At the Third U.S. Army Symposium on Gun Dynamics, a technique was reported which showed potential for the analysis of in-bore projectile motion. Since that time, the analytical techniques have been fully developed and have been used extensively as both research and engineering tools in the assessment of projectile behavior.

In this paper, we present the results of a series of experiments involving 37-mm projectiles. A complete description of the instrumentation and test fixture is given, as well as a detailed description of the analysis algorithms. Examples of balloting and non-balloting projectiles are given, and techniques for extracting such information as spin and yaw are discussed. Examples of anomalous in-bore behavior are presented to illustrate the investigative capabilities of the techniques.

BIOGRAPHY:

PRESENT ASSIGNMENT: Mathematician, U.S. Army Ballistic Research Laboratory, Aberdeen Proving Ground, Maryland.

DEGREES HELD: B.A., Susquehanna University, 1963.

IN-BORE PROJECTILE MOTION IN A 37-mm WEAPON SYSTEM

SUSAN A COATES*
JAMES N. WALBERT, Ph.D.
U.S. Army Ballistic Research Laboratory
Aberdeen Proving Ground, Maryland 21005-5066

1. Introduction

The importance of measuring the in-bore and launch motion of projectiles has long been recognized as being vital to the analysis of weapon performance and design. Historically, there have been numerous types of instrumentation and analysis techniques used to monitor in-bore projectile motion, with varying degrees of success. The two most frequently used methods are optical and microwave interferometry. Each method has its own particular problems, many of which are due to the presence of precursor shock and ionized gases. Optical techniques generally require modification of the projectile in order to provide a precision reflective surface. This is generally undesirable, not only from cost considerations, but also in view of the desire to conduct experiments under the most realistic ballistic conditions possible. While projectile modification may enhance the data taken from microwave radar, it is not necessary. Thus, if radar can be used, it allows study of projectile motion under realistic conditions.

It is the "if" of the previous sentence which this paper will address. There are two methods of analyzing a radar doppler signal: frequency analysis and wavelength analysis. Specifically, each cycle in the doppler corresponds to a target travel of a radial distance of one-half the transmitted wavelength. The wavelength analysis method thus provides a direct measure of the travel of a particular scattering surface on the projectile. Frequency analysis, on the other hand, determines velocity, utilizing the fundamental relationship

$$\rho = \frac{CF}{2f_t - F} \quad (1)$$

where ρ is the projectile velocity with respect to the radar (radial velocity), C is the velocity of light in the transmission medium, F is the doppler frequency, and f_t is the microwave transmission frequency. Reference 1 provides a complete derivation of this result, as well as a detailed discussion of its application to free-flight projectile motion analysis.

Under conditions of low acceleration, (i.e. slowly varying velocity) both methods work very well, although the wavelength analysis is somewhat tedious and may in fact reveal less information [1]. Eq. (1) is valid only if C , F , and f_t remain constant during the period of observation. For this reason, frequency analysis techniques have not been applied to in-bore doppler data, where high accelerations violate the assumptions of eq. (1). In this paper, techniques are presented which allow frequency analysis in this in-bore region. It is shown, moreover, that much new and valuable information about the in-bore motion can be determined in this manner.

2. Algorithms for Frequency Analysis

From a mathematical viewpoint, there are two problems with in-bore doppler data. First, the event timespan is too short, and second, the desired frequency resolution is too low. Those readers familiar with Fourier analysis realize that these two problems are really two aspects of the same limitation: frequency resolution increases with observation time, for a fixed data bandwidth. For example, if there are 20 data points available covering a bandwidth of 100 Hertz, then the Fourier spectrum will contain 10 points. This implies that two frequencies in the data must be separated by at least 20 Hertz to be distinguished from one another. If, on the other hand, the event is observed for twice as long, resulting in 40 data points, the resulting spectrum can distinguish frequencies separated by at least 10 Hertz.

For analysis of stationary time series, that is, ones with little or no variation in frequency content, there are several options available for increasing the frequency resolution. The simplest of those is to observe the event for a longer time period. The assumption that the frequency content is stationary ensures that longer observation times will not result in a smearing of the Fourier spectrum. In the interior ballistic regime, the doppler signal from a moving projectile is highly nonstationary; longer observation time is not possible. The usual technique for analyzing the frequency content of nonstationary time series is to divide the series into parts, or windows, during each of which the series is more nearly stationary. Of course, since each of these windows is of shorter time duration than the entire series, the corresponding frequency resolution is not as good.

The first method to be presented for increasing spectral resolution is the well-known zero-fill (ZF) technique. Implementation of ZF can be accomplished quite simply. One decides how long a data segment would be necessary for the desired resolution. Let $K > L$ denote this value. The actual data segment of length L is then expanded to include $K-L$ zeros, at the beginning or the end of the original segment. One could also append $(K-L)/2$ zeros to each end of the original data segment. When the ZF technique is used, the spectral window should be applied to the original data segment, not to the zero-filled one. In this way, the position of the zeros has no effect on the resulting spectrum.

The second technique for increased Fourier resolution will be termed the periodic continuation (PC) method. This is a modification of a technique used in some electronic frequency analyzers for so-called transient analysis [2]. In this method, the transient is captured in the memory of the analyzer and is then artificially repeated in memory a prescribed number of times. The resulting time series is transformed as though the transient event had occurred periodically. There are some important caveats to be noted concerning this method. If the original transient record does not begin and end at the zero level, the repetition introduces jump discontinuities. These may result in the introduction of low frequency content into the data, as well as causing leakage into side lobes of true spectral peaks. For the true transient, this generally poses no problem, since the event is of such short duration that it is analyzed in its entirety. Moreover, the transient is generally windowed in the frequency analyzer prior to being repeated, further reducing the problem.

3. Detailed Application Examples

There are two purposes for this section. The first is to demonstrate the utility of the algorithms developed in the previous section. The second purpose is perhaps the most important one: to indicate the techniques of radar data analysis. In the course of reviewing these examples, the reader will note the necessity of having a number of interactive computer routines for plotting, filtering, and other processes to aid in the interpretation of the results. The success of the algorithms in the analysis process depends heavily on the judgement and experience of the analyst. For this reason, none of the procedures described in this section should be considered as routine, nor should the examples presented be considered to be exhaustive of all possibilities.

The first example is intended to show the motivation for development of the algorithms. Figure 1 shows a plot of the doppler signal (direct recording) from the in-bore and very early free flight of a 37-mm projectile. Figure 2 shows the waterfall plot of the Fourier spectra computed from adjacent, nonoverlapping data segments of 1024 points each. No attempt has been made to enhance the frequency resolution of these spectra. The amount of information provided by this plot is clearly minimal; 16 data points is not a sufficient number to provide good definition of the trajectory.

More data points are obtained by overlapping the segments to be transformed. Figure 3 shows a waterfall spectrum plot of the same data, again using 1024-point transforms but overlapping them so that each transform is computed from the last 768 points of the previous transformed segment and the next 256 points of raw data. In this way, several features of the trajectory are discernable. One notes the apparent frequency shift at muzzle exit, marking the transition from waveguide to free space wavelength. Also visible is the doppler return from the ionized gases at muzzle exit, seen as the irregular peaks to the left of the projectile return. A great deal of irregularity in the progression of spectral peaks is noted, demonstrating the need for additional analysis. The most important feature of this plot, though, is the fact that in numerous instances, there is no change in the

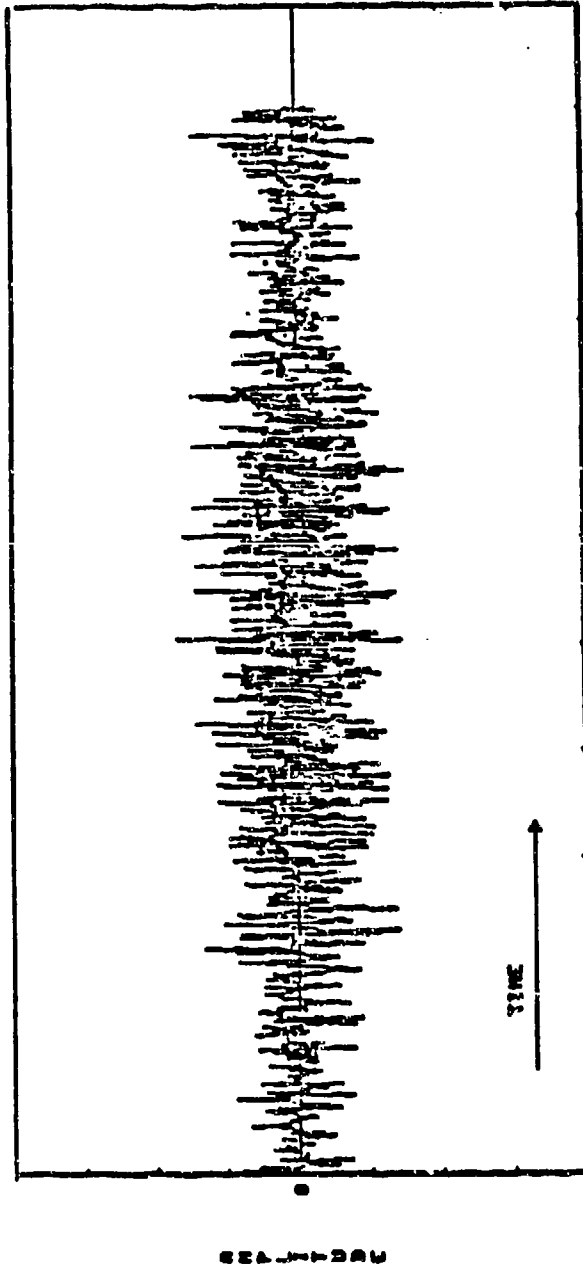


Figure 1. Raw Doppler Signal

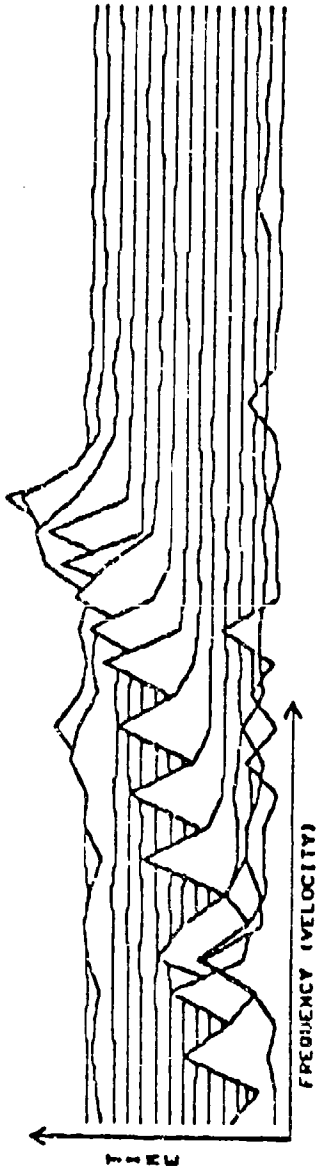


Figure 2. Waterfall Spectral Plot, No Overlap

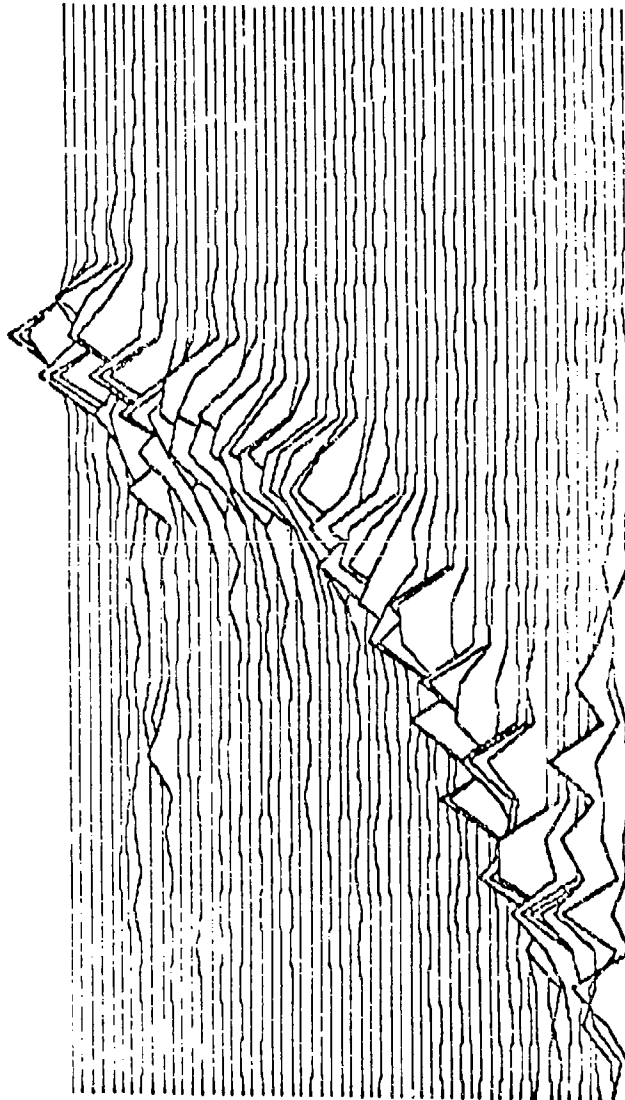


Figure 3. Waterfall Spectral Plot, Overlap 4

COATES, WALBERT

location of the spectral peak from one spectrum to the next. This is not an indication that the projectile velocity remained constant over the corresponding time interval, but rather that the velocity change was too small to be detected by the resolution of the transform. Using a higher-order overlap will provide no additional information about the trajectory unless the frequency resolution of the transform is also increased.

Figure 4 shows the waterfall plot of the same data with the same overlap (4), but with frequency resolution increased by a factor of 16 via the ZF method. That is, 15360 zeros are appended to each 1024-point data segment prior to transforming. The resolution is now sufficient to show smooth transition of the spectral peaks, and good definition of the transition to free-space wavelength. The most striking feature of the plot is the appearance of a second set of peaks just to the left of the main return. In order to view these peaks better, Figure 5 shows the plot of Figure 4 at the bottom and its mirror image at the top. One notes in the upper plot that the "second set" of peaks seems to have a sinusoidal variation in both amplitude and location. This variation is not well defined, which suggests that its appearance is "aliased" by not having a sufficient number of samples (transforms) to properly define it.

Consequently, the next step is to increase the overlap factor to 16. That is, each transform segment contains 960 data points from the previous segment and 64 new points. To these 1024 points are appended 15360 zeros. The result is the waterfall spectral plot of Figure 6. This plot shows quite clearly the progression of both "sets" of peaks. It reveals a sinusoidal variation of the frequency of each set, and a sinusoidal variation in the amplitude of the second set relative to the first. At this point it would be appropriate to mention that up to now all waterfall spectral plots were made with each spectrum being normalized to its own peak, independent of the other spectra. The advantage here is twofold. First, the peaks remain clearly visible even in regions of diminished signal amplitude. Second, any variations in the progression of spectral peaks such as those shown in Figure 6 are due solely to changes in frequency, and not amplitude. If the spectra were all normalized to the same value, signal amplitude variation would result in a plot of similar appearance, even though the peak frequency might be increasing quite smoothly. Not all is well however. There are times when waterfall plots with independent spectral normalization can be misleading.

At any rate, the variation in the progression of the main peaks in Figure 6 is due a variation in the main doppler frequency. Several features of the data are now quite well defined. Figure 7 shows the region of muzzle exit, with lines indicating the waveguide and free space frequencies. The difference between the two is almost exactly that predicted from the equations in reference 3. The secondary set of peaks disappears near muzzle exit. The indications are that these peaks are visible due to the presence of the waveguide (gun tube). These peaks are not artifacts of the radar/gun geometry, since they do not occur in every record. The most logical assumption is that a change in the aspect angle of the projectile with respect to the radar forces energy into the lower modes of propagation in the waveguide.

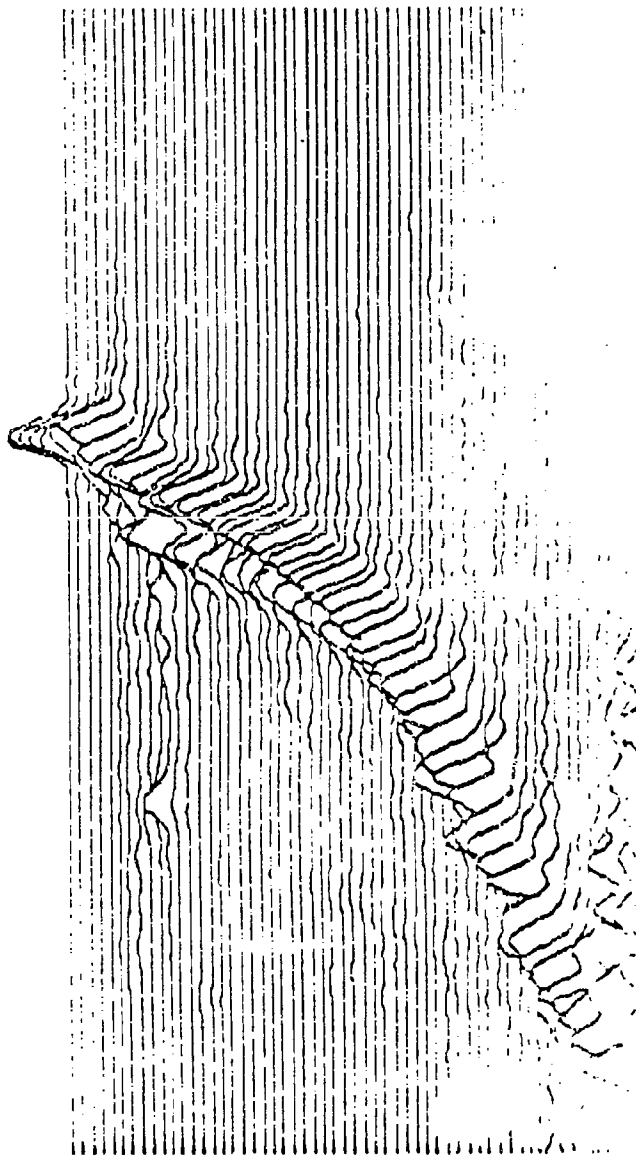


Figure 4. Waterfall Spectral Plot, Zero Fill, Overlap 4

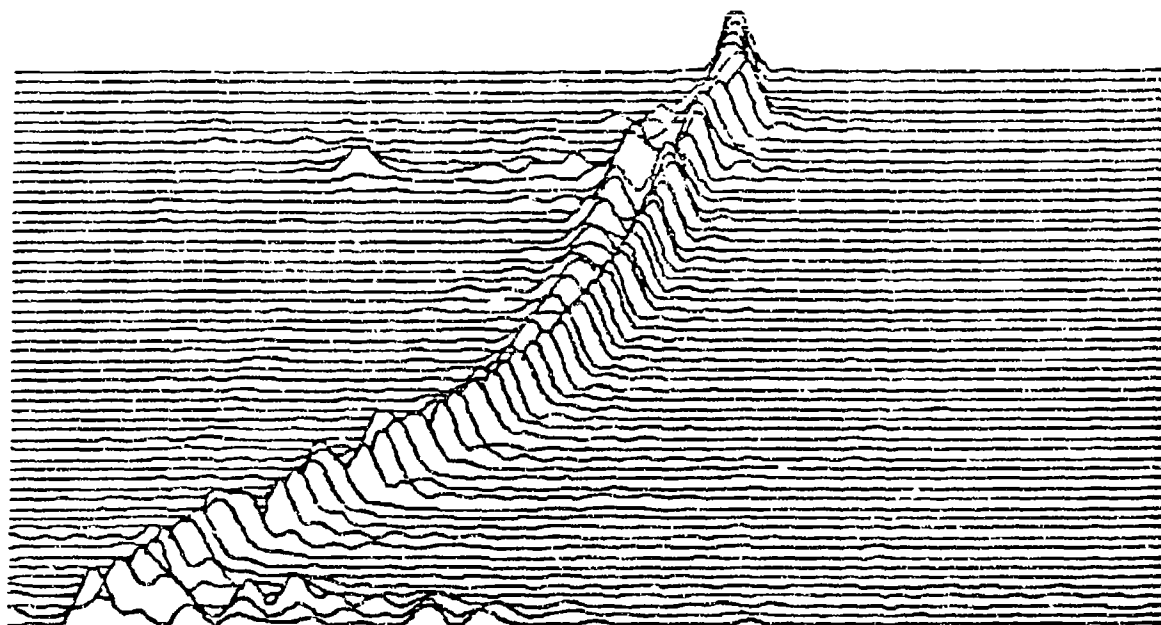
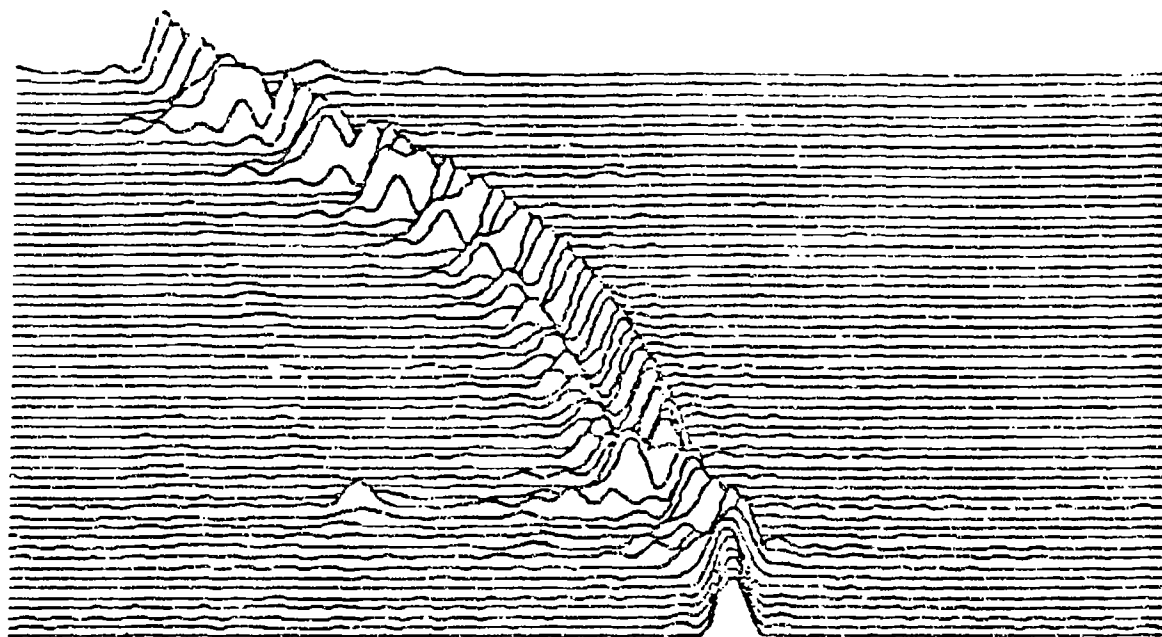


Figure 5. Plot of Figure 4 with Mirror Image

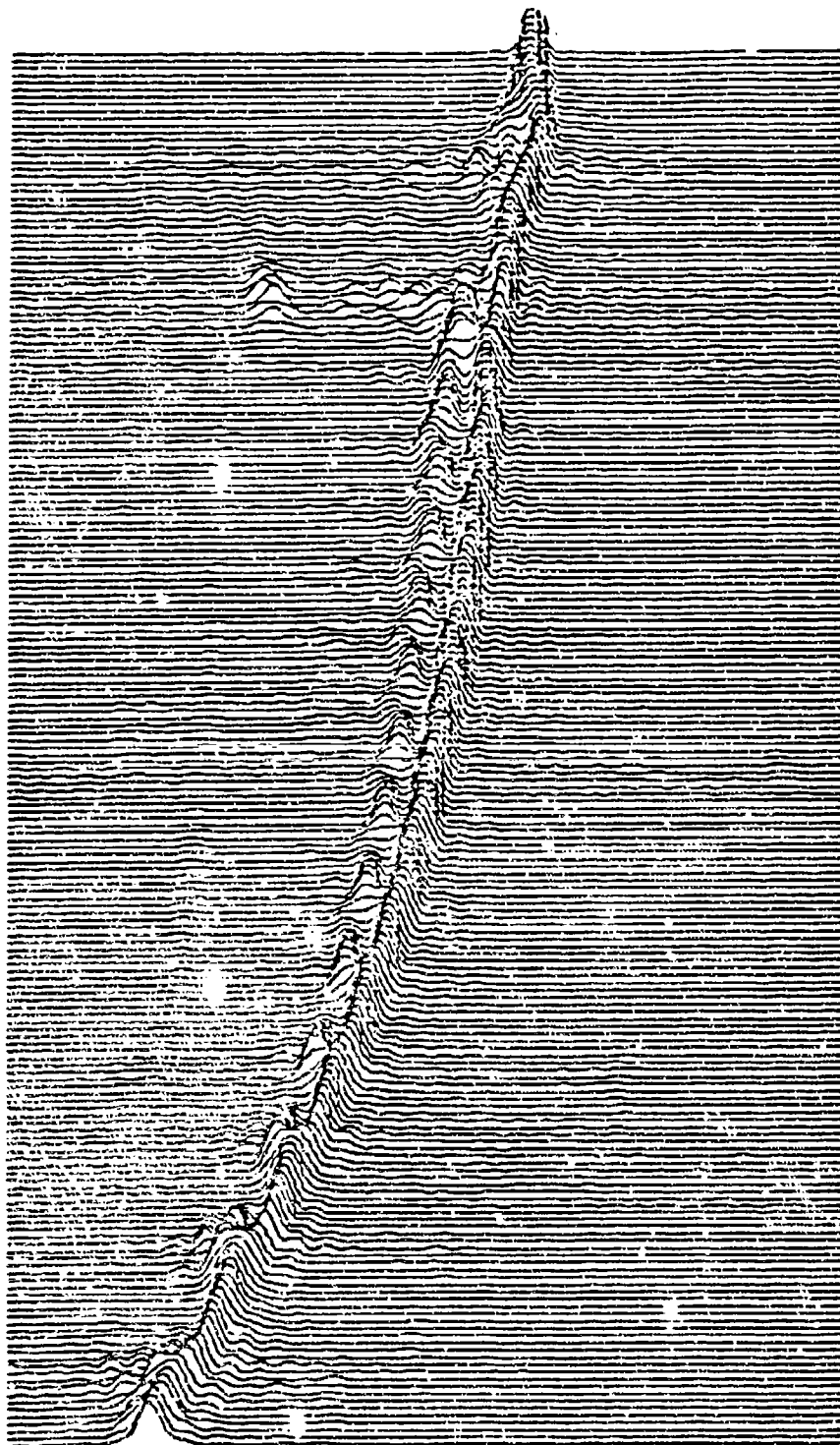


Figure 6. Waterfall Spectral Plot, Zero Fill, Overlap 16

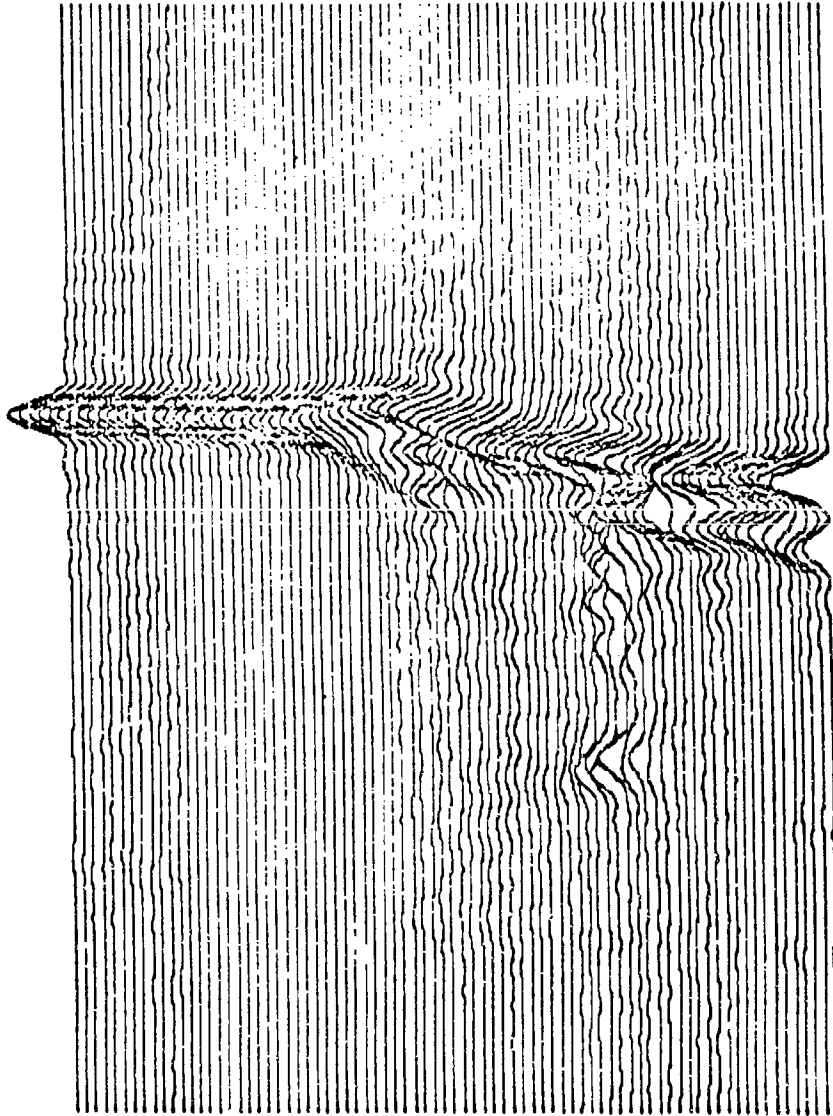


Figure 7. Detail of Region of Muzzle Exit From Figure 6

COATES, WALBERT

In fact, when the PC method is applied to this same data, as shown in Figure 8, at least two sets of secondary peaks are revealed. It appears that several lower propagation modes have been excited. The PC plot also reveals some sinusoidal frequency variation in the early free flight region. These variations are the result of the gyroscopic motion of the projectile as it enters the influence of the free-air boundary conditions. It should be emphasized that these variations cannot be related directly to velocity. In fact, it is readily apparent from comparison of Figures 6 and 8 that the amplitude of the frequency variation is somewhat dependent on the resolution of the spectra.

The radar data of the preceeding figures were from a relatively short (2-inch) projectile. The next example is from a 4-inch 37-mm projectile. One would expect this longer projectile to be more stable in-bore. The data in this example were sampled at half the rate of the previous data, so overlap 16 produces only half as many spectra. Figure 9 is a plot of the data from this long projectile. There is a marked difference in the appearance of this plot as compared to that of Figure 6. There are no secondary peaks, and the progression of the main peaks is quite smooth. Even though there are only half as many spectra as in the previous example, it is clear that no large sinusoidal variation of peaks exists in this record. It also appears that the transition to free flight is much smoother (compare Figure 7).

Figure 10 is a plot of the PC spectra of this same data. Even with the very narrow peaks produced by this method, there is no evidence of any secondary peaks. There are sidelobes, evenly spaced on either side of the main peak in each spectrum, which are artifacts of the mathematics. Their distance from the main peak is a constant for all of the spectra, which distinguishes them from the peaks noted in the previous example. There is some noticeable frequency variation after muzzle exit, again due to gyroscopic motion in free space. This variation was not readily discernable from the ZF spectra, although it is present.

The series of vertically-aligned peaks at the bottom of this plot are caused by the recording electronics. These peaks fade from view due to the normalization process as soon as the doppler from the projectile has sufficient amplitude. The data in all of these examples were processed from direct-recorded channels. While there is fairly good definition of the in-bore trajectory from about 150 ft/sec. of velocity on, there is no shot-start data.

Figure 11 is a plot of the same data with all 3 channels used. The start of motion is now clearly incorporated into the data, providing a complete record of the in-bore and early free-flight portion of the projectile trajectory. It should be noted that the channel alignment is most easily accomplished by spectral alignment, rather than by timing alignment. The reason is that each of the 3 channels passes through a different set of electronics during recording, giving it a different (and unknown or difficult to measure) phase delay from the other 2 channels. Since the doppler frequency from the projectile at a given instant is recorded in all 3 channels, their respective spectral peaks will be in the same location.

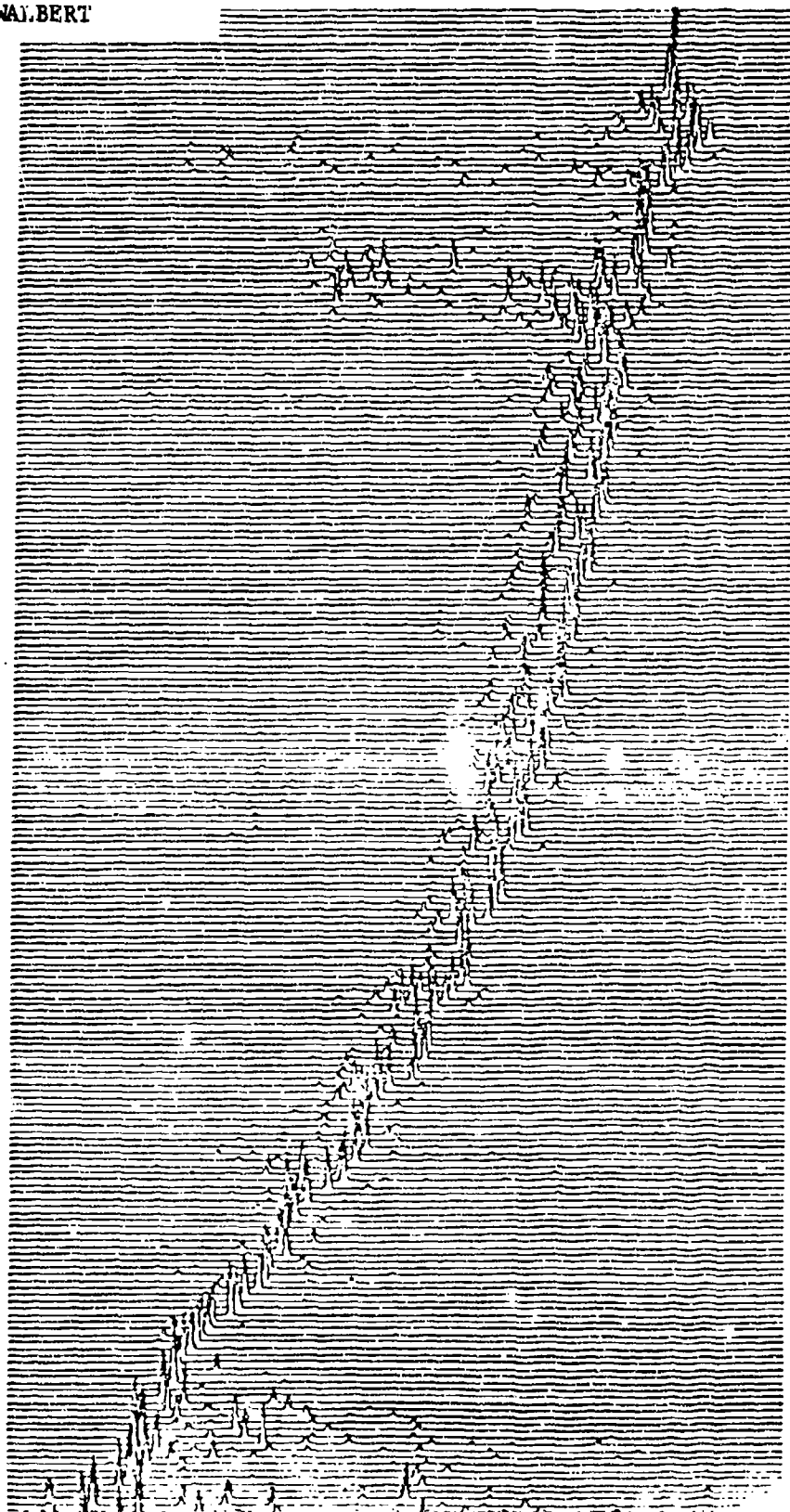


Figure 8. Waterfall Spectral Plot, Periodic Continuation, Overlap 16

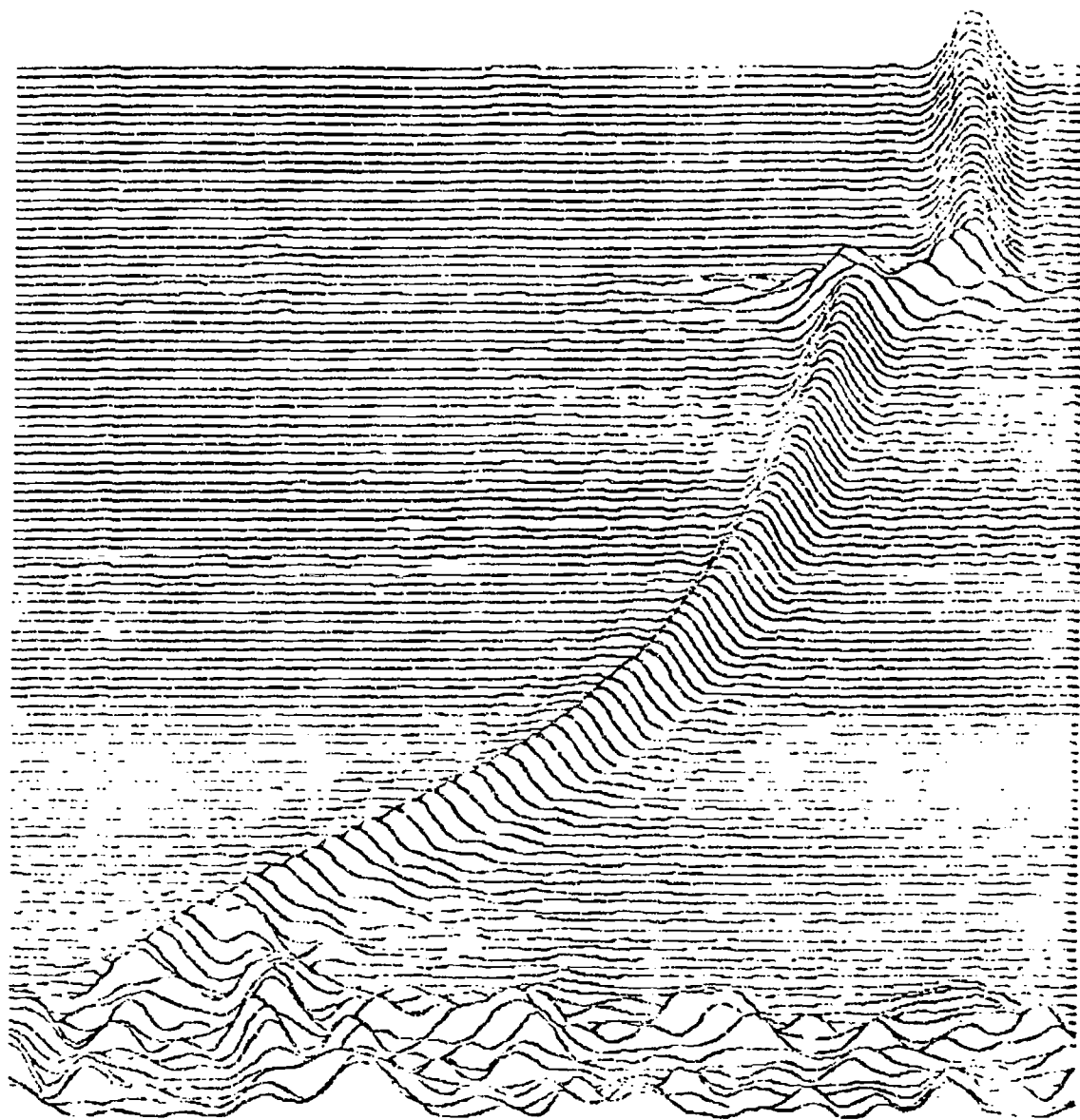


Figure 9. Waterfall Spectral Plot, Zero Fill, Overlap 16.
(Long Projectile)

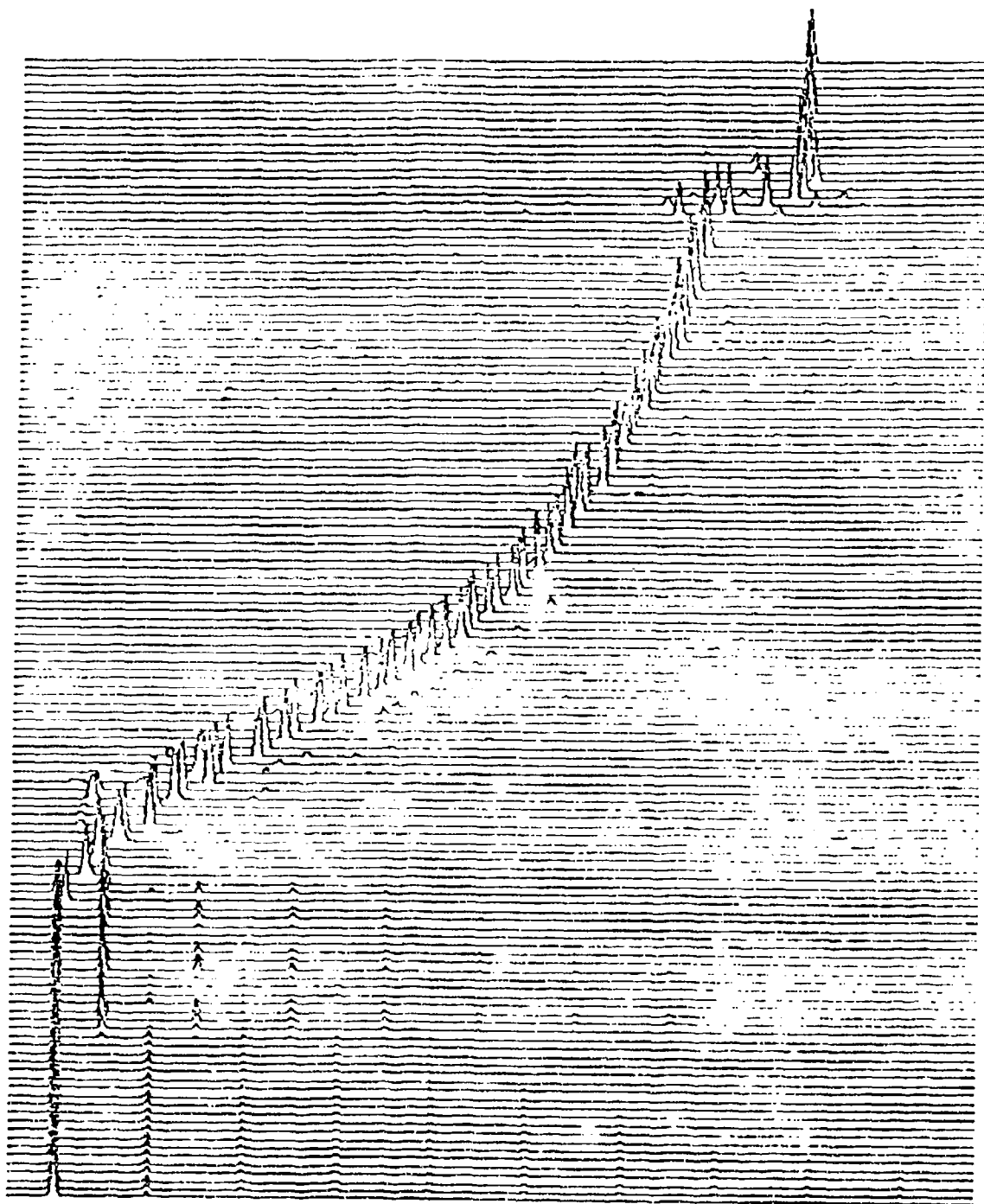


Figure 10. Waterfall Spectral Plot, Periodic Continuation, Overlap 16.
(Long Projectile)

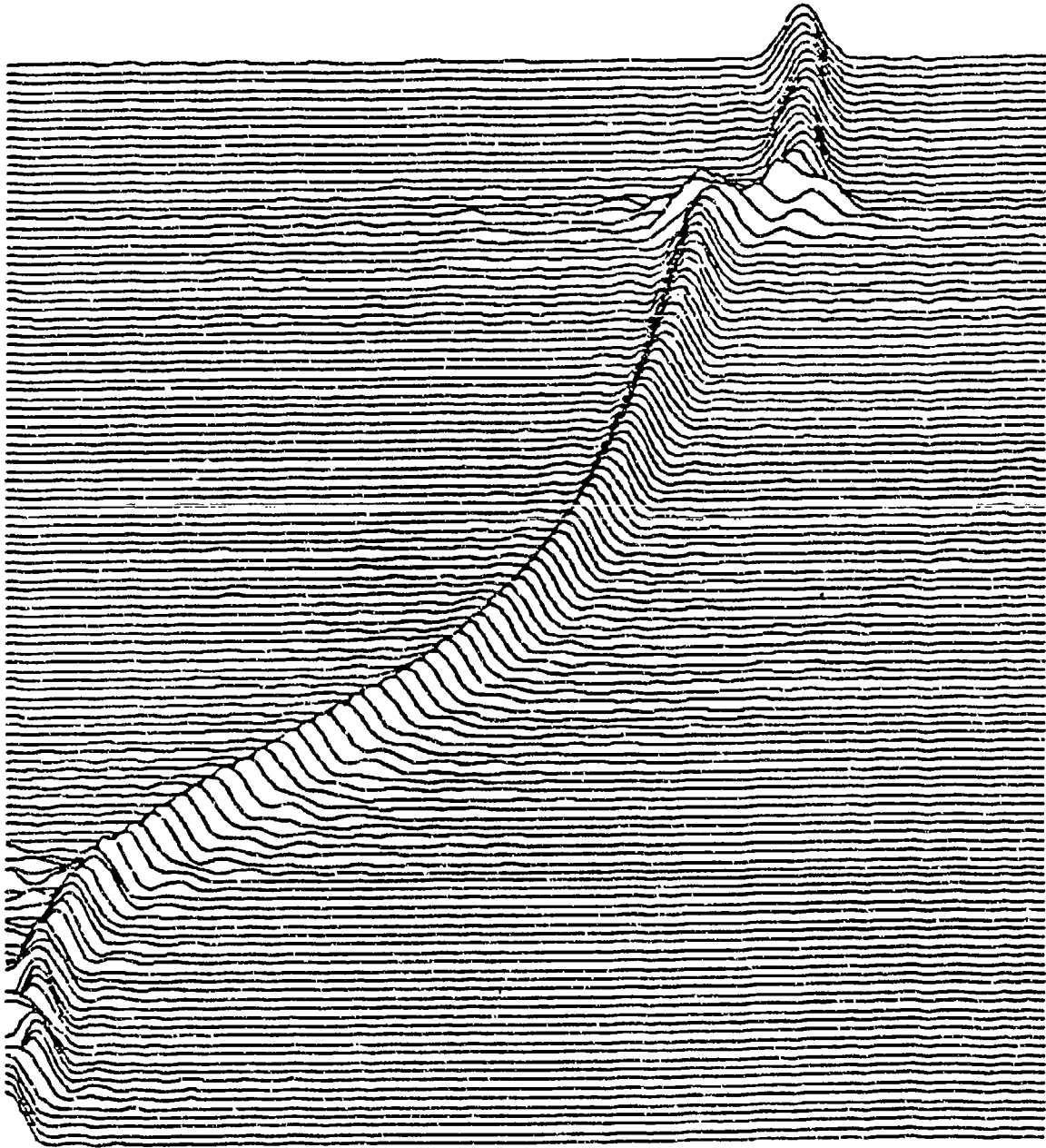


Figure 11. Waterfall Spectral Plot, Zero Fill, Overlap 16, 3 Channels Combined

COATES, WALBERT

Alignment is then simply a matter of positioning the 3 resulting waterfall spectra so the peaks at the end of one plot are aligned with those at the beginning of the next plot.

If the peak frequency of each spectrum from this data is plotted vs. time, as in Figure 12, the basic features are clearly visible. The transition to free-space wavelength is clearly defined, as is the sinusoidal frequency variation after muzzle exit. There are some sinusoidal variations visible early in the in-bore trajectory, which may indicate some initial balloting motion of the projectile. One very interesting feature of this data is the apparent return to zero frequency (velocity) after start of motion. This feature deserves more detailed discussion.

The first point to be made is that there is no doppler shift from a stationary object. The best that can be said about this "return to zero frequency" is that the doppler frequency was lower than could be detected by the analysis; in this example, less than about 11 Hz. Thus, the projectile slowed abruptly at this point, and then speeded up rapidly; it may or may not have stopped. In terms of the analysis process, the zero frequency indicates that during that particular data window, the doppler frequency was less than the resolution of the transform.

This preliminary movement may have been by the projectile alone, or by the projectile and gun as a rigid-body combination caused by hammer impact on the primer. If one assumes that the motion was of the projectile alone, an integration of this data after conversion to velocity shows a travel of 0.2 inches up to the "slowdown." This distance is commensurate with the estimated projectile "free run" up to the origin of rifling. The integral of the remainder of the data up to the muzzle exit point, with corrections made for projectile length, agrees in travel distance to within 0.5 inches of the measurement cited in the gun tube stargage report. Full details of this investigation will appear in another report [4]. It suffices to say here that this sudden change in acceleration could be of concern for fuzed or cargo-carrying projectiles.

As a final example, detailed frequency spectra from the early free flight portion of the trajectory of some 37mm projectiles will be presented. Figure 13 is an expanded version of the muzzle exit and free-flight portion of Figure 8. The rapidly-decaying sinusoidal motion is typical of the data analyzed by the authors. The transition to free flight from the constraints of the gun tube appears to be characterized by this adjustment of the projectile to its new boundary conditions. It is also during this time that the muzzle blast is enveloping the projectile. The resulting changes in air density have an effect on the apparent radar wavelength, making analysis in this region quite difficult. One goal of such analysis is the determination of the release mechanism between projectile and gun tube, and the subsequent effect on weapon system accuracy.

While it is difficult to assess which portion of this variation in doppler is due to atmospheric conditions and which portion is due to actual projectile motion, it is the opinion of the authors that atmospheric effect on the radar wavelength would manifest itself as an exponential change, rather

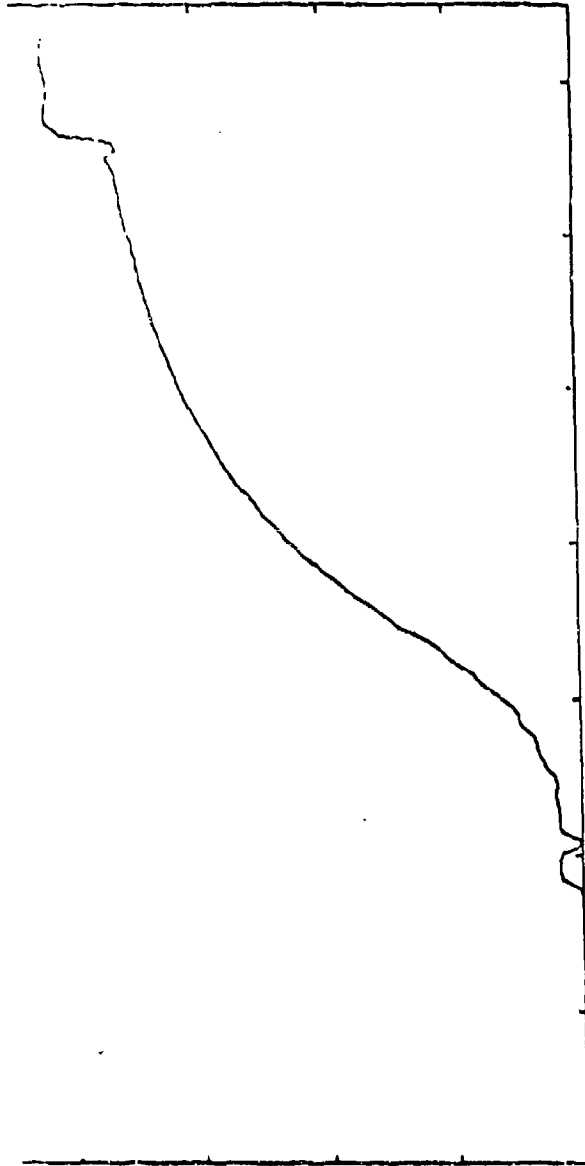


Figure 12. Frequency Profile from the Data of Figure 11

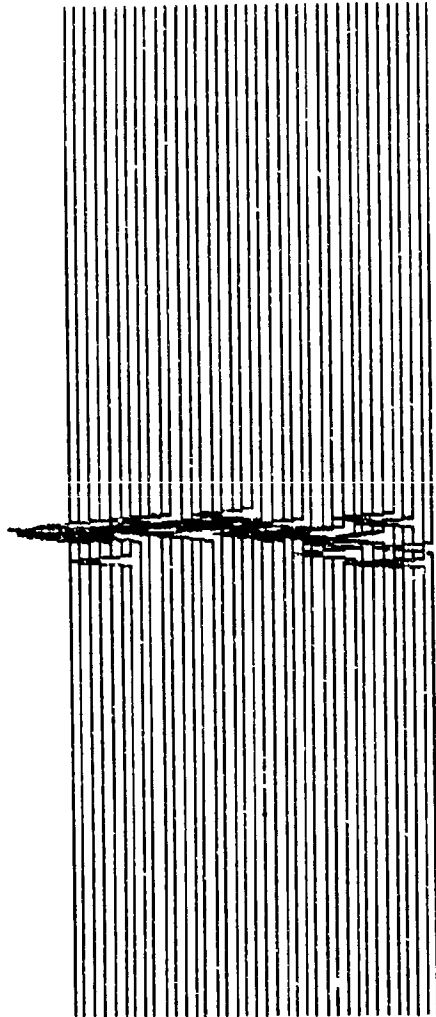


Figure 13. Detail of Region of Muzzle Exit from Figure 8

COATES, WALBERT

than a sinusoidal one. The reasoning is, simply, that the blast is an expanding sphere. As the radius of the sphere increases monotonically, the density within the sphere decreases monotonically. Sinusoidal variations in the density would require an alternating expansion and contraction of the sphere: an unlikely phenomenon. Therefore, with some correction for wavelength, the sinusoidal variation of the doppler in Figure 13 is due to a corresponding projectile motion. This motion has been observed by the authors in projectiles ranging in diameter from 37mm to 90mm, and is the subject of continuing research.

REFERENCES:

1. J.N. Walbert, "Fourier and Numerical Methods for the Derivation of Trajectory Data from Doppler Radar, "TECOM report APG-MF-5289, September 1979.
2. R.B. Randall, Frequency Analysis, Bruel and Kjaer, Denmark, 1977.
3. R.K. Loder, "Sensitivity Analysis of Michelson Type Microwave Interferometry for the Measurement of Projectile In-Bore Motion," Technical Report ARBRL-TR-02386, Ballistic Research Laboratory, January 1982.
4. J.N. Walbert, B.T. Haug, "On the In-Bore and Free Flight Motion of Some 37-mm Projectiles," Ballistic Research Laboratory Technical Report, to be published.

TITLE: The Relationship of Gun Dynamics to Accuracy in a 120-mm Tank Gun
JAMES N. WALBERT, Ph.D.
U.S. Army Ballistic Research Laboratory
Aberdeen Proving Ground, Maryland 21005-5066

ABSTRACT:

The role of gun tube dynamics in the accuracy of weapon systems has long been acknowledged. Frequently, however, gun dynamics effects have been considered to be small relative to other sources of error or dispersion, and therefore not of particular concern to the program manager or user. As a consequence, it has also been difficult to generate support among the user community for experimental measurements on "as-fielded" systems.

This paper describes the dynamic behavior of the M256 120-mm smooth-bore tank gun and its relationship to accuracy. Details of dynamic muzzle motion are presented, as well as normalized target impact data. A discussion of tube centerline profiles and how mounting and thermal jacketing affects these profiles is also given. Specific correlations between static tube centerline profiles, dynamic behavior and target impacts are presented. Finally, the gun tube/projectile interactions are discussed.

BIOGRAPHY:

PRESENT ASSIGNMENT: Research Mathematician, U.S. Army Ballistic Research Laboratory, Aberdeen Proving Ground, Maryland.

PAST EXPERIENCE: Mathematician, Materiel Testing Directorate, Aberdeen Proving Ground, Maryland (1974-1978).

DEGREES HELD: B.S., Mathematics, 1970; M.S., Mathematics, 1972; Ph.D., Mathematics, 1975, University of Delaware.

*This paper was classified Distribution Limited to US Government Agencies. Only the abstract appears in these Proceedings. Contact the author for further information.

TITLE: A STUDY OF PROJECTILE ACCURACY
Bailey T. Haug
U.S. Army Ballistic Research Laboratory, Aberdeen Proving Ground,
MD 21005-5006

ABSTRACT:

Expressions such as jump have been used to describe accuracy problems that could not be attributed to any known or understood phenomena. A carefully designed test project was developed at BRL to study accuracy effects in an attempt to shed some light on the term accuracy and the parameters that affect it. The long term objective of the program is to develop a comprehensive validated gun dynamics methodology for predicting in-bore and launch parameters insofar as they affect accuracy. The goals of the initial testing were to establish measurement techniques, to initiate a determination as to what measurements should be continued in future tests, to evaluate the relevance of the parameters measured, and the feasibility of making additional measurements.

This presentation will touch on all aspects of the instrumentation and data acquisition; the analysis presented will deal primarily with the results of the microwave measurements. In addition to measuring the tangential projectile velocity, it was desired to measure the spin and transverse projectile motion using the microwave.

BIOGRAPHY:

B.S./MS in Electrical Engineering, Oklahoma State University, Stillwater OK (1972-1973).

PRESENT ASSIGNMENT:

Electronics Engineer, Mechanics and Structures Branch, Interior Ballistics Division, Ballistic Research Laboratory, Aberdeen Proving Ground, MD 21005-5006.

PAST EXPERIENCE:

Ten years experience at the Interior Ballistics Division, BRL, in instrumentation, data acquisition and data analysis. Worked with optical measurement techniques, piezo-electric gauges for measuring pressure and acceleration, microwave interferometers, and strain gauges, performing kinematic evaluations of gun system performance, tube vibration studies and numerous investigations into the performance of gun systems and projectiles.

A STUDY OF PROJECTILE ACCURACY

MR. BAILEY T. HAUG
U.S. ARMY BALLISTIC RESEARCH LABORATORY
ABERDEEN PROVING GROUND, MD 21005-5006

1. INTRODUCTION

Jump has been used to describe accuracy problems that could not be attributed to any known or understood phenomena. As a part of the Ballistic Research Laboratory's (BRL's) Ballistic Technology Program, there is a continuing effort to study accuracy in an attempt to shed some light on accuracy and the parameters that affect it. The long term objective of this program is to develop a comprehensive validated gun dynamics methodology for predicting in-bore and launch force histories to aid in the structural analysis of projectiles and the predicting of final launch parameters insofar as they affect accuracy. The goals of the initial test were to establish measurement techniques, to initiate a determination as to which measurements should be continued in future tests, to evaluate the relevance of the parameters measured, and to determine the feasibility of making additional measurements.

Although this paper will discuss aspects of all the instrumentation and data acquisition involved in the initial testing, the discussion of the analysis of the data will concentrate on the microwave radar measurements, specifically the attempts to measure spin. Muzzleschmidt data¹ and the correlation of the muzzle data with that from the microwave is left to other papers. The initial objective in making microwave measurements was to determine the tangential projectile velocity from shot start to just prior to the impact in the sandbutt at the end of the range. Additionally, it was desired to measure the spin history of the projectile and the transverse projectile motion. With a one-dimensional fixed position radar unit only a qualitative analysis of transverse motion can be made; however, it was hoped that any information obtained could be compared to theoretical predictions of projectile motion to include those developed by F. V. Reno² and L. H. Thomas³.

2. PRELIMINARY PREPARATION

A 37-mm cannon was chosen as the test system because it was available in the laboratory, it could be fired in our indoor ranges, a supply of proof slugs was in our possession, and the tube was an easy size to work with as far as the Muzzleschmidt and the microwave were concerned. Before installing the tube in the range, it was sent to the Material Testing Directorate for star

HAUG

gauging. By star gauging the tube we were able to establish the condition of the tube. With this information, gun wear and build up could be included in the analysis of the microballistics. An extensive analysis of the pattern of the wear and build up was conducted by Dr. Rurik Loder and Mrs. Emma Wineholt.⁴

Additional preparation of the gun tube was done at BRL. Threads were cut on the muzzle to allow the Muzzleschmidt and the muzzle weight to be attached, as shown in Figure 1. The dual four coil Muzzleschmidt, developed by Jimmy Q. Schmidt at BRL, was one of the measurement techniques to be evaluated in this phase of the program. This instrument was designed not only to determine the angle of the projectile at exit, but also the rate of change of this angle.⁵ The muzzle weight added 27.2kg (60 lbs) to the mass of the muzzle. A V-block was designed to support the muzzle to prevent droop. As the program began, the desire was to eliminate some of the parameters that might complicate the analysis. The purpose of this muzzle weight was to restrain the transverse muzzle motion until after projectile exit. The muzzle weight incorporated the Muzzleschmidt assembly and the oscillator box.

To check out the Muzzleschmidt, three different size proof slugs were selected for this test. To improve the profile seen by the muzzle device, the projectiles were modified by machining a square notch on the leading edge of the bourrelet. In addition three V-shaped grooves were cut in the face of the projectiles to emphasize spin in the microwave return. A typical projectile is shown in Figure 2 with the dimensions of concern shown. The projectiles were measured carefully by personnel from Launch and Flight Division, BRL, and the weight, the location of the center of gravity and the linear dimensions were all documented.

In an attempt to check for symmetric engraving and to determine if asymmetric engraving might be a factor in projectile accuracy, a soft recovery system was designed in order to allow a visual inspection of the rotating band of the recovered projectile. It was conceded that it would be impossible to catch a projectile in the distance available without some damage to the projectile and band, but if the velocity could be reduced to a point where the damage on impact in the sand would be minimal then some analysis of the rotating band might be possible. Two 55 gal. drums were adapted to this purpose. With the ends removed and replaced with cellotex, the drums were half filled with a soft clay like material intended to be used to absorb oil spills on concrete floors. The drums were then laid end to end in stands and positioned so that the gun was aimed at the lower half of the barrels. By only filling the barrels halfway, the clay could expand when impacted by the projectile without splitting the barrels.

The 37-mm gun tube was mounted on a Franklin rest which was then bolted to the I-beams in the range with the muzzle just protruding through the blast window. As mentioned before, a 27.2 kg weight was mounted on the muzzle, and this weight included the Muzzleschmidt. The extra weight of the muzzle required a V-block support to prevent excessive droop. This V-block was placed in the blast window. The primers used were mechanical, and it was decided to use the lanyard to fire the gun rather than to attempt to arrange some solenoid firing mechanism and risk electrical interference on the data

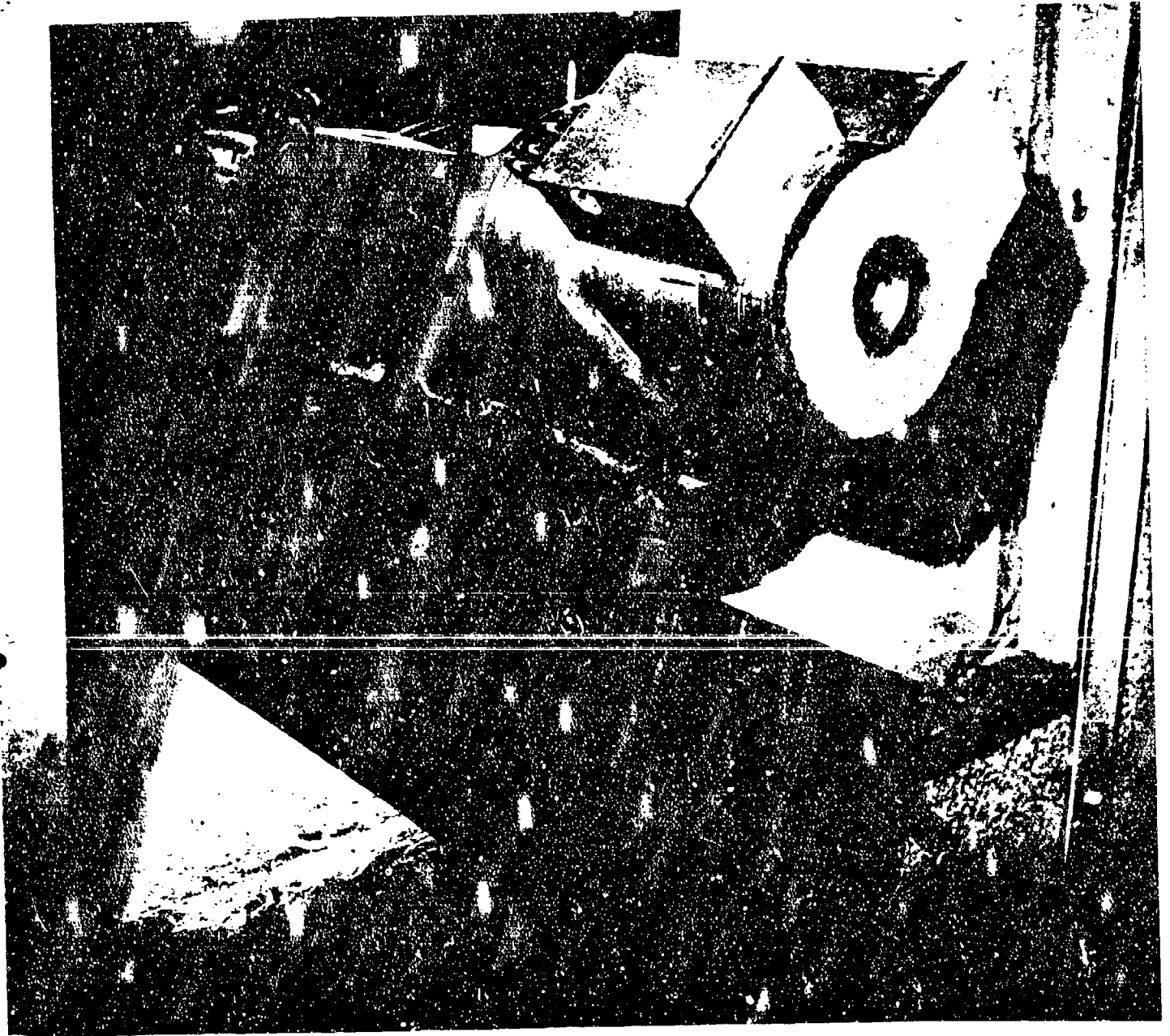
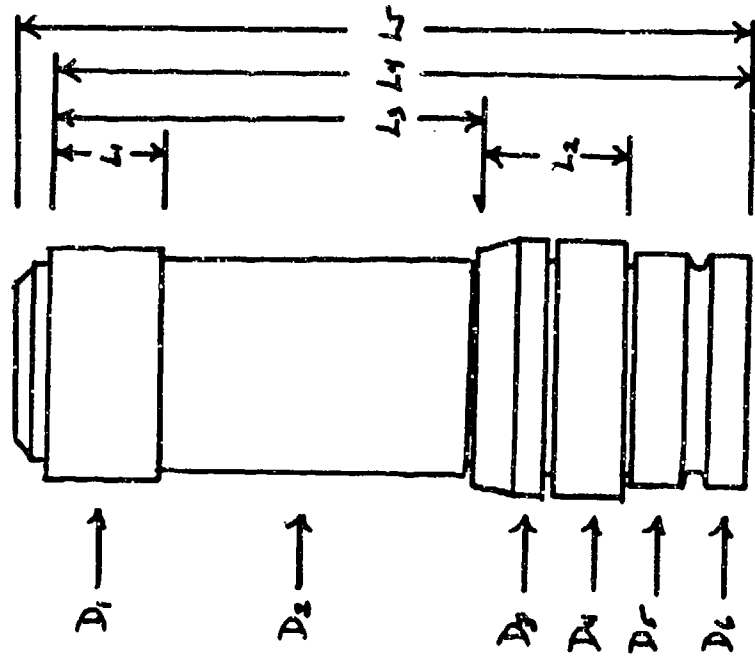


Figure 1. Photograph of Muzzleschmidt and Muzzle Weight

lines. In the past, current surges in firing solenoids had been a source of noise in the data.

A 10GHz microwave radar was placed approximately 18.25m (60 ft) down range along side the soft recovery barrels and aimed back towards the muzzle. The most effective alignment technique was to use a reciprocating saw with a large washer mounted with a bolt in place of a blade so as to present a large frontal surface approximately the area of the projectile face. The saw was placed in front of the muzzle with the washer aligned along the shot line

TYPICAL DIMENSIONS (mm)



| Dimensions | Type 508 | Type 510 | Type 625 |
|-------------|----------|----------|----------|
| L1 | 14.81 | 12.28 | 15.23 |
| L2 | 18.68 | 18.64 | 18.55 |
| L3 | 66.79 | 16.48 | 36.54 |
| L5 | 100.66 | 40.12 | 71.27 |
| L5 | 105.74 | 44.43 | 75.68 |
| D1 | 36.87 | 36.37 | 36.89 |
| D2 | 36.53 | 36.46 | 36.55 |
| D3 | 38.25 | 38.23 | 38.17 |
| D4 | 38.25 | 38.24 | 38.25 |
| D5 | 36.52 | 36.52 | 36.55 |
| D6 | 36.52 | 36.54 | 36.56 |
| Weight (kg) | 0.867 | 0.456 | 0.260 |

Figure 2. Projectile Dimensions

HAUG

and facing the microwave. The reciprocating surface moving with such regularity made alignment and tuning positive. As long as the angle between the radar beam and the gun tube center line was kept small, the microwave signal could be propagated down the tube to the face of the projectile and back to the antenna. The center of the antenna dish was less than one meter from the line of flight. Every effort was made to minimize the signal return caused by the recoiling parts of the gun by covering the muzzle face with microwave absorbing material.

Optrons were used to track recoil as well as vertical muzzle displacement on the first few shots. The unit at the muzzle was set up to check for muzzle motion prior to shot exit. The unit measuring recoil was to check the functioning of the recoil buffer, and also measured the recoil displacement prior to shot exit.

The only additional data taken were chamber pressure and targets. The pressure gage was a mini-hat gage mounted in the chamber. This required the cases to be drilled which is a standard procedure for measuring chamber pressure with an externally mounted gage. An attempt was made to measure downrange targets. The aim point was determined using a modified bore sight and the impact point recorded using a witness card. The standard 37-mm bore sight could not be used because the tapered collar used to center the sight was too short to reach through the muzzle device and center on the bore. An adapter was manufactured in the BRL shop.

This completes the description of the instrumentation and equipment in the range, and Figure 3 shows the location of each component of the test. Note in particular the location of the microwave unit, as this was not the conventional location used in most ballistic tests. Figure 4 is a photograph of the gun, showing the pressure gage and one of the Optrons. Notice the Muzzleschmidt attached to the muzzle.

3. DATA ACQUISITION

The data were acquired on analog tape with some channels backed-up by the digital data acquisition system. This was not the usual procedure for the recording room where the digital recording was the primary system; however, the microwave data were better handled by tape so that the data could be post processed using the HP1000 A/D facility. The microwave signal was recorded on three separate channels. The signal was low pass filtered, dc-10KHz, allowing the shot start motion to be recorded on a wide band FM channel. As the projectile velocity increased the doppler return was attenuated leaving only the contribution from the recoil of the gun. The doppler return was also recorded through a bandpass filter 1 KHz to 80 KHz, which overlapped the first channel in frequency content. This second channel recorded the projectile travel from shortly after shot start until the projectile left the view of the microwave unit, but successfully eliminated the signal contribution from the recoiling gun. This allowed the return from the projectile to be further amplified without the clipping that would have occurred if the large amplitude doppler signal due to recoil were still present. As a backup, and from experience, it was decided to also record the microwave return on a direct record channel using the same band-pass filter

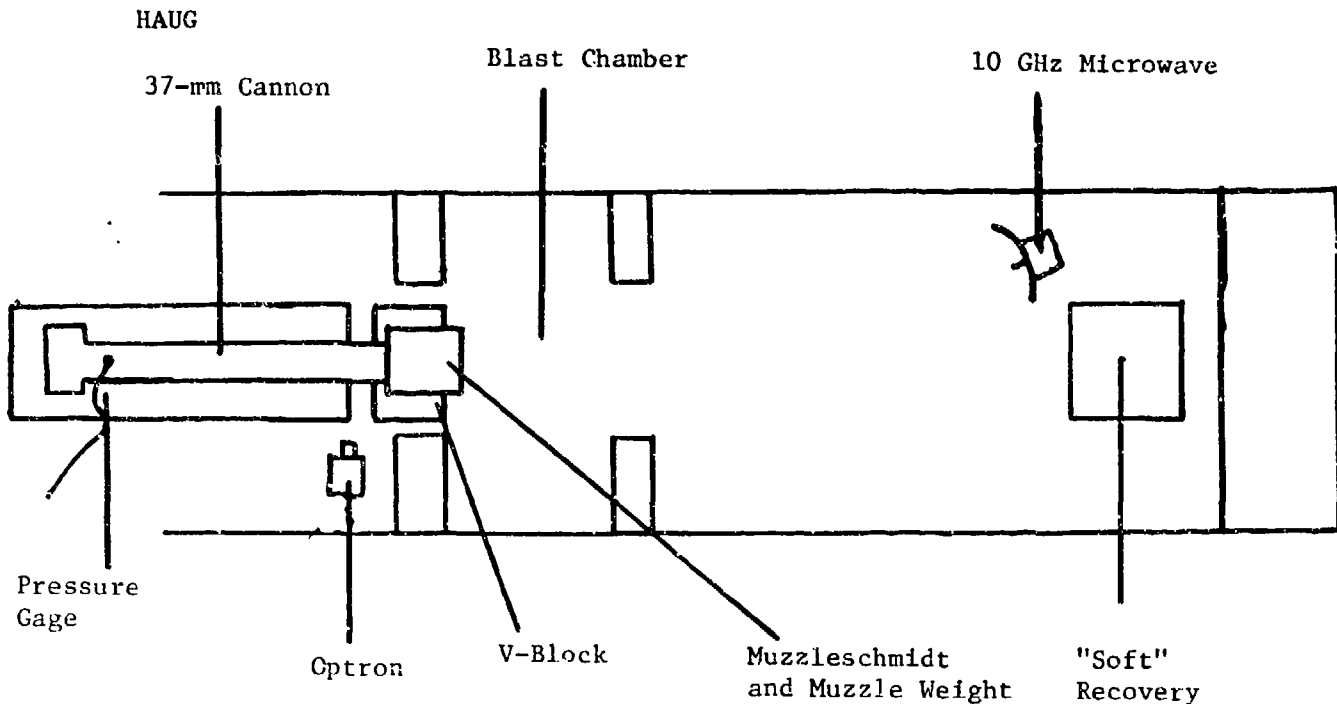


Figure 3. Range Instrumentation

settings. This recording procedure was selected with consideration given to the requirements of the analysis, in particular, the spectrum analysis of the microwave return. Other data recorded on tape included chamber pressure, a firing fiducial, and a muzzle exit fiducial generated by the Muzzleschmidt.

The dual four-coil Muzzleschmidt is made up of two sensors separated by 2.54cm. Each sensor consists of four coils and the output of each coil is proportional to the distance between the coil and the metal parts of the projectile. The outputs of the coils are combined to form up-down, up+down, left-right, left+right for both sensors. For this test the eight outputs from the muzzle device were captured on transient waveform recorders, Biomation model 805's. The units used did not have an output bus directly compatible with the HP 9845 which is the computer selected to read the Biomations. Earl Ball, an electronics technician at BRL, designed and assembled the required interface to feed the eight units to the HP 9845. As is the case whenever one has only the correct number of units and no spares, one of the Biomations failed and for most of the test only seven channels were recorded. In the analysis, the differences, L-R and U-D for each sensor were critical but it was not necessary to record all the sums.

4. FIRING PROCEDURE

The initial firings were used to test the new Muzzleschmidt and to experiment with different methods of implementing and recording the microwave. Considerable effort and time was expended to insure that the muzzle device was operating as designed and that the mounting procedure did

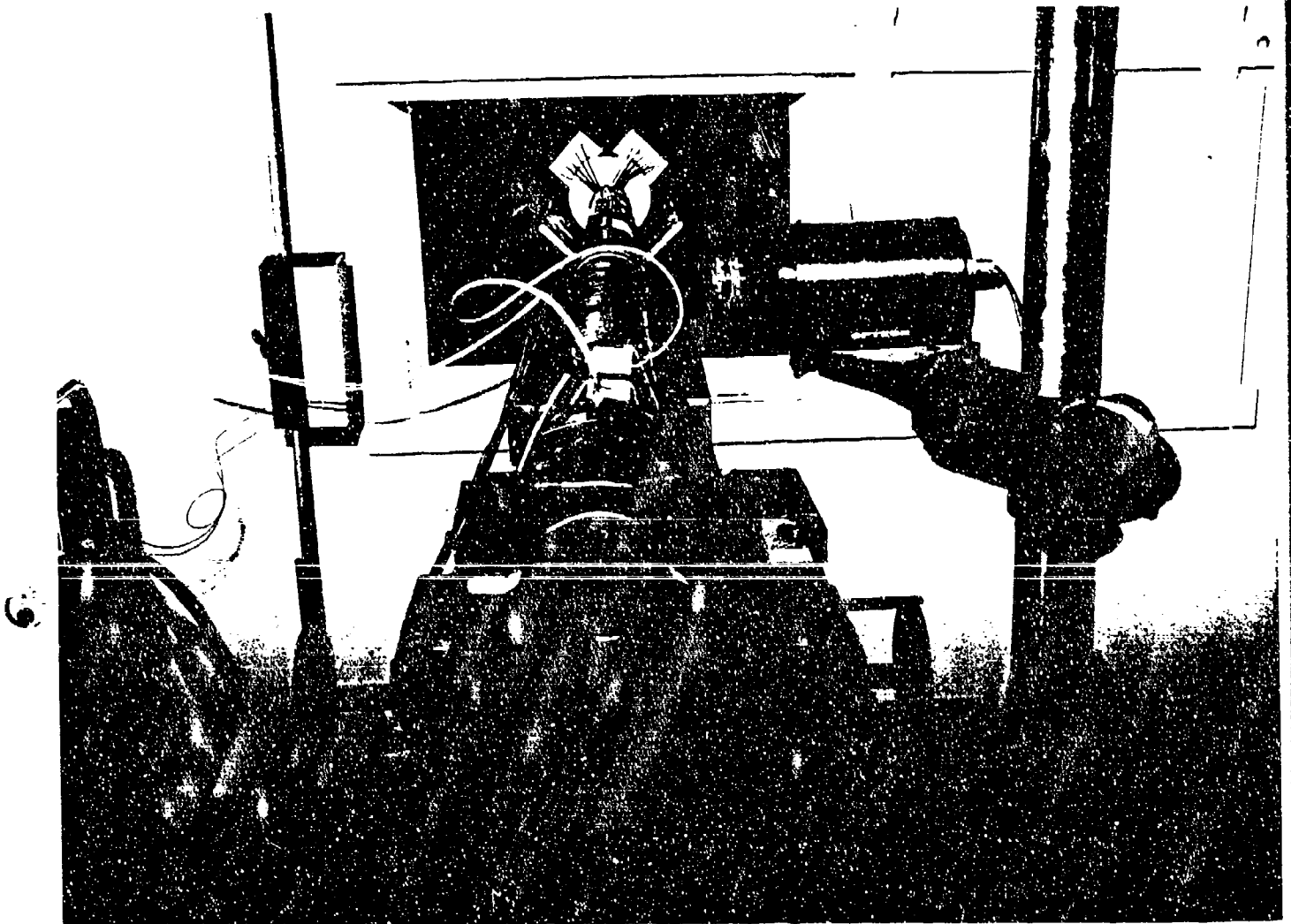


Figure 4. 37-mm Cannon With Showing Pressure Gage And Optron

not allow vibrations to alter the signal. The method of mounting the muzzle device had to be changed and then checked out again. During this process the techniques for handling the microwave measurements were firmed up.

Once the Muzzleschmidt was working properly and had been calibrated it was decided to fire a series of at least ten type 508 proof slugs at a reduced charge. Using this projectile made the measurements with the muzzle device easier to analyze due to the long section with constant diameter between the bourrelet and the rotating band. The procedure for firing the series was as follows:

1. clean tube after each shot in an attempt to get better microwave records;

HAUG

2. place a new target down range and mark the aim point as seen from muzzle sight;
3. record temperature and dew point for the gun room, blast chamber and range;
4. record the actual microwave frequency
5. for projectiles with grooves, note the orientation of the grooves as loaded in the gun;
6. cover the muzzle face with microwave absorber to reduce the magnitude of the return due to recoil.

By this time the idea of the soft recovery system had been abandoned because the projectiles were still being subjected to sufficient abrasion to alter the appearance of the rotating band. The initial projectiles that were recovered did show evidence of contact between the bourrelet and the gun tube. The recovery system slowed down the projectiles enough that the damage from the impact in the sand was minimal, and some analysis of the in-bore performance of the projectile could have been done. Future testing might have requirements that would benefit from this system, but at this point it was felt that there was no need to slow down the testing by using this device.

After a few rounds to check out the instrumentation, twelve of the machined 508 rounds were fired over a period of several days. The firing pace was determined by our ability to look at the data, make appropriate changes in the recording room and align the microwave unit which was reluctant to work consistently.

Spectrum analysis of the microwave data from this series of rounds and some of the preliminary rounds revealed details about shot start, and also showed possible balloting motion in-bore. To confirm this, additional firings were planned. The microwave record of most interest was from a long 508 round which had achieved a muzzle velocity of 642m/s. To explore the differences in doppler return from the two projectiles, several 508 rounds were fired with increasing charge loads to attempt to achieve the same muzzle velocity as the lighter 510 rounds without exceeding the pressure limits of the breech. The charge weight was increased to the point where the pressures were in the 434-441 MPA (63-64 kPSI) range, close enough to the design limit that we decided not to go any higher. The muzzle velocity achieved was 775m/s. At this point we fired several of the lighter and shorter 510 rounds at a nominal muzzle velocity of 1000m/s to gain additional data, and then fired several at lower charge weights attempting to match the 775m/s muzzle velocity of the 508's which allowed us to compare microwave returns from two different projectiles at essentially the same muzzle velocity. The details of the analysis are covered in a report by Dr. Walbert.⁶

5. RESULTS

In the initial phases of the testing, the tube was purged with nitrogen prior to each shot because it was felt that filling the tube with this inert

HAUG

gas would improve the transmission of the microwave signal during the in-bore cycle. At one point the supply of nitrogen was depleted but the firing was continued with no apparent change in the resulting microwave return; therefore, the procedure was changed to simply cleaning the tube prior to each shot. Several attempts were made to reflect the microwave beam down the tube from an aluminum plate and also a screen, but these attempts did not meet with the success experienced with aiming the microwave directly at the muzzle from down range as was described earlier in the discussion of range preparation. Attaching the microwave absorber to the muzzle face reduced the signal strength of the reflection from the muzzle prior to shot exit, but after shot exit the absorber was ripped off with the blast and recoil was clearly visible. The only successful way to eliminate this signal was to filter it out. This experience was what led to the recording technique using multiple channels to record overlapping time sections of the projectile travel.

To determine if the grooves on the face of the projectile would allow the measurement of spin, an experiment was done to spin a projectile with a drill. A projectile that had the grooves cut in it was drilled and tapped in the center of the base with $1/4$ -20 threads. A piece of all thread was screwed into the base of the projectile and then chucked in the drill. The microwave transmitter was aimed at the spinning projectile and various spin rates were tried. The resulting signal showed spin very clearly when analyzed on the spectrum analyzer, although it was not readily visible to the eye in the raw data. Several tests were recorded on analog tape and reduced using the Fast Fourier Transform programs. A plot of the results for a projectile with three V-shaped grooves typical of those fired is shown in Figure 5. The primary

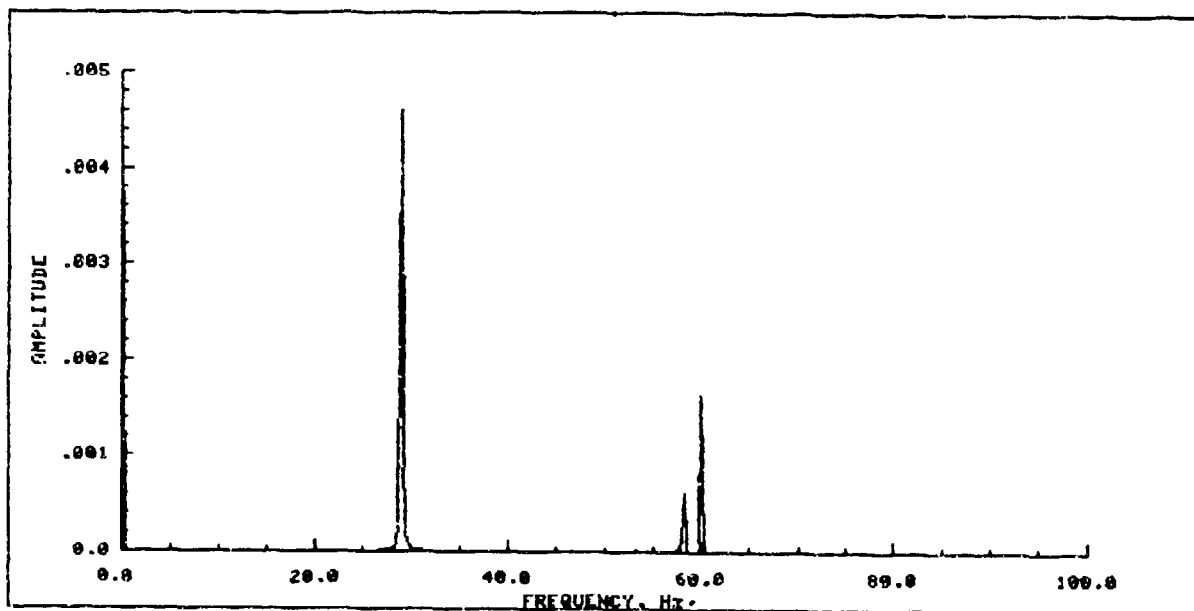


Figure 5. FFT of Spin Test, Projectile with V-Grooves

frequency at 28Hz represents a spin rate of 1680 rpm from the drill. Because of the symmetry of the grooves the second harmonic is apparent. Several suggestions to improve the spin measurements were made, including the

HAUG

attachment of a thin semicircular plate to the front of the projectile, or simply machining a flat-bottomed groove rather than the V-shape that was chosen for the firing tests. To help in the understanding of the results a projectile was machined with three flat grooves radiating at approximately 120 degrees from the center and was tested on the drill. The resulting FFT is shown in Figure 6, and the primary frequency is 24Hz and harmonics are more pronounced due to the groove arrangement. The question of what contribution the grooves make to the measurement of spin is addressed by Figure 7. This plot was the result of spinning a projectile with no grooves, so why was the

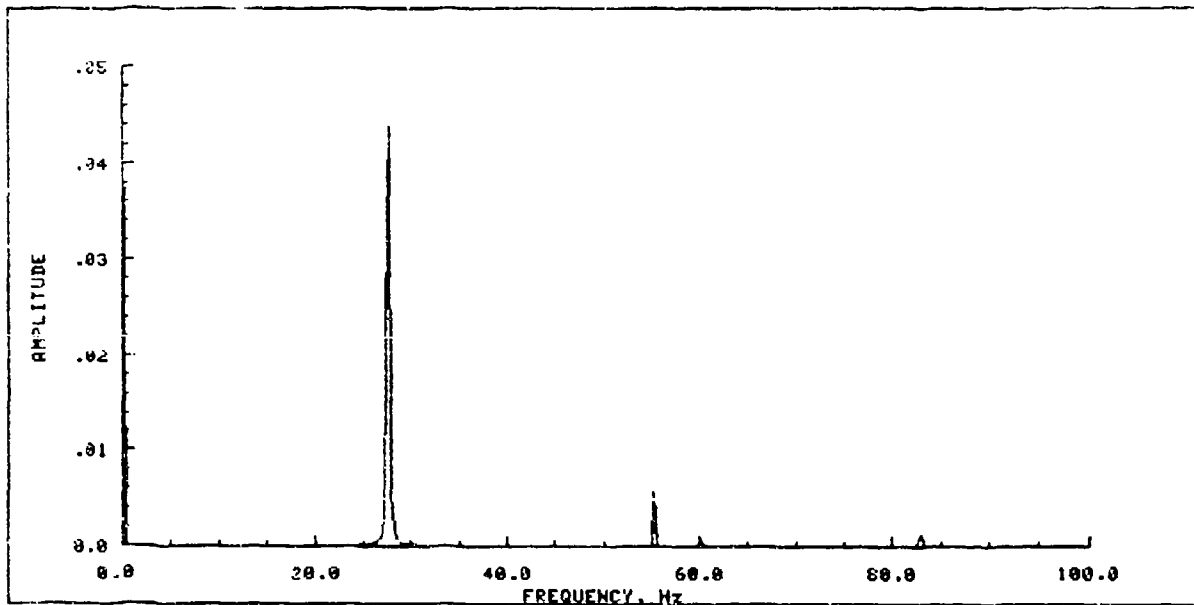


Figure 6. FFT of Spin Test, Projectile with Flat Grooves

spin so visible? Apparently the wobble of the projectile in the drill was sufficient to measure spin and since each of the projectiles tested mounted in the drill chuck at different angles, the projectile wobble contributed different amount of spin information in each test. The primary frequency component in the drill tests was due to the misalignment of the projectile in the drill.

Figure 8 was derived from actual data from the firing test. A section of the microwave data taken after muzzle exit was analyzed using periodic continuation to generate a high resolution FFT and the results show the velocity and the spin. The velocity can be computed to be 619m/s. Using this as an estimate of muzzle velocity and a twist rate of 1:25 calibers, the expected spin rate would be 670rev/s. Because of the geometry of the nose of the projectile, the expected frequency due to spin would be 1339Hz. The side lobes on the spectrum are 1287Hz away from the center frequency, and which represents 96% full spin. The techniques required to measure in-bore spin are still to be developed, and this measurement will be complicated by the fact

HAUG

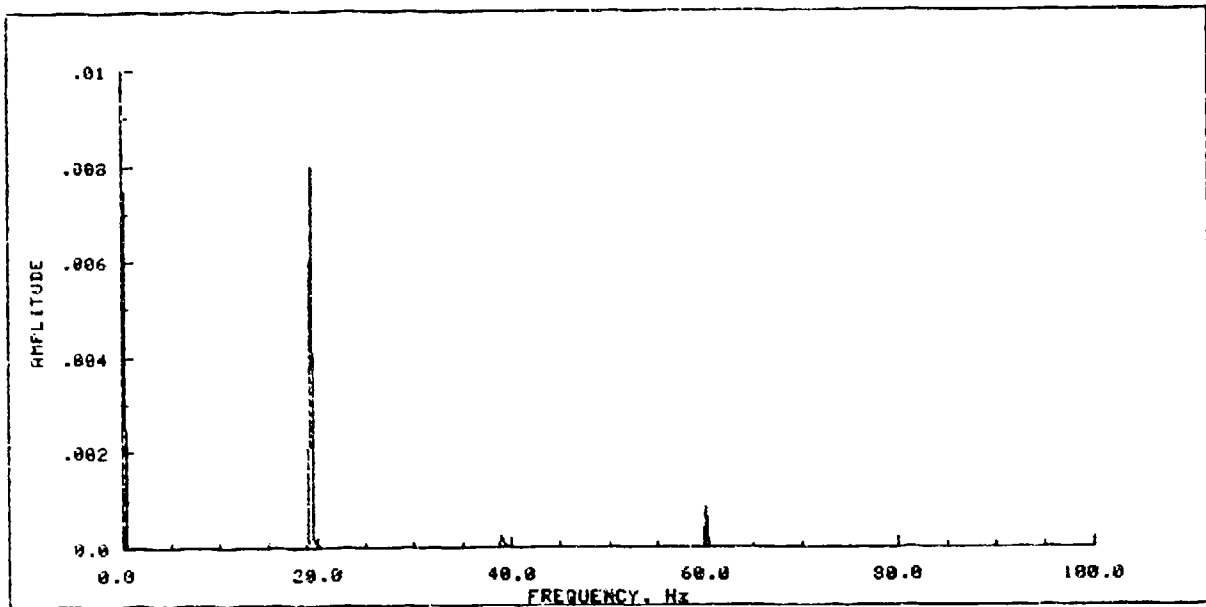


Figure 7. FFT of Spin Test, Projectile with No Grooves

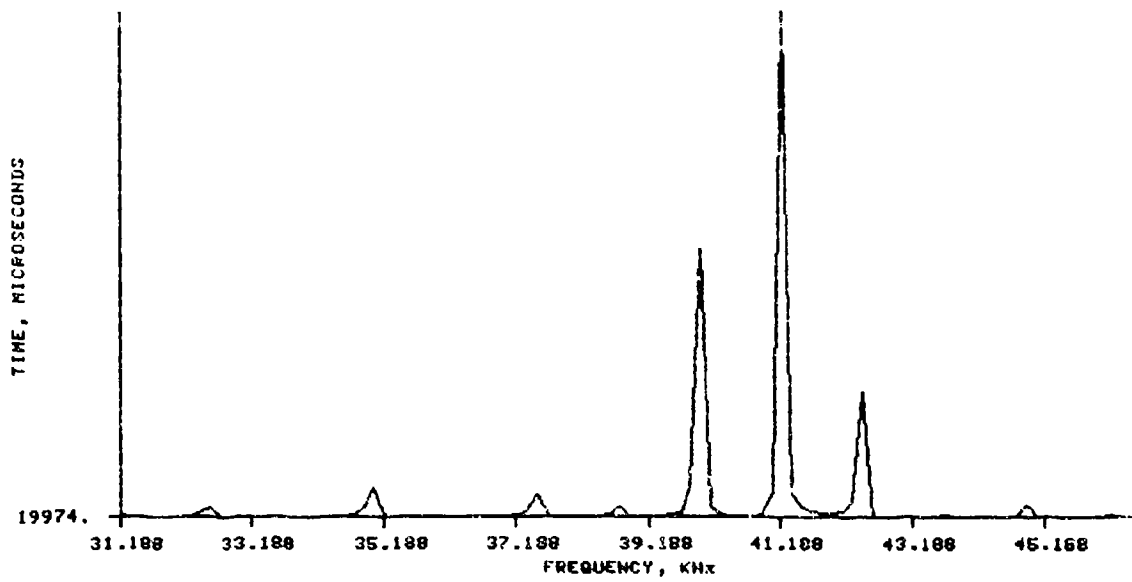


Figure 8. FFT of Projectile Spin from Firing Record

HAUG

that there are multiple transmission modes generated inside the gun tube. The balloting motion during the launch cycle will also complicate generating a spin-time history.

Overlapping FFT's of the microwave data were plotted in a waterfall format to reveal a velocity time history. The waterfall plots reveal such details as in-bore balloting and yaw after muzzle exit as shown in Figure 9.

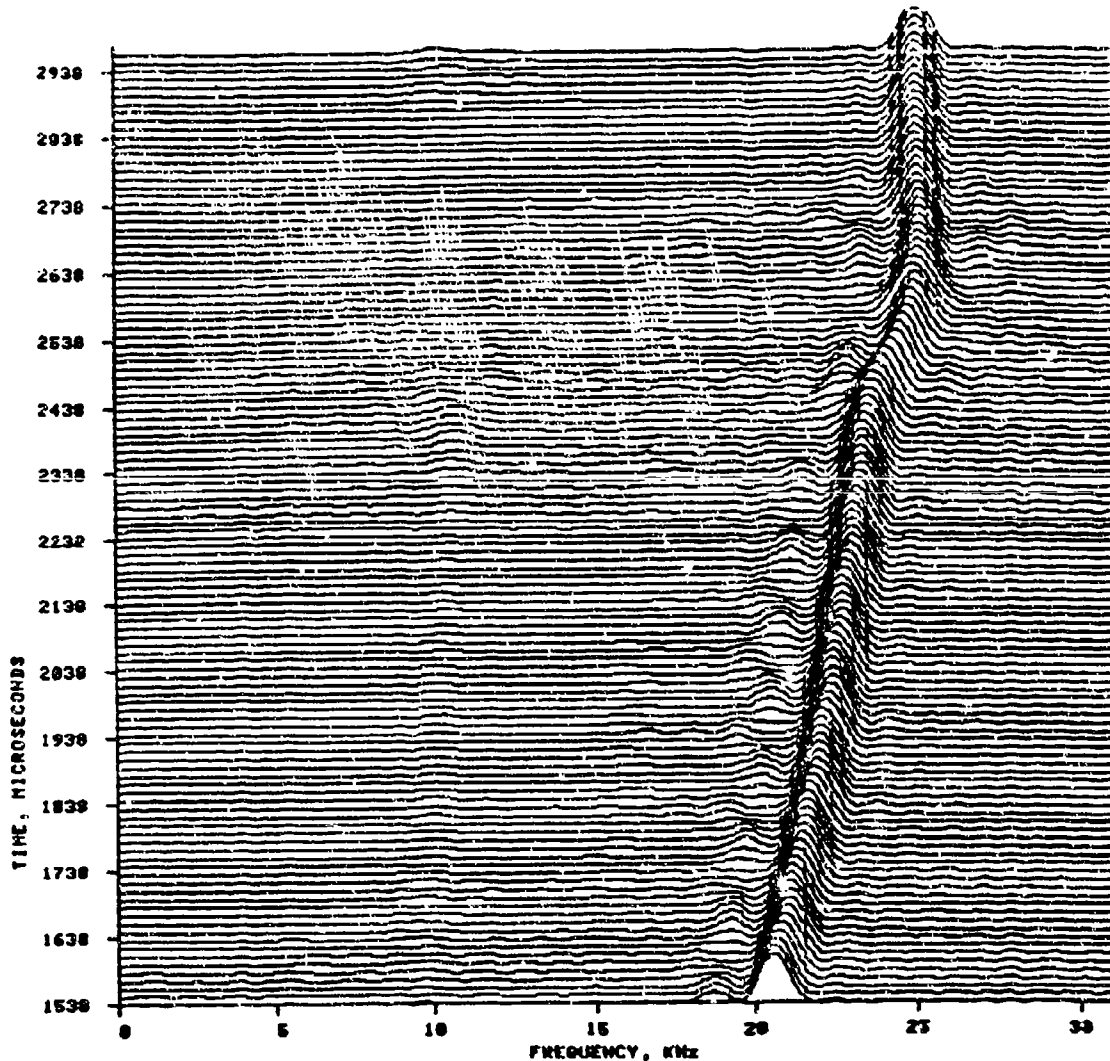


Figure 9. Waterfall Plot of ID5

Although projectile attitude can not be determined directly from this information, the plot can reveal the frequency of the oscillations involved as evidenced by the secondary peaks. Figure 10 shows the case where the projectile starts, stops when the band engages the rifling, and starts again as the pressure builds up to that required for engraving the rotating band. This test demonstrated the value of microwave measurements in analyzing

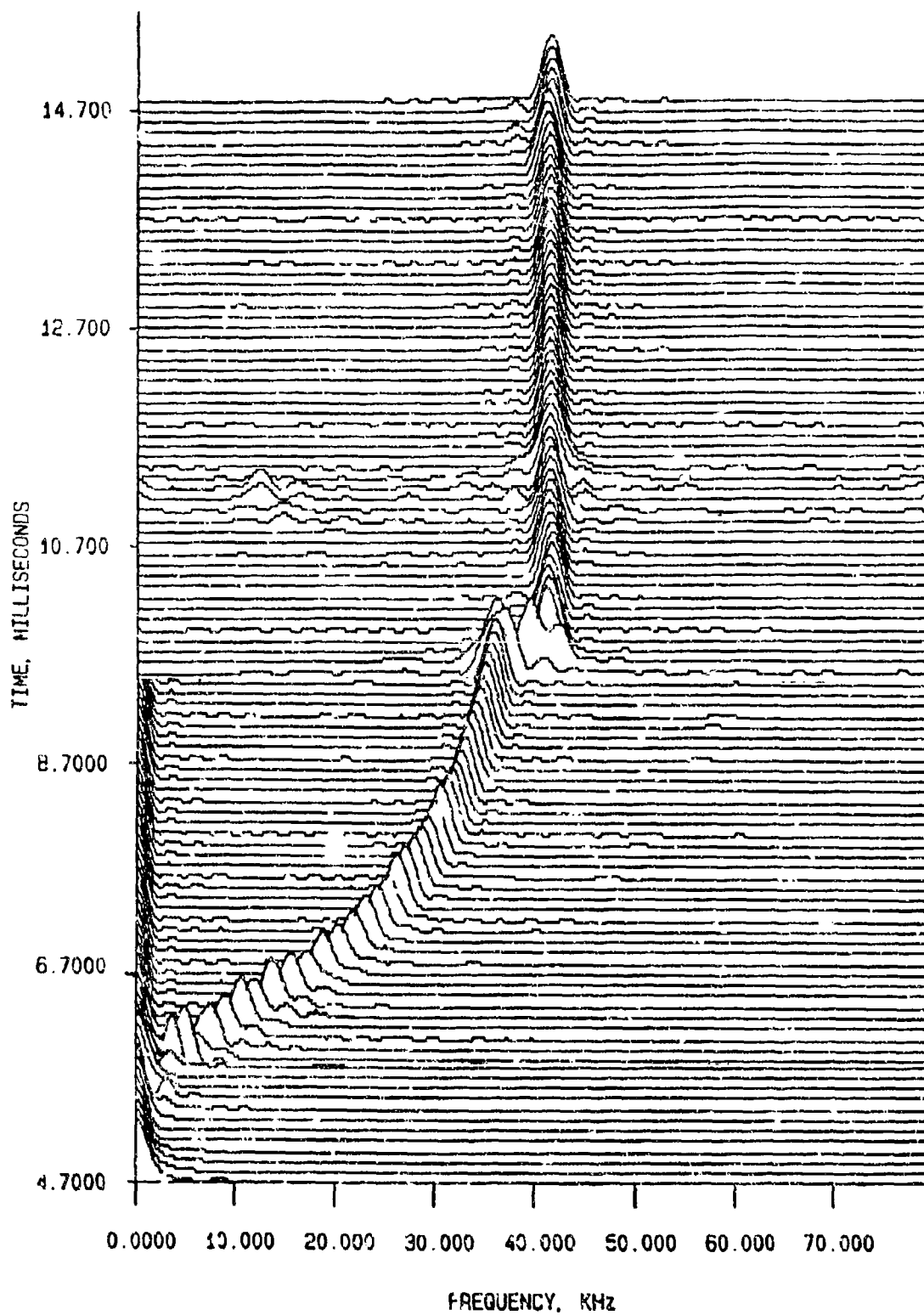


Figure 10. Waterfall Plot of ID31

HAUG

interior ballistics beyond simply a measure of muzzle velocity. In fact the Muzzleschmidt is much better suited for measuring velocity at muzzle exit due to the ambiguities introduced to the microwave measurements as the doppler signal changes from a waveguide mode to free space. This transition region is clearly shown in Figure 10. In the plot there appears to be a step in the velocity of the projectile at muzzle exit which is actually a change in the doppler wavelength.

The results of aiming with a borescope were disappointing. The modified sight did not have a method for collimation, thus the accuracy of the aim point was limited to the accuracy of the machining and to the fit in the bore. If the sight was rotated in the bore or if the sight was removed and reinserted with the viewer at a slightly different angle, the apparent aim point would shift. Also the round to round variation of impacts on the target was not enough to allow a measurement in this short range. The precision of the gun was better than that of the borescope or our ability to measure impacts. The muzzle sight was discontinued for the second phase of the test. If a muzzle sight and witness cards are to be valuable in future tests of this sort then the muzzle sight needs to be fitted more carefully to the bore, and allowance made for some method to collimate the boresight.

The concept of the muzzle weight and the support block worked well during the test and removed transverse motion as a parameter prior to muzzle exit. This was obviously an artificial restriction and will be removed in future testing. Once the muzzle is allowed to move prior to muzzle exit then we must measure this motion, and measure it by a noncontacting method to avoid altering the motion with the measurement. As an initial step the gun should be fired in the current range with the muzzle allowed to move freely. This may allow the target groups to open up enough to attempt a correlation between the muzzle position at exit and the projectile impact. For this initial test, aiming the gun from the muzzle and collecting the targets could have been done once for the entire test, as long as the same projectile and charge weight were used, because all the impacts fell on top of each other. If we are to discriminate shot fall from one round to the next with a muzzle weight in place, then the gun must be fired at a longer range, or a smaller caliber gun must be used.

6. APPLICATIONS

The technique to measure the spin was applied to the development of a rotating band for a 40mm model of a RAM Jet projectile. The combination of chamber pressure and microwave measurements and the flash x-ray allowed the detection of parts failure and the measurement of the percent of spinup. With this information, the time of failure and the pressure loading at failure was established. Finite element analysis resulted in the identification of the failure mechanism and the design was corrected.

The microwave and pressure measurements from firings of both projectile sizes were used by S&D Dynamics, Inc. to validate their model for projectile motion done under contract to BRL. The microwave waterfall plot shown in Figure 9 was used to establish the frequency of the balloting motion experimentally. The in-bore microwave data was used to determine coefficients

HAUG

of friction for the model. Further development of experimental techniques would be extremely valuable in the verification of mathematical models describing the projectile and gun tube dynamics.

Future efforts that will evolve from this work include developing a 5.56-mm gun tube model of the 105-mm M68 tank gun. This rifle barrel has been physically scaled to the dimensions of the 105-mm based on the ratio of the bore diameters. Using the small gun will increase the scaled length of the range to the equivalent of a 400m range with the tank gun and may allow us to make jump measurements in the indoor range. The microwave technology will be extended by the use of a "3-D Radar," which consists of a single transmitter and three receiving antenna. This will allow a more definitive measurement of the projectile flight path and should allow the quantitative measurement of balloting and yaw.

7. CONCLUSIONS

This paper makes no pretense to have resolved the question of jump, but progress has been made in the measurement and analysis of ballistic parameters that affect accuracy. The study of accuracy and jump at BRL is a multifaceted program and this work served as a baseline to help understand what is involved.

The study of projectile disengagement at the muzzle has continued based on these initial firings to a 40-mm gun tube where the muzzle was free to translate during the interior ballistic cycle. The tube motion was measured and combining the angular rate of motion of the tube with the angular rate of motion of the projectile at the muzzle represents a great stride forward in understanding the phenomenology of accuracy and jump.

The microwave measurements made demonstrated the capabilities of this instrumentation technique and have led to the purchase of new instrumentation and the development of the analysis algorithms required. The microwave data from the 37-mm gun firings were instrumental in the development of the capability to perform high resolution Fast Fourier Transforms at BRL and the application of the techniques to projectile/gun tube dynamics.

The continuation of the work with medium and small caliber guns in the indoor range represents an opportunity to experiment with measurement techniques and data analysis procedures at reasonable costs and in an environment that is conducive to the research effort involved. The data generated can be applied to gun tube modeling efforts both as input data and boundary conditions. The results of these efforts are readily transferred to large caliber systems such as the 105-mm and the 120-mm tank guns.

REFERENCES

1. J.Q. Schmidt, "A Radio Frequency Oscillator Technique for Measuring Projectile Transverse Displacement at Muzzle Exit," Ballistic Research Laboratory, Aberdeen Proving Ground, MD; ARBRL-TR-02448, November 1982.

HAUG

2. F.V. Reno, "The Motion of the Axis of a Spinning Shell Inside the Bore of the Gun," Ballistic Research Laboratory, Aberdeen Proving Ground, MD; BRL Report No. 320, February 1943.
3. L.H. Thomas, "The Motion of the Axis of a Spinning Shell Inside the Bore of the Gun," Ballistic Research Laboratory, Aberdeen Proving Ground, MD; BRL Report No. 544, May 1945.
4. E.M. Wineholt, R.K. Loder, "Wear Pattern of the 37mm M3/M6/M5A1 Cannon No. 120019," Ballistic Research Laboratory, Aberdeen Proving Ground, MD; ARBRL-MR-3376, September 1984.
5. R.K. Loder, E.M. Wineholt, J.Q. Schmidt, "Methodology for the Determination of the Mechanism of Projectile Disengagement from the Gun," Ballistic Research Laboratory, Aberdeen Proving Ground, MD. Memorandum Report currently being written.
6. J.N. Walbert, "Techniques for the Analysis of Radar Doppler from Projectiles in the In-Bore and Early Free-Flight Regions," Ballistic Research Laboratory, Aberdeen Proving Ground, MD (report to appear).
7. M.T. Soifer, "Projectile Motion in a Flexible Gun Tube," S&D Dynamics Inc., 755 New York Ave., Huntington, NY. Contract Report BRL-OR-536, October 1984.

**TITLE: TORSIONAL IMPULSE STUDY FOR ARTILLERY FIRED
155mm PROJECTILES**

NEIL A. LAPETINA

Sandia National Laboratories Livermore (SNLL)
Livermore, CA 94550-0096

JOHN M. MILLER

Harry Diamond Laboratories (HDL)
Adelphi, MD 20783-1197

KOK CHUNG

Armament Research and Development Center (ARDC)
Large Caliber Weapon Systems Laboratory
Dover, NJ 07801-5001

ABSTRACT:

As a part of a 155mm advanced projectile development, a major in-bore test program was conducted to characterize the torsional impulse environment utilizing a combination of US and NATO cannons and propellants. Instrumented 155mm projectiles with on-board telemetry systems have been designed at ARDC, HDL, and SNLL for the purpose of measuring axial and angular accelerations during gun launch. Tests have been conducted for determining the effects of cannon wear and propellant charge pressure rise-time. Results of the test program showed that large torsional impulse was experienced with worn NATO cannons and with fast pressure rise-time propellants.

BIOGRAPHY:

PRESENT ASSIGNMENT: Member of Technical Staff, Systems Engineering
Division, Sandia National Laboratories,
Livermore, CA

DEGREES HELD: B.S.M.E. University of Utah (1981),
M.S.M.E. University of California, Berkeley (1983).

TORSIONAL IMPULSE STUDY FOR ARTILLERY FIRED 155MM PROJECTILES†

Neil A. Lapetina*
 Sandia National Laboratories Livermore (SNLL)
 Livermore, CA 94550-0096

John M. Miller
 Harry Diamond Laboratories (HDL)
 Adelphi, MD 20783-1197

Kok Chung
 Armament Research and Development Center (ARDC)
 Large Caliber Weapon Systems Laboratory
 Dover, NJ 07801-5001

INTRODUCTION

As a part of a 155mm advanced projectile development, a major in-bore test program was conducted to characterize the torsional impulse environment utilizing a combination of US and NATO cannons and propellants. Torsional impulse, which first became of concern in 1976 as a result of an investigation of a threaded joint failure in an 8-inch projectile [Ref 1], is the result of the projectile achieving an initial axial velocity before engaging the cannon rifling. In certain cases during gun launch, referring to Figures 1 and 2, the projectile experiences axial displacement before the rotating band engages the cannon rifling, therefore there is no initial corresponding rotational motion. Consequently, when the rotating band engages the rifling, the projectile suddenly experiences a torsional impulse which results in angular velocity. The time rate of change of the torsional impulse results in an angular acceleration which can be very large and depends primarily upon the corresponding axial velocity and the ability of the rotating band to transmit the inertial forces [Ref 1, 2 & 3]. (Unless otherwise specified, peak angular acceleration will hereafter refer to the peak angular acceleration which occurs during torsional impulse, not peak pressure.)

The large angular accelerations corresponding to torsional impulse can lead to failure of structural and frictional joints, explosive charges, rotating bands, and components. Since the angular acceleration can exceed that corresponding to peak axial acceleration, the design limit based on peak axial acceleration can be exceeded. Frictional joints are of particular concern since (1) the minimum coefficient of friction required to transmit the inertia torque across the interface joint is proportional to the ratio of angular ($\ddot{\theta}$) and axial (a_z) accelerations,

$$\mu \sim \frac{\ddot{\theta}}{a_z}, \quad (1)$$

and (2) torsional impulse typically occurs when the axial accelerations are still relatively low. When a large angular acceleration is coupled with a comparatively low axial acceleration, an abnormally large coefficient of friction is required. If the coefficient of friction

† Work Supported by U.S. Department of Defense and Department of Energy

for the interface joint is too small, the joint will undergo a rotational slip. In this case, the angular acceleration does not necessarily need to exceed the design limit to cause failure [Ref 1 & 2].

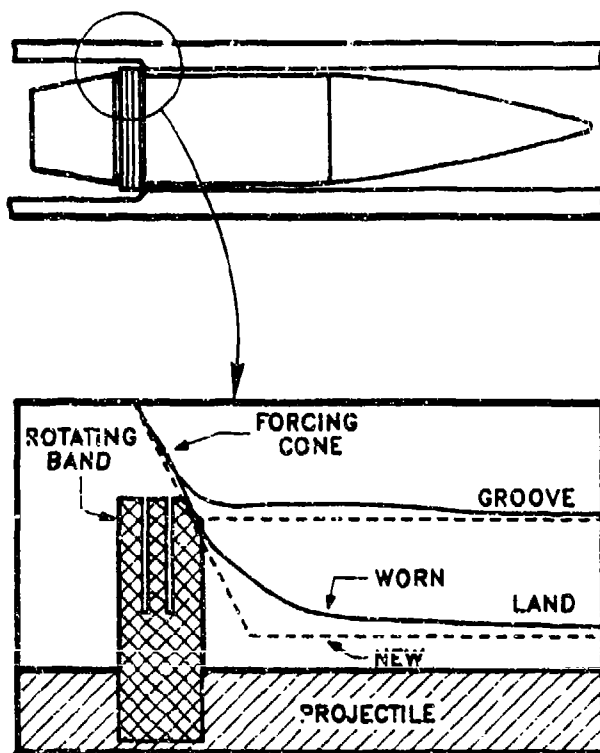


Figure 1. Projectile Rotating Band/Cannon Interface

To simplify further torsional impulse discussion, two terms describing the projectile motion are defined: "free-run" and "clutch-up" distances. The free-run distance is defined as the axial projectile travel occurring before start of spin-up, and the clutch-up distance is defined as the axial travel from end of free-run to the point where the spin rate corresponds to the cannon twist rate. These two parameters are a function of the cannon land wear profile near the origin of rifling, propellant charge pressure-time history, and projectile configuration.

In the investigation of torsional impulse in 8-inch projectiles [Ref 1 & 2], it was substantiated that the free-run distance was dependent on the rotating band design. In a new cannon, the rotating band should be in contact with the rifling after projectile ramming. However, in certain cases, the band outer diameter prohibited the band from making contact with the rifling, producing an axial free-run distance of approximately one inch. In some cases, the projectile velocity reached approximately 100 fps before the rotating band made initial contact with the rifling, causing a large torsional impulse.

In the case of worn cannons, it was also substantiated that decreasing the free-run distance by reducing the outside band diameter does not completely eliminate torsional impulse. As the cannon wears near the origin of rifling, the band/rifling engagement area

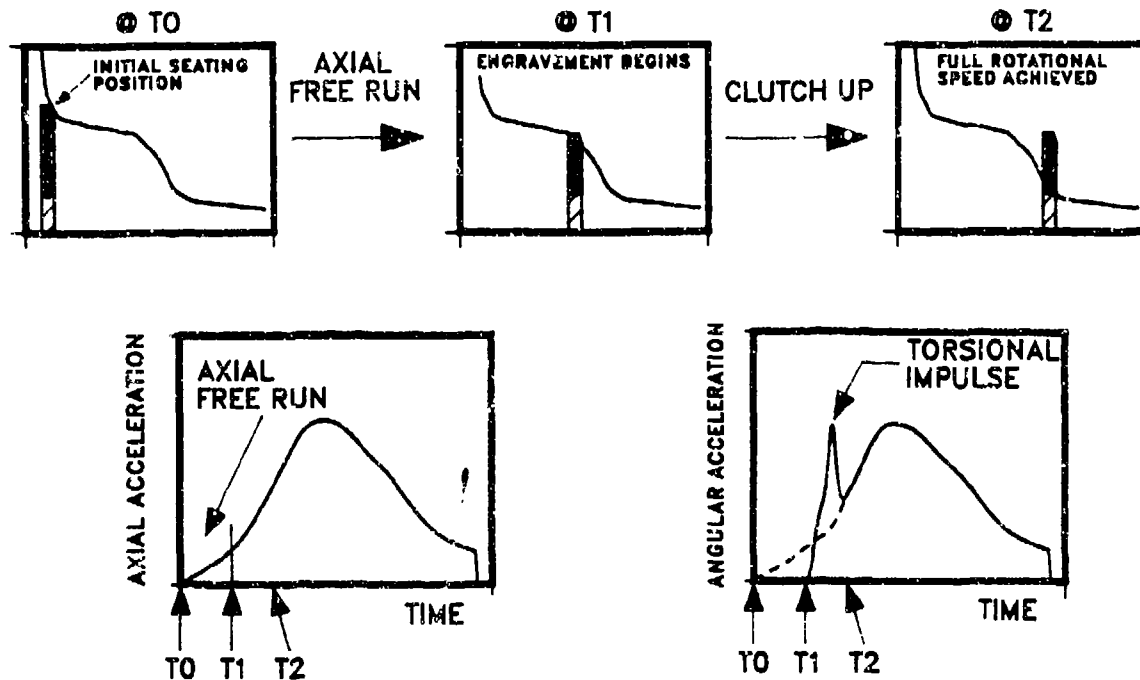


Figure 2. Sequence of Events in Torsional Impulse

during initial projectile motion may not be sufficient to transmit the inertia torque required for angular motion. Thus, the projectile experiences free-run. As a result, the torsional impulse level increases with progressive cannon wear [Ref 1 & 2].

Beginning in mid-1976, Sandia conducted a limited test program to characterize torsional impulse for 8-inch projectiles [Ref 1 & 2]. In this test program, a significant torsional impulse was measured in an 80% worn XM201 cannon, where the peak angular acceleration exceeded that corresponding to peak axial acceleration by 60%. Later in 1978, in-bore telemetry testing began for 155mm projectiles [Ref 4 & 5]. This test program revealed that torsional impulse increases significantly, beginning in the 3rd quarter, with progressive cannon wear in FH70 NATO cannons. The magnitude of the peak angular acceleration in an 80% worn NATO/FH70 cannon exceeded that associated with peak axial acceleration by about 10%. In a 5th quarter 155mm NATO cannon, using an M203 granular charge, the ratio of the maximum angular acceleration during torsional impulse to the angular acceleration associated with maximum axial acceleration was 1.45 and 1.73 when using a M549 and a M483 rotating band, respectively. When worn chrome plated US 155mm cannons were used, the ratio was as high as 2.3 [Ref 4].

Further investigation was conducted by ARDC [Ref 6] with emphasis on the analytical modeling of torsional impulse. A computer simulation was constructed in an attempt to model the gun-launched projectile motion, including torsional impulse. The projectile motion was simulated mathematically by a lumped parameter model using base pressure-time

history as the input forcing function. Though the mechanics of the model were defensible, the model contained some preliminary assumptions regarding the free-run and clutch-up distances. As a result, it was difficult to accurately predict the level of torsional impulse without the input of empirically determined free-run and clutch-up distances. Until the dynamics of the rotating band/rifling interface are better understood, the quantification of torsional impulse will depend on actual field tests.

TEST PROGRAM

Test Description

Instrumented 155mm projectiles with on-board telemetry systems were designed at ARDC, HDL, and SNLL (Figure 3) for the purpose of measuring axial and angular accelerations in the gun launch environment. Each test vehicle contained a set of calibrated axial and tangential accelerometers. Angular accelerations were determined from tangential acceleration measurements. It should be pointed out at this time that since the test vehicle design among the three agencies differed with respect to telemetry design, instrumentation positioning, projectile configuration, and mass properties (see Table I), some variation in the data was expected.

TABLE I. TEST VEHICLE DESIGN VARIATIONS

| <i>Agency</i> | <i>Aft Structural Material</i> | <i>Rotating Band Type</i> | <i>Weight (lbs)</i> | <i>Polar Moment (lbs-in²)</i> |
|---------------|--------------------------------|---------------------------|---------------------|--|
| SNLL | Titanium | M483 or L15-like | 95 | 465 |
| HDL | Steel | M483 or L15-like | 88 | 453 |
| ARDC | Titanium | L15-like | 94 | 495 |

The test projectiles were equipped with parachute recovery systems to allow soft recovery of the payload for reuse in subsequent tests. ARDC and SNLL test projectiles were fired vertically with nose-deployed parachute recovery systems, and HDL test projectiles were fired down-range with base-deployed parachute recovery systems. Gun-site ground station receivers were used to acquire and record the in-bore telemetry data transmitted from the projectile antenna.

For each telemetry test, additional gun-site instrumentation included crush and piezo-electric gages for chamber pressure measurements and doppler radar or velocimeter for measurement of barrel-exit velocity. These measurements were later compared with the measured in-bore data for validation purposes.

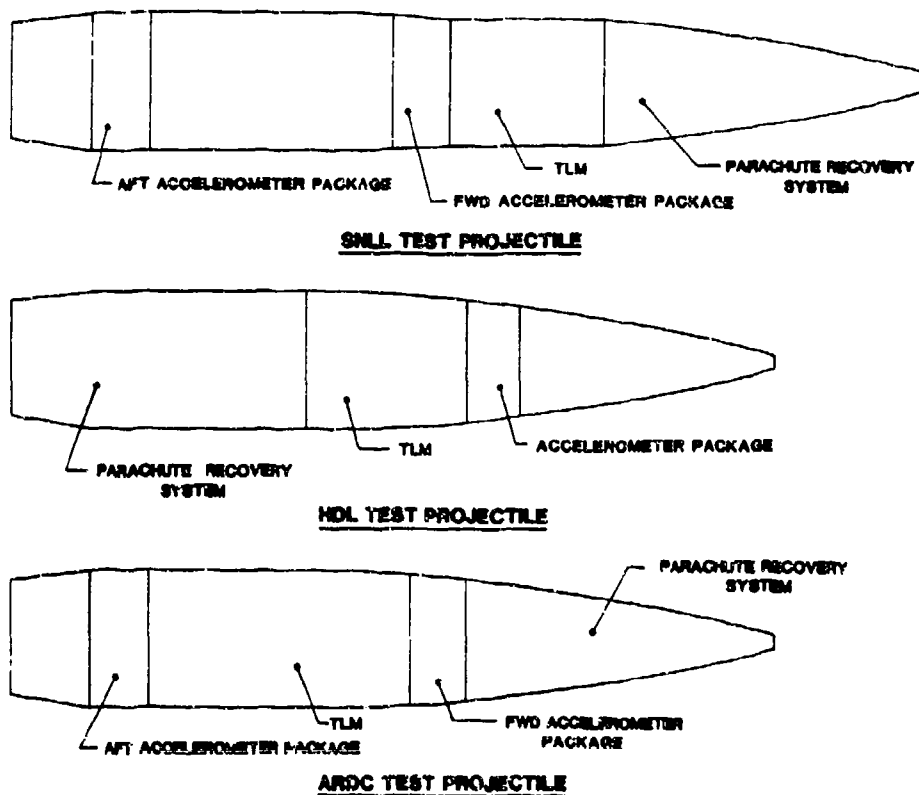


Figure 3. SNLL, HDL, & ARDC Test Vehicles

The test matrix, as shown in Table II, was constructed in a manner such that the effects of cannon wear (new and worn) and propellant charge pressure rise-time (granular and stick propellant charges) could be determined. A list of the tests with the specific types of cannons and propellants that were used is provided in Table III.

Vertical land wear profiles of the US M199 and NATO FH70 cannons listed in Table III are shown in Figures 4 and 5. It can be seen from Figure 6 that the wear profiles between US and NATO cannons differ. The NATO cannons exhibited greater wear at the origin of rifling, followed by a more abrupt wear recovery starting approximately seven inches from origin of rifling. It is believed that this difference in wear profile is due to the fact that US cannons are typically worn with granular charges (though this may change if the newly developed stick charges become type classified), and the NATO cannons are typically worn with CII or CIII stick charges. The difference in wear profile could also be attributable to the fact that the projectiles fired out of the NATO cannons were not equipped with plastic obturators to minimize gas blow-by, possibly contributing to the wear near origin of rifling.

The M203 granular and M203E2 stick propellants are standard high zone charges. The PXR6297 granular and M203E2P stick propellants are representative proof charges

TABLE II. IN-BORE ENVIRONMENT TEST MATRIX

| <i>Propellants</i> | <i>US M199 Cannons</i> | | <i>NATO FH70 Cannons</i> | |
|------------------------|----------------------------|-------------|------------------------------|-------------|
| | <i>New</i> | <i>Worn</i> | <i>New</i> | <i>Worn</i> |
| US M203 Granular | X | | X | X |
| US PXR6297 Granular | X | X | | X |
| US M203E2 Stick | X | X | | X |
| US M203E2P Stick | X | X | | |
| NATO CII Stick | | | | X |

designed to provide over pressure test levels. In this study, the peak pressure for the proof charges were approximately 10% greater than those produced by the standard charges. The CII stick charge is a standard NATO zone 7 charge. Since torsional impulse is a function of the propellant pressure rise-time [Ref 1, 2, 4 & 5], a comparison of the rise-times is provided in Table IV. The propellant pressure rise-time is defined as the time between 10% of peak pressure to peak pressure. It can be seen that the rise-times for the stick charges are faster than those of granular charges.

Data Reduction and Validation

The first step in the data analysis is to determine if the in-bore measured data can be validated by comparison to independently measured parameters. As illustrated in Figures 7a, b, and c, the axial accelerometer data are validated by comparison of the first and second integrals to the measured values of muzzle velocity (doppler or velocimeter) and tube length, respectively. The projectile travel in a 155mm/M199 cannon is approximately 200 inches. The data are considered valid if the agreement is within 5%.

The tangential acceleration data are validated by comparison to the validated axial acceleration data. First, the angular acceleration is computed from the measured tangential acceleration, a_t , by the relationship

$$\ddot{\theta}_t = \left(\frac{g}{r}\right) a_t, \quad (2)$$

TABLE III. IN-BORE ENVIRONMENT TESTS SUMMARY

| Test No. | Agency | Rotating Band | Cannon Type | Cannon S/N | Wear Status | Propellant Type |
|----------|--------|---------------|-------------|------------|-------------|------------------|
| FG159 | SNLL | L15-Like | M199 | 27485 | 1QTR | M203 Granular |
| FG801 | SNLL | L15-Like | M199 | 27485 | 1QTR | PXR6297 Granular |
| FG806 | SNLL | L15-Like | M199 | 27485 | 2QTR | M203E2 Stick |
| FG811 | SNLL | L15-Like | M199 | 27485 | 2QTR | M203E2P Stick |
| FG809 | SNLL | L15-Like | M199 | 27488 | 4QTR | M203E2 Stick |
| FG803 | SNLL | L15-Like | M199 | 27488 | 4QTR | M203E2P Stick |
| FG152 | SNLL | M483 | FH70 | PT20 | 2QTR | M203 Granular |
| FG153 | SNLL | M483 | FH70 | PT08 | 65% Worn | M203 Granular |
| FG154 | SNLL | M483 | FH70 | PT08 | 70% Worn | M203 Granular |
| FG155 | SNLL | M483 | FH70 | PT08 | 75% Worn | M203 Granular |
| FG151 | SNLL | M483 | FH70 | PT08 | 78% Worn | M203 Granular |
| FG158 | SNLL | L15-Like | FH70 | PT08 | 4QTR | M203 Granular |
| FG160 | SNLL | L15-Like | FH70 | PT08 | 4QTR | PXR6297 Granular |
| FG802 | SNLL | L15-Like | FH70 | PT08 | 4QTR | M203E2 Stick |
| FG807 | SNLL | L15-Like | FH70 | PT09 | 5QTR | PXR6297 Granular |
| SF303 | HDL | M483 | M199 | 28682 | 2QTR | M203 Granular |
| SF407R | HDL | L15-Like | M199 | 28682 | 2QTR | M203E2 Stick |
| SF401 | HDL | M483 | M199 | 27488 | 4QTR | M203 Granular |
| SF309 | HDL | M483 | FH70 | PT08 | 2QTR | M203 Granular |
| SF405 | HDL | M483 | FH70 | PT08 | 4QTR | M203 Granular |
| SF304 | HDL | M483 | FH70 | PT09 | 5QTR | M203 Granular |
| RND6 | ARDC | L15-Like | M199 | 28682 | 2QTR | M203E2P Stick |
| RND4 | ARDC | L15-Like | FH70 | PT08 | 4QTR | NATO CII Stick |

where $\bar{\theta}_t$ is the angular acceleration calculated from the measured tangential acceleration, g is the gravity acceleration, and r is the radial position of tangential accelerometer. This acceleration essentially represents the true angular acceleration of the projectile. The angular acceleration is also computed from the validated measured axial acceleration, a_z , in a 1/20 twist cannon, by the relationship

$$\bar{\theta}_z = \left(\frac{\pi g}{20r_o} \right) a_z, \quad (3)$$

where $\bar{\theta}_z$ is the angular acceleration calculated from the measured axial acceleration, and r_o is the radial position of rotating band. This represents the angular acceleration which would occur if torsional impulse was not present.

The non-simultaneity of axial and angular accelerations, if any, will be revealed when the angular acceleration data computed from both axial and tangential accelerations are

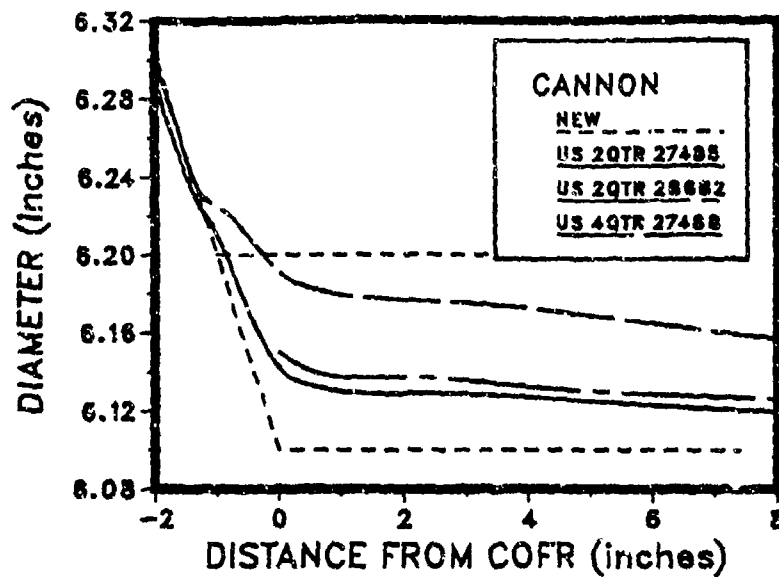


Figure 4. Vertical Land Wear Profile Comparison of US M199 Cannons

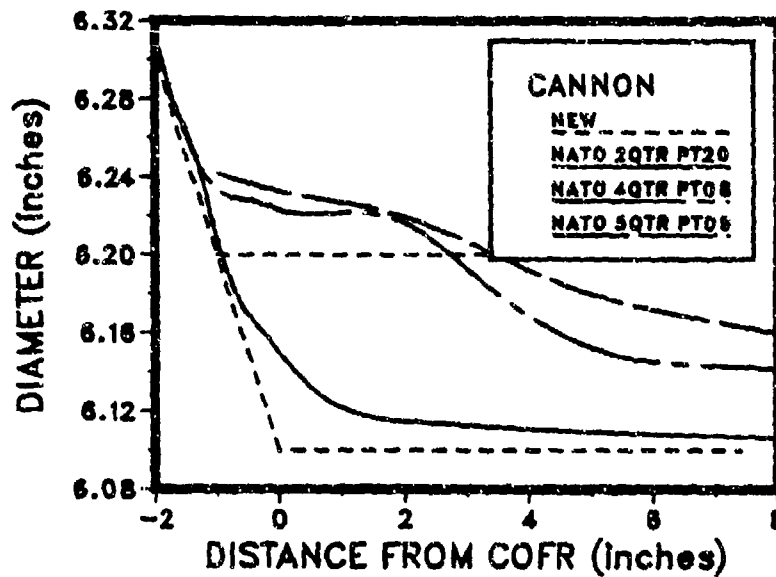


Figure 5. Vertical Land Wear Profile Comparison of NATO FH70 Cannons

compared (Figure 7d). Given the case of the non-simultaneity of axial and angular accelerations, the tangential data are validated through the comparison of angular velocity curves (Figure 7e). After torsional impulse (engraving) ends, the angular velocity curves should then trace each other.

If the axial and angular accelerations have been validated, then the peak angular acceleration at torsional impulse can be quantified. Figure 8 illustrates a simple technique

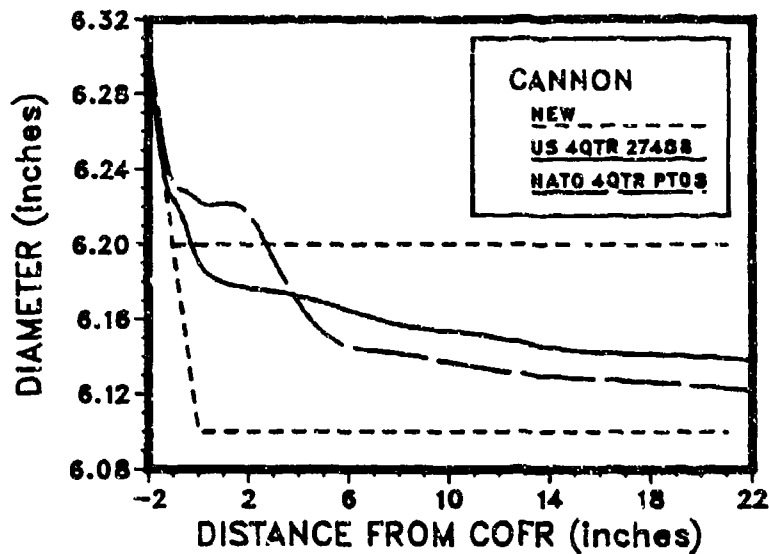


Figure 6. Vertical Land Wear Profile Comparison of US and NATO Cannons

TABLE IV. PROPELLANT RISE-TIME COMPARISON

| <i>Propellant</i> | <i>Pressure Rise Time</i> | <i>Peak Pressure</i> |
|-------------------|---------------------------|----------------------|
| M203 Granular | 4.8 msec | 47,500 psi |
| PXR8297 Granular | 4.8 msec | 56,900 psi |
| M203E2 Stick | 3.7 msec | 51,000 psi |
| M203E2P Stick | 3.1 msec | 58,650 psi |
| CII Stick | 2.8 msec | 48,700 psi |

of using ratios to quantify the results. Ratio 1 is defined as the ratio of peak angular acceleration during torsional impulse to the angular acceleration as calculated from the axial acceleration. This ratio, which is essentially proportional to the ratio of angular to axial acceleration during torsional impulse, is used to quantify the necessary friction factor required for no rotational slip at the frictional joints. Ratio 2 is defined as the ratio of peak angular acceleration during torsional impulse to peak angular acceleration during peak axial acceleration.

TEST RESULTS

The interior ballistic and torsional impulse data are listed in Tables V and VI. The torsional impulse data presented in this paper represent only those that were validated. Some degree of torsional impulse was observed in all tests, including new cannon (1QTR

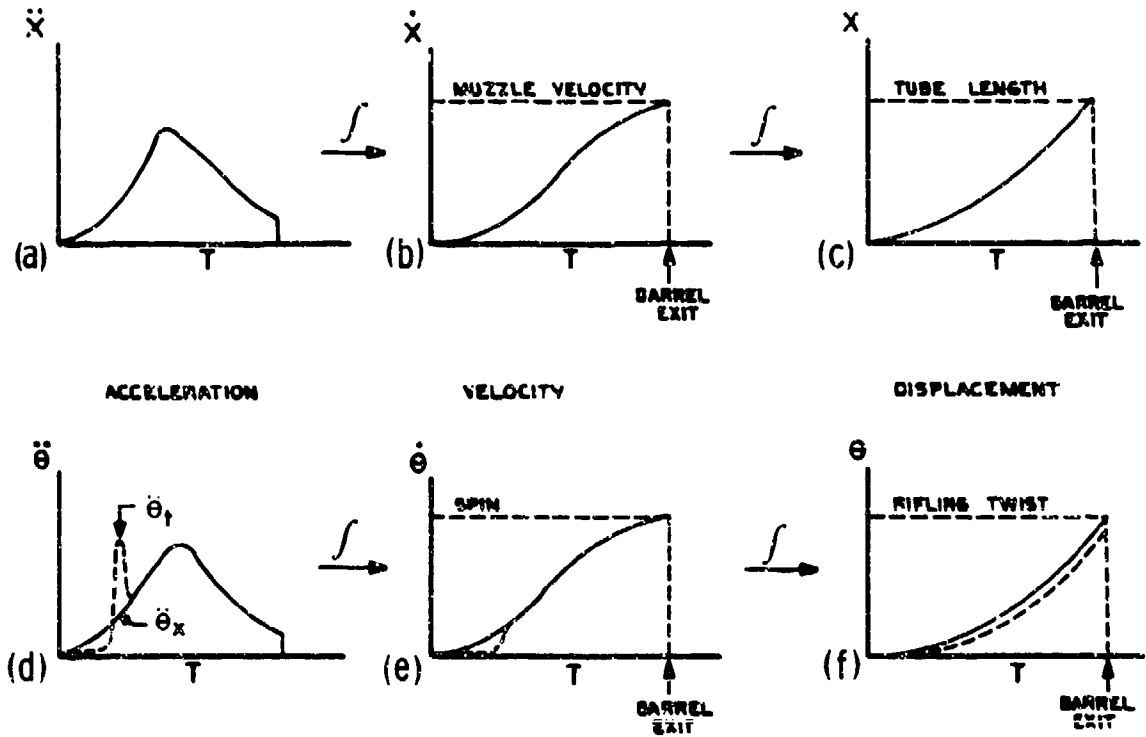


Figure 7. Axial and Tangential Acceleration Measurements and Their Validation

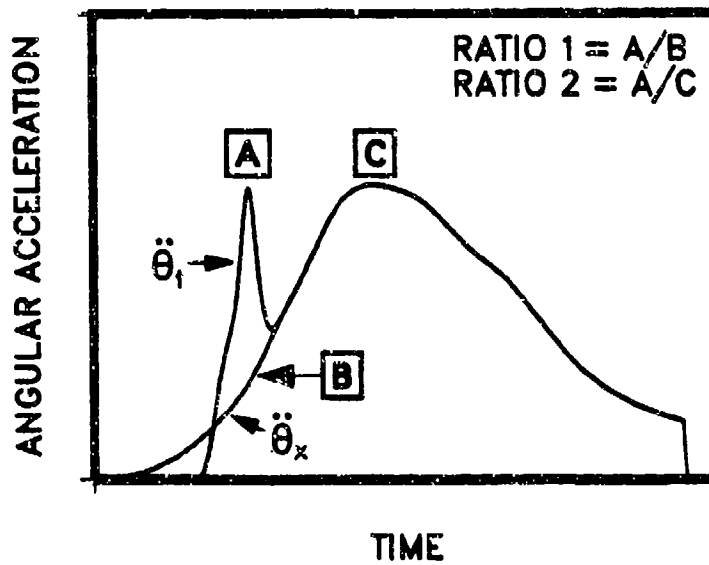


Figure 8. Definition of Torsional Impulse Quantification Ratios

TABLE V. INTERNAL BALLISTIC DATA SUMMARY

| <i>Test No.</i> | <i>Cannon S/N</i> | <i>Wear Status</i> | <i>Propellant Type</i> | <i>Crush Gage Peak Pressure (psi)</i> | <i>Muzzle Velocity (fps)</i> |
|-----------------|-------------------|--------------------|------------------------|---------------------------------------|------------------------------|
| FG159 | 27485 | 1QTR | M203 Granular | 46,600 | 2751 |
| FG801 | 27485 | 1QTR | PXR6297 Granular | 51,200 | 2842 |
| FG806 | 27485 | 2QTR | M203E2 Stick | 54,300 | 2760 |
| FG811 | 27485 | 2QTR | M203E2P Stick | 58,600 | 2905 |
| FG809 | 27488 | 4QTR | M203E2 Stick | 50,100 | 2745 |
| FG803 | 27488 | 4QTR | M203E2P Stick | 55,800 | 2871 |
| FG152 | PT20 | 2QTR | M203 Granular | 47,600 | 2760 |
| FG153 | PT08 | 65% Worn | M203 Granular | 44,800 | 2719 |
| FG154 | PT08 | 70% Worn | M203 Granular | 44,800 | 2700 |
| FG155 | PT08 | 75% Worn | M203 Granular | 44,400 | 2716 |
| FG151 | PT08 | 78% Worn | M203 Granular | 44,000 | 2703 |
| FG158 | PT08 | 4QTR | M203 Granular | 41,800 | 2684 |
| FG160 | PT08 | 4QTR | PXR6297 Granular | 48,000 | 2778 |
| FG802 | PT08 | 4QTR | M203E2 Stick | 48,100 | 2686 |
| FG807 | PT09 | 5QTR | PXR6297 Granular | 44,200 | 2738 |
| SF306 | 28682 | 2QTR | M203 Granular | 49,900 | 2883 |
| SF407R | 28682 | 2QTR | M203E2 Stick | 52,700 | 2877 |
| SF401 | 27488 | 4QTR | M203 Granular | 46,300 | 2847 |
| SF309 | PT08 | 2QTR | M203 Granular | 43,900 | 2780 |
| SF405 | PT08 | 4QTR | M203 Granular | 43,700 | 2781 |
| SF304 | PT09 | 5QTR | M203 Granular | 41,200 | 2797 |
| RND6 | 28682 | 2QTR | M203E2 Stick | 61,500 | 2881 |
| RND4 | PT08 | 4QTR | NATO CII Stick | 41,000 | 2140 |

and 2QTR) tests. It is apparent that the torsional impulse levels generally increased with increasing cannon wear and with faster propellant pressure rise-time.

Cannon Wear Effects

The results were consistent with those observed in previous 8-inch and 155mm tests [Ref 1, 2, 4 & 5] — that torsional impulse generally increases with increasing cannon wear. Firing with M203 granular charges, new US and NATO cannons produced minor torsional impulse. While moderate levels were observed in 4QTR worn US and NATO cannons, it appeared that the 5QTR worn NATO cannon (PT09) produced the largest levels. This observation supports the theory that significant origin wear followed by rapid wear recovery leads to large torsional impulse levels.

TABLE VI. TORSIONAL IMPULSE DATA SUMMARY

| Test No. | Cannon S/N | Wear Status | Propellant Type | Torsional Impulse | | |
|----------|------------|-------------|------------------|--|---------|---------|
| | | | | $\bar{\theta}_{peak}$ (rad/sec ²) | Ratio 1 | Ratio 2 |
| FG159 | 27485 | 1QTR | M203 Granular | 140,000 | 2.12 | 0.44 |
| FG801 | 27485 | 1QTR | PXR6297 Granular | 118,000 | 2.11 | 0.37 |
| FG806 | 27485 | 2QTR | M203E2 Stick | 240,000 | 1.70 | 0.91 |
| FG811 | 27485 | 2QTR | M203E2P Stick | 336,000 | 2.10 | 1.02 |
| FG809 | 27488 | 4QTR | M203E2 Stick | 329,000 | 1.29 | 1.27 |
| FG803 | 27488 | 4QTR | M203E2P Stick | 375,000 | 1.25 | 1.25 |
| FG152 | PT20 | 2QTR | M203 Granular | 135,000 | 1.98 | 0.53 |
| FG153 | PT08 | 65% Worn | M203 Granular | 140,000 | 1.65 | 0.60 |
| FG154 | PT08 | 70% Worn | M203 Granular | 190,000 | 1.96 | 0.86 |
| FG155 | PT08 | 75% Worn | M203 Granular | 200,000 | 1.75 | 0.85 |
| FG151 | PT08 | 78% Worn | M203 Granular | 230,000 | 1.60 | 0.98 |
| FG158 | PT08 | 4QTR | M203 Granular | 240,000 | 1.50 | 1.07 |
| FG160 | PT08 | 4QTR | PXR6297 Granular | 240,000 | 1.76 | 0.96 |
| FG802 | PT08 | 4QTR | M203E2 Stick | 350,000 | 1.70 | 1.40 |
| FG807 | PT09 | 5QTR | PXR6297 Granular | 360,000 | 1.95 | 1.56 |
| SF306 | 28682 | 2QTR | M203 Granular | 150,000 | 2.00 | 0.50 |
| SF407R | 28682 | 2QTR | M203E2 Stick | 350,000 | 2.00 | 1.10 |
| SF401 | 27488 | 4QTR | M203 Granular | 240,000 | 2.00 | 0.90 |
| SF309 | PT08 | 2QTR | M203 Granular | 240,000 | 1.80 | 0.90 |
| SF405 | PT08 | 4QTR | M203 Granular | 260,000 | 1.60 | 1.00 |
| SF304 | PT08 | 5QTR | M203 Granular | 390,000 | 2.00 | 1.50 |
| RND6 | 28682 | 2QTR | M203E2 Stick | 285,000 | 1.65 | 0.82 |
| RND4 | PT08 | 4QTR | NATO CH Stick | 353,000 | 1.95 | 1.40 |

It was interesting to observe, as shown in Figure 9, that the M203E2 and M203E2P stick charge/27488 (4QTR US) cannon tests resulted in low ratio 1 (1.25-1.29), but with a high ratio 2 (1.25-1.27). This was caused by the fact that simultaneity (i.e., spin rate corresponding to the cannon rifling twist rate) of the axial and angular accelerations was not achieved until after 17 inches of projectile travel, where the pressure peaked at approximately 12 inches. Therefore, a large axial acceleration was present during peak angular acceleration resulting in a low ratio 1. Consequently, the lands of the projectile rotating band showed evidence of significant rotational shearing. This phenomenon, which still leads to higher than predicted angular accelerations, is evidently a result of the slow wear recovery rate characteristic with 4QTR granular charge-worn US cannons.

On the other hand, results of the M203 granular charge in the same cannon yielded moderate torsional impulse where ratio 1 was higher (2.0) and ratio 2 was lower (0.90).

Ratio 1 was higher because torsional impulse occurred at about 4 inches of projectile travel where the axial acceleration was still relatively low. In addition, the lands of the rotating band showed little evidence of rotational shearing.

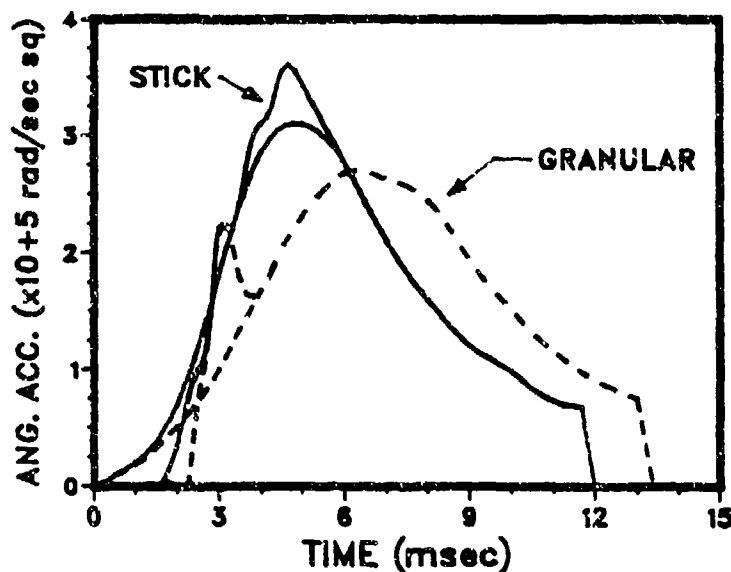


Figure 9. Torsional Impulse in US 27488 Cannon

The results also showed that the torsional impulse levels increased with progressive cannon wear. The distance to peak torsional impulse as a function of cannon wear for the NATO cannon/M203 granular charge combination is shown in Figure 10. The curve indicates that the free-run distance increases significantly beginning in 3QTR life. Figure 11 shows that the increasing free-run distance resulted in increasing peak angular accelerations, to the point where the angular acceleration corresponding to peak pressure was exceeded by at least 50%.

Propellant Effects

In studying propellant effects, there appeared to be a minimal difference in torsional impulse between the M203 and PXR6297 granular charges. However, as illustrated in Figure 12, it was clearly evident that the M203E2P stick charge produced significantly higher torsional impulse as compared to the PXR6297 granular charge in new and worn cannons. In addition, the CII stick charge, even with the lower peak pressure, produced a level similar to that observed with the M203E2P stick charge. All of the above observations substantiate that torsional impulse is a function of the propellant pressure rise-time (see Table IV) and not the peak pressure.

Specifically, the small difference in torsional impulse between the M203 and PXR6297 granular charges is consistent with the fact that the rise-times were essentially identical. In the 2QTR US cannon, the M203E2 stick charge yielded a torsional impulse level of approximately 110% greater than those produced by the M203 and PXR6297 granular

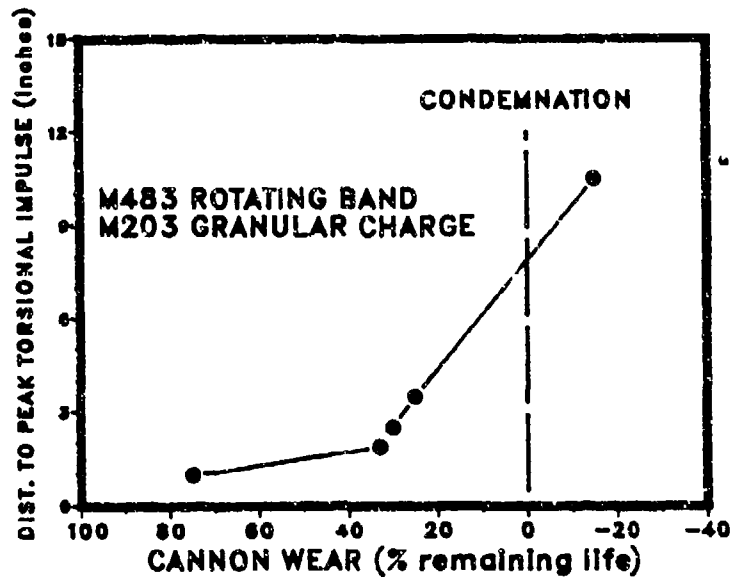


Figure 10. Distance to Peak Torsional Impulse Versus NATO Cannon Wear

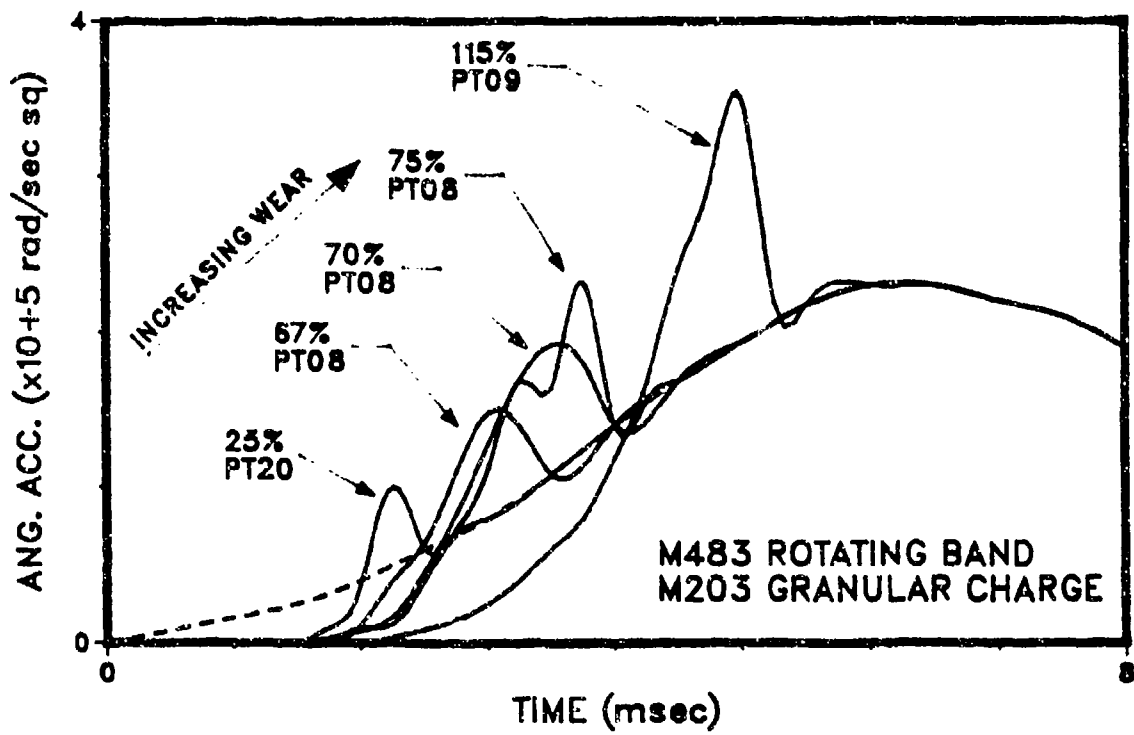


Figure 11. Torsional Impulse Versus NATO Cannon Wear

charges. In the same cannon, the M203E2P yielded the largest level, exceeding the M203 level by 160%. Again, these differences appear directly related to the variation in the pressure rise-times, since the rise-times of the stick charges are significantly faster.

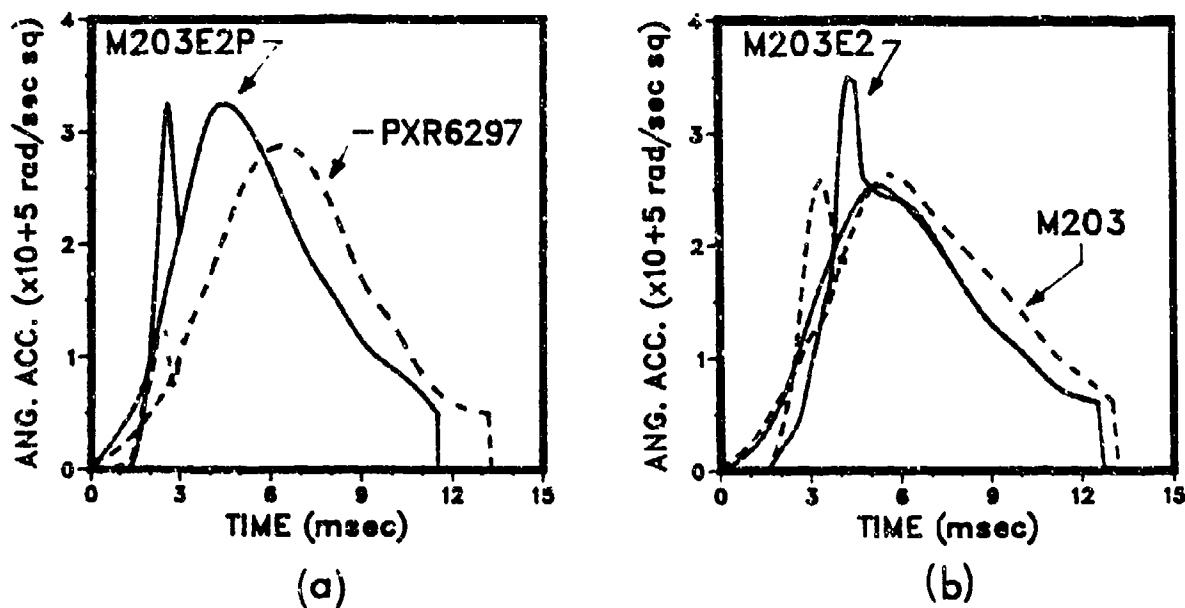


Figure 12. Effects of Propellants on Torsional Impulse for (a) New US 27485 Cannon and (b) Worn NATO PT08 Cannon

DISCUSSION

In order to gain a better understanding of the effects of cannon and propellant characteristics, an approximate relationship estimating the peak angular accelerations is presented*:

$$\bar{\theta}_{\text{peak}} \approx \frac{cv^2}{\Delta d}, \quad (4)$$

where $\bar{\theta}_{\text{peak}}$ is the peak angular acceleration, c is a constant defined by $c = 2\pi T/C$, T is the twist rate, C is the caliber, v is the axial velocity at peak torsional impulse, and Δd is the clutch-up distance.

It can be seen that the peak angular acceleration is strongly dependent on projectile velocity at torsional impulse and inversely proportional to the clutch-up distance. The axial velocity term increases with increasing free-run distance and faster propellant rise-time. Given that torsional impulse is inversely proportional to the clutch-up distance, the wear profiles exhibiting rapid wear recovery can lead to large torsional impulse. This is consistent with the observations that firing with the worn NATO cannons and/or with fast

* G. A. Benedetti, private communication

rise-time propellants yield the largest torsional impulse. For the worn NATO cannons, the excessive wear at the origin of rifling results in large free-run distances and the following rapid wear recovery results in small clutch-up distances, both of which contributed to the large observed torsional impulse.

In addition, a rotating band which causes the projectile to seat prior to engaging the origin of rifling can increase the free-run, which in turn can result in higher torsional impulse levels [Ref 1]. Furthermore, torsional impulse may also be a function of the projectile mass properties (particularly weight and polar moment of inertia). Since the axial velocity is a function of projectile weight and the inertia torque is a function of projectile polar moment of inertia, mass properties may influence torsional impulse. Since all firings essentially utilized identical mass properties, these effects have not been characterized.

Equation 4 can be used to predict peak angular acceleration levels for various charges if the torsional impulse is known for a particular projectile, propellant, and cannon. In estimating the torsional impulse level for other propellants, two key assumptions are made: (1) the distance to peak torsional impulse remains constant and (2) the clutch-up distance remains constant.

These assumptions are valid for wear profiles (near origin of rifling) with rapid wear recovery (i.e., 27485, PT08, and PT09) and are not appropriate for wear profiles with slow wear recovery (i.e., 27488). In the case of slow wear recovery, the clutch-up distance and the distance at point of torsional impulse is dependent on the propellant forcing function. Based on the above assumptions, the following approximate relationship is made

$$(\bar{\theta}_{\text{peak}})_2 \approx \left(\frac{v_2}{v_1}\right)^2 (\bar{\theta}_{\text{peak}})_1 \quad (5)$$

Therefore, the torsional impulse level of a second charge can be estimated, given (1) the torsional impulse level of one charge and (2) the square of the ratio of the axial velocity (at the distance corresponding to peak angular acceleration) of the two charges. This point is illustrated in Figure 13, where the peak torsional impulse is plotted against the axial velocity for two cannons, 27485 and PT08. Each curve represents a constant clutch-up distance: 0.85 inches for 27485 and 5.1 inches for PT08. The predicted curves appear to compare well with the actual data points.

CONCLUSIONS

The test results showed that with the US M203 granular charge, early-life US and NATO cannons produced minor torsional impulse. However, moderate to large torsional impulse was experienced in worn US and NATO tubes, with peak levels exceeding (by 50%) the angular acceleration associated with maximum axial acceleration. It was also substantiated that torsional impulse increases significantly (110 to 160%) with faster propellant charge pressure rise-time. Furthermore, the test results from a particular cannon/projectile combination can be used to predict peak angular acceleration for other propellants in cannons that exhibit rapid wear recovery. Further investigation will be required to determine the effects of projectile characteristics, particularly the rotating band configuration and projectile mass properties.

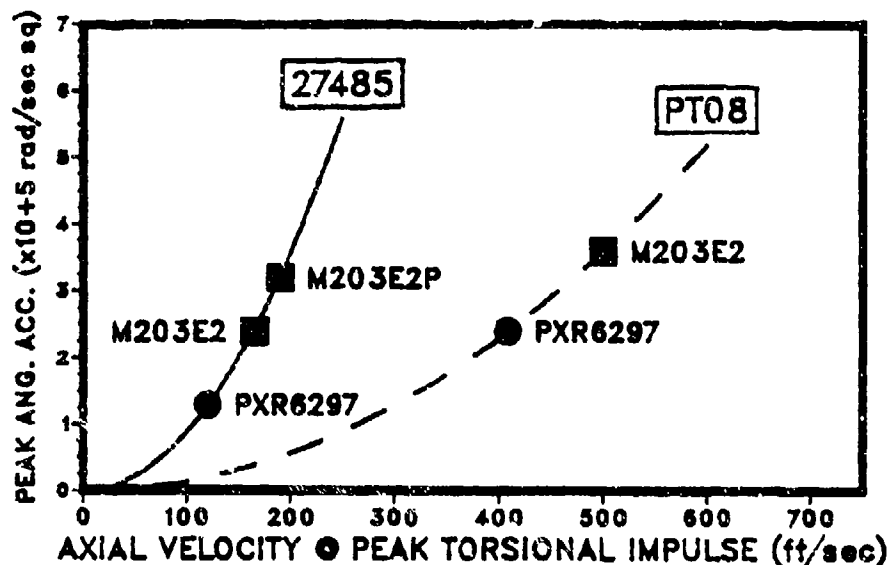


Figure 13. Peak Angular Acceleration Versus Corresponding Axial Velocity

The large torsional impulse associated with worn cannons and faster pressure rise-time charges can be a major design concern because the resulting inertia torques are not usually considered in the original projectile design. Torsional impulse can lead to several potential problems, including damage to the explosive charge, structural joints, and components. The observed torsional impulse levels indicate that the minimum coefficient of friction required for friction joints may be about twice that if no torsional impulse was present. Since it is likely that large torsional impulses can occur in various cannon/propellant combinations, quantification of the environment is required to assess the reliability of the projectile design.

REFERENCES

1. Benedetti, G. A., "Measurements of Torsional Impulse and Projectile Balloting for Artillery Fired Projectiles Using In-Bore Telemetry," Presented to NATO NAAG Panel IV, Surface-to-Surface Artillery, April 21-25, 1980.
2. Benedetti, G. A., "Measurement of Torsional Impulse and Projectile Balloting for Artillery Fired Projectiles Using In-Bore Telemetry," Presented to 3rd U.S. Army Symposium on Gun Dynamics, May 11-14, 1982.
3. Benedetti, G. A., "Dynamic Response of a Beam Subjected to Gun Launch Accelerations," Sandia National Laboratories, SAND83-8206, April 1983.
4. Benedetti, G. A., "Measurement of Torsional Impulse for Artillery Fired 155mm Projectiles Using In-Bore Telemetry," Presented to the Third Quadrilateral Ballistics Working Group, Fort Halstead, Kent, United Kingdom, April 22-23, 1982.

5. Waye, D. E., "NATO FH70 Cannon Tube Wear Versus Torsional Impulse Study for Artillery Fired 155mm Projectiles," Sandia National Laboratories, September 1, 1982.
6. Schmidlin, A. E., "Torsional Impulse in Gun Launched Projectiles," Technical Report ARLCD-TP-80037, Dover, NJ, March 1981.

SOIFER & BECKER

TITLE: In-Bore Projectile Motions
MARTIN T. SOIFER and ROBERT S. BECKER
S&D Dynamics, Inc.
755 New York Avenue
Huntington, N.Y. 11743

ABSTRACT:

The basic equations which describe the general motion of a projectile of finite geometry and inertia traveling in a flexible gun tube are developed and applied to a conventional round fired in a rifled-bore gun tube and a sabot round fired in a smoothbore gun tube. The conventional round is permitted six degrees-of-freedom relative to the gun tube, with allowance for mass eccentricity, elastic/plastic deformation of the rotating band, and bourrelet impact and rebound with the bore. The sabot round is permitted " $n + 6$ " degrees-of-freedom (where " n " denotes the number of sabot-segments), with allowance for sabot-segment motion relative to the penetrator, elastic/plastic deformation of the rear bore-riding surface, and sabot-segment impact and rebound with the bore and penetrator. Model predictions for "balloting" motions of a conventional 37mm round were correlated with in-bore radar doppler data. Model predictions for the in-bore motions of the 120mm XM829 and DM13 sabot rounds were obtained on both absolute and comparative bases.

BIOGRAPHY:

PRESENT ASSIGNMENT: President of S&D Dynamics, Inc., Principal Investigator for R&D programs, and Independent Consultant, 1972-Present.

PAST EXPERIENCE: Senior Project Engineer, Colt Firearms, Hartford, CT, 1970-72; Senior Project Engineer, Technik, Inc., Jericho, NY, 1968-70; Program Manager, Dynamic Science, Monrovia, CA, 1967-68; Research Scientist, New York University, Bronx, NY, 1964-67; Engineer, Technik, Inc., Jericho, NY, 1963-64.

DEGREES HELD: B.S. (Aeronautics & Astronautics), New York University, Bronx, NY, 1962; M.S. (Aeronautics & Astronautics), New York University, Bronx, NY, 1963; Ph.D. (Aeronautics & Astronautics), New York University, Bronx, NY, 1967.

IN-BORE PROJECTILE MOTIONS

MARTIN T. SOIFER, Ph.D.
*ROBERT S. BECKER, M.S.
S&D DYNAMICS, INC.
755 NEW YORK AVENUE
HUNTINGTON, NEW YORK 11743

1. INTRODUCTION

As part of the ongoing effort to achieve greater understanding of the mutual effects of projectile in-bore motion and gun tube flexibility, this paper is dedicated to the development and application of the basic equations which describe general in-bore projectile motion, with allowance for impact and rebound with the bore, and without restriction on gun tube motion. General considerations are presented first for a generic projectile traveling in a flexible gun tube. These considerations are further developed for a conventional projectile traveling in a flexible rifled-bore gun tube and a projectile with segmented sabot traveling in a flexible smooth-bore gun tube.

Development of the equations for the general, six degree-of-freedom, in-bore motion of a conventional round, with allowance for impact and rebound with the bore, as well as application to two distinct 37mm projectile designs fired from a specially configured test weapon, and correlation of model predictions with in-bore radar doppler data (made available by the U.S. Army Ballistic Research Laboratory) were accomplished under contract to the U.S. Army Research Office, Durham, NC, with funding provided by the U.S. Army Ballistic Research Laboratory, Aberdeen Proving Ground, MD.

Development of the equations for the general, " $n + 6$ " degree-of-freedom, in-bore motion of a sabot round with " n " sabot-segments, with allowance for sabot-segment motion relative to the penetrator, as well as impact and rebound with the bore and penetrator, and application to both the XM829 and DM13 rounds were accomplished under subcontract to Honeywell, Inc., Defense Systems Division, Edina, MN.

For all considerations presented, it is understood that to achieve the desired assessment of the mutual effects of projectile/gun-tube interaction, the formulations developed are to be solved simultaneously with the equations of a compatible gun dynamics simulation.

2. GENERAL CONSIDERATIONS FOR A GENERIC PROJECTILE TRAVELING IN A FLEXIBLE GUN TUBE

Consider a generic projectile, consisting of a principal component, secondary components and interface elements, traveling in a flexible, rifled or smoothbore gun tube, as depicted in Fig. 1. The principal projectile component is identified with either the main-body of a conventional round or the penetrator of a sabot round. Secondary projectile components are identified with the sabot-segments of a sabot round. Interface elements are identified with either the rotating band and bourrelet of a conventional round or the rear and forward bore-riding surfaces of a sabot round. Furthermore, for the purposes of this development, the projectile is considered to be semi-flexible in that principal and secondary projectile components are treated as rigid, with flexibility introduced at interface elements.

Referring to Fig. 1, the reference frame S' is defined as an inertial, space-fixed reference frame. The reference frame S is permanently attached to the c.g. of the principal projectile component. The reference frame S_i is permanently attached to the c.g. of the i^{th} secondary projectile component. Finally, the reference frame S_0 is defined as an intermediate reference frame, fixed neither in the projectile nor in the gun tube, which translates with the principal projectile component along the gun tube axis and rotates with it about the instantaneous tangent to the gun tube axis. Hence, S tracks motion of the c.g. of the principal projectile component relative to the gun tube; S_0 tracks motion of the gun tube relative to inertial space; while, S_i tracks motion of the i^{th} secondary projectile component relative to the principal component.

In view of the above definitions, the kinematic relations between S_0 and S' incorporate gun tube motions, as well as two degrees-of-freedom of the principal projectile component relative to the gun tube, namely, translational motion along the gun tube axis and rotational motion (projectile roll) about the instantaneous tangent to the gun tube axis. The remaining degrees-of-freedom depend upon the specific design characteristics of the projectile. As a minimum, they include the four degrees-of-freedom associated with projectile pitch, yaw and lateral translations, and are defined in S relative to S_0 . Additional degrees-of-freedom are formulated in each S_i relative to S for the purpose of tracking relative motions between the principal and secondary projectile components.

2. Equations of Motion

Treating each projectile component as a rigid body, the equations which describe in-bore motion are obtained by applying the principles of linear and angular momenta to each component, in the form

$$m \bar{a} = \bar{F} \quad (1)$$

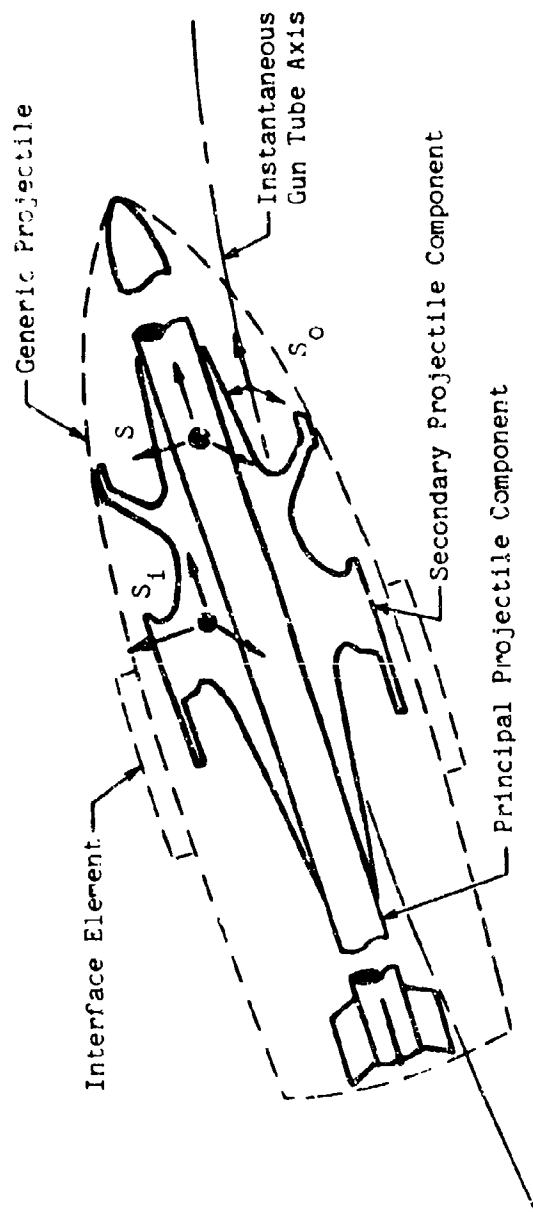


Fig. 1 - Generic Projectile Traveling in Flexible Gun Tube

$$\frac{d\bar{H}}{dt} = \bar{M} \quad (2)$$

where,

m - component mass

\bar{a} - total acceleration of component c.g.

\bar{F} - resultant load acting on component at its c.g.

\bar{H} - total angular momentum of component about its c.g.

\bar{M} - resultant moment acting on component about its c.g.

In general, the vectors \bar{a} and \bar{H} incorporate relative motions between projectile components, component motions relative to the gun tube and gun tube motions relative to inertial space. The vectors \bar{F} and \bar{M} incorporate loadings due to component weight, propellant gas and "ram" air pressures and projectile/bore and component interfacial contact.

Since, in general, gun tube motion and projectile/bore interfacial loads (which are functions of gun tube motion, as well as projectile motion relative to the gun tube) are not known a priori, Eqs. (1) and (2), applied to each projectile component, must be solved simultaneously with the equations of a compatible gun dynamics formulation, such as DYNACODE-G [1]. Indeed, such simultaneous solution is further mandated by the objective to assess the mutual effects of projectile/gun-tube interaction during in-bore motion and, in particular, at shot-exit. For present purposes, we shall assume the availability of a compatible gun dynamics simulation and restrict our attention to development of the in-bore motion formulation.

Eqs. (1) and (2) comprise an equation set which, as noted above, is to be applied to each applicable projectile component. Hence, the specific design characteristics of the projectile dictate the required number of such equation sets, as well as the constraints within each set and between sets. For example, considering a conventional round, Eqs. (1) and (2) applied to the projectile main-body comprise the only required equation set. Whereas, considering a sabot round with "n" sabot-segments, Eqs. (1) and (2) are applied to the penetrator and to each sabot-segment; resulting in "n + 1" equation sets.

Typically, constraints within an equation set relate to the number of degrees-of-freedom permitted a particular projectile component. Whereas, constraints between equation sets relate to the loadings transmitted across component interfaces. In addition, the specific design characteristics of the gun-tube bore dictates constraints with regard to projectile roll and/or torque transmission at the projectile/bore interface. Hybrid cases employing slip-ring or slip-clutch arrangements are not excluded but, rather, must be given special accommodation in the projectile characterization at the slip-ring or clutch interface.

2.2 Applied Loads and Moments

As was noted above, the loads and moments entering Eqs. (1) and (2)

for each projectile component include contributions due to component weight, propellant gas and "ram" air pressure, and projectile/bore and component interfacial contact. The latter loadings (due to interfacial contact between projectile components) may be viewed as internal loadings within the projectile system and eliminated (via combination of the individual sets of equations) in favor of a single set of projectile "system" equations. This approach, which has the advantage of reducing the number of equations requiring simultaneous solution, is adopted here.

Considering projectile weight loading, the weight of each projectile component acts vertically downward at its respective c.g. and, hence, contributes to \bar{F} without contribution to \bar{M} .

Considering projectile/bore interfacial contact, it is assumed that the rear interface element is oversized and in continuous contact with the bore, while the forward interface element is either also oversized or sub-caliber -- with allowance for impact and rebound with the bore. Hence, the rear interface element transmits continuous loadings which contribute to both \bar{F} and \bar{M} ; whereas, depending upon the specific projectile design, the forward interface element transmits either continuous or impulsive loadings.

Continuous loading of an oversized interface element includes projectile/bore interfacial friction, torque transmission (in a rifled-bore application) and radial compression. Impulsive loading of a sub-caliber interface element gives rise to "jump" conditions (sudden increments) on projectile linear and angular momenta which are evaluated by applying Eqs. (1) and (2), integrated with respect to time, to the projectile component undergoing impact.

Finally, considering loadings due to propellant gas and "ram" air pressure, it is assumed that these pressures are known functions of time only and, furthermore, that they are uniformly distributed over the respective projectile surfaces over which they act. Such "effective" hydrostatic pressures generate resultant loads acting at the geometric center of, and directed perpendicular to, the respective projectile/bore sealing planes over which they act. Hence, allowing for general projectile motion relative to the bore, these resultant loads contribute to both \bar{F} and \bar{M} .

3. APPLICATION TO A CONVENTIONAL ROUND FIRED IN A RIFLED-BORE GUN TUBE

The application considered here has been presented in detail in [2]. Hence, only salient features are repeated here for completeness.

3.1 Analytical Development

For the purposes of this application, the projectile is characterized as follows:

- (i) *the projectile consists of a main-body, rotating band and bourrelet;*
- (ii) *the projectile main-body behaves as a rigid body of finite*

geometry and inertia;

- (iii) the rotating band behaves elastically, with allowance for deformation in the plastic regime; radial elastic deformation is characterized by a Winkler foundation model, rendering a radially directed projectile/bore interfacial load distribution (with local magnitude determined by resultant local radial displacement) which varies circumferentially around the bore, as well as longitudinally along the length of the interface; it is noted that the latter variation gives rise to the so-called rotating band "foundation" moment;
- (iv) the bourrelet behaves elastically, with allowance for impact and rebound with the bore;
- (v) eccentricity is permitted between the projectile c.g. and geometric center;
- (vi) the projectile is permitted six degrees-of-freedom relative to the gun tube (whose motion is unrestricted), namely, three independent rotations of its main-body about its c.g. (corresponding to projectile pitch, yaw and roll relative to the gun tube) and three independent translations of its c.g.

In view of the above characterization, Eqs. (1) and (2) are applicable to the projectile main-body ε d, furthermore, comprise the only required projectile-component equation set.

Letting \bar{r}_0 denote the instantaneous position vector of S_0 relative to S' and \bar{r}_{cg} the position vector of S relative to S_0 , the instantaneous position of the projectile c.g. relative to S' , namely \bar{r} , may be written as

$$\bar{r} = \bar{r}_0 + \bar{r}_{cg} \quad (3)$$

Allowing S_0 angular velocity, $\bar{\omega}_0$, relative to S' and differentiating Eq. (3) with respect to time, there results the expression for \bar{a} ($= d^2\bar{r}/dt^2$) in the form

$$\bar{a} = \bar{a}_0 + \bar{a}_{cg} + 2 \bar{\omega}_0 \times \bar{v}_{cg} + \dot{\bar{\omega}}_0 \times \bar{r}_{cg} + \bar{\omega}_0 \times (\bar{\omega}_0 \times \bar{r}_{cg}) \quad (4)$$

where \bar{a}_0 denotes the translational acceleration of S_0 relative to S' , \bar{v}_{cg} and \bar{a}_{cg} respectively denote the translational velocity and acceleration of the projectile c.g. relative to S_0 , and $\dot{\bar{\omega}}_0$ denotes the angular acceleration of S_0 relative to S' .

For computational purposes, Eq. (1), with \bar{a} as given in Eq. (4), is most conveniently expressed in component form relative to the triad of S_0 . The interested reader is referred to [2] for details of this exercise. The results, presented as Eq. (35) in [2], are

$$\left. \begin{aligned}
 F_{x_0} &= m_p [a_{x_0} - 2 \omega_{z_0} \dot{y}_{cg} + 2 \omega_{y_0} \dot{z}_{cg} - (y_{cg} + \epsilon) (\dot{\omega}_{z_0} - \omega_{x_0} \omega_{y_0}) \\
 &\quad + z_{cg} (\dot{\omega}_{y_0} + \omega_{x_0} \omega_{z_0})] \\
 F_{y_0} &= m_p [a_{y_0} + \ddot{y}_{cg} - 2 \omega_{x_0} \dot{z}_{cg} - (y_{cg} + \epsilon) (\omega_{x_0}^2 + \omega_{z_0}^2) \\
 &\quad - z_{cg} (\dot{\omega}_{x_0} - \omega_{y_0} \omega_{z_0})] \\
 F_{z_0} &= m_p [a_{z_0} + \ddot{z}_{cg} + 2 \omega_{x_0} \dot{y}_{cg} + (y_{cg} + \epsilon) (\dot{\omega}_{x_0} + \omega_{y_0} \omega_{z_0}) \\
 &\quad - z_{cg} (\omega_{x_0}^2 + \omega_{y_0}^2)]
 \end{aligned} \right\} (5)$$

where m_p denotes the mass of the projectile, ϵ denotes eccentricity of the projectile c.g. relative to its geometric center, y_{cg} and z_{cg} denote translational displacements of the projectile c.g. relative to S_0 , and $()_{x_0}$, $()_{y_0}$ and $()_{z_0}$ denote the components of $()$ along the respective axes of S_0 .

Allowing S angular velocity, $\bar{\omega}_{cg}$, relative to S_0 , the total angular velocity of the projectile relative to S' is given by

$$\bar{\omega} = \bar{\omega}_0 + \bar{\omega}_{cg} \tag{6}$$

Differentiating Eq. (6) with respect to time, there results the total angular acceleration of the projectile relative to S' , namely

$$\frac{d\bar{\omega}}{dt} = \dot{\bar{\omega}}_0 + \dot{\bar{\omega}}_{cg} + \bar{\omega}_0 \times \bar{\omega}_{cg} \tag{7}$$

Noting that

$$\bar{H} = \bar{I} \bar{\omega} \tag{8}$$

where \bar{I} denotes the projectile inertia tensor, Eq. (2) is most conveniently expressed (to preclude introducing time derivatives of the elements of \bar{I}) in component form relative to the triad of S . The results of this exercise, presented as Eq. (36) in [2], are

$$\left. \begin{aligned}
 M_x &= I_{xx} \dot{\omega}_x + (I_{zz} - I_{yy}) \omega_y \omega_z + I_{xy} (\omega_x \omega_z - \dot{\omega}_y) - I_{xz} (\dot{\omega}_z \\
 &\quad + \omega_x \omega_y) - I_{yz} (\omega_y^2 - \omega_z^2) \\
 M_y &= I_{yy} \dot{\omega}_y + (I_{xx} - I_{zz}) \omega_x \omega_z + I_{yz} (\omega_x \omega_y - \dot{\omega}_z) - I_{yx} (\dot{\omega}_x \\
 &\quad + \omega_y \omega_z) + I_{zx} (\omega_x^2 - \omega_z^2) \\
 M_z &= I_{zz} \dot{\omega}_z - (I_{xx} - I_{yy}) \omega_x \omega_y + I_{zx} (\omega_y \omega_z - \dot{\omega}_x) - I_{zy} (\dot{\omega}_y \\
 &\quad + \omega_x \omega_z) - I_{xy} (\omega_x^2 - \omega_y^2)
 \end{aligned} \right\} (9)$$

where $()_x$, $()_y$ and $()_z$ denote the components of $(\bar{\quad})$ relative to the respective axes of S, and I_{xx} , I_{xy} , ..., I_{zz} denote the elements of \bar{I} written relative to S.

The motion parameters appearing in Eqs. (5) and (9) are defined in [2], without restriction on magnitude, in terms of gun tube motion parameters, rifling twist and projectile motion parameters relative to the gun tube. Noting that for most practical applications projectile pitch, ψ , and yaw, ϕ , relative to the gun tube are generally small, although not necessarily negligible, greatly simplifies the angular velocity and acceleration expressions entering Eq. (9), as well as the development of the force and moment expressions entering both Eqs. (5) and (9). Adopting this approach, Eqs. (5) and (9) result in a system of six simultaneous, non-linear, first order, ordinary differential equations for the determination of the six unknowns y_{cg} , z_{cg} , ψ , ϕ ; projectile roll, ϕ_0 , (or equivalently, projectile velocity along the gun tube axis, v_p), and the torque transmitted across the rotating-band/bore interface, T , as developed in [2].

To accommodate bourrelet/bore impact, Eqs. (1) and (2), integrated with respect to time, are written in the form

$$m_p \Delta \bar{v} = \hat{F} \tag{10}$$

$$\Delta \bar{H} = \bar{\ell} \times \hat{F} + \hat{T} \tag{11}$$

where $\Delta()$ denotes the "jump" (or sudden increment) due to impact, $\bar{\ell}$ denotes the position vector of the impact point relative to the projectile c.g., \hat{F} denotes the impulsive load generated at the bourrelet/bore interface, and \hat{T} denotes the impulsive torque simultaneously generated at the rotating-band/bore interface due to the rifling constraint.

Expanding Eqs. (10) and (11) in component form relative to S_0 and S respectively, and introducing the rifling constraint and coefficient of restitution and, in addition, assuming that the increment in gun tube momentum is negligible compared with the corresponding increment in projectile momentum, there results a set of seven simultaneous, linear, algebraic equations for the determination of the seven unknowns $\Delta \dot{y}_{CG}$, $\Delta \dot{z}_{CG}$, $\Delta \dot{\psi}$, $\Delta \dot{\phi}$, $\Delta \dot{\phi}_0$ (or equivalently, Δv_p), the radial component of the impulsive load, \hat{R} , and the magnitude of the impulsive torque, \hat{T} , as developed in [2].

Hence, Eqs. (5) and (9), in conjunction with the "jump" conditions described above, comprise the complete formulation for the in-bore motion of a conventional round fired in a rifled-bore gun tube. As presented in [2], the solution technique requires monitoring projectile motion as prescribed by Eqs. (5) and (9) to detect the onset of projectile/bore impact, implementing the "jump" conditions at impact, and continuing with Eqs. (5) and (9) between rebound and the onset of the next impact.

3.2 Correlation with Experimental Data

In order to assess the merits of the model developed, Mr. James O. Pilcher II and Dr. James N. Walbert of the Mechanics and Structures Branch, Interior Ballistics Laboratory, U.S. Army Ballistic Research Laboratory, Aberdeen Proving Ground, MD, provided in-bore radar doppler data for firings of two distinct 37mm projectile designs from a specially configured test weapon. The projectile designs consisted of solid, steel cores with copper rotating bands and sub-caliber, steel bourrelets. The test weapon consisted of a fully instrumented 37mm rifled-bore gun tube, with a constant twist of 25 calibers per turn and an in-bore projectile travel of 72.5 inches. To minimize gun tube motion, the system design incorporated a heavy, fixed-collar supported near the muzzle.

The model equations were applied to the test weapon and programmed in MBASIC for execution on the APPLE II+™ computer, with CP/M™ operating system. In addition, radial stiffness of the rotating band was modeled employing an elastic/plastic thick-walled tube analysis and "ram" air pressure was modeled via quasi-steady application of the 1-D shock tube relations.

The model was exercised first for the purpose of determining pertinent friction and engraving data via correlation with experimental data for non-balloting rounds. Employing these data, the model was then exercised to predict in-bore behavior of balloting rounds; identified by the existence of secondary peaks in its radar doppler "waterfall" plot [3,4]. Model predictions of the frequency of bourrelet/bore impacts correlate well with the experimentally derived frequency of secondary peaks, particularly in the mid-section of the gun tube. However, poorer correlation was realized in the neighborhood of the muzzle, which may reflect the effects of bore wear and dynamic erosion of the rotating band (neither of which are accounted for within the model). For illustrative purposes, a typical plot depicting model predictions of projectile yaw versus pitch for a balloting round is presented in Fig. 2.

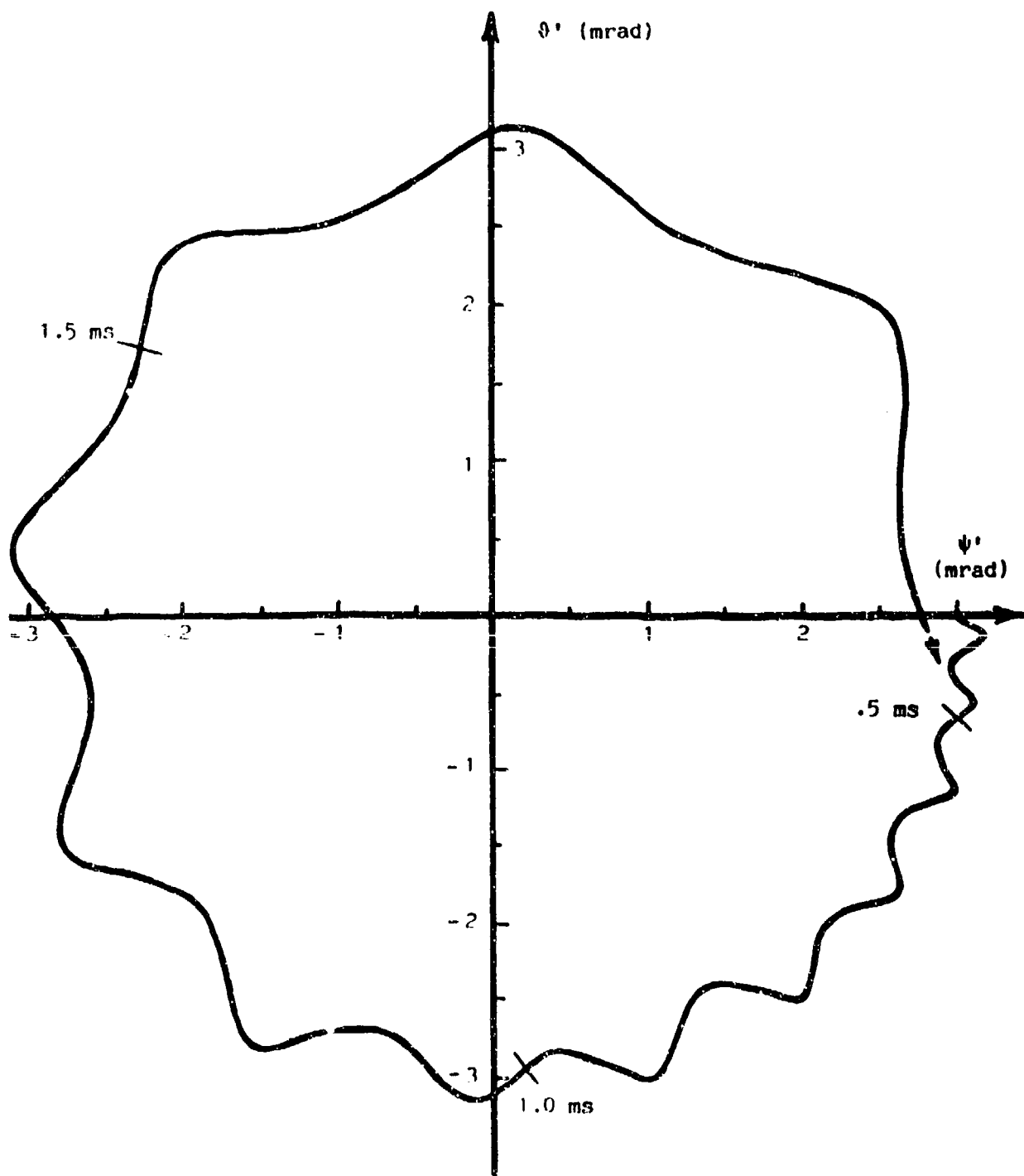


Fig. 2 - Model Prediction of Projectile Yaw vs. Pitch (Relative to S')

Several general observations cited in [2] regarding model predictions for balloting rounds are worthy of repeating here. First, the onset of balloting is dictated by the state of the projectile when fully engraved, as well as the presence of mass eccentricity. Second, model output for balloting rounds reveals high frequency content and large magnitudes in projectile/bore interfacial loading and transverse linear and angular velocities. Insight into the origin of the high frequency content is gained by examination of the expressions for the transverse loads and moments generated at the rotating-band/bore interface. Computation of rotating band "effective" radial and "foundation" moment stiffnesses correlate well with model output frequencies -- indicating that balloting motions are governed primarily by the physical design characteristics of the rotating band. In particular, three distinct frequencies were readily discernible in the balloting motion of the projectiles considered; a dominant frequency of approximately 5,000 Hz, dictated primarily by the response frequency of the rotating band in the "foundation" moment mode; a higher, superimposed frequency of approximately 50,000 Hz, dictated primarily by the radial response frequency of the rotating band; and finally, a much lower frequency of approximately 700 Hz, discernible as amplitude modulation of the dominant frequency and primarily attributable to the interior ballistics pressure and projectile/bore interfacial friction loads. Third, gyroscopic stabilization has a marked effect on the attenuation of balloting; affecting the loads transmitted through the rotating band and bourrelet, as well as the linear and angular velocities of the projectile throughout its in-bore travel and, in particular, at shot exit. Fourth, overall balloting motion as predicted by the model is of more consistent nature in terms of frequency content than was indicated in the experimental data provided, especially as the projectile approaches the neighborhood of the muzzle; which may warrant including the effects of bore wear and dynamic erosion of the rotating band, as noted above. A final observation, although speculative at this point, is nevertheless noteworthy. Gun tube motion predictions based on theoretical simulations generally contain considerably lower frequency content than do corresponding experimental data. Perhaps this disparity, which to date has been viewed by many investigators as an experimental anomaly, arises as a consequence of mutual projectile/gun-tube interaction. Indeed, the relatively high projectile/bore interfacial loads found to exist in a balloting situation lends credence to this speculation.

4. APPLICATION TO A SABOTED ROUND FIRED IN A SMOOTHBORE GUN TUBE

4.1 Analytical Development

For the purposes of this application, the projectile is characterized as follows:

- (i) *the projectile consists of a penetrator, $n \geq 2$ sabot-petals, an undersized, segmented, forward bore-riding surface, and an oversized, continuous, rear bore-riding surface;*
- (ii) *the penetrator and sabot-petals behave as rigid bodies of finite geometry and inertia;*
- (iii) *the rear bore-riding surface behaves elastically, with allowance for deformation in the plastic regime; radial*

elastic deformation is characterized by a Winkler foundation model (as described for the rotating band in Section 3);

- (iv) *each segment of the forward bore-riding surface behaves elastically, with allowance for impact and rebound with the bore;*
- (v) *the penetrator is permitted six degrees-of-freedom relative to the gun tube (whose motion is unrestricted), namely, three independent rotations of the penetrator about its c.g. (corresponding to pitch, yaw and roll) and three independent translations of its c.g.;*
- (vi) *each sabot-petal is permitted an additional degree-of-freedom to accommodate symmetric, as well as asymmetric petal "opening" relative to the penetrator during in-bore motion; achieved via pivoting of the sabot-petal about its rearmost contact with the penetrator.*

In view of the above characterization and the considerations presented in Section 2, Eqs. (1) and (2) are applied to the penetrator and to each sabot-petal; resulting in a system of "n + 1" equation sets.

As in the previous application considered, the kinematic relations between S_0 and S' incorporate gun tube motions, as well as two of the six degrees-of-freedom of the penetrator relative to the gun tube, namely, translational motion along the gun tube axis, v_p , and roll, φ_0 . The remaining four degrees-of-freedom of the penetrator relative to the gun tube, namely, the two translational displacements, y_{cg} and z_{cg} , of the penetrator c.g. relative to S_0 , and the two Euler angles ψ and ϑ (corresponding respectively to penetrator pitch and yaw) are formulated in S relative to S_0 . Allowing for asymmetric petal opening relative to the penetrator, the additional "n" degrees-of-freedom of the system are formulated in S_i ($i=1,2,\dots,n$) relative to S . Hence, there results a system of "n + 6" degrees-of-freedom.

The relative orientation of the i^{th} sabot-petal as it pivots about the penetrator is as depicted in Fig. 3. Referring to Fig. 3, \bar{F}_p and \bar{M}_p , and \bar{F}_i and \bar{M}_i denote the resultants of the applied loads and moments acting respectively at the penetrator and i^{th} sabot-petal c.g.'s. \bar{F}_{ip} and \bar{M}_{ip} (indicated as dashed) denote respectively the resultant interfacial load and moment acting on the i^{th} sabot-petal at the pivot interface, with equal and opposite reactions (not shown in the figure) acting on the penetrator.

Applying Eqs. (1) and (2) to the penetrator, there results the single equation set

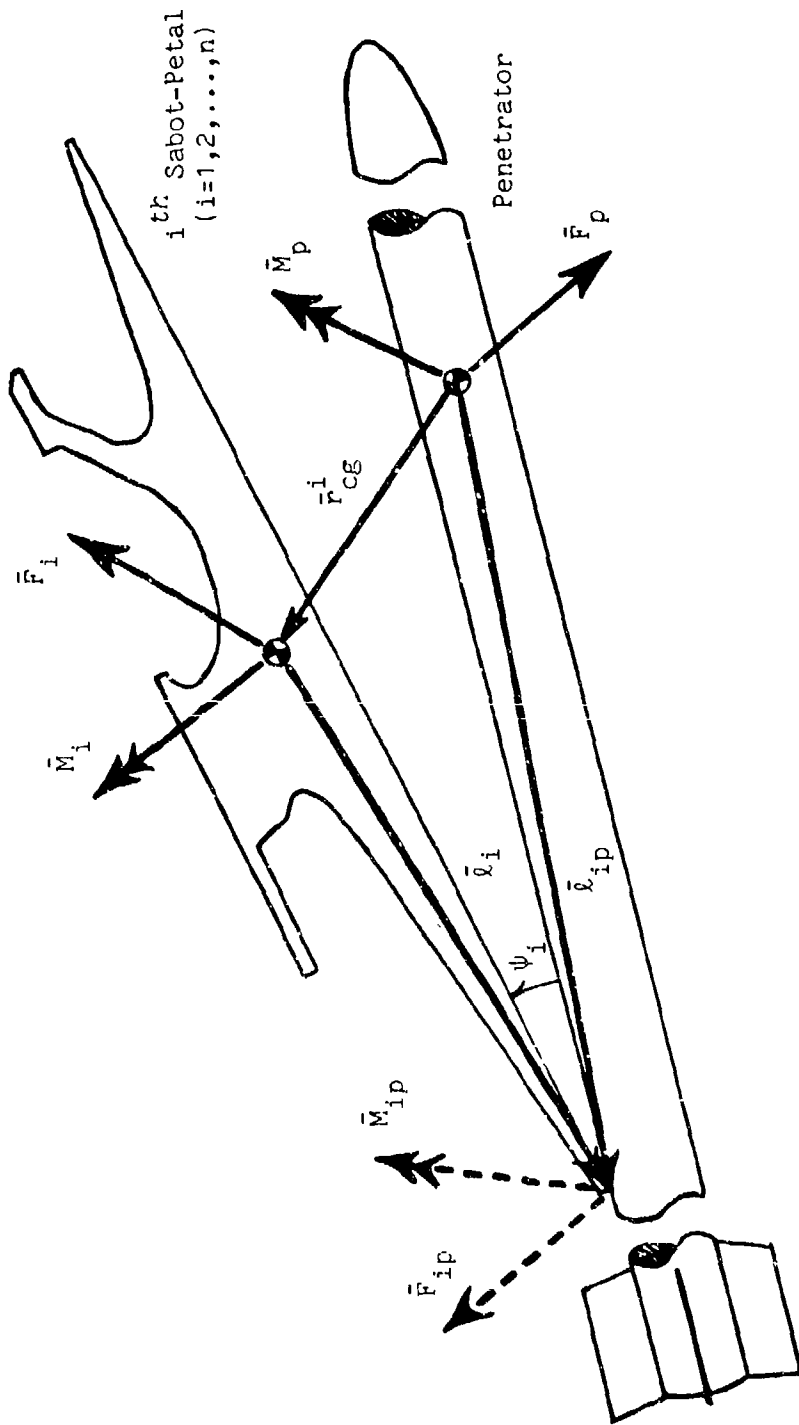


Fig. 3 - Orientation of i^{th} Sabot-Petal Relative to Penetrator

$$\left. \begin{aligned} m_p \bar{a}_p &= \bar{F}_p - \sum_{i=1}^n \bar{F}_{ip} \\ \frac{d\bar{H}}{dt}^p &= \bar{M}_p - \sum_{i=1}^n [\bar{M}_{ip} + \bar{l}_{ip} \times \bar{F}_{ip}] \end{aligned} \right\} \quad (12)$$

whereas, applying Eqs. (1) and (2) to each sabot-petal, there results the "n" equation sets

$$\left. \begin{aligned} m_i \bar{a}_i &= \bar{F}_i + \bar{F}_{ip} \\ \frac{d\bar{H}}{dt}^i &= \bar{M}_i + \bar{M}_{ip} + \bar{l}_i \times \bar{F}_{ip} \quad (i=1,2,\dots,n) \end{aligned} \right\} \quad (13)$$

Assuming sufficient interfacial load and moment between the penetrator and i^{th} sabot-petal to preclude all but the relative pivoting motion depicted in Fig. 3, Eqs. (12) and (13) are solved subject to the constraint that the component of the interfacial moment resisting pivoting motion is provided by the elasticity of the interface element (e.g., retaining ring). That is, the "n" (scalar) constraint equations

$$\bar{M}_{ip} \cdot \hat{k}_i = -c \psi_i \quad (i=1,2,\dots,n) \quad (14)$$

where c denotes the "spring" stiffness of the interface element resisting pivoting motion.

Eliminating the interfacial loads and moments in Eqs. (12) thru (14), there results the projectile "system" equation set, consisting of two vector plus "n" scalar equations (or equivalently, "n + 6" scalar equations), in the form

$$\left. \begin{aligned} m_p \bar{a}_p + \sum_{i=1}^n m_i \bar{a}_i &= \bar{F}_p + \sum_{i=1}^n \bar{F}_i \\ \frac{d\bar{H}}{dt}^p + \sum_{i=1}^n \left[\frac{d\bar{H}}{dt}^i + \bar{r}_{cg}^i \times m_i \bar{a}_i \right] &= \bar{M}_p + \sum_{i=1}^n \bar{M}_i + \sum_{i=1}^n \bar{r}_{cg}^i \times \bar{F}_i \\ \left[\frac{d\bar{H}}{dt}^i - \bar{l}_i \times (m_i \bar{a}_i - \bar{F}_i) - \bar{M}_i \right] \cdot \hat{k}_i &= -c \psi_i \quad (i=1,2,\dots,n) \end{aligned} \right\} \quad (15)$$

which are to be solved simultaneously for the "n + 6" unknowns v_p , φ_0 , y_{cg} , z_{cg} , ψ , ϑ , and ψ_i ($i=1,2,\dots,n$).

Retaining the previous definitions, the translational and angular accelerations of the penetrator relative to S' are as given in Eqs. (4) and (7), with \bar{a} replaced by \bar{a}_p and $\bar{\omega}$ replaced by $\bar{\omega}_p$, respectively.

Letting \bar{r}_i denote the instantaneous position vector of S_i relative to S' , the translational acceleration of the c.g. of the i^{th} sabot-petal, namely \bar{a}_i , is obtained following the procedure outlined in Section 3. That is, noting that

$$\bar{r}_i = \bar{r}_p + \bar{r}_{cg}^i \quad (16)$$

there results, differentiating with respect to time

$$\bar{a}_i = \bar{a}_p + \bar{a}_{cg}^i + 2 \bar{\omega}_{cg} \times \bar{v}_{cg}^i + \dot{\bar{\omega}}_{cg} \times \bar{r}_{cg}^i + \bar{\omega}_{cg} \times (\bar{\omega}_{cg} \times \bar{r}_{cg}^i) \quad (17)$$

Letting $\bar{\omega}_{cg}^i$ denote the angular velocity of S_i relative to S , the total angular velocity of the i^{th} sabot-petal is given by

$$\bar{\omega}_i = \bar{\omega}_p + \bar{\omega}_{cg}^i \quad (18)$$

Hence, differentiating Eq. (18) with respect to time there results

$$\frac{d\bar{\omega}_i}{dt} = \frac{d\bar{\omega}_p}{dt} + \dot{\bar{\omega}}_{cg}^i + \bar{\omega}_p \times \bar{\omega}_{cg}^i \quad (19)$$

Applying Eq. (8) to S for the penetrator and S_i for the i^{th} sabot-petal (to preclude introducing time derivatives of the inertia tensors), there results for application to Eq. (15)

$$\left. \begin{aligned} \frac{d\bar{H}_p}{dt} &= \bar{I}_p \frac{d\bar{\omega}_p}{dt} \\ \frac{d\bar{H}_i}{dt} &= \bar{I}_i \frac{d\bar{\omega}_i}{dt} \end{aligned} \right\} \quad (20)$$

where \bar{I}_p and \bar{I}_i respectively denote the penetrator and i^{th} sabot-petal inertia tensors.

The applied loads and moments entering Eq. (15) are as defined in the previous application. However, unlike the previous application, the equations in (15) are not separable with respect to preferred coordinates. Hence, the scalar equivalence to Eq. (15), representing the counterpart to Eqs. (5) and (9), requires multiple coordinate transformations involving tedious, algebraic manipulation.

Consideration must also be given here to sabot-petal impact with the bore, as well as with the penetrator. The former is treated via introduction of "jump" conditions for $m \leq n$ sabot-petals impacting the bore, in the form

$$\left. \begin{aligned}
 m_p \Delta \bar{v}_p + \sum_{i=1}^n m_i \Delta \bar{v}_i &= \sum_{j=1}^m \hat{F}_j \\
 \Delta \bar{H}_p + \sum_{i=1}^n [\Delta \bar{H}_i + \bar{r}_{CG}^i \times m_i \Delta \bar{v}_i] &= \sum_{j=1}^m (\bar{l}_{1j} + \bar{r}_{CG}^j) \times \hat{F}_j \\
 [\Delta \bar{H}_j - \bar{l}_j \times m_j \Delta \bar{v}_j + (\bar{l}_{1j} + \bar{r}_{CG}^j) \times \hat{F}_j] \cdot \hat{k}_j &\equiv 0 \quad (j=1,2,\dots,m)
 \end{aligned} \right\} (21)$$

where \bar{l}_{1j} denotes the position vector of the impact point on the j^{th} sabot-petal relative to its c.g.

As in the previous application, assuming that the increment in gun tube momentum is negligible compared with the corresponding increment in projectile momentum, the "jump" conditions in Eq. (21), in conjunction with the introduction of the coefficient of restitution for each impacting sabot-petal, represent a simultaneous system of "2m + 6" scalar equations for the determination of the "2m + 6" unknowns $\Delta \bar{v}_p$, $\Delta \dot{\phi}_c$, $\Delta \dot{y}_{CG}$, $\Delta \dot{z}_{CG}$, $\Delta \dot{\psi}$, $\Delta \dot{\theta}$, $\Delta \dot{\psi}_j$ ($j=1,2,\dots,m$), and the radial component of the impulsive load acting on the j^{th} sabot-petal, namely \hat{R}_j ($j=1,2,\dots,m$).

To accommodate sabot-petal impact with the penetrator requires modifying the corresponding petal constraint equation in (14). The constraint equations in (14) are valid provided either $\psi_i > 0$, or $\psi_i \equiv 0$ with $\dot{\psi}_i \geq 0$. If either of these conditions are violated, which would physically mean that the sabot-petal is permitted to pass through the surface of the penetrator, the corresponding constraint equation in (14) must be deleted, with the corresponding value of ψ_i set equal to zero, and an additional sabot-petal/penetrator interfacial load determined.

Hence, the solution technique requires monitoring penetrator motion, as well as the motions of each sabot-petal relative to both the bore and penetrator, via application of Eq. (15). The "jump" conditions prescribed in Eq. (21) are applied at the onset of one or more sabot-petals impacting the bore, while the constraint equations in (14) are modified as noted above at the onset of one or more sabot-petals impacting the penetrator.

As a final note regarding our treatment of sabot-petal/penetrator impact, a set of "jump" conditions comparable to Eq. (21) could also be introduced, however, in addition to further complicating an already intricate problem, it is observed that most practical designs employ sabot-petal/penetrator interface threads whose meshing on closure generate frictional forces which tend to slow the relative approach. Although these frictional forces have not been taken into account here, the treatment presented here is more amenable to their accommodation (both for closure, as well as opening).

4.2 Application to the XM829 and DM13 Rounds

The model equations developed above were programmed, along with the rear bore-riding surface stiffness and "ram" air pressure models previously described, in FORTRAN 77 for execution on the IBM PC (Model 176 with 8087 Math Co-Processor) under the DOS 2.10 operating system.

The model was exercised first for the purpose of determining pertinent friction and shot-start data via correlation with experimental data provided by the U.S. Army Ballistic Research Laboratory. Employing these data, the model was then exercised for the purpose of comparing the in-bore behavior of the XM829 and DM13 rounds, under both cold and ambient temperature conditions, and for firings in a simulated, rigid, straight gun tube; a simulated, rigid, curved gun tube; and a simulated, moving, curved gun tube. Simulation of the curved gun tube employed an approximation for the first two bending modes of the 120mm gun tube. Simulation of the moving, curved gun tube employed the above approximation, as well as the scaling of 75mm ADMAG gun tube motion data previously determined employing DYNACODE-G. In addition, the model was also exercised for the purpose of identifying XM829/DM13 design differences leading to in-bore behavioral differences.

Model output obtained from these studies are presently being prepared for Honeywell, Inc. Subject to Honeywell's authorization, pertinent findings will be presented at the Symposium.

5. CONCLUSIONS

The model herein developed is applicable to conventional ammunition fired in a flexible, rifled-bore gun tube and sabot ammunition fired in a flexible, smoothbore gun tube. The model predicts general, in-bore "balloting" motions, including impacts and rebounds with the bore. For both ammunition types, flexibility is introduced at interface elements (e.g., rotating band, bourrelet, etc.).

Considering a conventional round, the model is capable of predicting the full six degree-of-freedom motion of the projectile relative to the gun tube; namely, translational motion along the gun tube axis, lateral motions relative to the gun tube, and projectile pitch, yaw and roll. Considering a sabot round consisting of a penetrator and "n" sabot-segments, the model is capable of predicting the full six degree-of-freedom motion of the penetrator relative to the gun tube, as well as asymmetric "opening" of the sabot-segments relative to the penetrator.

Model predictions for "balloting" motions of a 37mm conventional round were correlated with in-bore radar doppler data. Unfortunately, the data samples were limited and corresponding experimental data for a sabot round are not available. Nevertheless, it is expected that the model will prove to be a valuable design aid if used appropriately on a comparative basis.

As previously noted, in order to assess the mutual effects of projectile/gun-tube interaction during in-bore motion and, in particular, at shot-exit, requires the simultaneous solution of the in-bore motion equa-

tions with the equations of a compatible gun dynamics simulation.

ACKNOWLEDGEMENTS

The authors wish to express their appreciation to the U.S. Army Research Office, Durham, NC, and to the U.S. Army Ballistic Research Laboratory, Aberdeen Proving Ground, MD, for their support in the development of the model for application to conventional ammunition, and to Honeywell, Inc., Defense Systems Division, Edina, MN, for their support in the development of the model for application to sabotaged ammunition.

REFERENCES

1. Soifer, M.T. and Becker, R.S., "Gun Dynamics Simulation Model of the 75mm ADMAG Gun System", Proceedings of the Third US Army Symposium on Gun Dynamics, Volume I, pp. I-48 thru I-71, 11-14 May 1982.
2. "Projectile Motion in a Flexible Gun Tube", S&D Dynamics, Inc., BRL Contract Report BRL-CR-536, October 1984.
3. Walbert, J.N., "Techniques for the Analysis of Radar Doppler from Projectiles in the In-Bore and Early Free-Flight Regions", U.S. Army Ballistic Research Laboratory, Aberdeen Proving Ground, MD, (Awaiting Publication).
4. Walbert, J.N., "Analysis of the In-Bore Motion of Several Types of Projectiles", U.S. Army Ballistic Research Laboratory, Aberdeen Proving Ground, MD, (Awaiting Publication).

BENZKOFER

TITLE: Automated Dynamic Analysis of Weapon Systems
PHILIP BENZKOFER
US Army Armament Research and Development Center
Fire Control and Small Caliber Weapon Systems Laboratory
Armament Division, Technology Branch
Dover, NJ 07801-5001

ABSTRACT:

Resolution of hardware problems in armament systems is generally accomplished by a combination of procedures. Certainly the first approach is to utilize experience acquired with the same or similar system, perhaps leading to an obvious correction to the problem. If a solution does not result from this exercise, the next most likely step is to instrument hardware and perform experimental testing. This testing may identify critical areas and or components of the system. Invariably redesign is the best solution. An alternate procedure is to approach the problem from an analytical point of view. This is not to say the analytical approach can replace the first approach, but to rather complement and enhance it. If analysis can be applied in the conceptual, and certainly design, stages, then clearly some costly hardware development and testing can be avoided.

The analytical approach has evolved into a very sophisticated methodology. The state-of-the-art in analysis has advanced to include the automated generation of the equations of motion for mechanical systems. One such equation generating computer code is the Dynamic Analysis Design Systems, or DADS[1]. This code is ideally suited for dynamic analysis of high rate of fire automatic machine guns.

The author's latest application of the code is to an externally powered high rate of fire machine gun. The kinematics and dynamics of critical components such as the bolt and bolt carrier have been analyzed.

The carrier motion is treated as a constraint and appends to the equation of motion of the main gun. The DADS code allows appendage of algebraic constraint equation as functions of time and or displacement. Bolt rotation is treated in a spatial sense in a planar version of the code. This rotation is then analyzed utilizing a constraint equation deriving the relationship between bolt angular displacement and bolt carrier linear displacement. A kinematic study of the chain/track assembly to include stage by stage chain slider position has been conducted.

BIOGRAPHY:

PRESENT ASSIGNMENT: Armament/Weapon/Mechanisms Analysis, US Army Armament Research and Development Center, 1977 to present.

PAST EXPERIENCE: Math Analysis, GEN T. J. Rodman Laboratory, Rock Island, IL, 1966 to 1977.

DEGREES HELD: B.S., Mathematics, Iowa State University, 1965, M.S., Mechanical Engineering, University of Iowa, 1980.

AUTOMATED DYNAMIC ANALYSIS OF WEAPON SYSTEMS

PHILIP D. BENZKOFER, MR.
US ARMY ARMAMENT RESEARCH AND DEVELOPMENT CENTER
FIRE CONTROL & SMALL CALIBER WEAPON SYSTEMS LABORATORY
DOVER, NJ 07801-5001

THE WEAPON SYSTEM

System Definition

The 30-mm Hughes weapon system is mounted on the YAH-64 aircraft shown in figure 1. This analysis addresses strictly the weapon, and the aircraft/weapon interface is not discussed. A view of the system can be seen in figure 2. Figure 3 shows componentry and interface. There are eight major components including the recoil adapters which connect to the turret, one on either side. The turret is considered a ground for the purpose of this analysis. The major components are:

- index drive assembly
- bolt carrier assembly
- chain drive assembly
- recoil adapters
- blast suppressor
- barrel and barrel support
- drive motor
- receiver assembly

Figures 4 through 9 are good references for the following description. The index drive assembly is mounted on the rear top section of the receiver assembly (figure 4). The drive assembly contains a feed sprocket that receives ammunition from the gun transfer assembly. The feed sprocket feeds rounds to the rotor, and in turn, this rotor feeds rounds to the bolt face. The second major component is the bolt carrier assembly, which mounts on the forward track assembly inside the forward section of the receiver (figure 5). The carrier assembly consists of a bolt, bolt carrier, and a firing

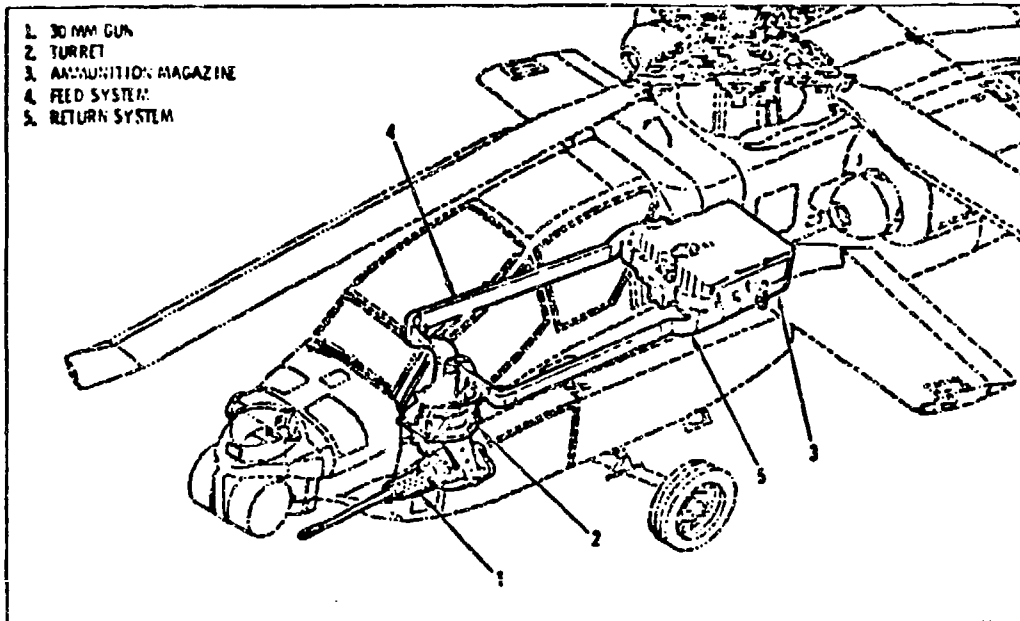


Figure 1. Weapon mounted on aircraft

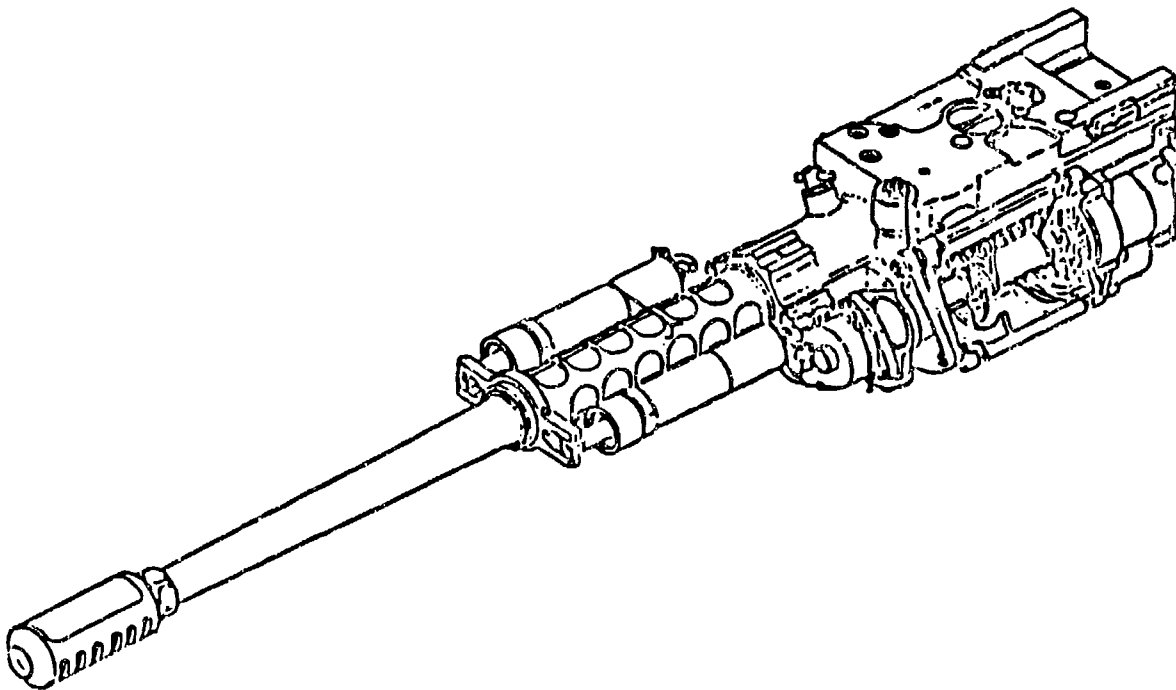
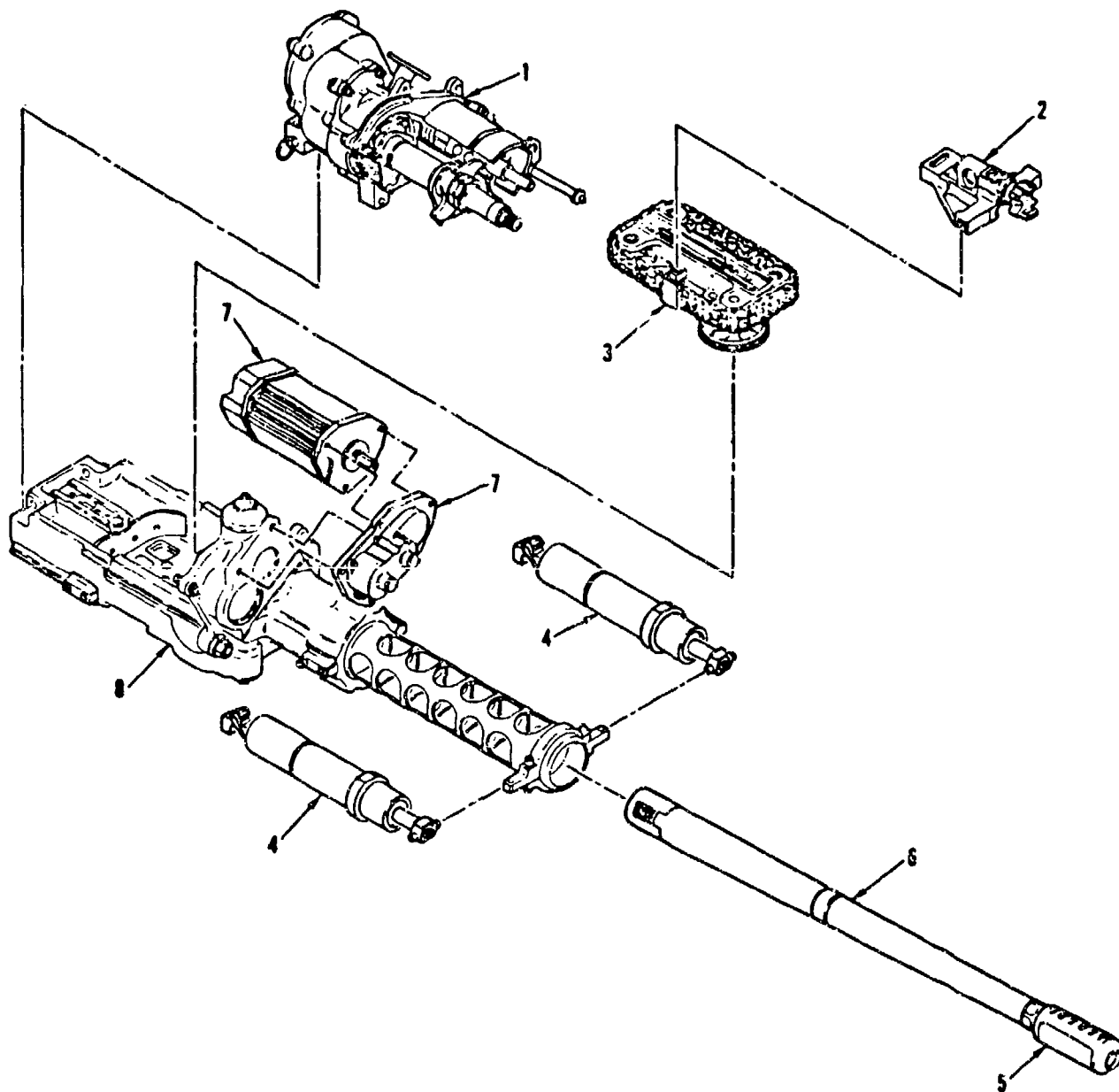


Figure 2. Weapon System

BENZKOFER



1 INDEX DRIVE ASSEMBLY
2 BOLT CARRIER ASSEMBLY
3 CHAIN DRIVE ASSEMBLY
4 RECOIL ADAPTERS

5 BLAST SUPPRESSORS
6 BARREL
7 DRIVE MOTOR
8 RECEIVER ASSEMBLY

Figure 3. Weapon System Componentry

BENZKOFER

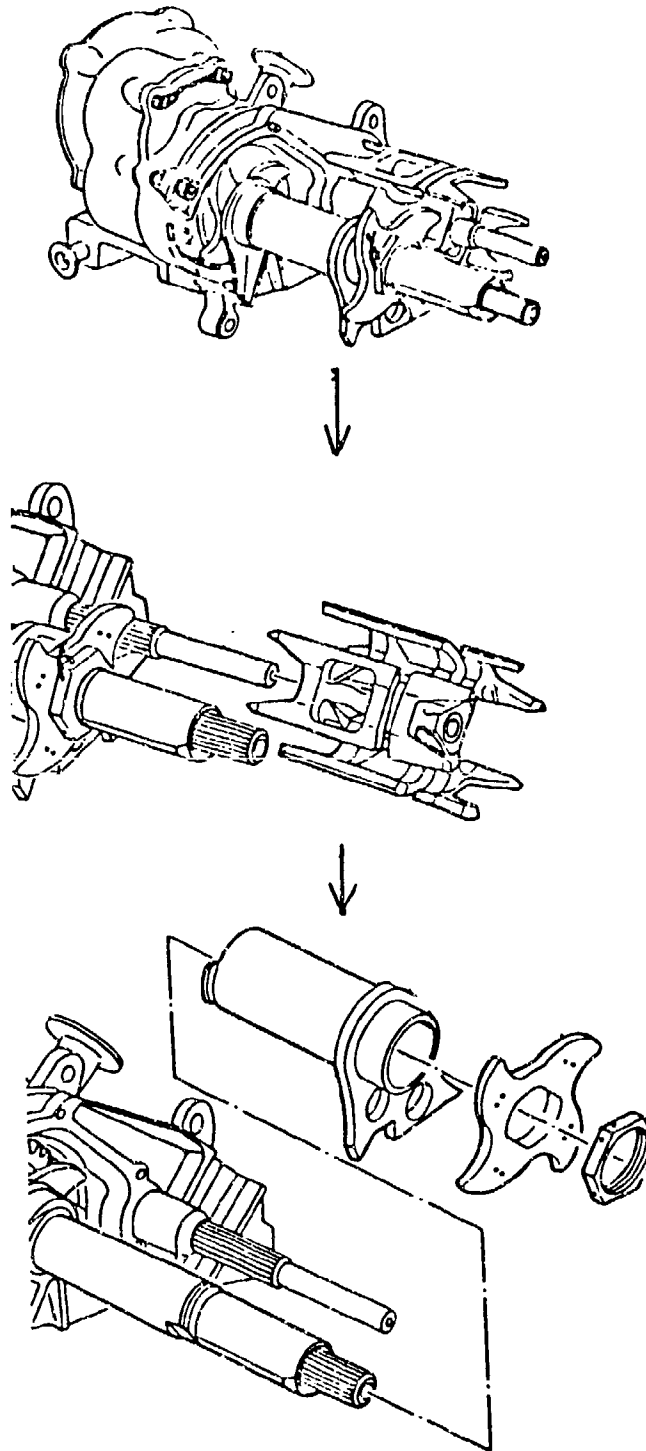


Figure 4. Index Drive Assembly

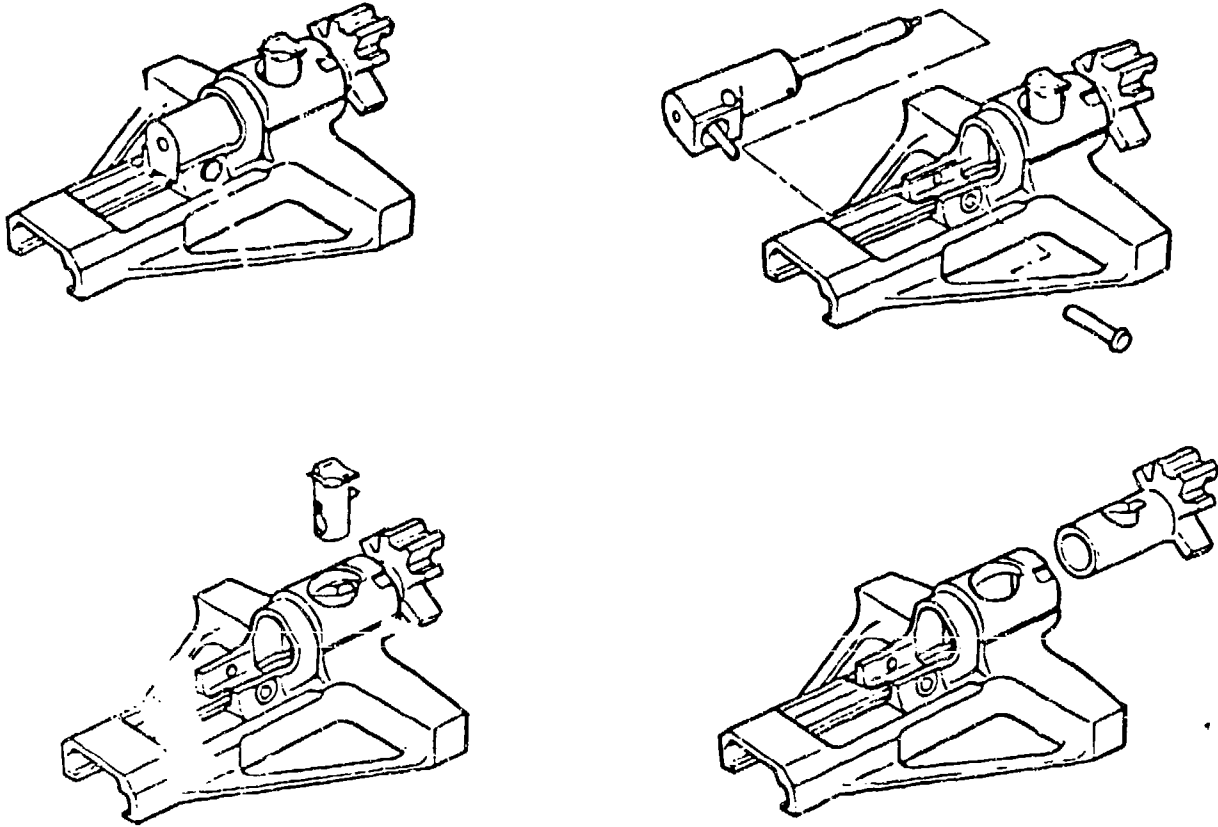


Figure 5. Bolt Carrier Assembly

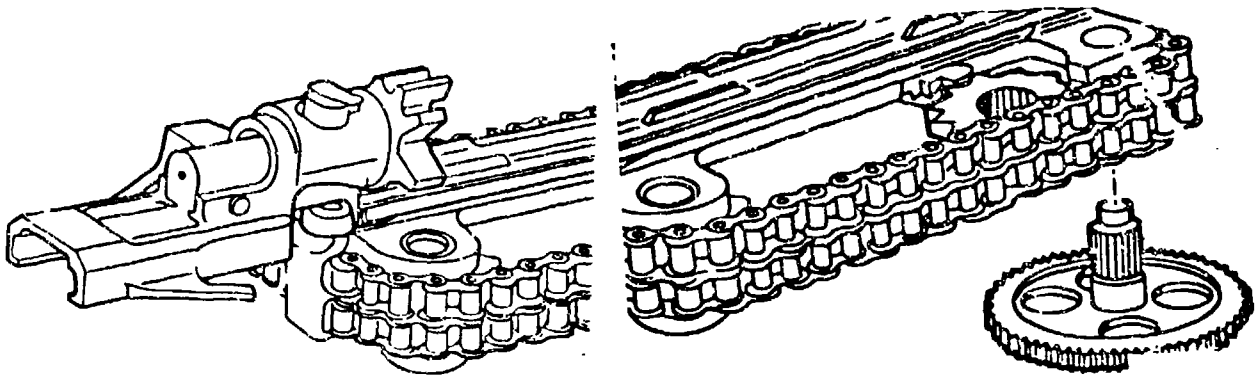


Figure 6. Bolt on Track Assembly

Figure 7. Chain Drive Assembly

pin assembly. The bolt is carried by the bolt carrier and slides back and forth on a track (figure 6). The carrier is driven by a slider mounted on the roller chain of the chain drive assembly. The chain drive assembly consists of a double row roller chain that rides on four sprocket wheels (figure 7). One sprocket drives the chain and the other three simply serve as idlers. One link of the chain has the slider attachment above that engages the track on the bolt carrier bottom. This slider drives that bolt carrier and bolt back and forth as the chain cycles around the sprocket wheels. The two recoil adapters are located on the forward section of the 30-mm gun, one mounted on each side of the gun support (figure 8). At the aft end, these adapters connect to the gun turret. These adapters absorb the recoil force when the gun is fired. The drive motor mounts on the lower section of the receiver assembly and is secured in place by three bolts. The motor is 5.25 horsepower (HP) with a speed of 11,500 revolutions per minute (RPM). This provides the drive power required for gun operation. An electric brake stops the gun in the open bolt position for the next cycle. The receiver assembly slides into place on the cradle of the turret (figure 9). This assembly provides attachment and support for all the gun components.

System Operation

The weapon system of figure 2 is an open bolt and derives all its power from the electric motor. The firing rate is 625 ± 25 shots per minute (SPM). Various burst capabilities are available ranging from 10 up to 550 rounds. A summary of the operation is as follows:

The 30-mm gun incorporates a rotating bolt mechanism that is driven by a chain drive.

A 5.25 HP, AC electric motor, mounted on the receiver, drives the internal mechanism of the gun.

Ammunition feeding, loading, firing, extraction and ejection are controlled by the motor.

The firing pin assembly is mounted in the bolt and is attached to the bolt carrier.

The chain drive mechanism converts rotating gear motion to forward and aft motion of the bolt assembly.

The bolt carrier assembly receives this forward and aft motion, as well as dwell time, from the chain drive via a slider assembly.

The index drive assembly transfers power from the vertical drive shaft to the feed shaft and rotor.

The feed sprocket receives the ammunition from the transfer housing and feeds the ammunition to the rotor.

The rotor places the round into the bolt face.

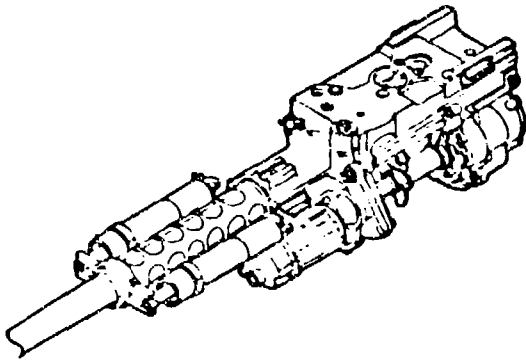


Figure 8. Barrel supports

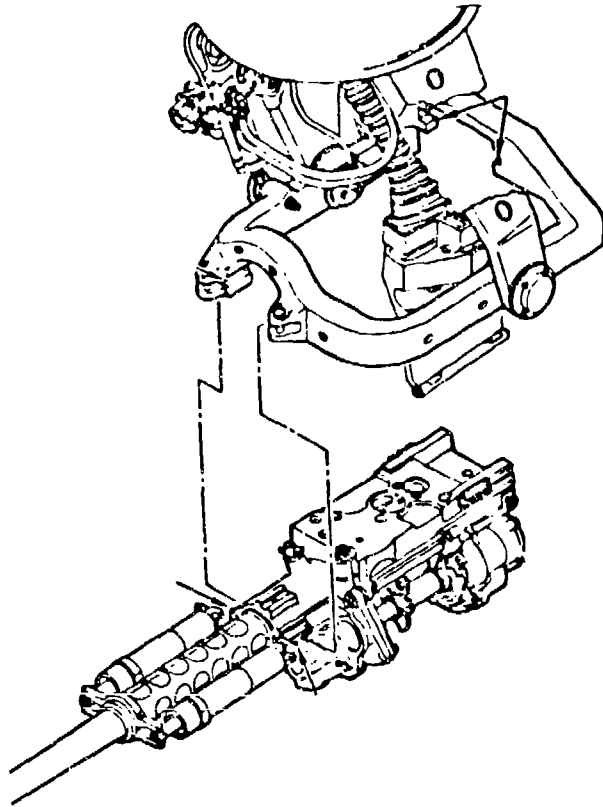


Figure 9. Receiver assembly on cradle

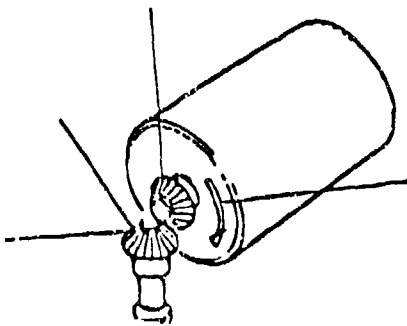


Figure 10. Motor, vertical drive shaft interface

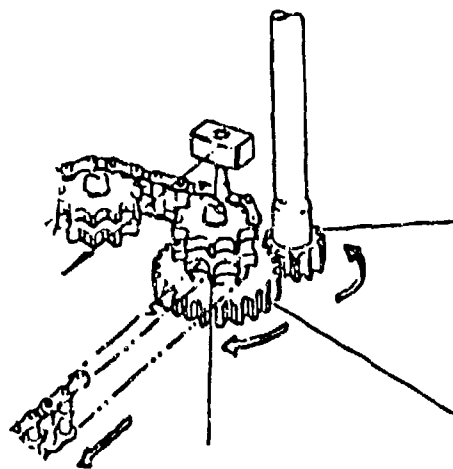


Figure 11. Vertical drive shaft, drive sprocket interface

BENZKOFER

While the bolt carrier is moving forward to the firing position, the bolt is forced by a cam action to rotate into a locked position.

The firing pin then makes contact with the chambered round.

An electrical circuit is completed to fire the round.

The system then has four basic groups:

chain drive

bolt/carrier

feed system

power transmission system

The central part of the chain gun is a double row of roller chains which cycle in a racetrack pattern on four sprockets - one driver and three idlers, as shown in figure 7. An accommodating slot in the bolt carrier provides space for the transversing slider fixed on the chain. The carrier slides on the track. The chain slider provides reciprocating motion to the bolt by acting on the T-slot on the underside of the bolt carrier. This chain then moves the bolt and bolt carrier assembly. As shown in figure 5, the bolt carrier assembly consists of a bolt and bolt carrier. The bolt is carried by the bolt carrier and the bolt cam pin rotates in the cam slot cut in the bolt carrier to lock up with the barrel extension. The bolt carrier moves only fore and aft in an axial direction. All lateral motion of the slider in the transverse slot coincides with dwell time for the carrier for the firing and feeding portions of the cycle. At the forward end, this dwell allows time for the barrel pressure to return to ambient after firing. The firing pin assembly is completely enclosed within the bolt and attached to the bolt carrier. The falling of the firing pin ignites the primer. As the bolt head passes through the locking lugs in the barrel extension, a downward projecting tang on the firing pin is stopped by a block in the carrier track.

Another aspect of operation is the gearing sequence. The bevel gear on the motor shaft meshes with a bevel gear on the vertical drive shaft (VDS) as shown in figure 10. The gear reduction from the motor rpm to the vertical shaft rpm is simply a ratio of gear teeth on each shaft.

$$\text{VDS rpm} = 17/21 (11,500) = 9310 \quad (1)$$

This is then the VDS rpm. At the base of the vertical shaft there is a reduction from the VDS to the drive sprocket as shown in figure 11. This reduction is then

$$\text{drive sprocket rpm} = 18/60 (9,310) = 2795 \quad (2)$$

WEAPON SYSTEM MODELING

Kinematic Analysis

Kinematics is defined as the study of the motion of a mechanical system without regard to forces. The kinematics of the system shown in figure 2 are essentially dictated by the driving motor. The bevel gear pair of the motor and vertical shaft initiate the motion of the driveshaft. This shaft ultimately drives the drive sprocket of the chain drive assembly. The bolt carrier assembly motion then is the result of the drive sprocket rotation and consequent chain rotation. Figure 6 shows the chain and bolt carrier assembly. One of the sprockets is a drive while the other three serve as idlers. A schematic representation of the chain is shown in figure 12. The chain is divided into eight distinct stages. The chain motion is in a clockwise direction as illustrated. Critical dimensions are also shown. Gun system functions are also outlined on the figure. The amount of chain travel is denoted as S and its corresponding values are shown at each stage position. One cycle of travel of the slider represents one firing cycle of the weapon. Figure 13 illustrates the sequence of stages, the values of S and the crank angle θ . One firing cycle will result from four and one half rotations of the drive sprocket. At this point, a stage by stage discussion will be useful. Each stage will be described as well as summaries given of current chain travel, slider position, range of crank angle values and so forth. As the drive sprocket rotates due to motor rpm, the chain is engaged and begins to move in a racetrack type pattern. Note that in stage one, the slider is moving transversely and that the bolt carrier assembly is not moving. After one half rotation of the drive sprocket, the slider moves three inches laterally. The slider sees no rotation during this stage. The position of the slider can be measured in a rectangular cartesian coordinate system. The value of S_1 is defined as $r\theta$, where S_1 is the current value of chain position. Figure 14 gives stage details. Notice the drive sprocket rotates from 180° to 270° , or 90° in stage two. The current crank angle θ increases from an initial value of θ , to a final value, specifically 270° . The total chain travel at the end of stage two is $S_1 + S_2$. Subscripts of S denote stages, S_1 is stage one chain travel, S_2 is stage two chain travel and so on. During this stage the crank angle begins at 270° and rotates through 720° . The chain slider moves in a straight path with no angular motion during stage three. This distance traveled is 7.5 inches. Stage four details are shown in figure 14. Stage five is similar to stage one in total rotation. At the end of this stage the crank has rotated 990° , or nearly three revolutions. Stage six is similar to two and four in that 90° of crank rotation takes place. Stage seven is similar to three, in that the chain slider moves in a straight line path and sees no angular motion. The final stage, eight, is similar to two, four and six as the slider moves in an arc of one fourth of a circle.

RUZVODPP

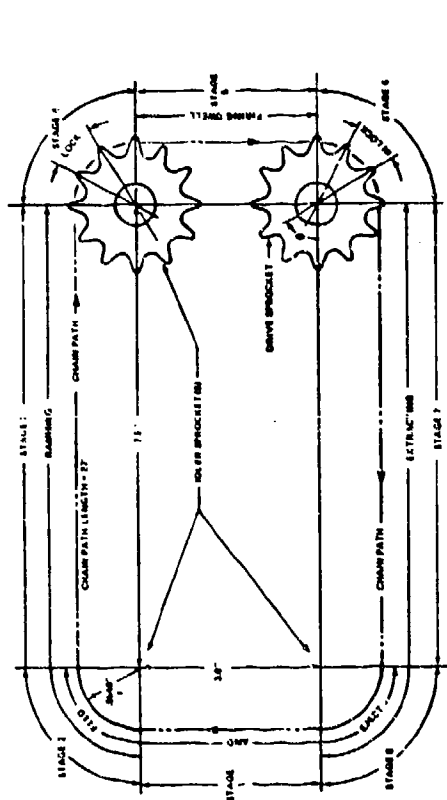


Figure 2. Schematic of RZ38 Chain

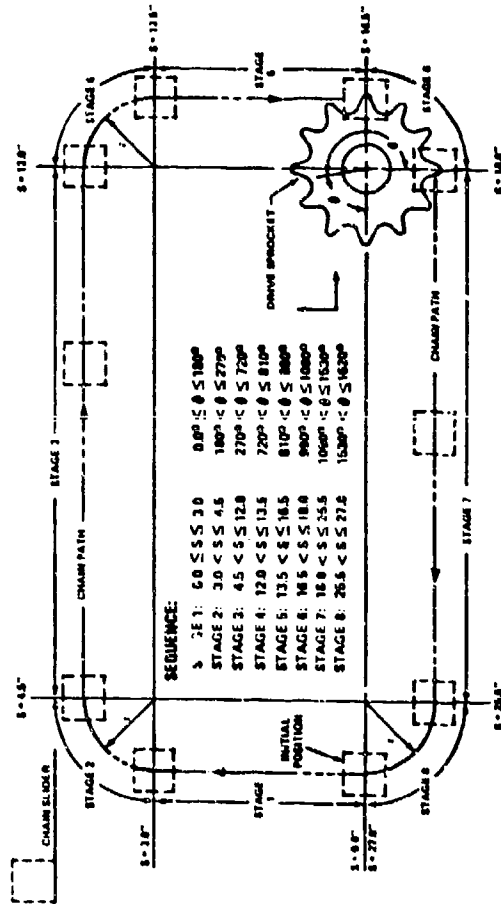


Figure 13. Schematic of chain/chain slider

BENZKOFFER

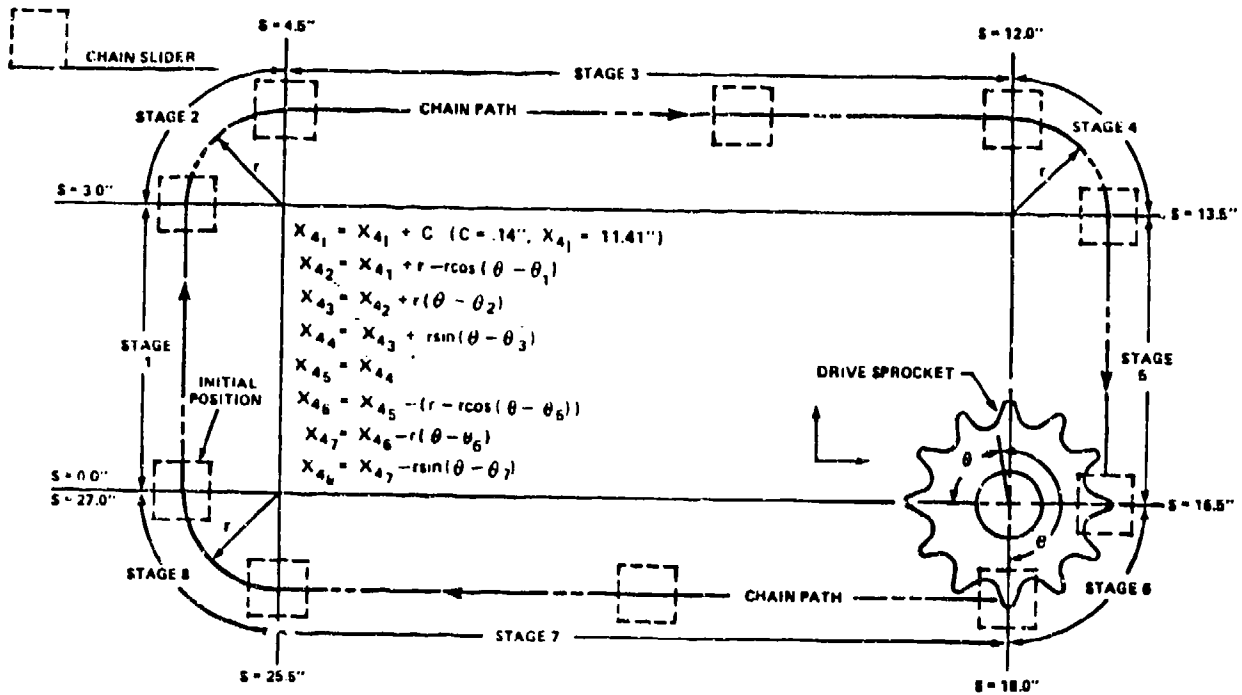


Figure 14. Stage equations

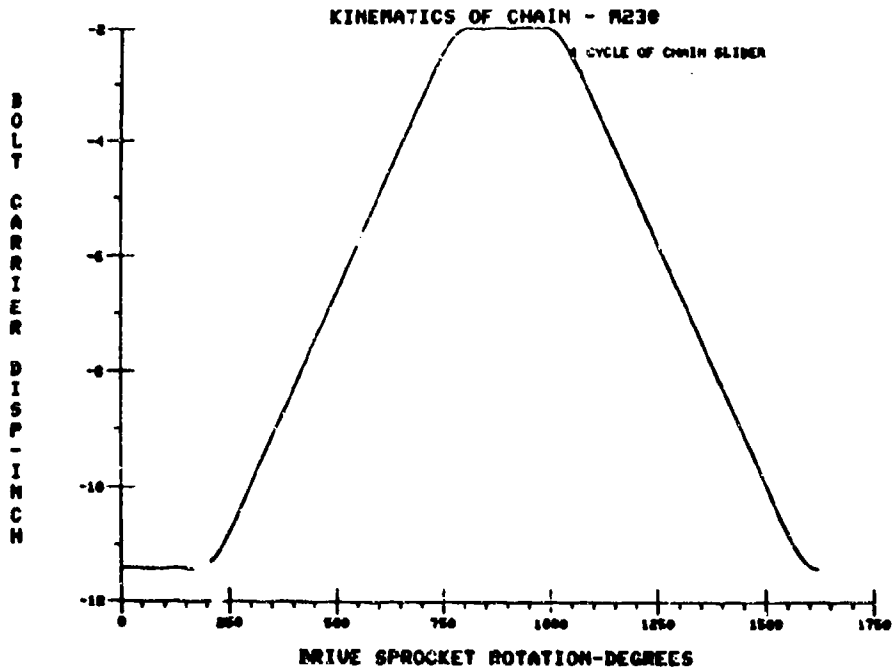


Figure 15. Bolt carrier displacement vs sprocket rotation (degrees)

Kinematic Results

In order to simulate the bolt carrier mechanism motion, a kinematic driver is utilized. The drive angle θ from 0° to 1620° , or 0 radians to 9π radians is incrementally increased. The kinematic model discussed was computerized and coded. Figure 15 gives the bolt carrier displacement in inches versus drive sprocket rotation in degrees. This displacement begins at its initial position and returns to its initial value. Stage one results show no motion as expected while stage two results depict initiation of carrier motion. Stage three motion is linear in shape and continues to be until the initiation of stage four. Displacement in this stage, similarly to stage two, is curvilinear due to the arc type motion of the slider around the corner. At the end of this stage, the maximum forward displacement of the carrier is reached. During stage five, the carrier is stationary and consequently sees no motion. Stage six is identical to four except the motion is curvilinear in the rearward direction. Stage seven is identical to stage three as the motion is linear but in the rearward or aft direction. Stage eight is the final stage and mirrors stage two motion. The bolt carrier has completed one cycle or one round of simulated firing after eight stages of motion.

Dynamic Analysis

The dynamic motion of a weapon system is initiated by externally applied forces, or disturbing forces. These forces are generally the breech forces created by burning propellant gases developed in the chamber and the recoil forces developed by the recoil mechanism. Assuming these are known forcing functions and that weapon system drawing information is available, a computer model can then be prepared. This computerization identifies the rigid masses, or bodies, and their connectivity to other components of the system. In the process of identifying rigid body motion, components can be grouped as composites due to their rigid connections. Such is the case for the 30-mm weapon system of figure 2. For example, the receiver assembly is rigidly connected to the barrel assembly, and so forth. Figure 16 shows a sketch of a schematic model of the weapon system. Each rigid body mass is located from an arbitrary inertial reference frame (IRF) as shown in the figure. This frame gives us an absolute reference from which the defined rigid bodies may be located. Reference frames are defined for each of these bodies, and are called local reference frames. This local system is assumed to be located at the mass center of the body. These local frames of reference are indicated on figure 16.

Quantification of this schematic model is pertinent at this point. The mass located at 3.22 inches from the IRF is a composite of the eight major components listed in the System Definition section with the exception of the bolt carrier assembly, chain drive assembly and recoil adapters. The connectivity between these masses is essentially translational; in other words, they translate with respect to each other. The freedom of motion of the total system is three times the number of defined rigid bodies less the number of defined constraint equations. For this particular model, a constraint equation (due to the gearing process) for the bolt carrier displacement must be defined. Another constraint that needs to be considered is the camming

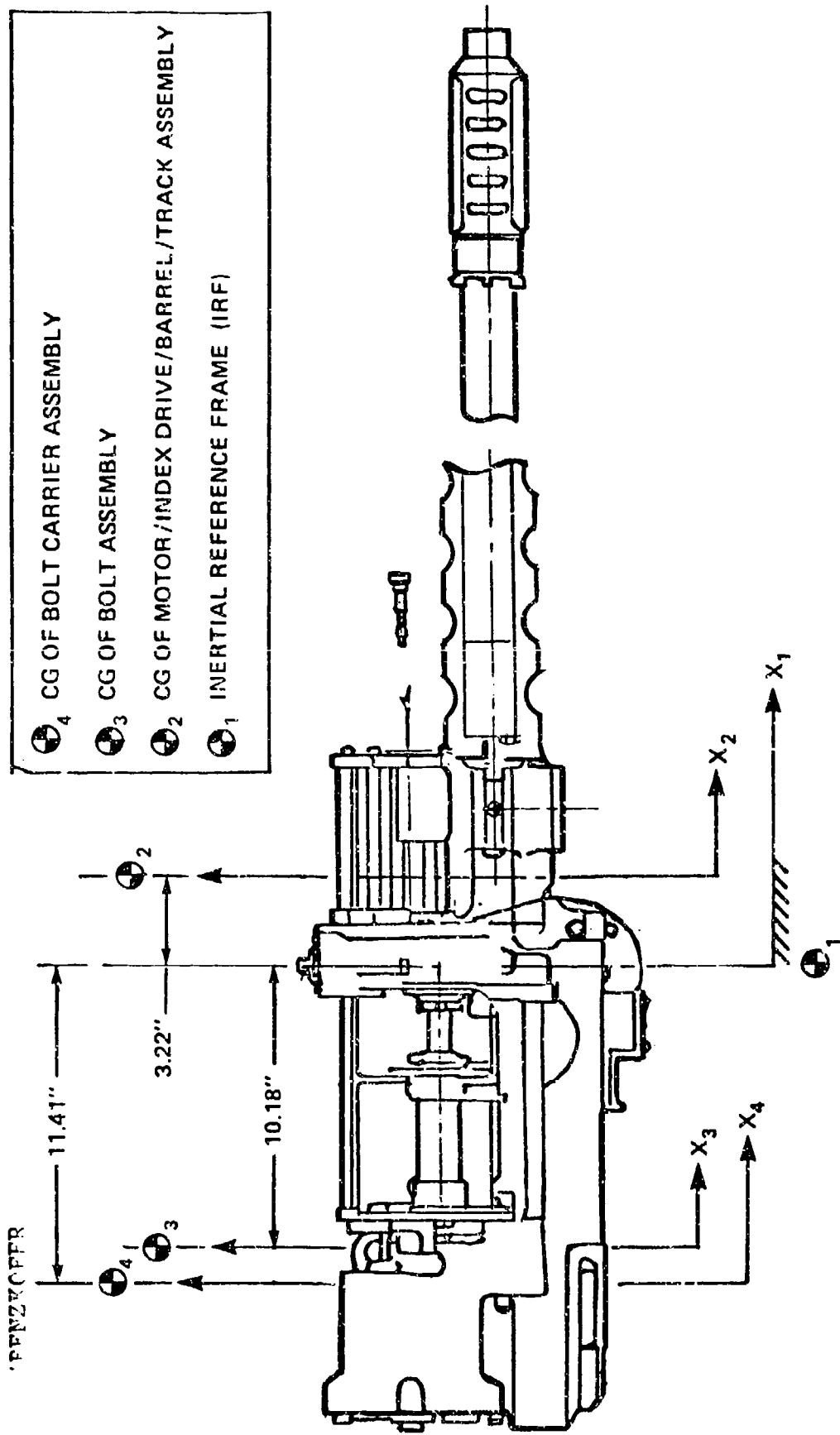


Figure 16. Schematic model of weapon system

action between the bolt pin and the bolt carrier. Figure 5 shows the bolt pin riding in the cam slot cut in the body of the carrier. The purpose of the camming is the closing and opening of the bolt. To achieve a closed system in which the round or projectile can be detonated, the bolt mechanism is utilized. The bolt lugs move through the mating lug opening in the barrel extension and contact the barrel face. The forward motion of the bolt carrier causes the cam pin to ride in the bolt carrier slot and rotate the bolt. The lugs are now rotated and the bolt is essentially locked to the breech or barrel extension. This is commonly called bolt closing. In order to then extract a spent cartridge after weapon firing, this closed bolt must be rotated in the opposite direction and the bolt pulled rearward. The constraint imposed is then the bolt angle rotation as a function of bolt carrier motion. The bolt drawing gives this history, and it is utilized in the computer model.

At this point, a general discussion of the coding of the model is appropriate. The equations of motion of the defined system will be generated by the dynamic analysis design systems code. The number of these equations coincides with the number of defined coordinates, or three for each mass. The equations of constraint for the bolt carrier are exactly the equations shown in the kinematic analysis, figure 14.

In order to utilize the constraint equations of the kinematics section in a dynamic sense, a calculation must be made. The motivation for this derivation is to define θ or drive sprocket rotation as a function of time. Recalling equation (2) of the System Operation section of the report.

$$\text{drive sprocket rpm} = 2795 \quad (2)$$

Then

$$\frac{2795 \text{ rev}}{60 \text{ sec}} = \frac{1 \text{ rev}}{t \text{ sec}} \quad (9)$$

Equivalently

$$\frac{2795 \text{ rev}}{60 \text{ sec}} = \frac{\theta}{2t \text{ sec}} \quad (10)$$

Solving for θ ,

$$\theta = \frac{559}{6} t \quad (11)$$

where t is time in seconds.

This equation for θ will be substituted into all kinematic equations to obtain explicit functions of time for the displacement of the bolt carrier.

At each stage of motion an equation of constraint is defined for bolt carrier motion. At the appropriate time these equations are invoked, since they are explicit, equations of time.

An additional feature of the DADS computer code is the utilization of the Lagrange Multiplier Method for append the algebraic constraint equations to the system differential equations. Advantages of this method, in addition to numerical consideration, is the code gives as output these multiplier values at each reporting time step. These multipliers are related to the measure of the level of force produced due to the constraint on the system. These outputs will be specifically addressed in the results section of this report.

The input forces are the breech and recoil forces. These two inputs are the basis for main gun forward and recoil motion. Negligible motion of the main gun is evidenced in the output. The cyclic time for one round of the weapon, detailed in the System Operation section, is in the range of 90 to 100 milliseconds. The simulation results are detailed in the following section.

Dynamic Results

The overall outputs of the simulation are shown in figures 17 through 28. The acceleration versus time of the main gun is given in figure 17. Similarly, linear and angular displacement, linear and angular velocity and angular acceleration of the bolt versus time are shown in figures 18 to 23. Time varying values of bolt carrier displacement, velocity and acceleration are shown in figures 24 to 26. The main gun motion is slight due to the recoil adapters. Consequently, small velocity values are attained during the cycle. The bolt motion is identical to bolt carrier motion for all stages except during stages four and six, at which time the bolt locks to and unlocks from the barrel extension. From figure 18 note that in stage one there is no bolt motion, and similarly for a portion of stage four. During stage five, dwell time is required for bolt lock and firing, consequently there is no bolt motion during this time. In stage six, unlocking of the bolt from the barrel extension results in bolt motion. During stage seven the bolt is being carried by the bolt carrier. The bolt also extracts and ejects the cartridge case. This action is not modeled. At the end of stage eight the bolt is in its initial position for the next round. Figure 19 shows the angular position of the bolt over the full cycle. The effects of bolt locking, dwell and unlocking are shown. The linear velocity of the bolt is shown in figure 20. There is no bolt velocity during stage one. In stage two the velocity increases to a peak value of approximately 300 inches per second. During stage three this velocity remains constant. In stage four the velocity goes to zero. The bolt is closed and at rest. In stage five there is no bolt velocity due to dwell time. During stage six the linear velocity increases to approximately -300 inches per second the negative sign denoting the rearward direction. During stage seven this velocity is maintained and in stage eight this value goes to zero. This is the end of the cycle. The angular velocity is shown in figure 21. The velocity is zero except at bolt lock and unlock. The maximum rate is approximately ± 500 radians per second. The linear and angular accelerations are

BENZOCOPPER

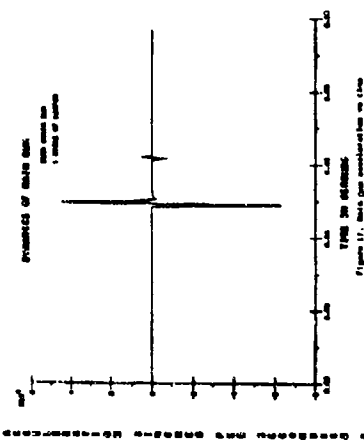


Figure 11. Belt velocity distribution in time

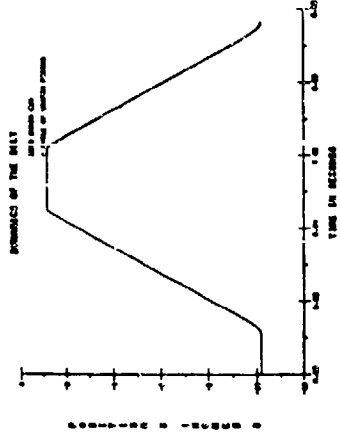


Figure 12. Linear belt acceleration in time

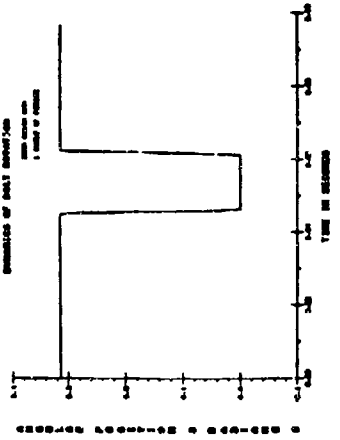


Figure 13. Angular belt displacement in time

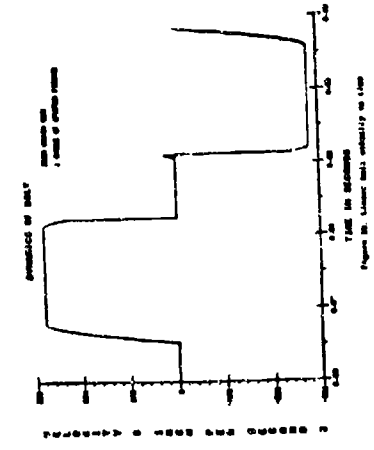


Figure 14. Linear belt velocity in time

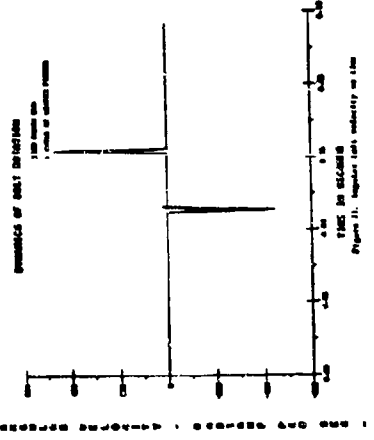


Figure 15. Angular belt velocity in time

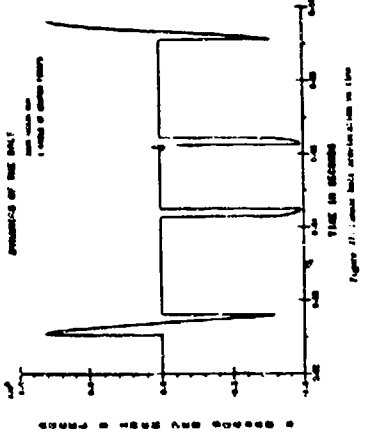


Figure 16. Linear belt displacement in time

shown in figures 22 and 23. The magnitude of angular acceleration in figure 23 is larger for bolt locking than bolt unlocking, due to the fact the carrier velocity is greater at locking time. Bolt carrier displacement, velocity and acceleration are shown in figures 24 through 26. Peak velocities are approximately 280 inches per second, and depict typical chain gun velocity profiles.

The last two figures, 27 and 28, represent the values of a term called the Lagrange Multiplier discussed earlier. The results of their influence on the system equations are shown in these multipliers. As a parallel, suppose one has a revolute or pin joint connection between two bodies. Then in the DADS code the two multipliers are calculated for this joint connection - one representing X-direction and the other Y-direction. These values turn out to be the reaction forces at the pin connection. In a similar manner, then, measures of constraint are calculated for the equations discussed above and are shown in figure 27. A second constraint built into the model is the equation representing the effect of the cam path. The results of the inclusion of this equation into the model is output of the Lagrange Multiplier as shown in figure 28. These multipliers can be resolved into physical units with appropriate vector and matrix multiplication, but are not in this paper.

CONCLUSIONS AND RECOMMENDATIONS

This modeling effort was based on constrained bolt carrier motion. If the model were to incorporate the modeling of gear interface and interaction, then some detailed results could be attained. This assumes that gear modeling modules are available for dynamic analysis. Extensive mathematics have been generated in the area of gears, higher pair joints and so forth. However, extensive dynamic algorithms embellished in a code are not available. This type of dynamics modeling capability would be a strong feature. The application in a sense drives the need for complex equation generating computer codes.

This particular effort emphasized constraint equation application to two main areas, these being bolt lockup and unlock and enforced displacement as a function of time. The DADS code was utilized to accomplish this analysis by incorporation of constraint equations as an appendage to the governing equations of motion for the system. Resolution into actual forces needs to be addressed.

This mathematical model is a good working model for the 30-mm chain gun. The model can serve as a basis for future model development in support of the lightweight compact armament system (LWCAS) program. Considerations may be identification of critical components in terms of their performance and/or material. Determination of system malfunction due to mechanical or thermal failure may well be important. In anticipation of parametric evaluations of componentry and connectivity, this analysis effort has identified basic component groups and simulated their performance. The input or driving force to the system was described as carrier constraint requirements. This input could be motor torque and consequent drive sprocket reaction. As an initial level of effort, the system has been defined and

PENZKOTER

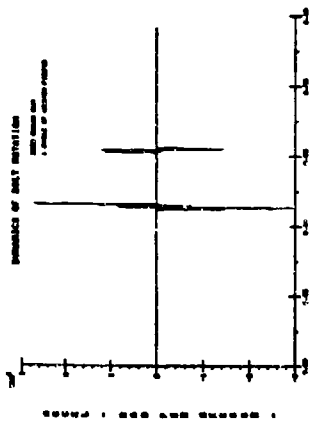


Figure 13. Angular rate contribution to line

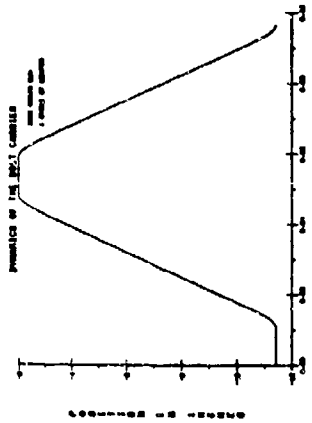


Figure 14. Bolt rotation displacement to line

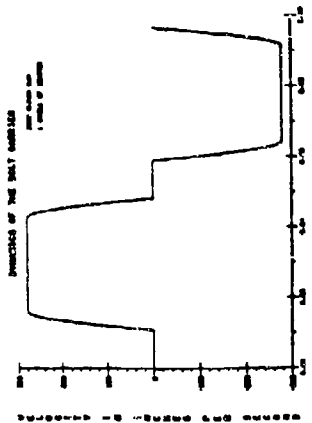


Figure 15. Bolt rotation velocity to line

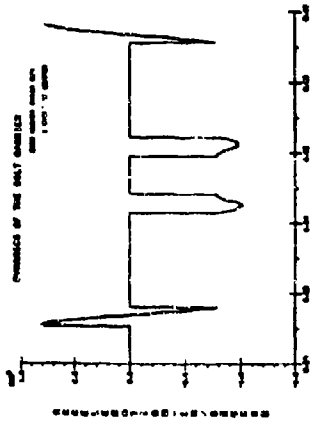


Figure 16. Bolt carrier contribution to line

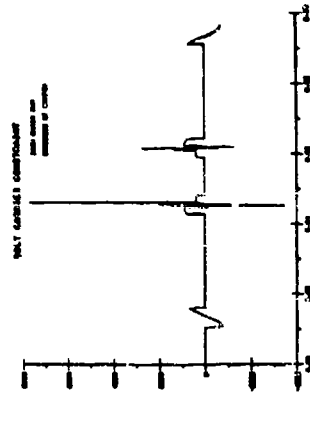


Figure 17. Bolt carrier contribution to line

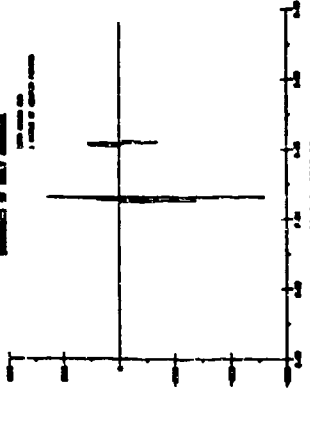


Figure 18. Bolt carrier contribution to line

BENZKOFER

modeled and simulation results have been obtained. Continuous interface as an integral part of the lightweight program will be essential to improve and extend the modeling effort. As extensions are made to models such as in the lightweight program, modules or libraries of subsystem and/or componentries can be developed, improved, extended and optimized.

Reference

1. Wehage, R.A. and Haug, E.J., "Generalized Coordinate Partitioning for Dimension Reduction in Analysis of Constrained Dynamic Systems," ASME Journal of Mechanical Design, Vol. 104, No. 1, 1982, pp. 247-255.

Effects of Recoiling Mass
Reduction of Active Recoil Control

Authors: Philip E. Townsend, ARDC, FSL
Robert F. Gartner, Honeywell, Inc.

The trend in aircraft armament has been toward increased impulse to the point that mechanical recoil control is marginally acceptable in terms of peak force levels. Exploratory concept testing has shown that peak recoil forces generated by automatic cannons can be reduced as much as 75% using hydraulic activators controlled by a microprocessor. This concept has been demonstrated on both the 30MM Chain Gun (M230) and 30MM Gatling Guns (GAU-13/A) using many of the same components. The latest thrust in aircraft armament design is towards drastic component weight reduction. This trend forces a trade-off between peak recoil force and recoil travel. This paper will address the issues relating to this trade off as applied to the Constraints of the Family of Light Helicopters (LHX) Armament Concepts.

TOWNSEND
GARTNER

EFFECTS OF RECOILING MASS REDUCTION ON
ACTIVE RECOIL CONTROL

PHILIP E. TOWNSEND*
US ARMY ARMAMENT RESEARCH AND DEVELOPMENT CENTER
FIRE CONTROL & SMALL CALIBER WEAPONS SYSTEMS LABORATORY
DOVER, NJ 07801-5001

ROBERT F. GARTNER
HONEYWELL, INC.
EDINA, MINNESOTA 55436-5000

1. INTRODUCTION

There is an ever present need to improve weapon systems. This paper offers a means of improved effectiveness by the routes of increasing the hit probability of existing weapons or upgunning with new weapons. The technical area for future improvement is the interface area of weapon recoil dynamics and gun pointing control.

In the recent past, very little could be done to relieve the sharp recoil loads without serious degradation to the operation of the gun. There are .50 caliber machine guns that will not fire consistently when mounted on recoil adapters that smooth out the recoil forces. This applies to the entire class of self-powered guns. However, the externally powered guns will fire regardless of the recoil loads. This feature now enables recoil force control to be separated from gun function gaining the benefits of lower and smoother forces on the supporting structure.

The paper is divided into two parts:

Part 1 - Describes the recoil device and its relative benefits applied to the 30mm M230 weapon on a proposed mounting for the LHX helicopter.

Part 2 - Describes how to use closed form equations for a simple analysis that enables the designer to make tradeoffs between peak recoil force and recoil travel.

Part 1. Active Recoil Control versus Reduced Recoiling Mass

The basic consideration of the armament design in mounting the subsystems for helicopters is to minimize the peak forces transmitted to the helicopter. These forces typically have a very fast rise time as the gun fires to some peak force that is determined by the recoil control design; This is also the point of maximum recoil. At this point the stored energy of the recoil spring drives the weapon back through its original position and beyond with some amount of overshoot, again depending on the recoil control design. Current helicopter design practice limits the peak force to about 3000 pounds. Because of the vibrational nature of these repeated peak forces and counter recoil forces, certain firing rates must be eliminated from consideration due to the helicopter's sensitivity to certain harmonic frequencies. This problem was so severe in some early helicopter armament developments that dangerous tail assembly motion was recorded as well as vibration in the crew compartment that shook needles off of flight instruments and blackened the gunner's eyes as he attempted to sight the weapon on the target.

It was this situation together with the trend toward ever increasing weapon impulse with each new attack helicopter development that brought about the consideration of active recoil control. The objective of the active control system is to control the weapon dynamics during the firing process to reduce the peak forces to a minimum. Early studies indicated that with proper design of the spring mount and controlling the firing point of the weapon, a significant reduction was possible. Unfortunately, this control of the firing point is difficult with externally powered weapons because of the inertias involved with starting and stopping the weapon mechanism.

It was at this point that two changes were incorporated into the concept. The first was out-of-battery firing of the weapon. This was a concept that had been evaluated for artillery weapons to reduce recoil forces. The concept was to drive the recoiling mass forward (out-of-battery) until its momentum was equal to one-half the momentum of the ammunition. When fired at this point, one-half the energy of the ammunition is used to stop the forward motion of the weapon's mass, the other half of the ammunition's energy drives the recoiling mass to its original position (battery). This concept not only reduced the recoil peak force but also minimized recoil displacement. The other change to the normal mount concept was the addition of a computer controlled hydraulic actuator to control the weapon's motion. The computer was provided sensor data on the gun's dynamics, ammunition impulse and firing rate. This data allowed the computer to control the hydraulic actuator which in-turn controlled the gun's motion. The computer could anticipate the gun's firing point and could correct any variations from the norm established by the basic design.

This concept successfully demonstrated a 75% reduction in peak recoil force using both the M230 30mm automatic cannon that is mounted on the Apache

TOWNSEND
GARTNER

Attack Helicopter and the 30mm GAU-13/A four-barrelled version of the gatling gun mounted on the A-10 Close Support Fighter. The same computer (Motorola 6800), hydraulic servo-valves, and sensors were used on both guns even though the GAU-13/A has an impulse nearly three times that of the M230. Naturally the hydraulic actuators had to be designed for the particular application to provide the proper force levels and stroke differences. The weight, impulse and firing rates of these two weapons were such that a reasonable recoil stroke could be achieved with the design.

But what happens when the interrelated factors of the design does not allow the optimum solution? The latest entry into the attack helicopter arena is the LHX, an ultra-light weight, highly complex weapon system planned for fielding in the 1990's. This helicopter is to fly nearly fifty demanding missions that requires high mobility and maneuverability. The attack version is targeted to weigh 8000 pounds, significantly less than today's attack helicopters, but it is to have equal to or greater performance. The design will incorporate the latest technology in the application of composite materials to reach this weight goal and to achieve the desired dynamic performance characteristics. In the case of the armament subsystems, the demand is for more firepower coupled with reduced weight. Figure 1 illustrates the armament weight allocation associated with the current Cobra helicopter and from a straight percentage of weight distribution what this would be for a 350 pound LHX armament system.

| | COBRA ALLOCATION (LBS) | LHX ALLOCATION (LBS) |
|--------------------------|-----------------------------------|---------------------------------|
| GUN/DRIVE | 156.5 | 80 |
| RECOIL ADAPTER | 12.0 | |
| TURRET | 177.0 | 100 |
| CONTROL BOXES (3) | 28.0 | |
| FEEDER | 22.5 | |
| CHUTING | 16.0 | 70 |
| MAGAZINE | 101.0 | |
| SUBSYSTEM, EMPTY | 507 | 250 .. |
| AMMUNITION (750) | 427 | 100 (130) |
| LINKS | 88 | |
| SUBSYSTEM TOTAL | 1022 | 350 |

FIGURE 1

TOWNSEND
GARTNER

One of the early candidate guns for the LHX was the M230 automatic cannon used on the Apache Attack Helicopter and tested with the active recoil control concept described above. The current weight of the M230 is approximately 122 pounds. Analysis of the gun design has lead its developer to project a weight reduction to 85-90 pounds which is near the projected weight allocation shown in Figure 1.

But what does this reduced mass do to the dynamics in the active recoil control concept?

Another factor effecting the recoil control design is reduced rate of fire. The LHX will carry a reduced quantity of ammunition to meet weight constraints. The projected design philosophy is to increase the weapon accuracy to maintain the same level of effectiveness with fewer rounds of ammunition. In transitioning from the traditional area fire design to get as many rounds on target in the shortest time to the point target design of high first round hit probability, the rate of fire can be reduced. By reducing the rate of fire the loading on the aircraft is reduced as well as reducing the power required to drive the weapon.

But what does reduced firing rate do to the dynamics in the active recoil control concept?

Both factors - - reduced recoiling mass and reduced firing rate - - increase the weapon displacement. However, this displacement must be limited because it affects the volume of the weapon turret which is normally the way the weapon is mounted in the helicopter. The turret approach is used to allow wide angles of coverage and fast response attack of targets in the helicopter's perimeter.

The volume subtended by the recoiling weapon establishes the volume of the turret which in turn relates to the weight and volume required to mount the subsystem in the helicopter.

Another aspect of the recoil travel is the distance the gun translates along its aim line. Maintaining that aim line accurately during the translation is more difficult as the distance increases.

The recoil travel also effects the ammunition feed system interface. The ammunition must travel through a chute from the magazine used to store the ammunition to the gun which is being directed over wide excursion angles by the turret. This feed chute must be allowed to flex in roll and fan positions as it travels the route from the magazine to the ammunition feeder of the weapon. Long recoil travel can contribute to reduced reliability of the feeding operation as the ammunition is transported along the complex path of the chute that culminates at a rapidly oscillating weapon. It is obvious that the designer is left with a trade off situation with the design parameters of recoiling mass, rate of fire, recoil distance and peak recoil force for a

TOWNSEND
GARNER

particular round of ammunition. As indicated previously Part 2 of this paper describes a simple analysis using closed form equations to enable the designer to evaluate these tradeoffs.

Part 2. Trade Off Analysis

The forces that are applied to the weapon from the gun mount are the ones being discussed. The pressure forces are not considered in detail as the recoil adapters prevent the pressure forces from the firing of the gun from reaching the mount. The pressure forces are considered as impulses applied to the recoil adapters at the firing rate.

The two main modes of gun recoil motion that are considered are in-battery and out-of-battery. These are described briefly as follows:

In-battery: This is the normal recoil operation in which the gun does not move until the gun fires. Since it is the classical recoil motion that is used with the first automatic weapons it is well understood and easily visualized. Its major advantage is its simplicity - a spring damper system is all that is needed. Another advantage is that the recoil stroke is short. The tradeoff is large recoil forces and short recoil motion versus lower forces and longer recoil motion. As indicated above short recoil is desirable, unfortunately the resulting forces are very large and oscillatory - ideal for stimulating vibrations. Also the large accelerations of the gun responding to the large recoil forces make the connection to the external feed complicated.

Out-of-battery: In this mode the gun recoil motion starts before the gun fires. This mode requires an intelligent system that synchronizes gun firing with proper recoil motion. The gun actually fires at the end of the forward stroke. The main advantage of this mode is the recoil forces can be reduced to the lowest constant value consistent with the gun firing rate and the ammunition impulse. It also has the shortest recoil stroke for a constant recoil force level. The disadvantage is the synchronizing system that requires controllable force actuators to be used instead of simple spring mechanisms.

The simple formulae presented are applicable to automatic guns firing at constant rates of fire. The first assumption is that a recoil force is constant during the time of its application. This assumption eliminates the complexity of including the force variation with recoil travel which requires knowledge about the type of force actuator. The second assumption is that the gun forces are applied continuously during a firing burst.

The first equation defines the average recoil force. It is equal to the impulse of the ammunition multiplied by the firing rate in shots per second. This equation, based upon the conservation of momentum, holds for both recoil modes. This force is used as the basis to compare the forces of both recoil modes. This is the lowest possible recoil force and can only be

reached in the out-of-battery firing mode.

$$F_{AVG} = I \cdot R \quad \text{Equation 1}$$

where:

F_{AVG} = average force (pounds)
 I = ammunition impulse (pound-seconds)
 R = shots per second (1/seconds)

The second equation relates the dither distance (recoil travel) to the firing rate, recoiling mass and ammunition impulse. This equation is based on the out-of-battery firing mode operating at the average force level. It represents the largest travel necessary to smooth out the recoil forces. It is used as a standard to compare recoil dither distances.

$$X_{CF} = I / (8 \cdot M \cdot R) \quad \text{Equation 2}$$

where:

X_{CF} = Constant Force Recoiling Dither Distance (feet)
 M = Recoiling mass (slugs)

By simple algebraic manipulation the recoil forces for both the in and out-of-battery modes can be written in terms of the average force, F_{AVG} and constant recoil dither distance, X_{CF} .

Figures 2 and 3 illustrate the result of these manipulations. Figure 2 shows the constant force, F_{AVG} , over the firing cycle for one shot, T . F_1 and F_2 illustrate the trade off of peak recoil force versus recoil travel. X_{CF} is the recoil travel based on equation 2 and X is the travel if the peak force F_1 is applied for time T_1 and F_2 is applied for time T_2 . Figure 3 is actually two curves. The upper curve is the ratio of F_1/F_{AVG} versus the X/X_{CF} . The time ratio T_1/T , that F_1 is applied found on the upper border of the plot. T_2/T , the complement of T_1/T , is found on the lower border.

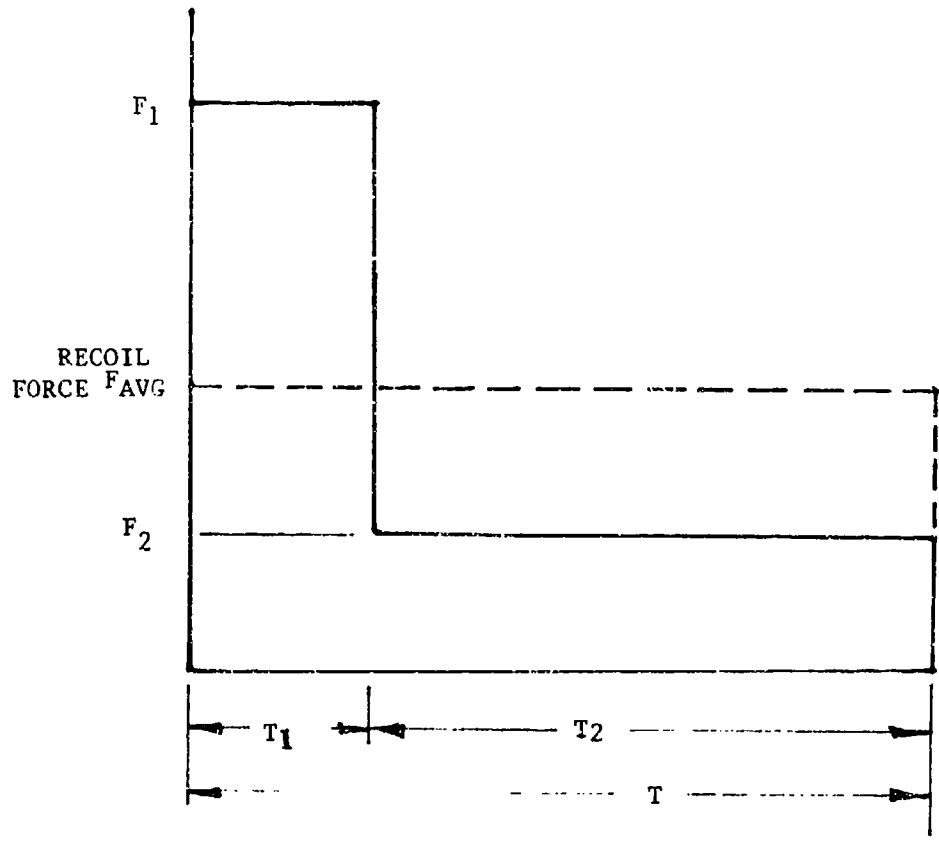
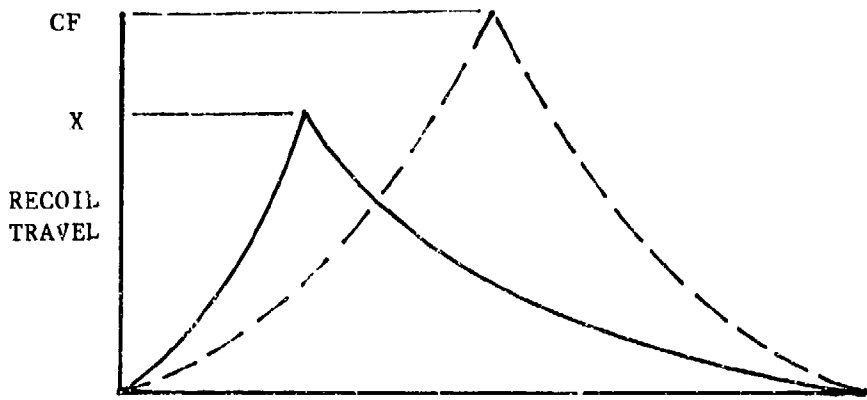
An example of how Figure 3 can be used is as follows:

Constant Force Condition

The M230 Weapon with muzzle brake is to fire at 625 shots per minute. The data for this condition is:

- | | |
|------------------------|-----------------------------|
| (1) Recoil Weight | 122 pounds |
| (2) Ammunition Impulse | 47.5 pound-seconds |
| (3) Shots per second | 10.4 (625 shots per minute) |

Equation 1 yields $F_{AVG} = 495$ pounds



FIRING CYCLE
TIME
FIGURE 2

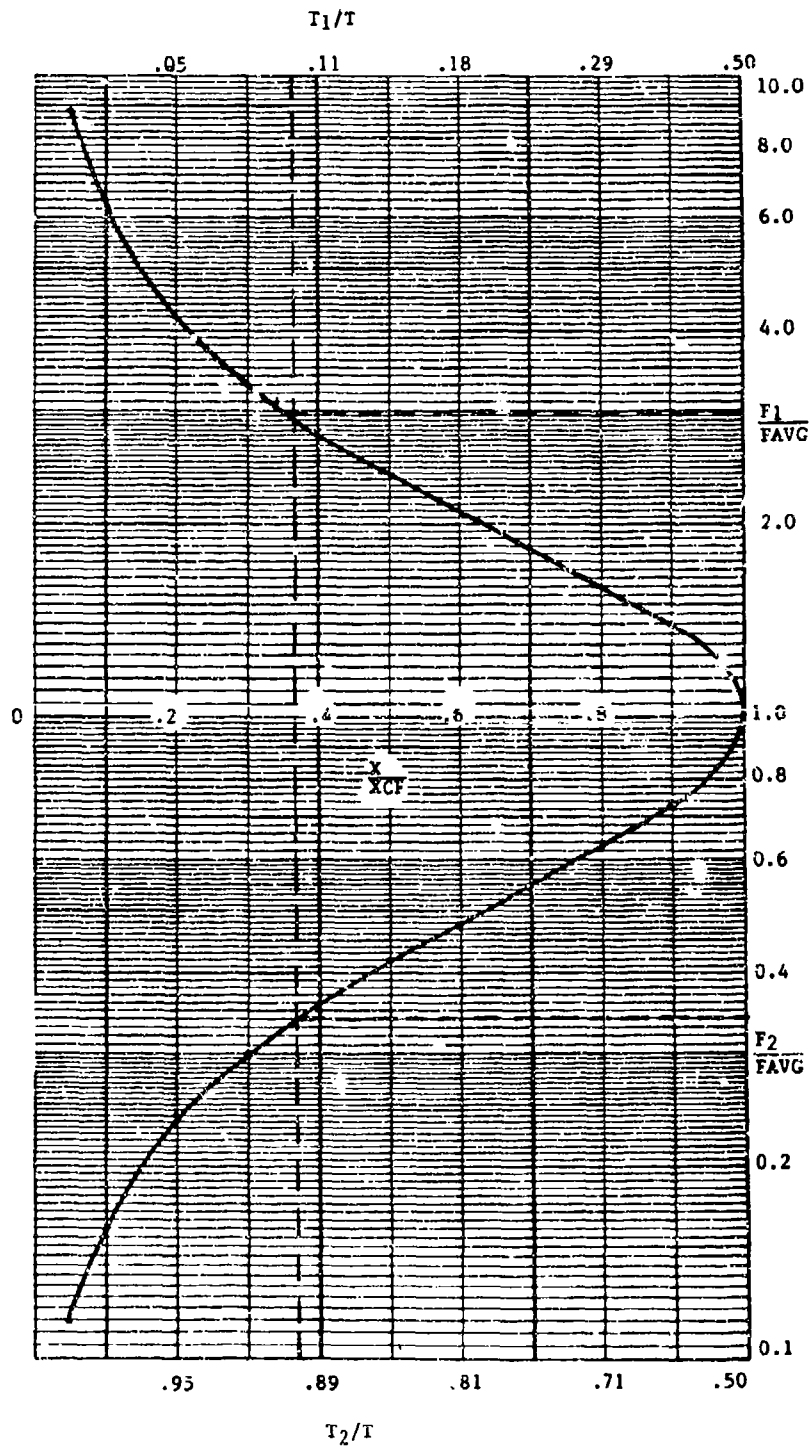


FIGURE 3

TOWNSEND
GARTNER

Equation 2 yields $X_{CF} = 1.8$ inches

This gives the normal constant force solution for the M230 weapon.

Reduced Mass Condition

If, however, the gun weight is reduced to 80 pounds as required to meet the IIN requirement, $X_{CF} = 2.75$ inches. If the desired recoil travel is 1 inch, as an example, the ratio of $X/X_{CF} = 1/2.75 = .36$. Using Figure 3 as shown by the dotted line yields:

$$\begin{array}{lll} F_1/F_{AVG} = 2.95 & T_1/T = 0.1 & T = 0.096 \text{ seconds} \\ F_2/F_{AVG} = 0.34 & T_2/T = 0.9 & \end{array}$$

Then $F_1 = 2.95 \times 495 = 1460$ pounds
 $F_2 = 0.34 \times 495 = 168$ pounds

$$\begin{array}{l} T_1 = 0.0096 \text{ seconds} \\ T_2 = 0.0864 \text{ seconds} \end{array}$$

Reduced Mass and Firing Rate Condition

If both the gun weight and the rate of fire are reduced, the data for this condition is:

- | | |
|--------------------------|----------------------------|
| (1) Recoil Weight | 80 pounds |
| (2) Ammunition Impulse | 47.5 pound seconds |
| (3) Shots per second | 5.0 (300 shots per minute) |
| $F_{AVG} = 237.5$ pounds | |
| $X_{CF} = 5.73$ inches | |

If the desired recoil travel is still 1 inch:

$$\begin{array}{ll} X/X_{CF} = 0.174 & T = 0.200 \text{ seconds} \\ F_1/F_{AVG} = 4.57 & T_1/T = 0.045 \\ F_2/F_{AVG} = 0.219 & T_2/T = 0.955 \end{array}$$

then $F_1 = 1085$ pounds
 $F_2 = 52$ pounds

$$\begin{array}{l} T_1 = 0.009 \text{ seconds} \\ T_2 = 0.191 \text{ seconds} \end{array}$$

TOWNSEND
GARTNER

From the examples, it can be seen that the curve form is a useful tool to quickly evaluate the various trade offs considered in using an active recoil control system. As indicated previously these are idealized conditions and the solutions are conservative. However, the force levels predicted are significantly below what would be expected for the system using ordinary spring-type recoil adapters. A more sophisticated simulation can now be used to generate the actual control algorithms. LHX armament subsystem will be a challenge in terms of weight reduction and aiming accuracy. It is apparent however, that the recoil can be controlled within acceptable limits if active control is employed.

TITLE Dynamic Modeling of the Advanced Gun Mount for the
 Howitzer Improvement Program
 WILLIAM T. ZEPP
 U.S. Army Armament, Munitions, and Chemical Command
 Armament Research and Development Center
 Large Caliber Weapon Systems Laboratory
 Dover, NJ 07801-5001

ABSTRACT:

In response to requirements placed upon the Howitzer Improvement Program (HIP) system, a new gun mount was required to support new cannons. From the system requirements a system model must be developed to determine component characteristics, system performance, and component interactions. This model is derived from Newton's second law of motion with appropriate simplifying assumptions of the various reaction forcing functions.

The model derived will provide accurate results for a gun mount system. It is used for gross simulation of a gun mount and for development of required subassembly operating characteristics.

BIOGRAPHY:

PRESENT ASSIGNMENT Mechanical Engineer, U.S. Army Armament Research &
Development Center, LCWSL, Weapons Division, Dover, NJ

PAST EXPERIENCE: Mechanical Engineer with U.S. Army at Dover, NJ (1977-
1985).

DEGREES HELD: B S.M E. State University of New York at Buffalo (1977).d

DYNAMIC MODELING OF THE ADVANCED GUN MOUNT
FOR THE HOWITZER IMPROVEMENT PROGRAM

WILLIAM T. ZEPP
U.S. ARMY ARMAMENT MUNITIONS, AND CHEMICAL COMMAND CENTER
ARMAMENTS RESEARCH AND DEVELOPMENT
LARGE CALIBER WEAPON SYSTEMS LABORATORY
DOVER, NJ 07801-5000

1. INTRODUCTION

As part of the Howitzer Improvement Program (HIP) for the US Army improvements to the main armament system were required. These requirements are based on deficiencies identified in the field artillery Mission Element Needs Statement (MENS) and derived from analysis done under the Enhanced Self-Propelled Artillery Weapons System (ESPAWS) and Division Support Weapons System (DSWS) programs. These improvements are to help meet the need to provide continuous and close field artillery fire support to the maneuver elements of mechanized infantry and armored forces during the 1990-2010 timeframe. This will be accomplished by providing improved indirect fire support with emphasis on responsiveness, survivability, terminal effects, and reliability availability and maintainability (RAM).

After compiling the results of the ESPAWS and DSWS analysis, it was concluded that the present 155mm self-propelled artillery main armament system was incapable of being adapted or modified to meet all the requirements placed upon it under HIP. Therefore, the new main armament option of the DSWS program was pursued. Only the efforts on the gun mount portion of the new main armament assembly will be discussed in this paper. Design requirements and the system modeling of the derived configuration will be presented to illustrate the methodology used in developing the new gun mount.

2. DESIGN REQUIREMENTS

Along with the capabilities of the present mount, the additional design requirements can be lumped into two main groupings. Those addressing RAM (increased operational availability) and those addressing survivability, terminal effects, and responsiveness. These requirements were derived from overall system performance requirements for the DSWS program. A system requirement was placed on the gun mount that it be retrofitable into the M109A2/A3 SPH.

The war time operational availability requirement established for the self-propelled howitzer system was 75%. This requirement is a significant increase over the 51% of the present M109A2 system. To meet this requirement, both a reduction of mission critical failures and a drastic reduction of maintenance and administrative logistic down times were required. After a subsystem analysis and reliability apportionment, the gun mount mean rounds between operation mission failure (MRBOMF) requirement was 12,200, significantly greater than the present M178 gun mount at 5960. The mean time

to repair (MTTR) an operation mission failure requirement was 1.3 hours again much lower than the present gun mount's 4.0 hours. It should be noted that an operation mission failure is defined as a failure that prevents the main armament from firing a maximum range of 9.8 kilometers at a rate of 4 rounds per minute. These requirements required a semi-redundant, modular configuration.

Requirements were placed upon the gun mount that reflected required capabilities defined by analysis of system requirements. To meet the system survivability, it was required that all mission essential components of the gun mount, such as the recoil brakes and the recuperators, be provided ballistic protection equal to at least 1.25 inches of 5083 aluminum armor. A sustained rate of fire of 6 rounds per minute was required to minimize system exposure, an increase over the present 4 rounds per minute. To meet the system terminal effects requirements, the gun mount was required to accommodate a larger and heavier cannon assembly. To meet the system responsiveness requirements, the gun mount was required to allow the system to fire all missions in all of three scenarios. These scenarios represented sustained, intense, and surge conditions in wartime. This required cooling of the gun mount to prevent heat buildup.

3. THE GUN MOUNT MODELING

The design of the new HIP gun mount progressed in two phases. First, a system level development and modeling phase was executed to define subsystem requirements, performance, and characteristics and to establish overall gun mount characteristics. The second phase for subsystem design and detailing commenced once the requirements and parameters were set for each subsystem in phase one. A discussion of only the systems modeling used in the first phase will be presented in this paper.

The system level effort defined the approach to be taken to meet the requirements placed on the gun mount by the overall system specifications. The concept definition process will not be presented here with all its system and RAM modeling, trade-off's and howitzer system requirement redefinitions. The gun mount concept is summarized and presented for background material. They include:

- a) Dual independant modular Recoil Brakes
- b) Dual independant modular Recuperators
- c) Tube sleeve interfacing cannon and mount
- d) Dual elevation/equilibration cylinders
- e) Armored cradle

To derive predictions for gun mount performance and subsystem requirements, a mathematical model of the system was developed. This model treated the recoiling parts as a point mass and lumped all characteristics at that point. The behavior of this point which represents the recoiling mass is one dimensional with respect to the gun mount cradle and can be defined with respect to one coordinate, x , and must follow Newton's law of motion:

$$F = M\ddot{x}$$

(1)

Where:

- F = The net force applied (lbf)
- M = The point mass on which the force is acting (slugs)
- \ddot{x} = Acceleration of the point mass (in/sec²)

Upon inspection of Newton's equation, the mass is readily obtained from summing the estimates for the recoiling parts. The force, F, is not as simple. The forces acting upon the recoiling parts are shown in Figure 1. The force applied to the recoiling parts is a function of both the displacement, x, velocity, \dot{x} , and time, t. The force, F can be defined by:

$$F = BF(t) + W_r \sin\theta - T_{ube\text{fr}} - KREC(x, \dot{x}) - KRECUP(x) \quad (2)$$

Where:

- BF(t) - The net force applied to the recoiling mass by the propellant gases as a function of time
- W_r - Weight of the recoiling mass
- θ - Angle of elevation (Deg)
- T_{ube}fr - frictional force applied to the recoiling mass by its bearings
- KREC(x, \dot{x}) - force generated by the hydraulic recoil brakes as a function of displacement and velocity
- KRECUP(x) - force generated by the pneumatic springs used for recuperation.

The breech force BF(t) is defined by the specified projectile, charge, and cannon to be used and their physical and thermal condition and is obtained from interior ballistic analysis of the combination specified in the requirements. Thus, the breech force is assumed to be given for the analysis.

The component of the weight of recoiling parts in the direction of the cannon axis in the direction of recoil is obtained by the product of:

$$W_r \sin\theta \quad (3)$$

and is constant throughout each simulation. The weight of the recoiling parts is a design variable and is traded off with non-recoiling weights to optimize the gun mount with respect to all of the requirements and limitations placed upon the main armament system.

The tube friction is assumed to remain constant throughout the recoil cycle by neglecting any drop in the coefficient of sliding friction between the slide surfaces and the bearings. This can be done with little, if any loss in accuracy due to the low magnitude of the forces with respect to the other forces acting.

The value of the recuperator force, KRECUP, is a function of the displacement of the recoiling parts by the gas law.

$$P = P_0 \left(\frac{V_0}{V_0 - APCR \cdot X} \right)^{1.4} \quad (4)$$

Where:

PO - Initial Nitrogen precharge pressure (psi)
VO - Initial nitrogen volume (in³)
APCR - Area of recuperator piston (in²)

And the pressure obtained above by:

$$KRECUP = (Arecup * P - Sealfr(P)) * NRCP \quad (5)$$

Where:

Arecup - Is the effective area of one recuperator piston (in²)
Sealfr(P) - Is the total seal friction generated within the recuperator by the piston and rod seals (lbf)
NRCP - Is the number of recuperators used in the system

The recuperator model presented is for a pneumatic recuperator.

The force generated by the recoil brakes, KREC, are the most important force in arresting the recoiling masses of large caliber guns. They are also the most complex to control and model. The derivation presented here is for an independent hydraulic brake with an integral spear buffer. If an external buffer is to be used, the buffing force is removed from the brake and stands alone in equation (2).

The recoil braking force is modeled by the following expression:

$$KREC = (AREC * Pr + RECFRIC(Pr) - Kbuff) * NREC \quad (6)$$

Where:

AREC - the effective area of one recoil piston
Pr - the pressure developed in the recoil brake by the throttled oil (psi)
RECFRIC(P) - frictional force generated by recoil rod seal (lbf)
Kbuff - force created by the integral spear buffer (lbf)
NREC - number of recoil brakes in the configuration

The area of the recoil piston is another design parameter which can be considered in trade-offs. This area affects both size and weight of the gun mount by influencing cylinder spacing, wall thicknesses, maximum and operating pressures required to produce the desired recoil brake force, etc.

The recoil brake oil pressure is the most important and most difficult to model accurately. At this phase, one is not doing the detailed designing of the brake but just coming up the required characteristics of the brake such as recoil distance, piston area, braking force vs time, recoil and counter-recoil velocities vs time, recoil oil pressure vs. time, etc. Thus, effects that must be accounted for during the actual designing of the brake, such as elongation of the recoil rod and cylinder, expansion of cylinder

walls, compression effects of the hydraulic oil, actual control rod dimensions, and variation of discharge coefficients, can be neglected allowing for a model that will not design your brakes but will allow you to design the system and its performance characteristics with a great degree of accuracy.

The oil pressure is calculated from:

$$Pr = ((VO/CD * AREA)) **2) *W/ 772.8 \quad (6)$$

Where:

- VO - estimated volume of fluid which is required to flow through the control orifice (in³)
- CD - discharge coefficient for the control orifice (assumed constant)
- AREA - area of control orifice (in²)
- W - density of the hydraulic fluid at the pressure of the previous time step (lb/in³)

Either the pressure or the area is given to the equation. If the model is on an initial optimizing run, the required pressure is calculated from the required total recoil brake force. If the model is on a variation run, the control orifice areas from a previous run are provided.

Now, with all components of the force exerted upon the recoiling mass defined, a computer code was developed around equation 1 with the required input/output routines, all routines required for estimating values of parameters, and an integration routine. A simple Trapezoidal rule numerical integration scheme was used because of its self starting capability and simplicity along with a fine step size of five ten thousandths of a second to retain accuracy.

The computer code must have, for an optimization run, a total retarding force vs time curve which the system is expected to follow as close as possible. This curve is illustrated in figure 2. The curve presented is that of a trapezoid. Use of this curve minimizes the value of K0 but increases shock loads. Other curves such as sinusoidal, ramp, triangular, each could be substituted as required depending upon system requirements and optimization restrictions.

4. MODEL RESULTS

The computer code developed from the model that was discussed was used in the system definition of the new gun mount which is to meet all of the design requirements. The model was evaluated for accuracy by modeling both the M178 and M174 gun mounts. Actual and predicted performance are presented in figures 3 for the M178 gun mount and figures 4 for the M174 gun mount.

The resulting design of the new gun mount is depicted in figures 6 and 7 with predicted performance in figure 8. Prototype hardware is in fabrication with testing expected to begin in September 1985.

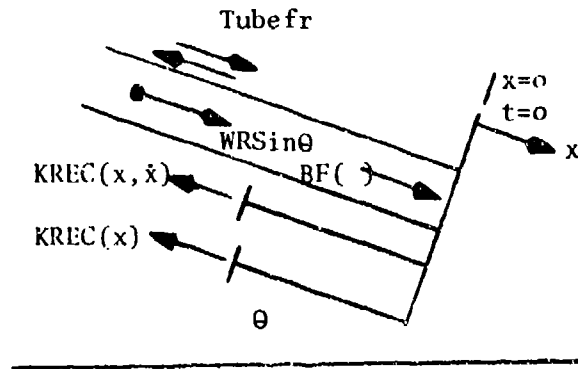
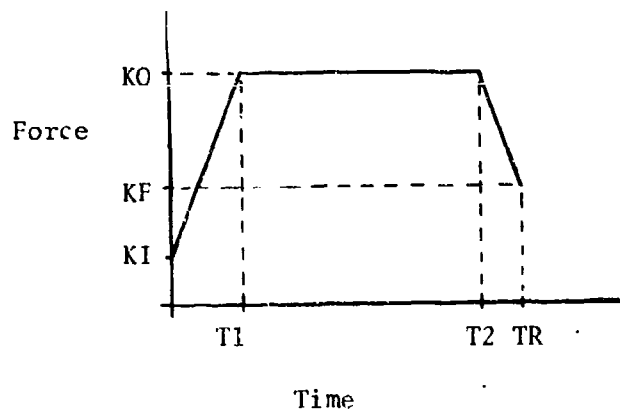


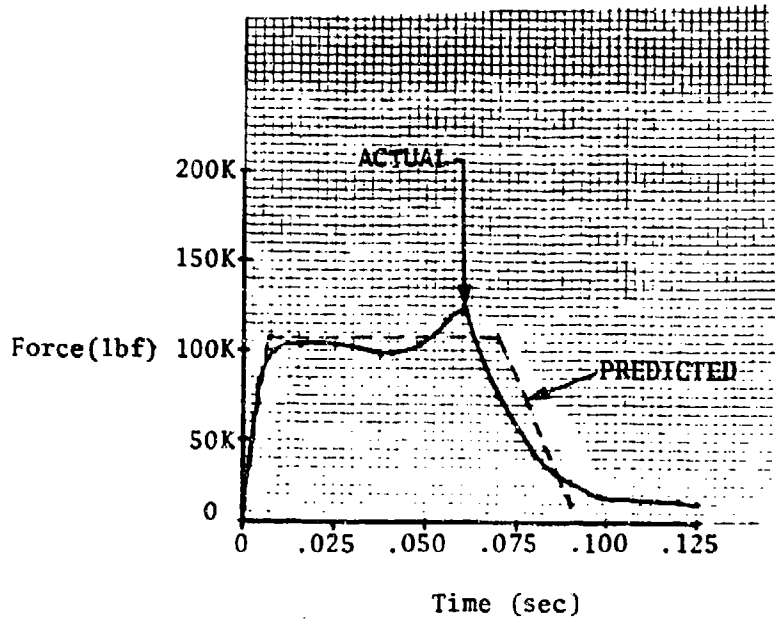
Figure 1



Where:

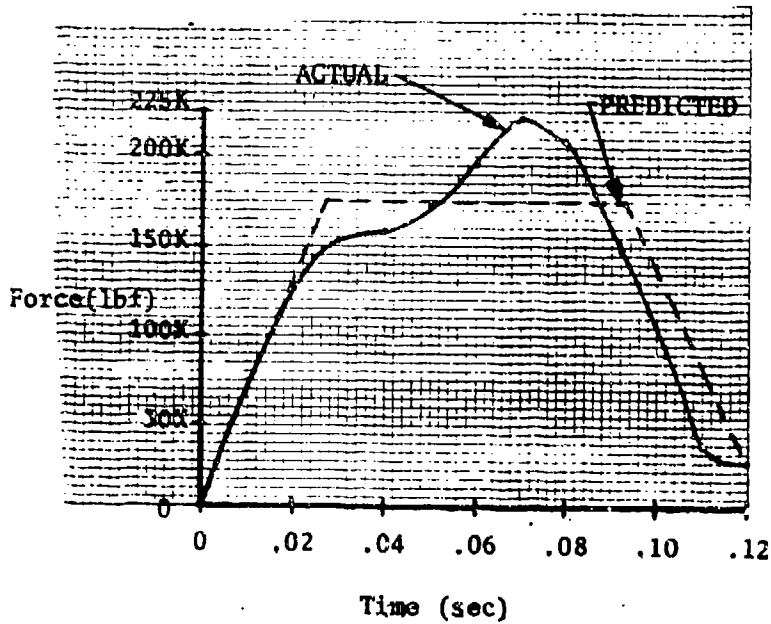
- KO - Steady state total retarding force
- KF - Final total retarding force at completion of recoil
- KI - Initial total retarding force
- T1 - Time at which KO level is initially reached
- T2 - Time at which KO level is dropped
- TR - Time to recoil

Figure 2



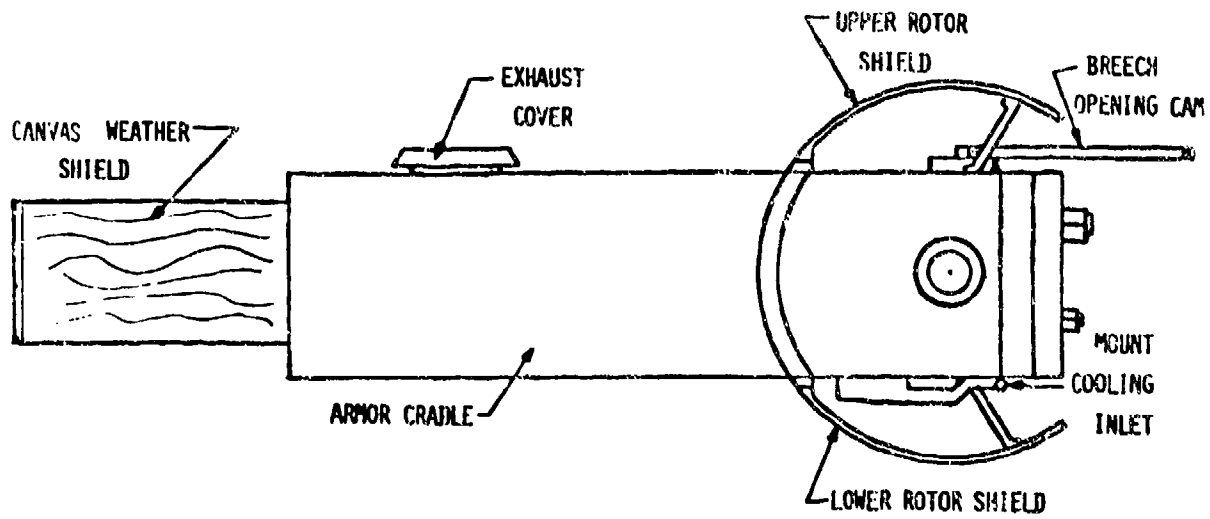
Actual and Predicted Total Retarding Force vs Time for the M178 Gun Mount

Figure 3



Actual and Predicted Total Retarding Force vs Time for the M174 Gun Mount

Figure 4



ADVANCED GUN MOUNT

Figure 5

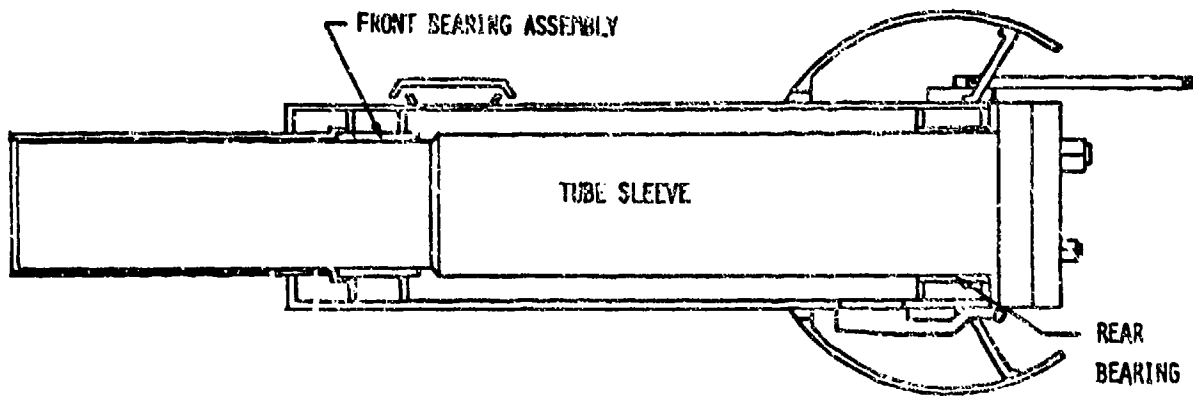


Figure 6

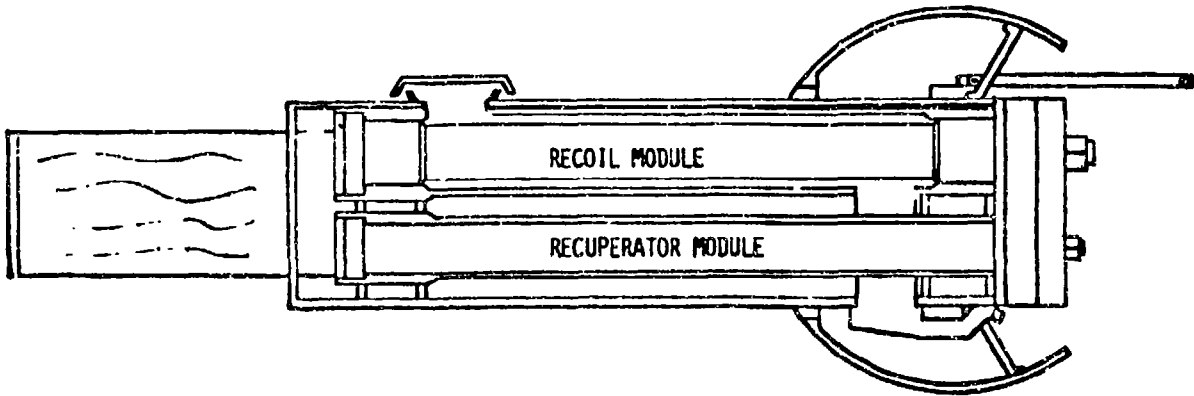
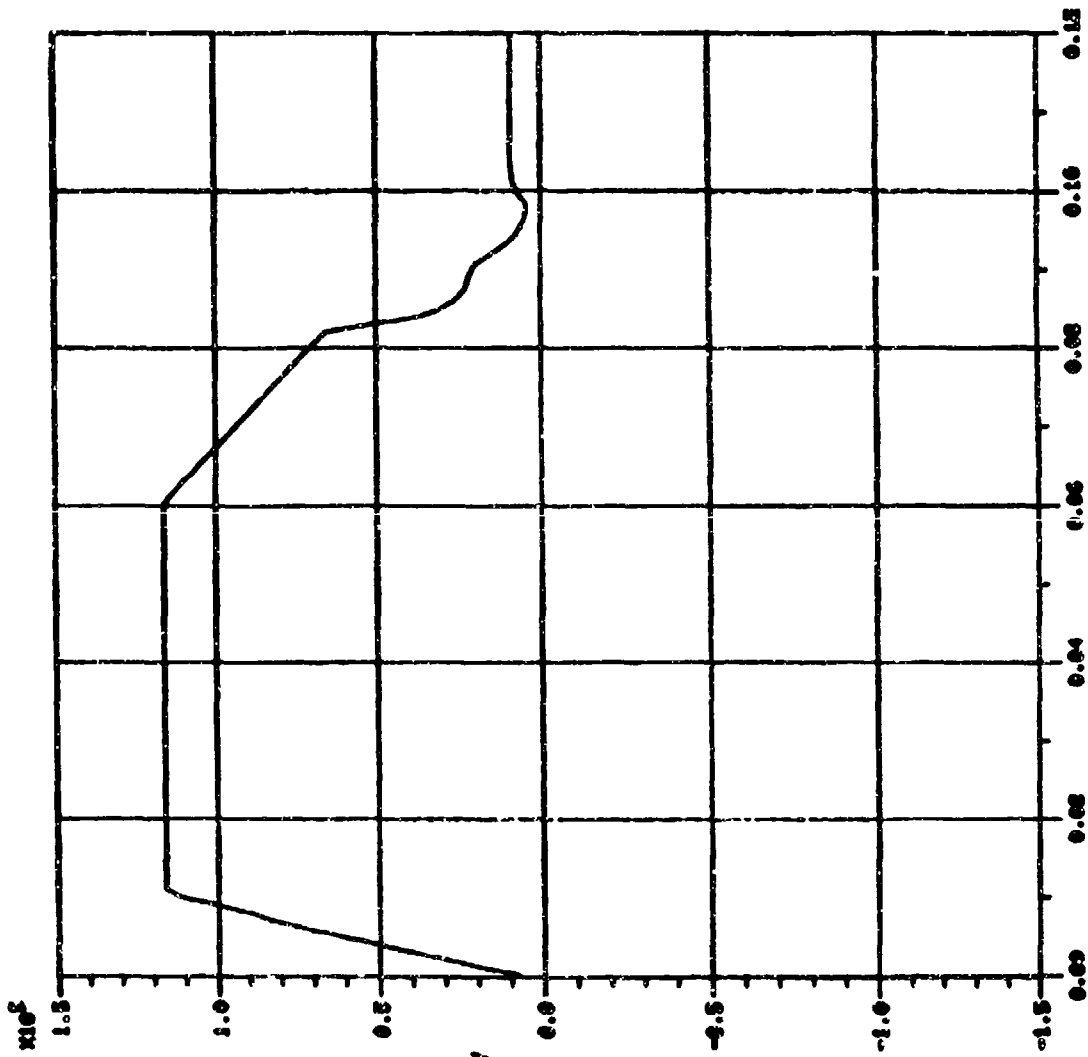


Figure 7

TOT RETARD FORCE (LBS) URS. TIME (SEC)



SELECT OPTIONS:
1-RETURN TO MENU
2-SCALE X AXIS
3-SCALE Y AXIS
4-SCALE BOTH X & Y

Figure 8

PAULY

Title: Measurements of Muzzle Blast Shaping and Loading
Exerted Upon Surrounding Structures of Aircraft
Guns

GERT PAULY

Erprobungsstelle 91 der Bundeswehr

D-4470 Meppen

Federal Republic of Germany

Abstract:

The problem of blast produced at the muzzle of a 27 mm automatic gun and its reduction by means of different muzzle devices (blast deflectors) has been investigated experimentally. In these experiments different types of blast deflectors constructed from different designs have been investigated.

In order to visualize the flows developing around the muzzle a Cranz-Schardin multi-spark camera has been used.

To investigate the direct effect of a muzzle blast on the structures close to the muzzle, a momentum sensor has been developed which allows to measure the momentum exerted by the muzzle blast onto the structure. The device operates according to the principle of integrating piezo-electrical force measuring. It also allows to measure the muzzle blast in the immediate vicinity of the muzzle without damaging the sensors.

*The author was unable to present this paper at the Symposium.

PAULY

MEASUREMENT OF MUZZLE BLAST SHAPING AND
LOADING EXERTED UPON SURROUNDING STRUCTURES
OF AIRCRAFT GUNS

GERT PAULY, Dipl.-Ing
ERPROBUNGSSTELLE 91 DER BUNDESWEHR; D-4470 MEPPEN
FEDERAL REPUBLIC OF GERMANY

1. INTRODUCTION

When firing with guns onboard combat aircraft strong vibrations are produced in the aircraft structure with possible detrimental effects on the instruments in the aircraft.

In order to protect the instruments against vibrations it is possible to insulate them. In practice however, this method is limited as to its application, mainly due to considerable costs.

A better way to do it is to reduce the muzzle blast itself by changing the gas pulse/momentum exerted on the aircraft skin in front of the muzzle in such a way that the vibrations induced into the structure remain as small as possible.

One solution is the use of a so-called blast deflektor. It is a ring-shaped device on the muzzle of an automatic gun which prevents the escaping propellant gases from expanding. Thus the effect of the muzzle blast on the surrounding structures is reduced.

The purpose of the present study is to answer the following questions:

- how big is the load of the gas pressure exerted on structures in a lateral position of the muzzle?
- what would a blast deflector look like which would allow the reduction of the stress caused by the pressure?

2. MEASURING PROCEDURE

Fig. 1 shows the test arrangement that has been used. A 27 mm-automatic gun is set up in a laboratory in such a way that photographs can be taken of the muzzle while firing. At the same time the pressure pulse exerted by the muzzle blast on the surrounding structure is measured by means of a special measuring device. In order to examine the flow at the muzzle a Cranz-Schardin multi-spark camera is used which operates with point sparks as sources of light. The duration of the sparks sets the exposure time in the dark laboratory. By using this camera the expansion of the propellant gases outside the muzzle can be shown by means of high resolution and high frame frequency photographs. The measurement of the loading exerted by the muzzle blast on the surrounding structure poses a particular problem. There are two ways of solving this problem.

One is to use pressure sensors of the usual type for measuring the pressure of gas onto the structure. This allows results to be obtained of the pressure distribution. What stands in the way of this approach is the fact that the sensors are very costly and can be easily destroyed due to the heavy mechanical and thermal effects which are produced close to muzzles.

A more efficient way of determining the pressure pulse exerted on the structure is by supporting the surfaces under impact with force gauges. The gas pressure acts on a sensor surface which is composed of several metal sheets (Fig. 2) and which is on fixed top of the force sensors. As a result the sensitive measuring devices are protected from unwanted external effects caused by propellant gases. By this measuring procedure a low-frequency transfer of the muzzle blast is achieved and the measuring arrangement forms a spring-mass-system with low natural frequency. The data to be evaluated is therefore not the force-time-flow $F(t)$, but the integral

$$I(t) = \int_0^t F(t') \cdot dt'$$

hence the momentum transferred via the force sensor. In order to determine the distribution of the momentum conveyed on the surface of the structure a measuring device is set up which reproduces the structure by using several such measuring elements (fig. 3). A total of fifteen surface elements is used over a length of one meter, 10 of which measure 50 x 100 sq.mm and 5 which measure 100 x 100 sq.mm.

The measuring device which is called the momentum sensor in this context is set up in such a way that the muzzle of the gun is positioned 100 mm behind the edge of the first measuring element while the gun is at the run-out position. Hence the muzzle is at the beginning of the third measuring element. Only one force gauge (quartz-crystal) is used for each measuring element which is pre-stressed to measure the force in both directions. Fig. 3 shows a blast deflector attached to the muzzle of the gun (top left).

In the trials shown here the distance between the surface of the momentum sensor and the tube axis is 60 mm.

The recoil distance of the gun is measured by a displacement gauge. Thereby the effect of the deflectors acting as a recoil buffer can be measured.

3. MEASURING RESULTS

The electrical measuring signals provided by the sensors are amplified and recorded on magnetic tape. After digitization the data reduction is performed by a computer. Hereby the registered force-time function is integrated for each surface element.

The integral final values provided by the individual measuring elements are shown in a bar diagram, hence providing a picture of the local momentum stress on the structure under impact (fig. 4, bottom). All calculated integral curves are then summed up and plotted, allowing the time factor of the momentum exerted on the structure to be examined (fig. 4, top).

The integration is performed for a period of 25 msec after the ignition of the round. Because of $dI/dt = F(t)$ the slope of the curve indicates the momentary load situation of the momentum sensor: the ascending curve corre-

PAULY

sponds to a compressive force (increasing or constant rate) while the descending curve corresponds to a tensile force. A horizontal curve means that there is no effect of force at all.

In the examples shown (figures 4 to 10) the tube end of the gun with the appropriate blast deflector is entered each time as a correct scale in the bar diagram to illustrate the trials situation.

Fig. 11 shows the Cranz-Schardin photograph (muzzle without deflector) corresponding to fig. 4. The time interval between the 24 pictures is 0.1 msec (= 10,000 frames per sec.).

Since all objectives of the camera are open when the projectile is fired, the light appearance of the muzzle flash is superimposed to all the frames.

The following pattern applies to the sequence of pictures:

| | | | |
|---|----|----|----|
| 6 | 12 | 18 | 24 |
| 5 | 11 | 17 | 23 |
| 4 | 10 | 16 | 22 |
| 3 | 9 | 15 | 21 |
| 2 | 8 | 14 | 20 |
| 1 | 7 | 13 | 19 |

Fig. 12 shows the discharge procedure with the blast deflector (in this case the momentum sensor is positioned lower than in the previous picture). The effect of the deflector on the flow is clearly discernible. While, as in fig. 11, the dark powder gases are for the most part escaping to the front and to the sides, the gases in fig. 12 are partly diverted to the back by the deflector ring. The load diagram corresponding to the trial of fig. 12 is shown in fig. 5. The top curve shows the ignition signal at 0.000 sec, at 0.004 sec the shell is ejected from the muzzle. Before the shell is ejected a momentum rise is caused by the precursor wave before projectile exit. At 0.004 sec the actual load to the structure due to the propellant gases escaping is beginning.

PAULY

The bottom diagram in fig. 5 shows that the second measuring element located behind the muzzle is under the biggest load and is exposed to the greatest stress due to the gas deflection at the baffle of the deflector. The first element which is situated right next to the previous element is exposed to tensile force momentum. Behind the fourth element, i.e. 100 to 150 mm before the muzzle the force is considerably decreased.

To compare the results of the trials without a deflector (fig. 4): in this case the main load is distributed over the third and fourth measuring element. Without a deflector only two elements are under heavy stress, with a deflector three elements. The deflector causes an extension of the zone under impact.

Fig. 6 shows the results of several trials with a blast deflector which is fixed at different distances (a) in front of the muzzle. The change as to how the momentum is distributed on the individual elements becomes clearly discernible. At $a = 63$ or 73 mm the deflector produces precisely the opposite effect as at $a = 33$ or 43 mm. It is not a reduction of the local stress which is obtained but a local focussing of the compressive force.

Fig. 7 shows a deflector having no effect as a muzzle brake. It mainly consists of a long tube with several lateral slits. Here the momentum stress covers a larger area in front of the muzzle, and the individual measuring elements are not very much stressed.

Fig. 8 shows a shortened deflector tube of the same type. Despite the reduced length the way the load is spread does not change very much.

Regarding the deflector type in fig. 9, the flow of propellant gases escaping from the deflector mouth are influenced in such a way that close to the muzzle the pressure is reduced.

Fig. 13 shows the flow with this deflector. The lateral expansion of gases takes place at a greater distance in front of the muzzle than with the other deflectors. This becomes particularly evident regarding the air flow before the ejection of the shell.

PAULY

Fig. 10 depicts a deflector which only differs from the previous trial by its slightly different insert ring. Despite this relatively small difference the gas flow is changed to such an extent that the pulse value increases by one third.

4. CONCLUSION

It has been proved that measuring the muzzle blast of an automatic gun in immediate vicinity to the muzzle is possible without damaging the sensors. Performing the integration of the measuring signals one achieves an important value to evaluate the effect of the muzzle blast.

The investigations have shown that the muzzle blast of an automatic gun can be clearly influenced by a blast deflector. Both an increase and a decrease of the muzzle blast are possible. In particular the pressure distribution can be influenced so that e.g. the construction of the shroud-plate and its positioning can be adapted accordingly.

The present measuring is limited by the fact that only single rounds were measured which are fired like the ones from an aircraft on the ground (in resting position). Now that a suitable routine measuring procedure is available it is planned to simulate the conditions of a round fired from a flying aircraft in future trials.

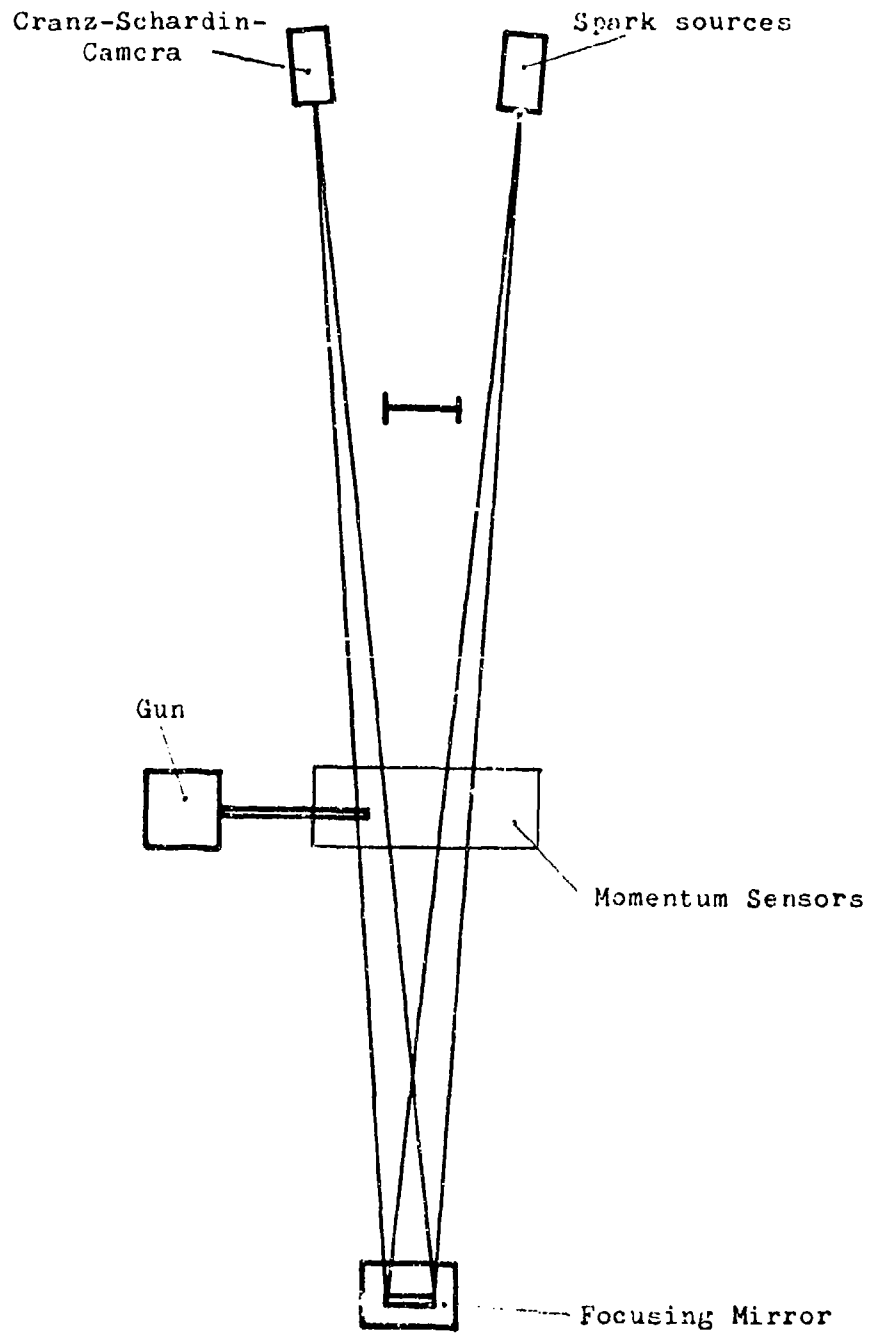


Fig. 1 Test set-up for investigation of muzzle blast
of an aircraft gun

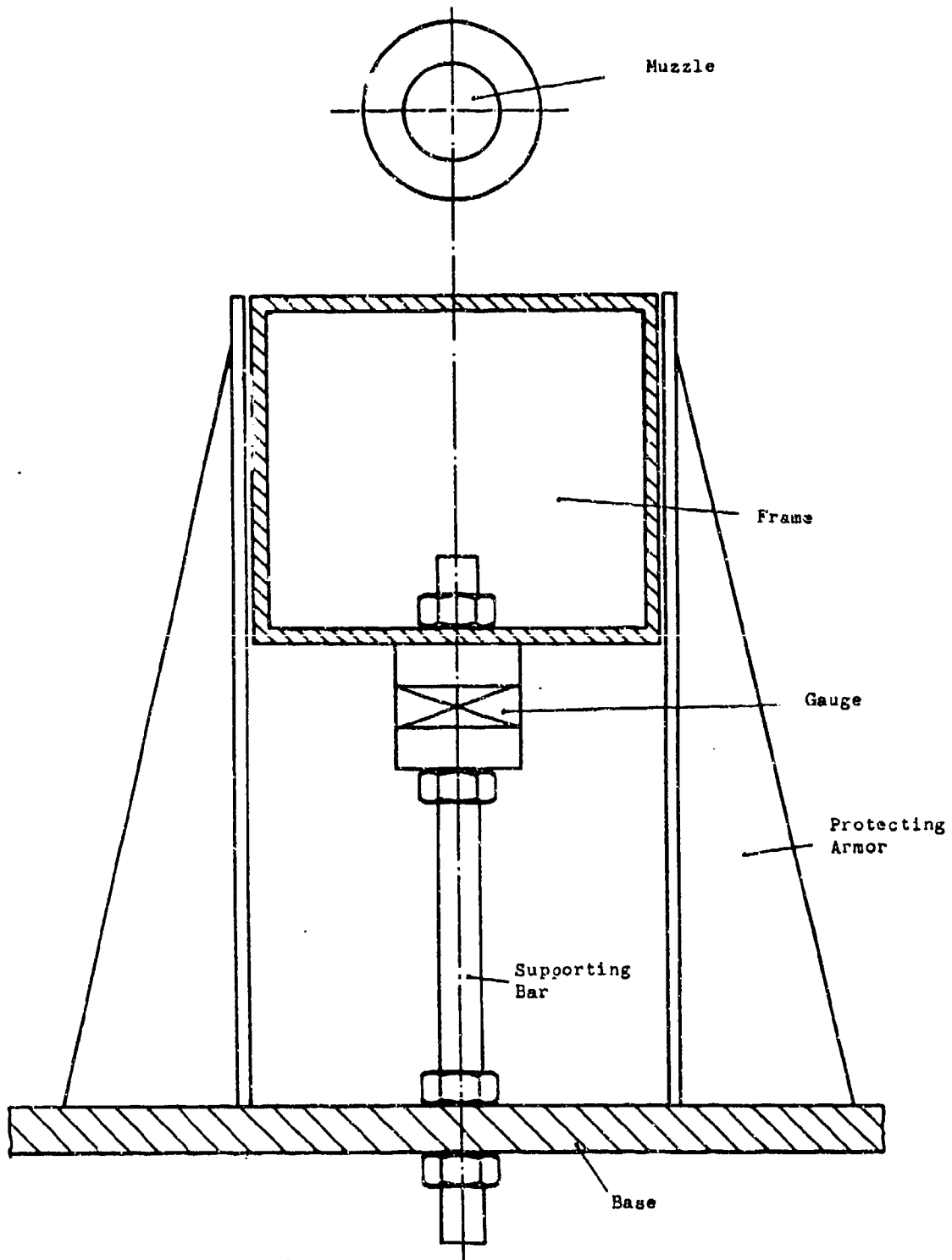


Fig. 2

Cross section of momentum sensor element

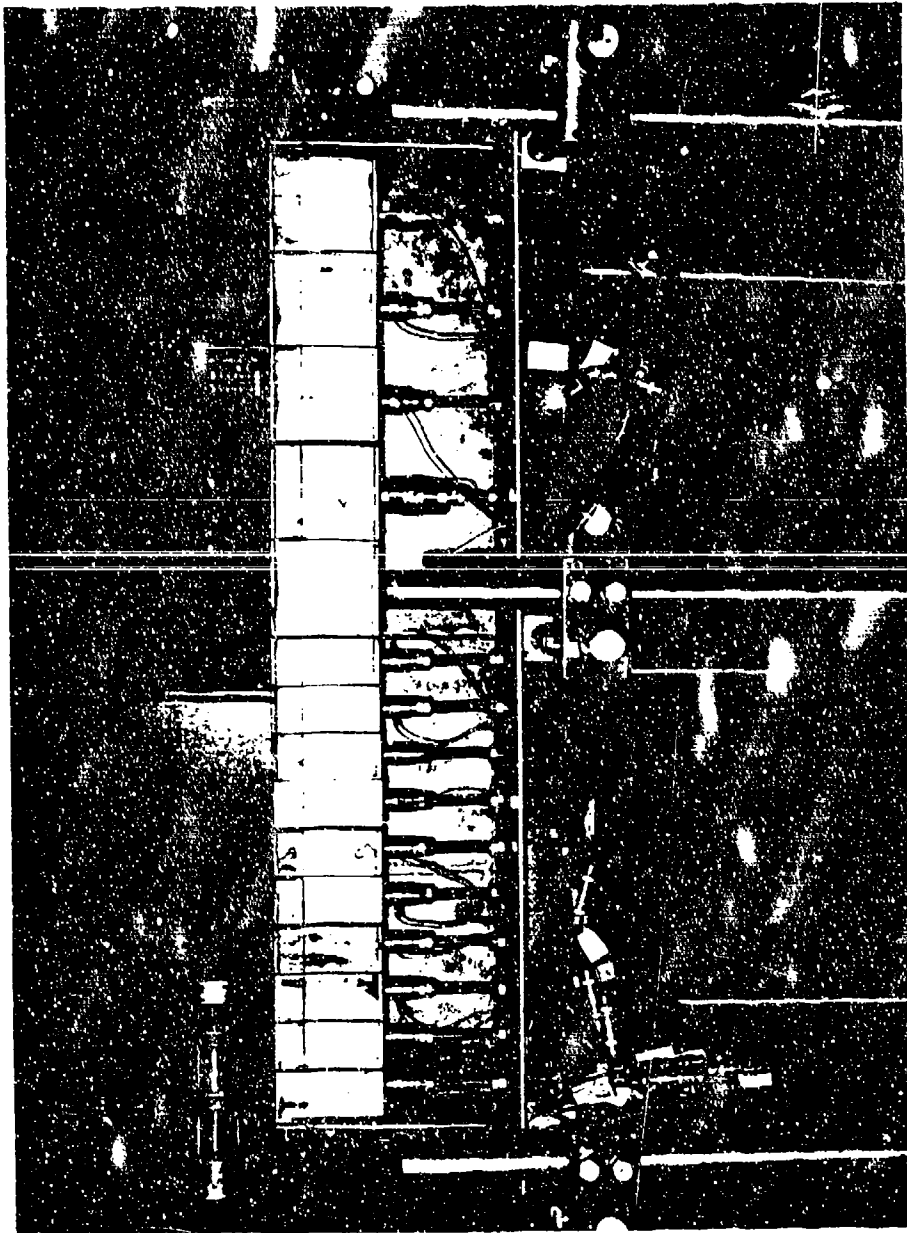
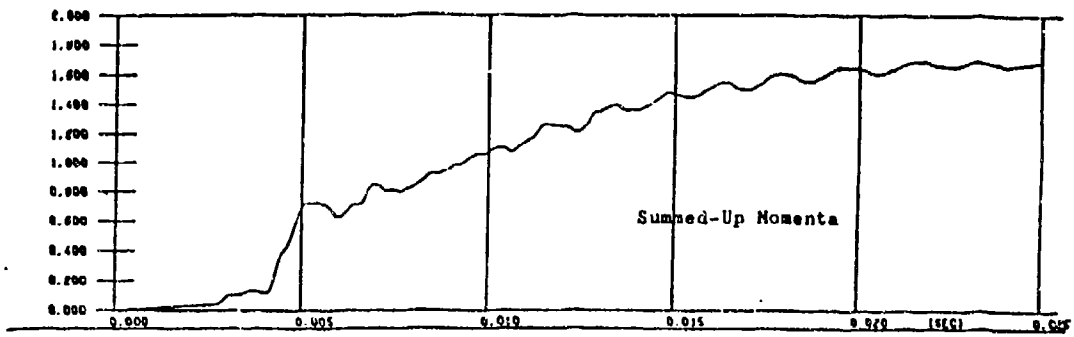


Fig. 3 Side view of the Momentum Sensors



Ordinate: $1.000 \pm 2.2 \cdot 10^3$ Pa-sec

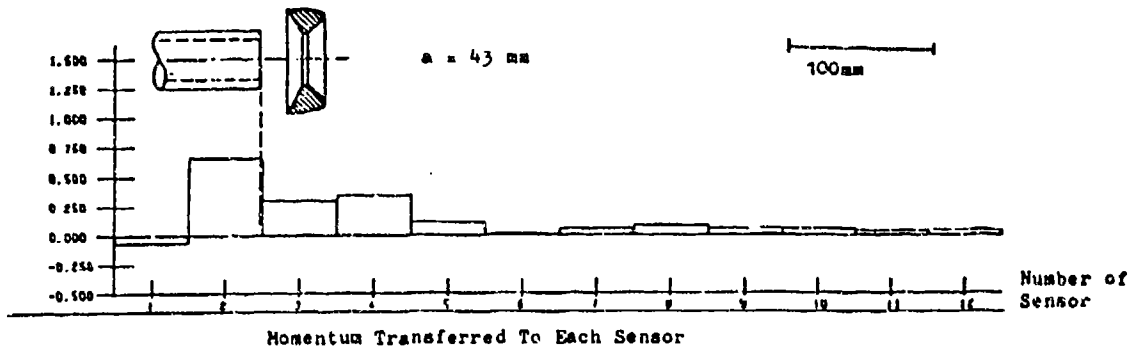
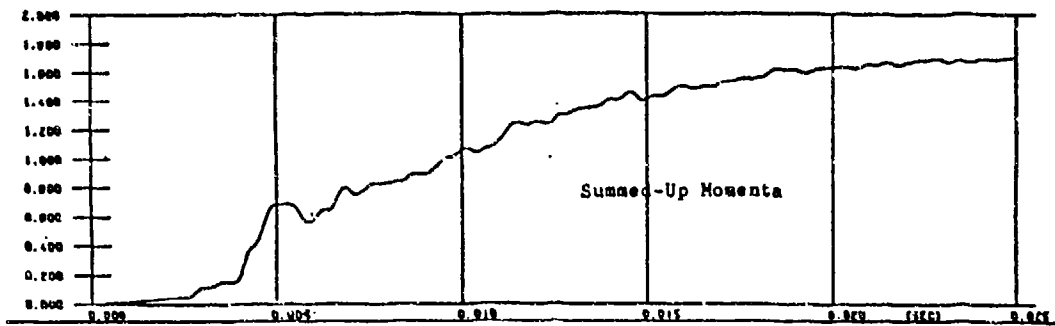


Fig. 5



Ordinate: $1.000 \pm 2.2 \cdot 10^3$ Pa-sec

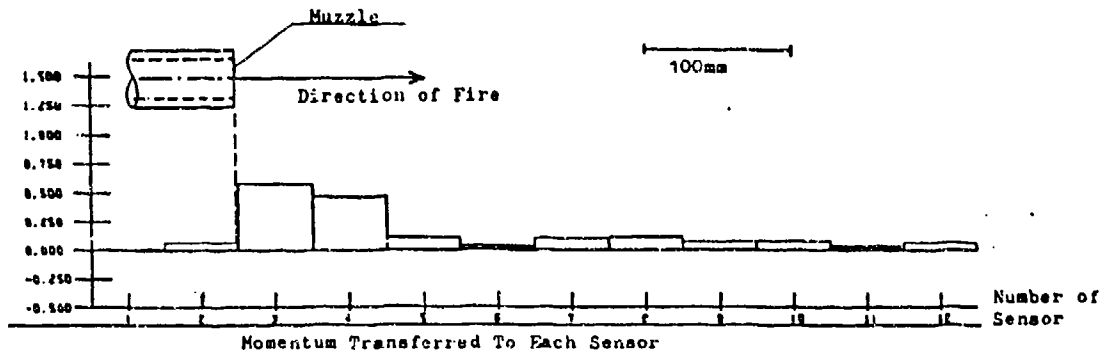


Fig. 4

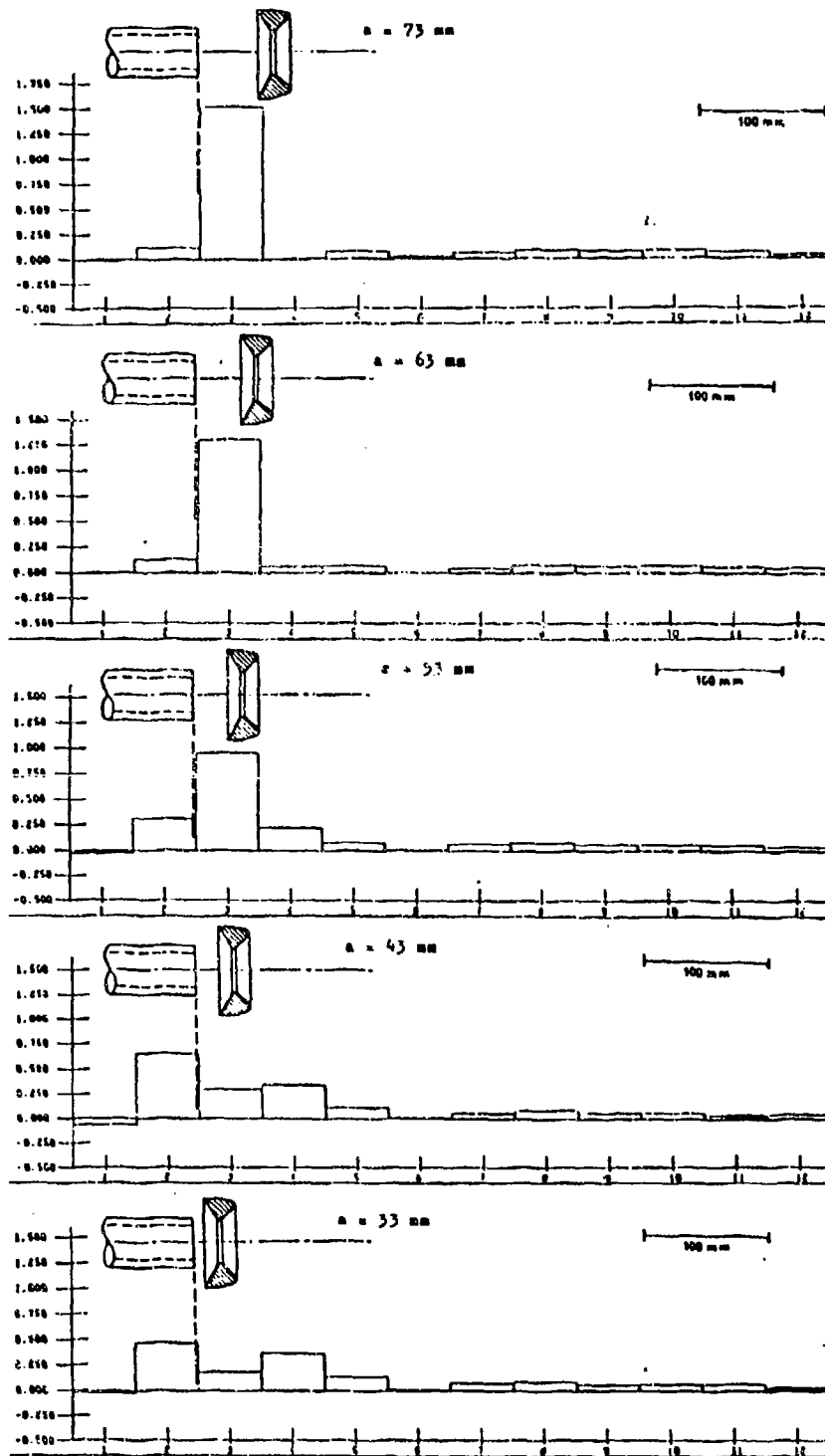


Fig. 6 Ordinate and abscissa scale same as in Fig. 4

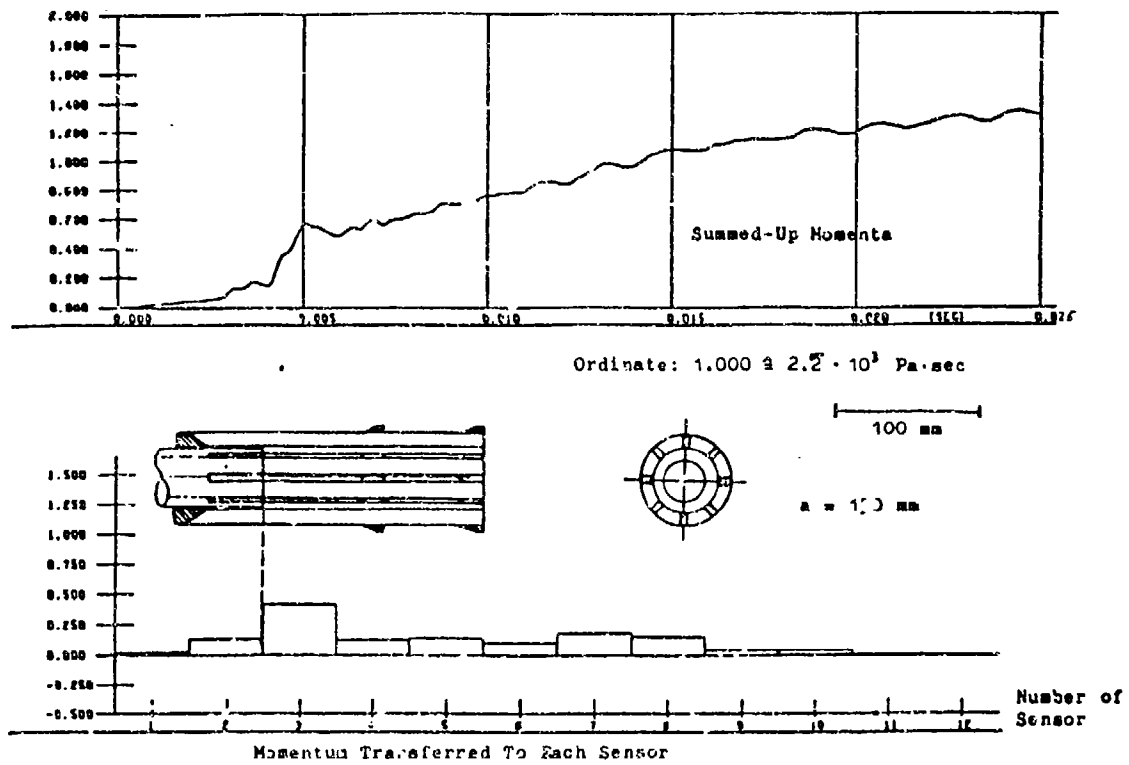


Fig. 7

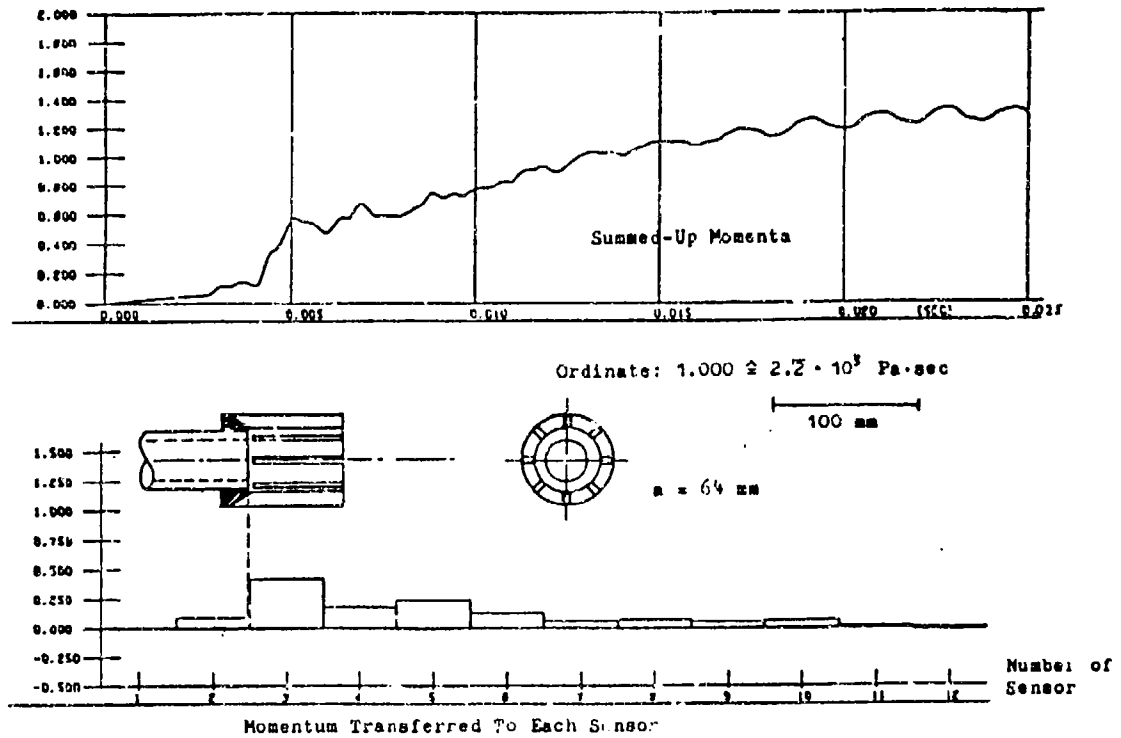
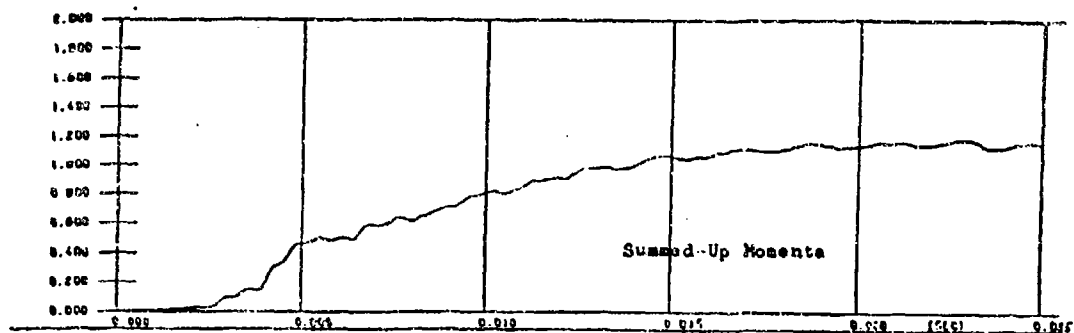


Fig. 8



Ordinate: $1.000 \pm 2.2 \cdot 10^3$ Pa-sec

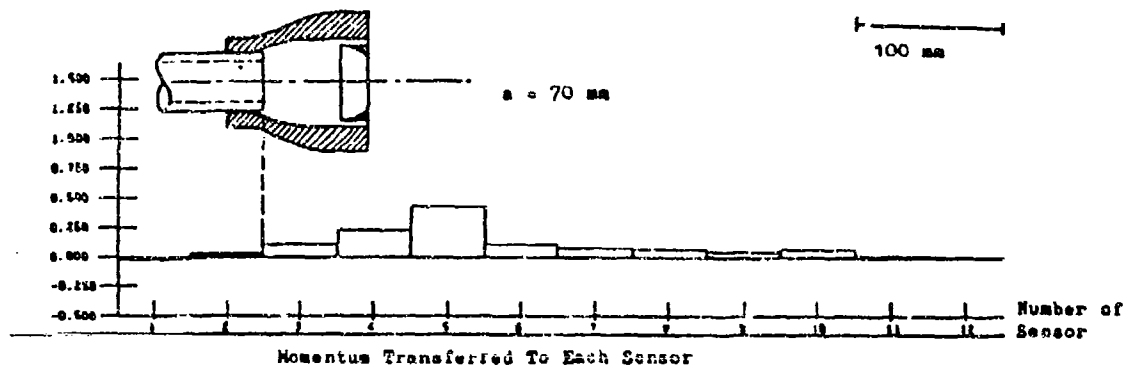
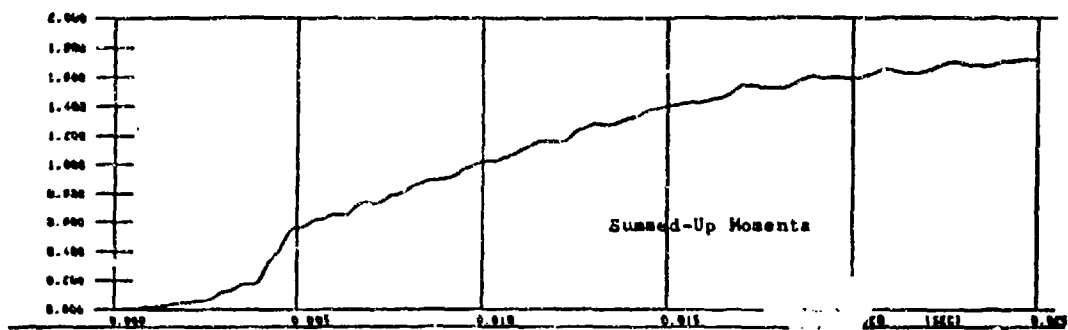


Fig. 9



Ordinate: $1.000 \pm 2.2 \cdot 10^3$ Pa-sec

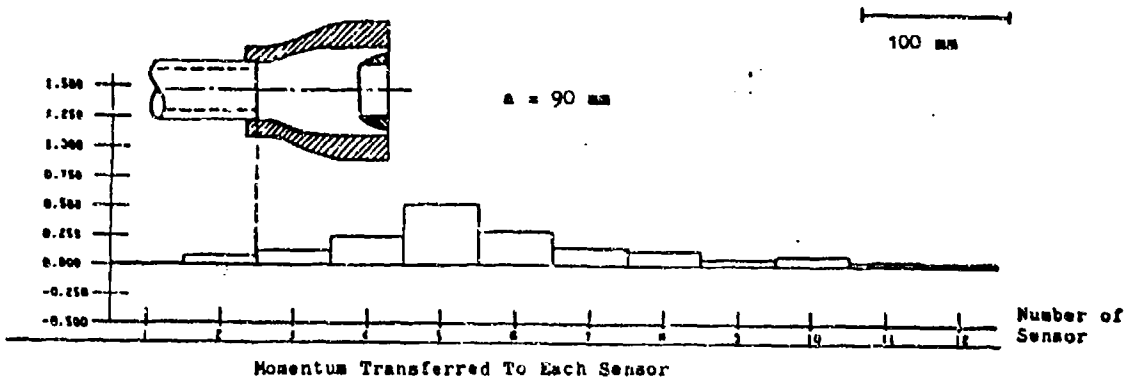


Fig. 10

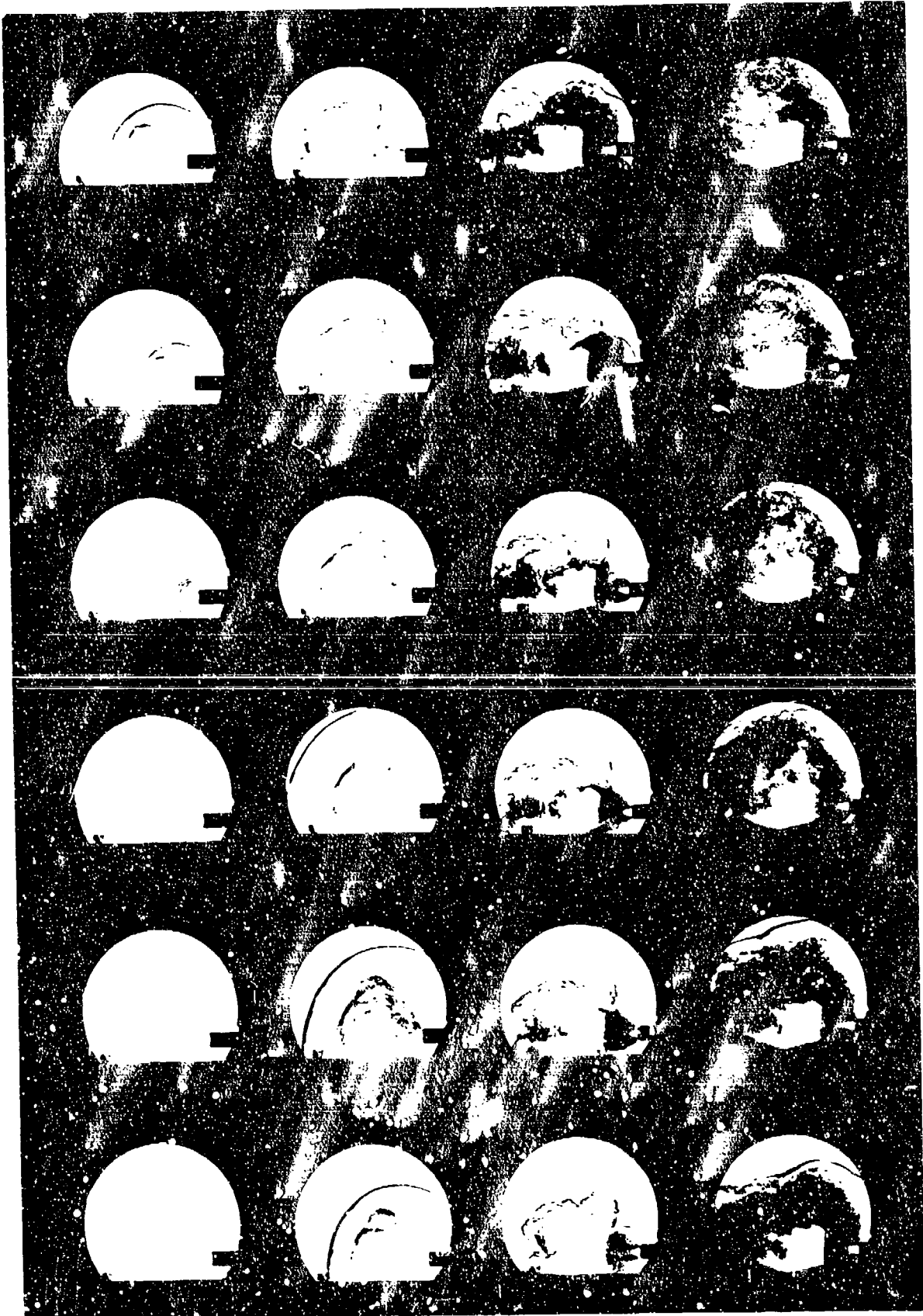


Fig. 11

- Frame No. 1, left-hand bottom m. of Z, made after ignition of the round
- Time interval between frames .1 msec
- Visible slit in frame No. 1

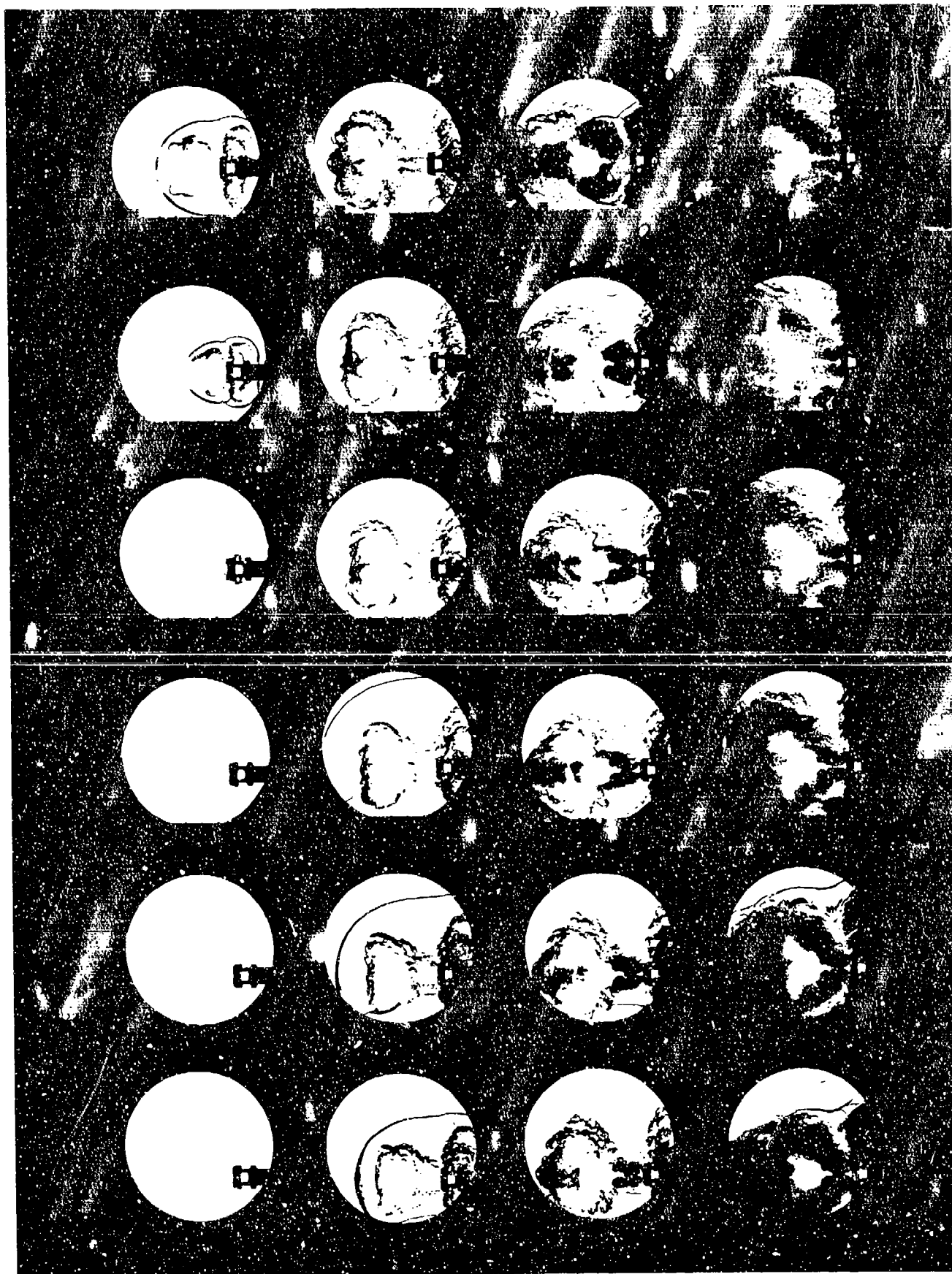


Fig. 24 - frame No1, left-and bottom, 2.050 msec after
 ignition of the round
 - Time interval between frames .1 msec
 - Muzzle exit in Frame No16

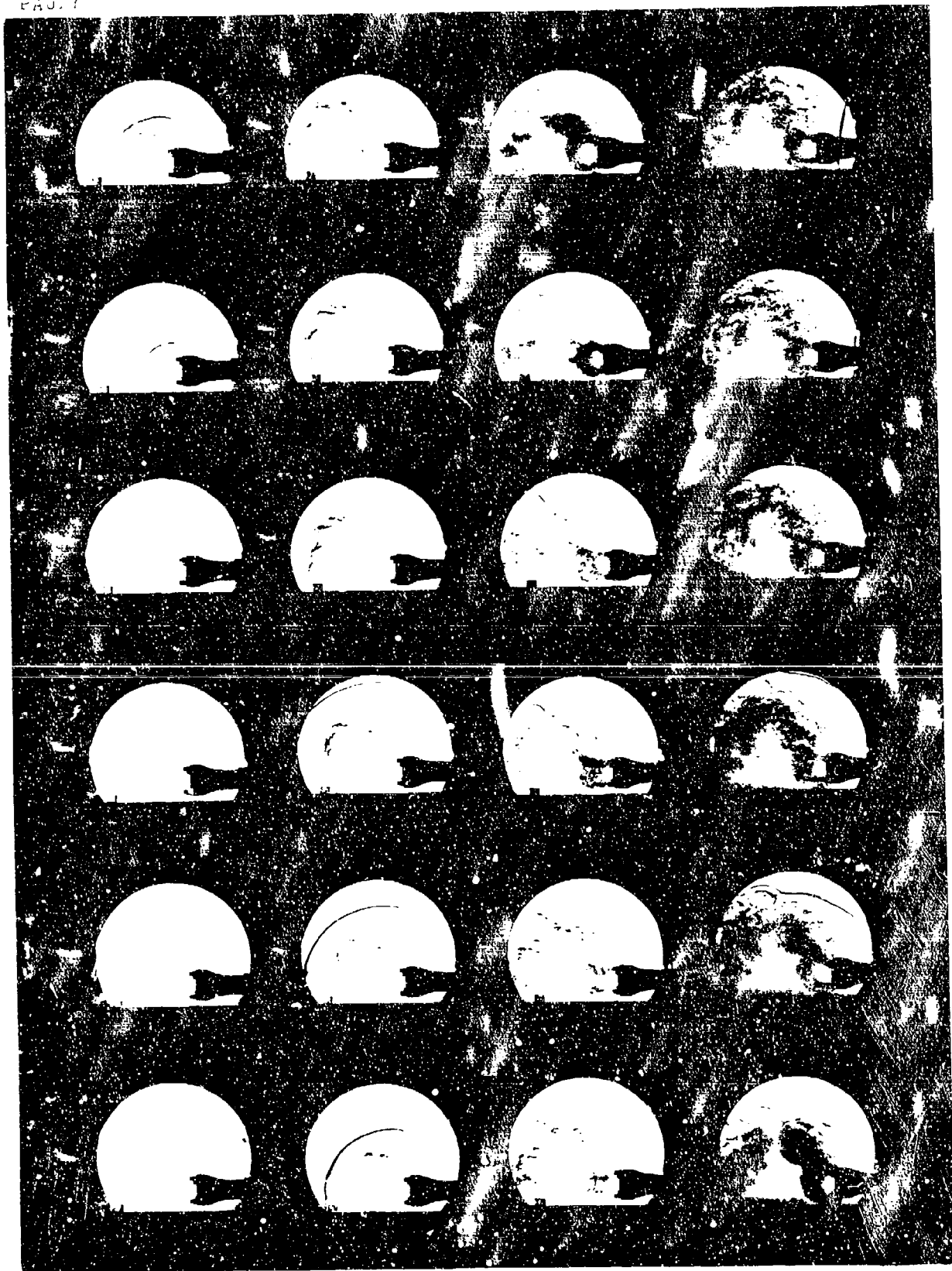


Fig. 17

- Frame No1, left-end bottom, 2.00 msec after initiation of the round
- Time interval between frames 1.4 msec
- Round exit in Frame No17

THOMAS

TITLE: Weapon Recoil Forces and Vehicle Motions
MARTIN D THOMAS
Royal Armament Research & Development Establishment
Chobham Lane, Chertsey, Surrey. KT16 OEE
United Kingdom of Great Britain & Northern Ireland

ABSTRACT: Various test-rigs are described which are being used to measure the recoil forces generated by the different vehicle mounted armaments being used in the British Army. Results are presented where they are available.

Computer models are being developed to predict vehicle motions due to these firing forces. Some mechanisms have already been modelled. Others have yet to be included.

BIOGRAPHY:

PRESENT ASSIGNMENT: Scientific Staff, RARDE (CH)
DEGREES HELD: BSc Birmingham University UK (1969),
PhD Birmingham University UK (1972)

THOMAS

WEAPON RECOIL FORCES AND VEHICLE MOTIONS

Dr MARTIN D THOMAS

Royal Armament Research & Development Establishment (Chertsey)
Chobham Lane, Chertsey, Surrey, KT16 0EE
United Kingdom of Great Britain & Northern Ireland

1. INTRODUCTION

Weapon platform stability governs both the accuracy of any weapon and its rate of fire. If a gun muzzle moves from its point of aim before the projectile leaves the gun, the point of impact will be displaced. Also, recoil forces may cause the weapon platform to be displaced, so that the next round cannot be fired until platform oscillations have decayed and the weapon has been re-aimed.

The Vehicles Department of the Royal Armament Research and Development Establishment (RARDE(CH)) is wholly or partly responsible for mounting weapon systems on any tracked or wheeled vehicles used by the British Armed Forces. Part of its research effort is therefore directed towards measuring or predicting the firing forces produced by these weapon systems, and developing techniques for predicting the resulting vehicle motions.

This paper describes the various test rigs being developed and the trials which have been undertaken so far. It covers investigations into both main armament and secondary armament on Armoured Fighting Vehicles (AFVs).

2. ORDNANCE BL 120mm Tk GUN L11A5

This tank gun is the current main armament on all British Chieftain and Challenger Main Battle Tanks (MBTs). It fires spin-stabilised APDS and HESH rounds as well as APFSDS. Its total recoiling mass is nearly two tonnes. As with all MBT guns, the recoil distance is severely limited, and this results in high trunnion loads. In this case, the gun recoil is 14 inches, and the peak trunnion load is 63 Tmf when firing the APDS round.

The recoil system consists of two hydraulic buffers, together with an expansion/replenisher cylinder, to dissipate energy during recoil, and a hydro-pneumatic recuperator to bring the gun back to battery after recoil. The buffers are designed to produce uniform trunnion loads throughout recoil.

Copyright © Controller HMSO London 1985

THOMAS

The energy is dissipated in the form of heat produced when hydraulic fluid is forced past the moving piston through slots machined on the inside of the cylinder.

In the early stages of the design of an MBT, development of the suspension is to some extent governed by the recoil forces generated by the buffers. Since the gun mass and impulse are known, it is possible to design a suitable recoil system, but if new rounds are being developed, evaluation is often delayed. As firing trials are expensive and as component failure can produce disproportionate damage, an hydraulic test-rig has been developed.

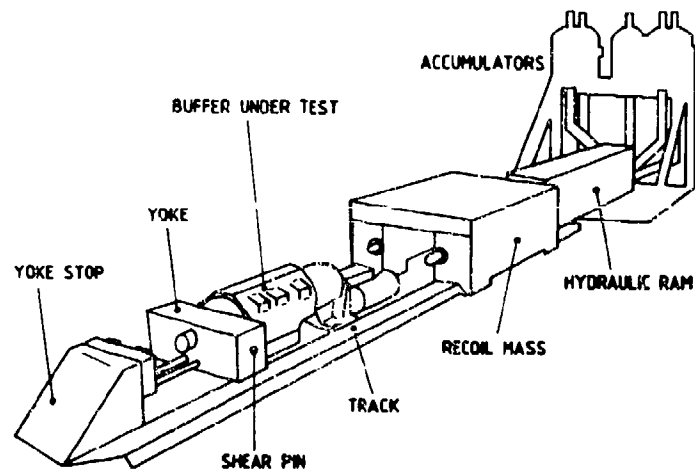


Figure 1 Schematic of Gun Recoil Test Rig

The rig consists of an hydraulic ram which accelerates a one tonne mass (half the recoiling mass) along a track. This mass impacts against a yoke which is connected to the buffer under test. The buffer then brings the yoke and the mass to rest over the appropriate distance. In the event of component failure, pins in the yoke shear, and the mass is brought to rest by a separate system. With this rig however, it is possible to increase the impulse in controlled steps and so reduce the risk of such a failure.

In this way it is possible to obtain early estimates of the real impulse being generated, so that due account can be taken at an early stage in the vehicle design.

Figure 2 shows a typical Chieftain trunnion pull record derived from buffer pressure measurements. This buffer

THOMAS

design dates from the 1950s when experimental optimisation was too expensive and theoretical techniques were not sufficiently advanced. Consequently, although it was designed to produce a constant load, too little energy is dissipated during the recoil stroke and a pressure peak occurs where the slots taper down to nothing. This effect could be eliminated by fine tuning but, as the buffer works perfectly well, there is no case for doing so.

3. GUN 76mm ARMD.C L23A1

This is the gun fitted in the Scorpion fire support version of the British air-portable Combat Vehicle Reconnaissance (Tracked) - CVR(T)FS. The recoil system is similar to that described for the 120mm gun except that a single buffer is used. The gun is allowed to recoil up to 11 inches.

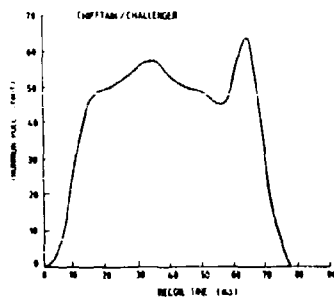


Figure 2
Typical Trunnion Pull
Chieftain/Challenger

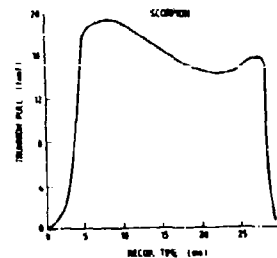


Figure 3
Typical Trunnion Pull
Scorpion

Figure 3 shows a typical trunnion pull record for Scorpion, which has been determined from the buffer pressure-time records in the same way as was done for the 120mm L11A5 gun. Here however, it would appear that slightly more energy could be dissipated during the middle part of the recoil stroke. Again, fine tuning cannot be justified as the buffer works perfectly well as it is.

Of more importance in this case is the fact that the peak trunnion pull is 19.4 Tonf on a vehicle weighing 8 Tons. This pull is much higher than normal for a vehicle of this size. As a rule of thumb for conventional AFVs, if vehicle motions are not to be excessive, it is considered desirable that the ratio of the Trunnion Pull to the Vehicle Weight should not exceed 2.5. Thus the Scorpion can be considered to be on the upper limit for crew comfort.

In reality, it is the impulse which governs the magnitude of vehicle motions, not the trunnion pull, but this rule of thumb has proved satisfactory since recoil distance is closely related to vehicle weight for conventional AFVs. If an unconventional vehicle design is adopted where, for example very long recoil is possible, the rule breaks down. The pull is reduced by making the force act for longer, but the total recoil time will still be small compared with the periodic time of the vehicle on its suspension, so there will be little or no change in the resulting vehicle motions.

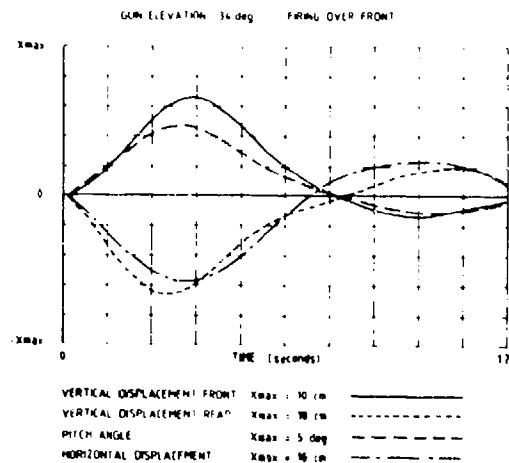


Figure 4 Experimental Scorpion Hull Motion Measurements

As the Scorpion is near the limit for crew comfort, it is being used as a test case for verification of computer models being developed to predict vehicle motions due to firing forces. Vehicle motions have been measured from film records of firing trials. These records are digitised and smoothed to remove measurement errors. A typical plot of vehicle motion when firing over the front is shown above.

4. ORDNANCE ML 81mm MORTAR L16A2

In addition to its ground role, the 81mm Mortar is also fired from the British F 432 Armoured Personnel Carrier. Here, it is mounted on a special bed-plate which is partly isolated from the vehicle floor by Bellville washer packs and a sponge rubber pad.

The presence of this pad has made it impossible to make a realistic theoretical estimate of the magnitude of the forces being transmitted to the vehicle structure. A special test-rig has therefore been developed to simulate the floor of the FV432. The rig incorporates four three-axis load cells

THOMAS

mounted one at each corner (Figure 5). The signal conditioning makes it possible to record the three force components and the three moments produced on firing. This test-rig is to be used in firing trials later this year.

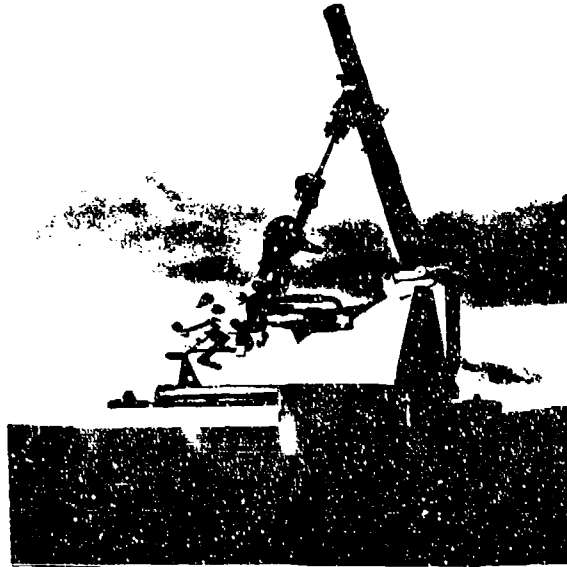


Figure 5 81mm Mortar Recoil Force Test Rig

5. MACHINE GUN 7.62mm GPMG

This is the General Purpose Machine Gun mounted on most British AFVs and it is a version of the Belgian FN Type MAG 7.62 Machine Gun. It is sometimes mounted co-axially, and sometimes pintle-mounted. In either case it may be used with or without buffering.

A test-rig similar to that to be used for the 81mm Mortar firings has been developed (Figure 6), except that the plane of the four load cells is now vertical. This has been used to measure the recoil forces with and without buffering. Figure 7 shows a comparison between the two force cycles measured when firing a clip of five rounds. Despite the high frequency ringing, it is clear that buffering produces a marked improvement. The large spike at the end of the burst in Case B is caused by the gun running forward at the end of the burst, and impacting against its stops. This could easily be eliminated.

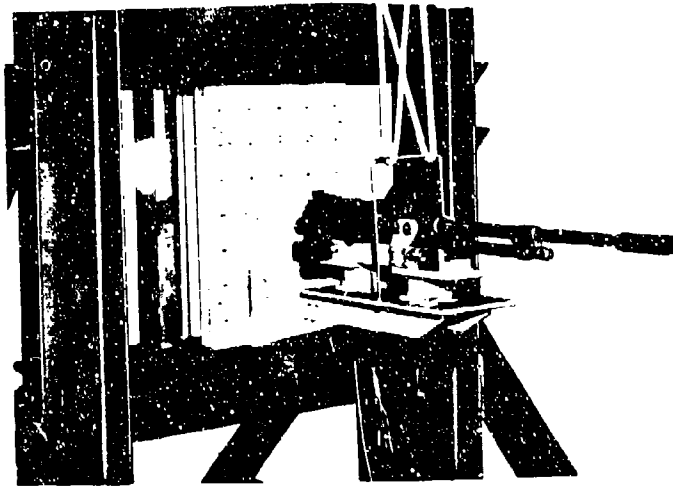


Figure 6 GPMG Recoil Force Test Rig

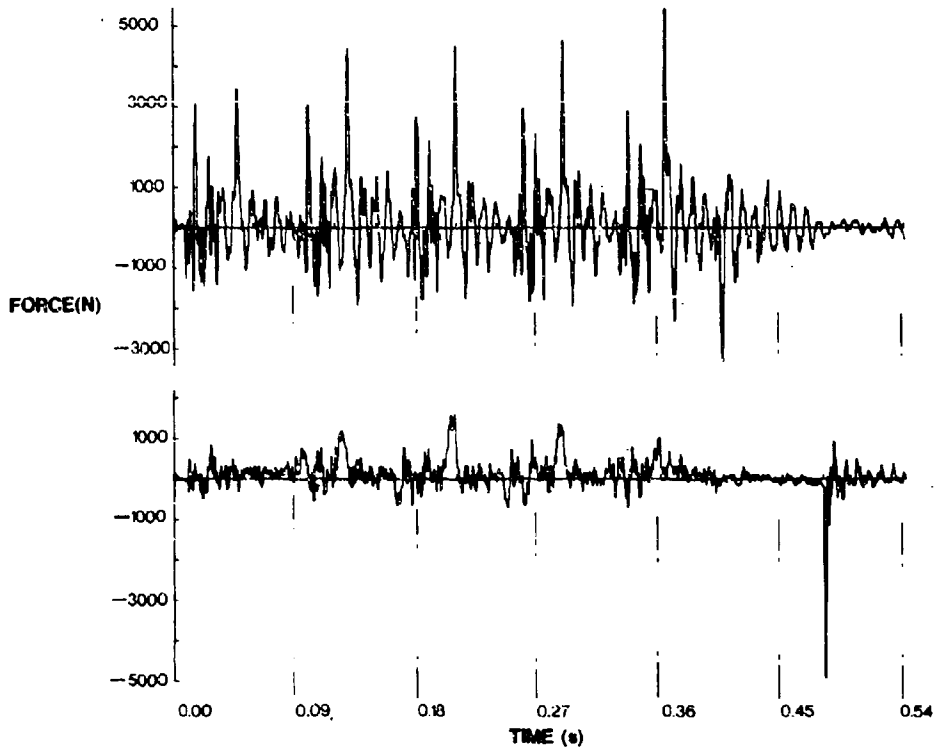


Figure 7
GPMG Recoil Force Records A - No Buffer B -Sprung Buffer

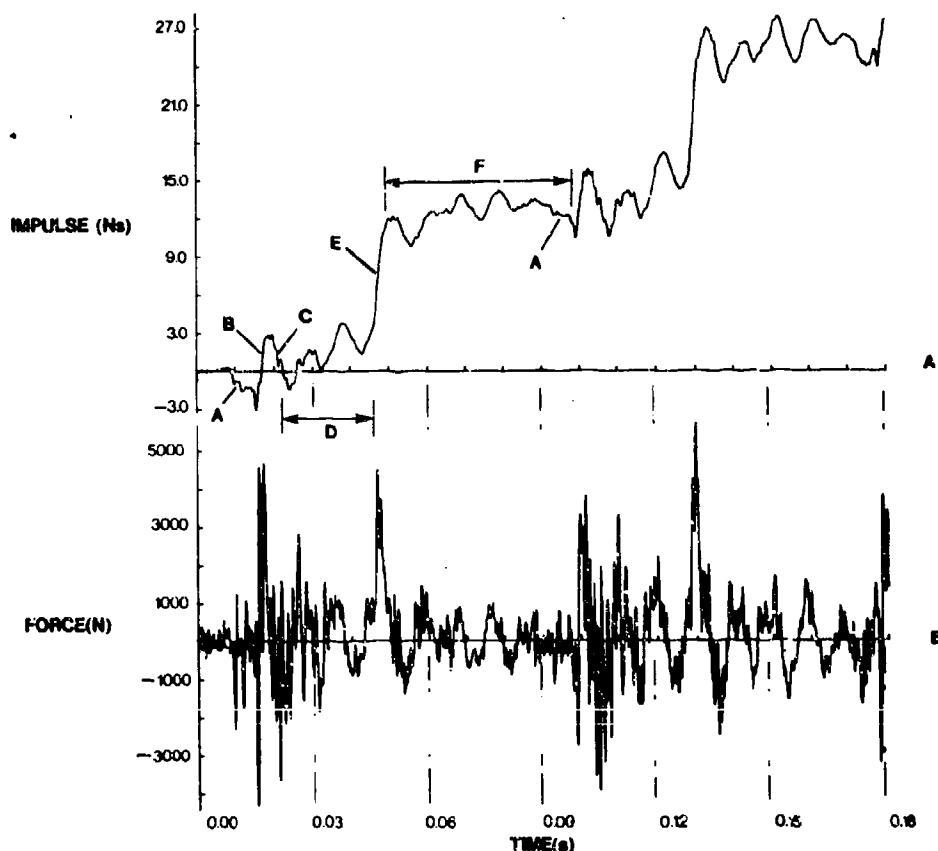


Figure 8
GPMG Recoil Force & Impulse
A - Force Integral B - Force Record

Figure 8 shows one cycle in more detail, together with its integral. Integrating the Force-Time record makes it possible to identify the principal force components without being confused by the various rattles which occur. The bolt runs forward, stripping a round from the clip (A). The gun fires (B) and the gas pressure throws the bolt back (C). The bolt travels back (D) until it impacts against its buffer (E), generating the main recoil impulse. The bolt then travels forward again (F) until it strips off the next round (A) and the cycle repeats.

6. COMPUTER MODELLING OF VEHICLE MOTIONS

Initially, it was hoped that it would be possible to make use of suspension models developed to predict vehicle ride characteristics when driving cross-country. It was found however, that these models were inadequate as, in addition to

THOMAS

the vehicle pitch and bounce motions which might be expected, the vehicle moves backwards when the gun is fired, taking up any track slack. The taut track then compresses the rear suspension units as the vehicle moves further back.

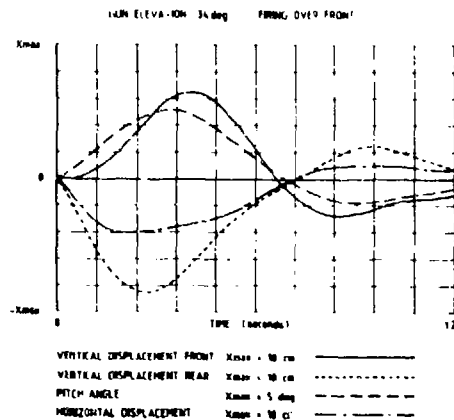


Figure 9 Theoretical Prediction of Scorpion Hull Motions

An output from a three degree-of-freedom model which includes simulation of this effect, is shown in Figure 9. This compares quite well with the experimental results shown in figure 4.

The model is now being enhanced to include all six degrees-of-freedom, as it has been found that four were not enough to account for the motions when firing over the side, and the motions are even more complex when firing at some intermediate angle. The lateral stiffness of the vehicle suspension is too low to prevent sideways motion relative to the ground, so this effect is being modelled. It is also necessary to include vehicle yaw as the turret axis does not pass through the vehicle centre of gravity.

7. EVALUATING FUTURE AFVs

There is always a requirement to mount high performance weapons on smaller and smaller vehicles. In these circumstances, traditional rules of thumb can no longer be trusted, and new procedures must be developed to help the designer predict vehicle performance at the concept stage.

This paper has described the trials which are being conducted to measure the forces produced by various weapons, and the computer models which are being developed to make it

THOMAS

possible to predict the effect which these forces will have on the stability of weapon platforms.

There is still more work to be done in this area. In particular, it is still necessary to validate the computer models being developed. Clearly, a computer model developed to account for the motions of one vehicle, will have to be demonstrated on a second, before the vehicle designer could be convinced of its merits. This paper is intended only to summarise the work which has been done to date.

AUTHOR INDEX

| | <u>Page</u> |
|-----------------------------|-----------------------------------|
| Andrews, T. O. | II-51 |
| Andrisani, D. | I-68 |
| Becker, R. S. | II-70 |
| Benzkofer, P. | II-89 |
| Brennan, R. X. | V-57 |
| Brooks, J. | V-79 |
| Bulman, D. N. | IV-54 |
| Chu, S. H. | V-12 |
| Chung, K. | II-51 |
| Coates, S. A. | II-12 |
| Dolce, T. | V-80 |
| Fancett, R. K. | III-50; III-76; III-78 |
| Floroff, S. G. | V-39 |
| Fornoff, J. M. | I-86 |
| Gartner, R. F. | III-1 |
| Gast, R. | I-22 |
| Gleason, D. | I-68 |
| Groff, J. | V-80 |
| Haug, B. T. | II-34 |
| King, W. P. C. | V-92 |
| Kingsbury, H. B. | I-1 |
| Kochenderfer, J. W. | IV-94 |
| Kuhl, F. P. | I-68 |
| Lapetina, N. A. | II-51 |
| Lionetti, N. | V-39 |
| Loder, R. K. | III-50; III-76; III-77; III-78 |
| Miller, J. M. | II-51 |
| Patton, E. M. | I-51 |
| Pauly, G. | III-23 |
| Penny, P. H. G. | V-92 |
| Peterson, R. | II-1 |
| Pflegl, G. | IV-1 |
| Powell, S. E. | IV-77 |
| Radkiewicz, R. | II-1 |
| Scanlon, R. D. | IV-1 |
| Schmidt, E. M. | IV-94 |
| Schmidt, J. Q. | III-51 |
| Seymour, M. J. | IV-46 |
| Simkins, T. E. | IV-1 |
| Sneck, H. J. | I-22 |
| Soifer, M. T. | II-70 |
| Thomas, M. | III-40 |
| Thomasson, P. G. | IV-17 |

| | <u>Page</u> |
|--------------------------|-----------------------|
| Townsend, F. E. | III-1 |
| Vance, K. | IV-46 |
| Walbert, J. N. | II-12; II-33; V-80 |
| Watson, C. | I-106 |
| Wineholt, E. | III-76; III-77 |
| Zepp, W. T. | III-12 |
| Zimmerman, K. L. | V-1 |

TECHNICAL REPORT INTERNAL DISTRIBUTION LIST

| | <u>NO. OF COPIES</u> |
|---|--------------------------|
| CHIEF, DEVELOPMENT ENGINEERING BRANCH | |
| ATTN: SMCAR-LCB-D | 1 |
| -DA | 1 |
| -DP | 1 |
| -DR | 1 |
| -DS (SYSTEMS) | 1 |
| -DE (ICAS GROUP) | 1 |
| -DC | 1 |
| -DM | 1 |
| CHIEF, ENGINEERING SUPPORT BRANCH | |
| ATTN: SMCAR-LCB-S | 1 |
| -SE | 1 |
| CHIEF, RESEARCH BRANCH | |
| ATTN: SMCAR-LCB-R | 2 |
| -R (ELLEN FOGARTY) | 1 |
| -RA | 1 |
| -RM | 2 |
| -RP | 1 |
| -RT | 1 |
| TECHNICAL LIBRARY | |
| ATTN: SMCAR-LCB-TL | 5 |
| TECHNICAL PUBLICATIONS & EDITING UNIT | |
| ATTN: SMCAR-LCB-TL | 2 |
| DIRECTOR, OPERATIONS DIRECTORATE | 1 |
| DIRECTOR, PROCUREMENT DIRECTORATE | 1 |
| DIRECTOR, PRODUCT ASSURANCE DIRECTORATE | 1 |

NOTE: PLEASE NOTIFY DIRECTOR, BENET WEAPONS LABORATORY, ATTN: SMCAR-LCB-TL,
OF ANY ADDRESS CHANGES.

TECHNICAL REPORT EXTERNAL DISTRIBUTION LIST

| | <u>NO. OF COPIES</u> | | <u>NO. OF COPIES</u> |
|--|---|--|--------------------------|
| ASST SEC OF THE ARMY RESEARCH & DEVELOPMENT ATTN: DEP FOR SCI & TECH THE PENTAGON WASHINGTON, D.C. 20315 | 1 | COMMANDER US ARMY AMCCOM ATTN: SMCAR-ESP-L ROCK ISLAND, IL 61299 | 1 |
| COMMANDER DEFENSE TECHNICAL INFO CENTER ATTN: DTIC-DDA CAMERON STATION ALEXANDRIA, VA 22314 | 12 | COMMANDER ROCK ISLAND ARSENAL ATTN: SMCRI-ENM (MAT SCI DIV) ROCK ISLAND, IL 61299 | 1 |
| COMMANDER US ARMY MAT DEV & READ COMD ATTN: DRCDE-SG 5001 EISENHOWER AVE ALEXANDRIA, VA 22333 | 1 | DIRECTOR US ARMY INDUSTRIAL BASE ENC ACTV ATTN: DRXIB-M ROCK ISLAND, IL 61299 | 1 |
| COMMANDER ARMAMENT RES & DEV CTR US ARMY AMCCOM ATTN: SMCAR-LC SMCAR-LCE SMCAR-LCM (BLDG 321) SMCAR-LCS SMCAR-LCU SMCAR-LCW SMCAR-SCM-O (PLASTICS TECH EVAL CTR, BLDG. 351N) SMCAR-TSS (STINFO) DOVER, NJ 07801 | 1 1 1 1 1 1 1 1 2 | COMMANDER US ARMY TANK-AUTMV R&D COMD ATTN: TECH LIB - DRSTA-TSL WARREN, MI 48090 | 1 |
| DIRECTOR BALLISTICS RESEARCH LABORATORY ATTN: AMXBR-TSB-S (STINFO) ABERDEEN PROVING GROUND, MD 21005 | 1 | COMMANDER US ARMY TANK-AUTMV COMD ATTN: DRSTA-RC WARREN, MI 48090 | 1 |
| MATERIEL SYSTEMS ANALYSIS ACTV ATTN: DRXSY-MP ABERDEEN PROVING GROUND, MD 21005 | 1 | COMMANDER US MILITARY ACADEMY ATTN: CHMN, MECH ENGR DEPT WEST POINT, NY 10996 | 1 |
| | | US ARMY MISSILE COMD REDSTONE SCIENTIFIC INFO CTR ATTN: DOCUMENTS SECT, BLDG. 4484 REDSTONE ARSENAL, AL 35898 | 2 |
| | | COMMANDER US ARMY FGN SCIENCE & TECH CTR ATTN: DRXST-SD 220 7TH STREET, N.E. CHARLOTTESVILLE, VA 22901 | 1 |

NOTE: PLEASE NOTIFY COMMANDER, ARMAMENT RESEARCH AND DEVELOPMENT CENTER,
US ARMY AMCCOM, ATTN: BENET WEAPONS LABORATORY, SMCAR-LCB-TL,
WATERVLIET, NY 12189, OF ANY ADDRESS CHANGES.

TECHNICAL REPORT EXTERNAL DISTRIBUTION LIST (CONT'D)

| | <u>NO. OF COPIES</u> | | <u>NO. OF COPIES</u> |
|---|--------------------------|---|--------------------------|
| COMMANDER US ARMY MATERIALS & MECHANICS RESEARCH CENTER ATTN: TECH LIB - DRXMR-PL WATERTOWN, MA 01272 | 2 | DIRECTOR US NAVAL RESEARCH LAB ATTN: DIR, MECH DIV CODE 26-27, (DOC LIB) WASHINGTON, D.C. 20375 | 1 1 |
| COMMANDER US ARMY RESEARCH OFFICE ATTN: CHIEF, IPO P.O. BOX 12211 RESEARCH TRIANGLE PARK, NC 27709 | 1 | COMMANDER AIR FORCE ARMAMENT LABORATORY ATTN: AFATL/DLJ AFATL/DLJG EGLIN AFB, FL 32542 | 1 1 |
| COMMANDER US ARMY HARRY DIAMOND LAB ATTN: TECH LIB 2800 POWDER MILL ROAD ADELPHIA, MD 20783 | 1 | METALS & CERAMICS INFO CTR BATTELLE COLUMBUS LAB 505 KING AVENUE COLUMBUS, OH 43201 | 1 |
| COMMANDER NAVAL SURFACE WEAPONS CTR ATTN: TECHNICAL LIBRARY CODE X212 DAHLGREN, VA 22448 | 1 | | |

NOTE: PLEASE NOTIFY COMMANDER, ARMAMENT RESEARCH AND DEVELOPMENT CENTER,
US ARMY AMCCOM, ATTN: BENET WEAPONS LABORATORY, SMCAR-LCB-TL,
WATERVLIET, NY 12189, OF ANY ADDRESS CHANGES.

NOTE: COPY TO EACH SYMPOSIUM ATTENDEE.

the combined effect of axial and transverse loads. (The plus sign is for fibers in which the direct stress and the bending stress are in the same direction, the minus sign for fibers in which they are in opposite directions.) If a column is comparatively stiff so that the bending moment due to the axial load is negligible, M may be set equal to the maximum moment due to transverse loads M_t alone. This may be done with an error of less than five percent if $P < 0.125 EI/L^2$ for cantilever beams, $P < 0.5 EI/L^2$ for beams with pinned ends, or $P < 2EI/L^2$ for beams with fixed ends.

If $0.125 EI/L^2 < P < 0.8 EI/L^2$ for cantilever beams and $0.5 EI/L^2 < P < 3 EI/L^2$ for beams with fixed ends, the value of M for Equation (1-43) may be given by*

$$M = \frac{M_t}{\left(1 + K \frac{PL^2}{EI}\right)} \quad (1-44)$$

for an error of less than five percent where K is given in Table 1-11 for various manners of loading and end support. The plus sign is used in the denominator if P is a tensile load and the minus sign is used if P is a compressive load. Equation (1-44) is appropriate only for beams in which the maximum bending moment and maximum deflection occur at the same section.

TABLE 1-11

Values of α for Equation (1-44)

| Manner of Loading and Support | K |
|--------------------------------|---|
| Cantilever, end load | 1/3 |
| Cantilever, uniform load | 1/4 |
| Pinned ends, center load | 1/12 |
| Pinned ends, uniform load | 5/48 |
| Equal and opposite end couples | 1/8 |
| Fixed ends, center load | 1/24 |
| Fixed ends, uniform load | 1/32 (for end moments) 1/16 (for center moments) |

1.4.2 Exact Method for Beams Under Combined Axial and Transverse Loads - Beam Columns

Table 1-12 gives exact formulas for the bending moment, M , deflection, y , and end slope, θ , in beams which are subjected to

* Griffel, William, Handbook of Formulas for Stress and Strain

TABLE 1-12

Formulas for Beams Under Combined Axial and Transverse Loading

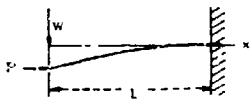
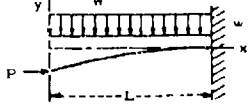
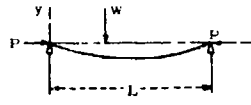
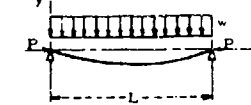
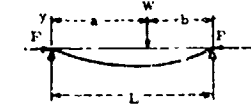
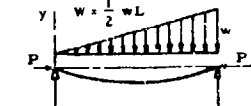
| Case | Formulas |
|--|--|
| <p>1</p>  | <p>Max M = -WL tan U/U at x = L</p> <p>Max y = -$\frac{W}{P}$ (L tan U/U - L) at x = 0</p> <p>$\theta = -\frac{W}{P} \left(\frac{1 - \cos L/U}{\cos L/U} \right)$ at x = 0</p> |
| <p>2</p>  | <p>Max M = -$\frac{wL}{U} [L(1 - \sec U/U + L \tan U)]$ at x = L</p> <p>Max y = -$\frac{wL}{PU} \left[\frac{L}{U} \left(1 + \frac{1}{2} U^2 - \sec U \right) + L(\tan U - U) \right]$ at x = 0</p> <p>$\theta = \frac{wL}{P} \left[\frac{1}{\cos U} - \frac{1 - \cos 2U}{U \sin 2U} \right]$</p> |
| <p>3</p>  | <p>Max M = $\frac{WL}{2U} \tan \frac{1}{2} U$ at x = $\frac{1}{2} L$</p> <p>Max y = $\frac{1}{2} \frac{WL}{PU} \left(\tan \frac{1}{2} U - \frac{1}{2} U \right)$ at x = $\frac{1}{2} L$</p> <p>$\theta = -\frac{W}{2P} \left(\frac{1 - \cos \frac{1}{2} U}{\cos \frac{1}{2} U} \right)$ at x = 0</p> |
| <p>4</p>  | <p>Max M = $wL^2 \left(\sec \frac{1}{2} U - 1 \right) / U^2$ at x = L/2</p> <p>Max y = $\frac{wL^2}{PU^2} \left(\sec \frac{1}{2} U - 1 - \frac{1}{6} U^2 \right)$ at x = $\frac{1}{2} L$</p> <p>$\theta = -\frac{wL}{PU} \left[-\frac{1}{2} U + \frac{1 - \cos U}{\sin U} \right]$ at x = 0</p> |
| <p>5</p>  | <p>Moment equation x = 0 to x = a</p> <p>$M = \frac{WU}{\sin U} \sin \frac{bU}{L} \sin \frac{xU}{L}$ Max M at x = $\frac{\pi L}{2U}$ if $\frac{\pi L}{2U} < a$</p> <p>Moment equation x = a to x = L</p> <p>$M = \frac{WU}{\sin U} \sin \frac{aU}{L} \sin \frac{(L-x)U}{L}$ Max M at x = $\left(L - \frac{\pi L}{2U} \right)$ if $\left(L - \frac{\pi L}{2U} \right) > a$ if $\frac{\pi L}{2U} > a$ and $\left(L - \frac{\pi L}{2U} \right) < a$, Max M is at x = a</p> <p>Deflection equation x = 0 to x = a $y = \frac{WU}{PU} \left(\frac{\sin \frac{bU}{L} \sin \frac{xU}{L}}{\sin U} - \frac{bxU}{L^2} \right)$</p> <p>Deflection equation x = a to x = L $y = \frac{WU}{PU} \left(\frac{\sin \frac{aU}{L} \sin \frac{(L-x)U}{L}}{\sin U} - \frac{aU(L-x)}{L^2} \right)$</p> <p>$\theta = -\frac{W}{P} \left(\frac{1}{L} + \frac{\sin \frac{aU}{L}}{\tan U} - \cos \frac{aU}{L} \right)$ at x = 0 $\theta = \frac{W}{P} \left(\frac{a}{L} - \frac{\sin \frac{aU}{L}}{\sin U} \right)$ at x = L</p> |
| <p>6</p>  | <p>Moment equation x = 0 to x = L $M = \frac{Wx^2}{U^2} \left(\frac{\sin Ux}{\sin U} - \frac{x}{L} \right)$</p> <p>Max M at x = $\frac{L}{U} \arccos \left(\frac{\sin U}{U} \right)$</p> <p>Deflection equation</p> <p>x = 0 to x = L: $y = -\frac{W}{P} \left(\frac{x^3}{6L} + \frac{L^2}{U^2} \frac{\sin Ux}{\sin U} - \frac{Lx}{U^2} - \frac{1}{6} Lx \right)$</p> <p>$\theta = -\frac{W}{P} \left(\frac{1}{U \sin U} - \frac{L}{U^2} - \frac{1}{6} L \right)$ at x = 0</p> <p>$\theta = \frac{W}{P} \left(\frac{L}{U \tan U} + \frac{L}{U^2} - \frac{1}{3} L \right)$ at x = L</p> |

TABLE 1-12

Formulas for Beams Under Combined Axial and Transverse Loading (continued)

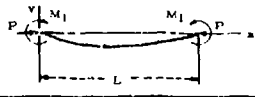
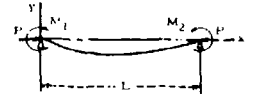
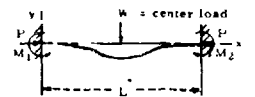

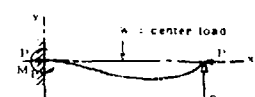

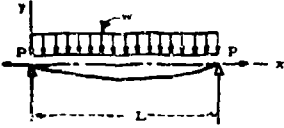
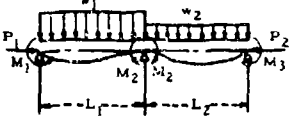
| Case | Formulas |
|---|---|
| 7 |  <p>Max $M = M_1 \sec \frac{1}{2} U$ at $x = \frac{1}{2} L$</p> <p>Max $y = -\frac{M_1}{P} \left(\frac{1 - \cos \frac{1}{2} U}{\cos \frac{1}{2} U} \right)$ at $x = \frac{1}{2} L$</p> <p>$\theta = -\frac{M_1 U}{PL} \tan \frac{1}{2} U$ at $x = 0$</p> |
| 8 |  <p>Moment equation: $x = 0$ to $x = L$: $M = \left(\frac{M_2 - M_1 \cos U}{\sin U} \right) \sin \frac{xU}{L} + M_1 \cos \frac{xU}{L}$</p> <p>Max M at $x = \frac{1}{U} \arccos \tan \left(\frac{M_2 - M_1 \cos U}{M_1 \sin U} \right)$</p> <p>Deflection equation: $x = 0$ to $x = L$: $y = \frac{1}{P} \left[M_1 + (M_2 - M_1) \frac{x}{L} - (M_2 - M_1 \cos U) \frac{\sin \frac{xU}{L}}{\sin U} - M_1 \cos \frac{xU}{L} \right]$</p> <p>$\theta = \frac{1}{P} \left[\frac{M_2 - M_1}{L} - \frac{U(M_2 - M_1 \cos U)}{L \sin U} \right]$ at $x = 0$</p> <p>$\theta = \frac{1}{P} \left[\frac{M_2 - M_1}{L} - \frac{U(M_2 - M_1 \cos U)}{L \sin U} + \cos U + \frac{M_1 U}{L} \sin U \right]$ at $x = L$</p> |
| 9 Beams with fixed ends under axial compression and transverse center load |  <p>$M_1 = M_2 = \frac{WL}{2U} \left(\frac{1 - \cos U}{\sin U} \right)$</p> <p>At $x = \frac{1}{2} L$: $M = \frac{WL}{2U} \left(\tan \frac{1}{2} U + \frac{1 - \cos U}{\sin U} \right)$</p> <p>Max $y = -\frac{WL}{2PU} \left[\tan \frac{1}{2} U + \frac{1 - \cos U}{\sin U} \right]$</p> |
| 10 Beams with fixed ends under axial compression and uniform transverse load |  <p>$M_1 = M_2 = \frac{wL^2}{U^2} \left(1 - \frac{1 - \cos U}{\sin U} \right)$</p> <p>At $x = \frac{1}{2} L$: $M = \frac{wL^2}{U^2} \left(\frac{1}{2} - \frac{1 - \cos U}{\sin U} \right)$</p> <p>Max $y = -\frac{wL^2}{PU^2} \left[\frac{1}{2} - \frac{1 - \cos U}{\sin U} + \frac{1 - \cos U}{\sin U} \right]$</p> |
| 11 Beams with one end fixed, other end pinned under axial compression and transverse center load |  <p>Max $M = M_1 = \frac{WL}{2U} \left[\frac{\tan U \sec \frac{1}{2} U - U}{L \tan U - L} \right]$</p> <p>$R = \frac{1}{2} W + \frac{M_1}{L}$</p> <p>Moment equation: $x = \frac{1}{2} L$ to $x = L$: $M = M_1 \left(\frac{\sin \frac{Ux}{L}}{\tan U} - \cos \frac{Ux}{L} \right) + \frac{WL}{U} \left(\sin \frac{1}{2} U \cos \frac{Ux}{L} - \frac{\sin \frac{1}{2} U \sin \frac{Ux}{L}}{\tan U} \right)$</p> <p>Deflection equation: $x = \frac{1}{2} L$ to $x = L$: $y = \frac{1}{P} \left[M_1 \left(1 - \frac{x}{L} + \frac{\sin \frac{Ux}{L}}{\tan U} - \cos \frac{Ux}{L} \right) - \frac{WL}{U} \left(\frac{1 - \cos \frac{Ux}{L}}{\tan U} + \frac{\sin \frac{1}{2} U \sin \frac{Ux}{L}}{\tan U} - \sin \frac{1}{2} U \cos \frac{Ux}{L} \right) \right]$</p> |
| 12 Beams with one end fixed, other end supported, under axial compression and uniform transverse load |  <p>Max $M = M_1 = \frac{wL^2}{U} \left[\frac{\tan U (\tan \frac{1}{2} U - \frac{1}{2} U)}{\tan U - 1} \right]$</p> <p>$R = \frac{1}{2} wL + \frac{M_1}{L}$</p> <p>Moment equation: $x = 0$ to $x = L$: $M = M_1 \left(\cot U \sin \frac{Ux}{L} - \cos \frac{Ux}{L} \right) + \frac{wL^2}{U^2} \left[\frac{\sin \frac{Ux}{L}}{\sin U} - 1 \right] \cos U + w \cos \frac{Ux}{L} - 1$</p> <p>Deflection equation: $x = 0$ to $x = L$: $y = -\frac{1}{P} \left[M_1 \left(1 - \frac{x}{L} + \cot U \sin \frac{Ux}{L} - \cos \frac{Ux}{L} \right) - \frac{wL^2}{U^2} \cot U \sin \frac{Ux}{L} - \frac{\sin \frac{Ux}{L}}{\sin U} - \cos \frac{Ux}{L} + \frac{(Lx - x^2)U^2}{2L^2} + 1 \right]$</p> |
| 13 Same as Case 1 (cantilever with end load) except that P is tension | <p>Max $M = -W \tanh U/U$ at $x = L$</p> <p>Max $y = -\frac{W}{P} \left(L - \frac{1}{U} \tanh U \right)$ at $x = 0$</p> |
| 14 Same as Case 2 (cantilever with uniform load) except that P is tension | <p>Max $M = -wL \left[L \tanh U + \frac{1}{U} (1 - \operatorname{sech} U) \right] / U$ at $x = L$</p> <p>Max $y = -\frac{wL^2}{PU} \left[\frac{1}{2} (1 - \frac{1}{2} U^2 - \operatorname{sech} U) - L (\tanh U + U) \right]$ at $x = 0$</p> |
| 15 Same as Case 3 (pinned ends, center load) except that P is tension | <p>Max $M = \frac{WL}{U} \tanh \frac{1}{2} U$ at $x = \frac{1}{2} L$</p> <p>Max $y = -\frac{W}{P} \left(\frac{1}{4} L - \frac{1}{2U} \tanh \frac{1}{2} U \right)$ at $x = \frac{1}{2} L$</p> |
| 16 Same as Case 4 (pinned ends, uniform load) | <p>Max $M = wL^2 (1 - \operatorname{sech} \frac{1}{2} U) / U^2$</p> <p>Max $y = -\frac{w}{P} \left[\frac{1}{8} L^2 - \frac{1}{U^2} (1 - \operatorname{sech} \frac{1}{2} U) \right]$</p> |
| 17 Same as Case 9 (fixed ends, center load) except that P is tension | <p>$M_1 = M_2 = \frac{WL}{2U} \left(\frac{\cosh \frac{1}{2} U - 1}{\sinh \frac{1}{2} U} \right)$</p> <p>Max $M = \frac{WL}{2U} \left(\frac{1 - \cosh \frac{1}{2} U}{\sinh \frac{1}{2} U \cosh \frac{1}{2} U} + \tanh \frac{1}{2} U \right)$ at $x = \frac{1}{2} L$</p> <p>Max $y = \frac{WL}{2PU} \left[\frac{1}{2} U - \tanh \frac{1}{2} U - \frac{(1 - \cosh \frac{1}{2} U)^2}{\sinh \frac{1}{2} U \cosh \frac{1}{2} U} \right]$</p> |

TABLE 1-12

Formulas for Beams Under Combined Axial and Transverse Loading (concluded)

| Case | Formulas |
|---|---|
| <p>18. Same as Case 10 (fixed ends, uniform load) except that P is tension</p> | $M_1 = M_2 = \frac{wL^2}{U^2} \left(\frac{1}{2} U - \frac{\tanh \frac{1}{2} U}{\tanh \frac{1}{2} U} \right)$ $\text{Max } M = \frac{wL^2}{U^2} \left(1 - \frac{\tanh U}{\sinh U} \right) \text{ at } x = \frac{1}{2} L$ $\text{Max } v = \frac{wL^2}{8PU^2} \left[\frac{4U(1 - \cosh \frac{1}{2} U)}{\sinh \frac{1}{2} U} + U^2 \right] \text{ at } x = \frac{1}{2} L$ |
| <p>19. Beam with ends pinned to rigid supports so horizontal displacement is prevented. Uniform transverse load and unknown axial tension</p>  | $\frac{E^2 A^2 k^6}{w^2 \delta} U^9 = \frac{1}{24} U^3 - \frac{5}{4} U + \frac{5}{2} \tanh \frac{U}{2} + \frac{U}{4} \tanh^2 \frac{U}{2} \text{ where } k = \sqrt{\frac{1}{A}}$ <p>This equation is solved for U, and P determined therefrom</p> <p>When C = $\frac{wL^4}{16EAk^2}$ is small (less than 4), $P = \frac{68}{630} \frac{EIC^2}{L^2} \left(1 - \frac{62}{2835} C^2 \right)$</p> <p>When C is large (greater than 15), $P = \frac{4EI}{L^2} \left[\left(\frac{C^2}{6} \right)^{\frac{2}{3}} - 2 \right]$</p> <p>When P has been found by one of the above formulas, M and v may be found by the formulas of Case 16</p> |
| <p>20. Continuous beam, spans 1 and 2 unequal and unequally loaded</p>  | $\frac{M_1 L_1}{I_1} \left(\frac{U_1 \operatorname{cosec} U_1 - 1}{U_1^2} \right) = \frac{M_2 L_2}{I_2} \left(\frac{U_2 \operatorname{cosec} U_2 - 1}{U_2^2} \right)$ $= M_2 \left[\frac{L_1}{I_1} \left(\frac{1 - U_1 \operatorname{cosec} U_1}{U_1^2} \right) + \frac{L_2}{I_2} \left(\frac{U_2 \operatorname{cosec} U_2 - 1}{U_2^2} \right) \right]$ $= \frac{w_1 L_1^3}{I_1} \left(\frac{\tan \frac{1}{2} U_1 - \frac{1}{2} U_1}{U_1^3} \right) = \frac{w_2 L_2^3}{I_2} \left(\frac{\tan \frac{1}{2} U_2 - \frac{1}{2} U_2}{U_2^3} \right)$ <p>(Theorem of Three Moments. Subscripts with P, L, w, I, and U refer to first and second spans. M2 acts on span 1, M2' on span 2)</p> |

combined axial and transverse loading. Although these formulas should be used if $P > 0.125 EI/L^2$ for cantilever beams, $P > 0.5 EI/L^2$ for beams with pinned ends, or $P > 2 EI/L^2$ for beams with fixed ends, they may be used for beams with smaller axial loads. In these formulas, $U = L\sqrt{P}/EI$. The quantity U may be found rapidly through the use of the nomogram in Figure 1-40. The formulas for beams under a compressive axial load may be modified to hold for a tensile axial load by making the following substitutions: $-P$ for P ; $\sqrt{-I}$ for U ; $\sqrt{-I} \sinh U$ for $\sin U$; and $\cosh U$ for $\cos U$. This has been done for some of the more common loadings and the resulting formulas given in cases 13 to 18 of Table 1-12.

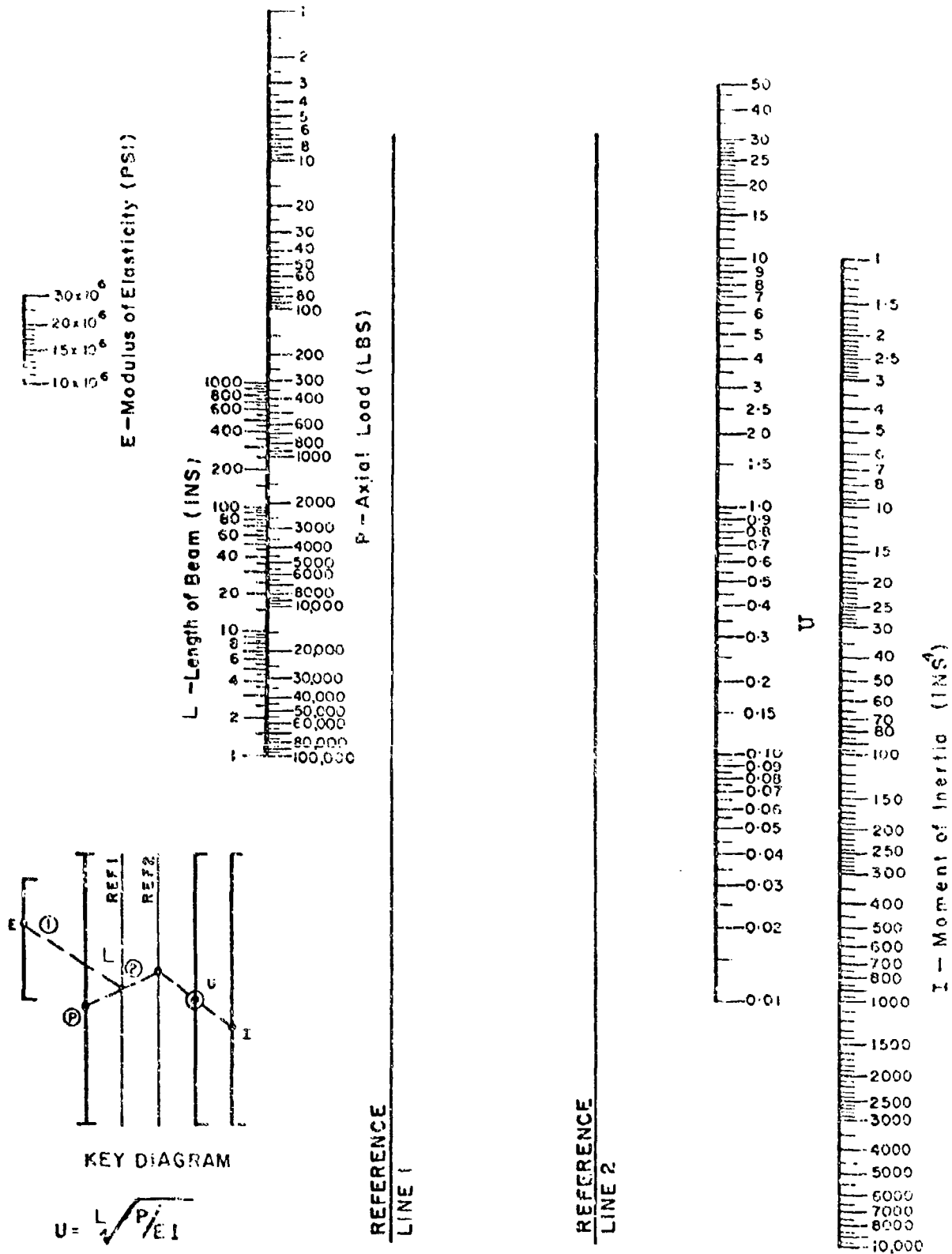


Figure 1-40. Nomogram for Determining U*

* Griffel, William, Handbook of Formulae for Stress and Strain

1.4.3

Sample Problem - Beams Under Combined Axial and Transverse Loads - Beam Columns

Given: The beam column shown in Figure 1-41.

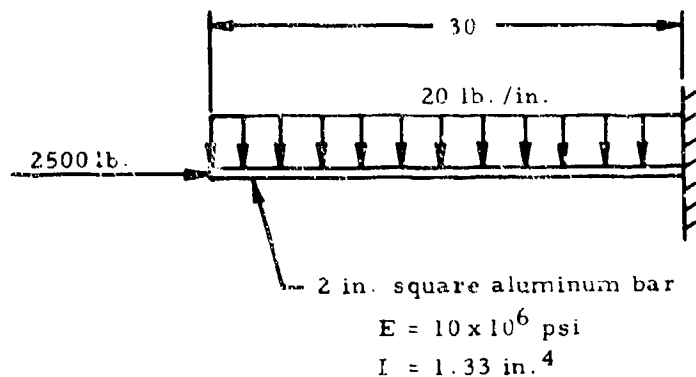


Figure 1-41. Cantilever Beam Under Combined Axial and Transverse Loads

Find: The maximum bending moment, M , vertical deflection, y , and angular deflection, θ , of the bar.

Solution:

$$0.125 \frac{EI}{L^2} = 0.125 \frac{(10 \times 10^6)(1.33)}{(30)^2} = 1,850 \text{ lb.}$$

According to Section 1.4.2, the exact method must be used for cantilever beams if $P < 0.125 EI/L^2$ as is true in this case. From Figure 1-40,

$$U = L \sqrt{\frac{P}{EI}} = 30 \sqrt{\frac{2500}{(10 \times 10^6)(1.33)}} = 0.41$$

From Table 1.12, Case 2,

$$\begin{aligned} \text{Max } M &= \frac{-wL}{U} \left[\frac{L}{U} (1 - \sec U) + L \tan U \right] \\ &= \frac{-20(30)}{0.41} \left[\frac{30}{0.41} (1 - \sec 0.41) + 30 \tan 0.41 \right] = 8200 \text{ in. lb.} \end{aligned}$$

$$\begin{aligned} \text{Max } y &= \frac{-wL}{PU} \left[\frac{L}{U} \left(1 + \frac{1}{2} U^2 - \sec U \right) + L (\tan U - U) \right] \\ &= \frac{w20(30.0)}{2500(0.40)} \left\{ \left[\frac{30}{0.41} \left(1 + \frac{0.41^2}{2} - \sec 0.41 \right) \right] \right. \\ &\quad \left. + [30 (\tan 0.41 - 0.41)] \right\} = 2.92 \text{ in.} \end{aligned}$$

$$\begin{aligned} \theta &= \frac{w}{P} \left[\frac{L}{\cos U} - \frac{L}{U} \left(\frac{1 - \cos 2U}{\sin 2U} \right) \right] \\ &= \frac{20}{2500} \left[\frac{30}{0.915} - \frac{30}{0.41} \left(\frac{1 - \cos 0.82}{\sin 0.82} \right) \right] = 0.0095 \text{ rad} \\ &= 0.55^\circ. \end{aligned}$$

1.5 Introduction to Beams in Torsion

For purposes of discussion, beams in torsion are broken into two categories: circular beams, which are treated in Section 1.5.1, and non-circular beams, which are treated in Section 1.5.2. Circular beams are further divided into those with uniform cross sections (Section 1.5.1.1) and those with nonuniform cross sections (Section 1.5.1.2). Noncircular beams are divided into open noncircular beams (Section 1.5.2.1) and closed or hollow ones (Section 1.5.2.2), and the effect of end restraint on non-circular beams is treated in Section 1.5.2.3.

Section 1.5.3 treats the membrane and sandheap analogies for beams in torsion. Since the loading of the wires of helical springs is primarily torsional, they are listed under beams in torsion and treated in Section 1.5.4.

1.5.1 Circular Beams in Torsion

This section considers the torsion of solid or concentrically hollow circular beams.

1.5.1.1 Uniform Circular Beams in Torsion

Figure 1-42 shows a uniform circular beam in pure torsion. If the stresses in such a beam are in the elastic range, the stress distribution at a cross section is as shown in Figure 1-43.

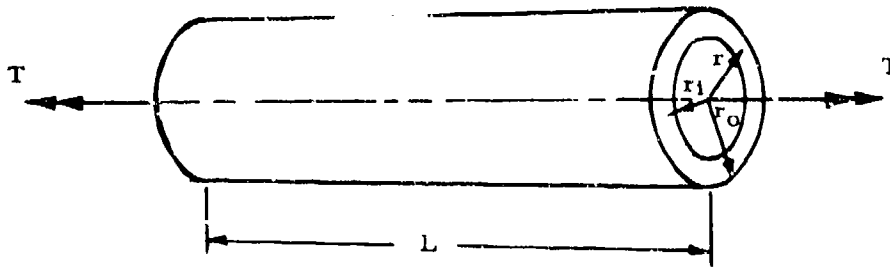


Figure 1-42. Uniform Circular Beam in Torsion

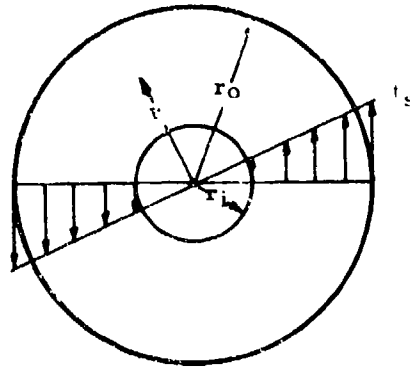


Figure 1-43. Stress Distribution of Circular Beam in Torsion

The shear stress at a distance r from the center is given by

$$f_s = \frac{Tr}{I_p} \quad (1-45)$$

The angle of twist of the beam is

$$\theta = \frac{TL}{GI_p} \quad (1-46)$$

Inserting the value of I_p for a circular cross section into Equations (1-45) and (1-46) gives

$$f_s = \frac{2 Tr}{\pi (r_o^4 - r_i^4)} \quad (1-47)$$

and

$$\theta = \frac{2 TL}{\pi (r_o^4 - r_i^4)G} \quad (1-48)$$

In order to treat solid circular shafts, r_i may be set equal to zero in Equations (1-47) and (1-48).

It should be noted that Equations (1-47) and (1-48) apply only to beams with circular cross sections.

The maximum shear stress occurs at the outside surfaces of the beam and may be computed by setting r equal to r_o in Equation (1-47). The maximum tensile and compressive stresses also occur at the outside surface and both are equal in magnitude to the maximum shear stress.

If a circular beam is twisted beyond the yield point until the outer portions are at the ultimate torsional stress, a stress distribution such as that shown in Figure 1-44 is obtained. The maximum torque that such a beam may sustain in static loading is given by

$$T_{max} = \frac{F_{st} I_p}{r_o} \quad (1-49)$$

where F_{st} is designated as the torsional modulus of rupture. This torsional modulus of rupture is shown graphically for steel beams in Figure 1-45.

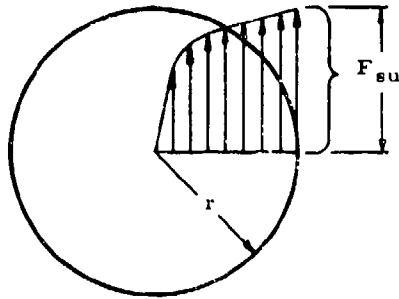


Figure 1-44. Plastic Stress Distribution of Circular Beam in Torsion

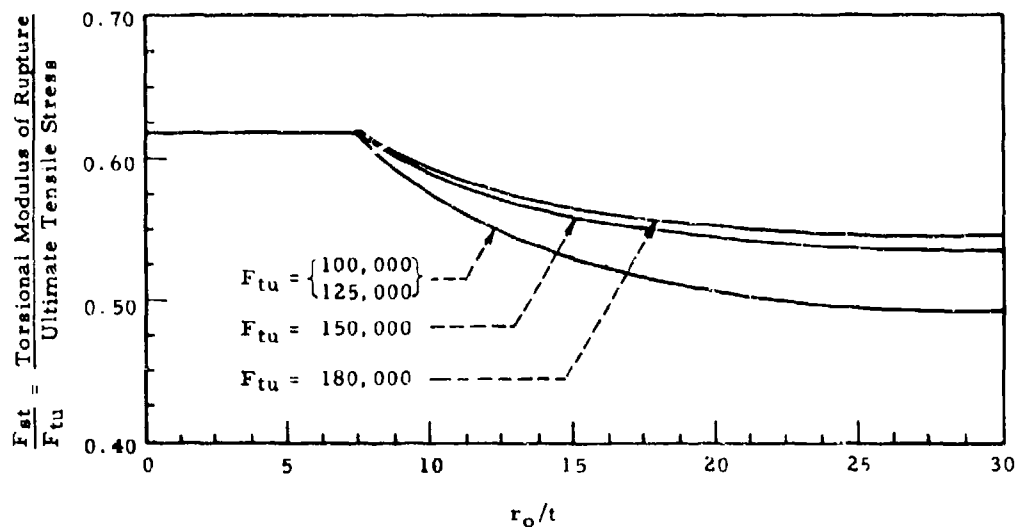


Figure 1-45. Torsional Modulus of Rupture for Steel Beams

In many cases, the torsional modulus of rupture of a material may not be available. These may be treated by assuming the uniform shear stress distribution shown in Figure 1-46.

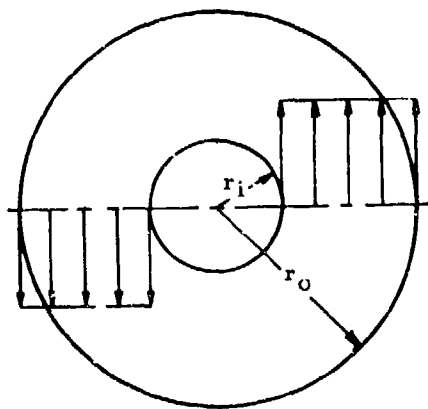


Figure 1-46. Assumed Plastic Stress Distribution of Circular Beam in Torsion

The magnitude of the uniform shear stress may be assumed to be equal to the yield shear stress (F_{sy}) for conservative results or the ultimate shear stress (F_{su}) for nonconservative results. In the first case, the maximum torque in the beam may be expressed as

$$T_{\max} = \frac{4}{3} \frac{F_{sy} I_p}{r_o} \quad (1-50)$$

and in the second case, the maximum torque in the beam may be expressed as

$$T_{\max} = \frac{4}{3} \frac{F_{su} I_p}{r_o} \quad (1-51)$$

It should be noted that the possibility of crippling in thin-walled tubes was not considered in the previous discussion. Crippling of circular tubes is treated in Chapter 8. These tubes should be checked for crippling.

1.5.1.2 Nonuniform Circular Beams in Torsion

When a circular beam of nonuniform cross section is twisted, the radii of a cross section become curved. Since the radii of a cross section were assumed to remain straight in the derivation of the equations for stress in uniform circular beams, these equations no longer hold if a beam is nonuniform. However, the stress at any section of a nonuniform circular beam is given with sufficient accuracy by the formulas for uniform bars if the diameter changes gradually. If the change in section is abrupt, as at a shoulder with a small fillet, a stress concentration must be applied as explained in Chapter 10.

Figure 1-47 shows a nonuniform circular beam in torsion.

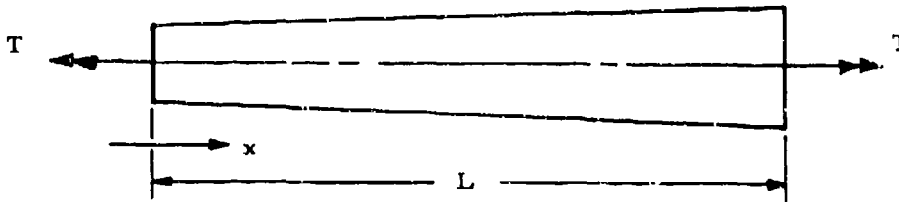


Figure 1-47. Nonuniform Circular Beam in Torsion

If its diameter changes gradually, its angle of twist is

$$\theta = \frac{T}{G} \int_0^L \frac{dx}{I_p} \quad (1-52)$$

This equation is used to obtain the formulas for θ for various beams of uniform taper that are shown in Table 1-13.